Dispersion state, interfacial phenomena and dielectric properties in high-permittivity polymer-based nanocomposites

Nicolas Uguen

N° d'ordre NNT :
2022LYSE1032

THESE de DOCTORAT DE L'UNIVERSITE DE LYON

opérée au sein de

l'Université Claude Bernard Lyon 1

Ecole Doctorale N° 34

École Doctorale Matériaux de Lyon

Spécialité de doctorat : Physique et Sciences des Matériaux

Soutenue publiquement le 15/03/2022, par :
Nicolas UGUEN

Dispersion state, interfacial phenomena and dielectric properties in high-permittivity polymer-based nanocomposites

---

Devant le jury composé de :

Fulchiron, René	Professeur	Université de Lyon	Président
Colin, Annie	Professeure	ESPCI	Rapportrice
Dantras, Eric	Maitre de conférences	CIRIMAT	Rapporteur
Genix, Anne-Caroline	Maître de conférences	Lab. Charles Coulomb	Examinatrice
Sotta, Paul	Directeur de recherche	IMP	Directeur de thèse
Trouillet-Fonti, Lise	Ingénieur de recherche	SOLVAY	Encadrante Solvay

« Réussir sans faire le bien c'est perdre ! »

Oreslan

Remerciements/Acknowledgements

Je tiens à remercier les nombreuses personnes qui ont contribué de près ou de loin à ce travail de thèse, mais aussi à ma formation et mon épanouissement durant ces quelques années.

Tout d'abord, j'adresse un grand merci à Florence Clément et Didier Long, respectivement directrice et directeur adjoint du Laboratoire des Polymères et Matériaux Avancés (LPMA) qui m'ont offert l'opportunité d'effectuer ce travail au sein de leur équipe. Merci Florence pour l'intérêt que tu as porté sur nos travaux et le lien que tu as fait entre les thésards et Solvay. Didier, merci pour les nombreux échanges et discussions intéressantes que nous avons eu.

Mes plus profonds remerciements vont à mes encadrants, Paul Sotta, directeur de thèse et Lise Trouillet-Fonti, encadrante industrielle.

A deux, vous avez su m'apporter un cadre de travail idéal, favorisant mes recherches et mon apprentissage dans une ambiance décontractée. Merci pour votre confiance, pour votre soutien et tout le temps que vous m'avez consacré pendant ma thèse. Merci également pour votre patience et vos corrections lors de la fastidieuse rédaction de mon manuscrit. Paul, merci pour ton enseignement et toutes les discussions scientifiques qui ont consolidé les bases scientifiques qu'on n'apprend plus au jeune aujourd'hui à l'école (ou peut-être que les jeunes ne retiennent plus, je ne sais plus). Lise, merci pour toute l'énergie que tu as employé pendant toutes ces années afin de rendre cette thèse la plus enrichissante pour moi en favorisant les nombreuses collaborations que j'ai pu réaliser. Une belle synergie s'est créée de notre complémentarité, favorisant un avancement aisé dans ces thématiques relativement nouvelles au sein du laboratoire.

Je tiens à remercier Annie Colin et Eric Dantras, pour avoir accepté de rapporter ce travail, et d'avoir pris le temps de l'évaluer. Merci à Anne-Caroline Genix et René Fulchir pour avoir accepté de participer à la lecture du manuscrit et au jury lors de ma soutenance. Merci à toutes et à tous pour la discussion lors de la soutenance qui a été très enrichissante.

Je souhaite également remercier Laurianne D'Alençon et Julien Jolly pour les collaborations autour des questions de caractérisation et de modification de chimie de surface des particules ainsi qu'autour des paramètres d'interactions. Nos discussions

nous ont toujours été d'une grande utilité et votre contribution dans ces travaux en est d'autant plus importante. Merci également à Julien Laurens, Marie Plissonneau et Ludivine Malassis pour votre implication dans ces collaborations.

A huge thanks to Alessio Marani and Ryan Murphy for having followed my researches with interest and for the interesting discussions we had.

Merci à Mathieu Oullion, Olivier Giacomoni et Arnaud Collin pour m'avoir accueilli dans vos laboratoires au bâtiment K et pour toute l'aide que vous m'avez apportée autour de mes essais de diffusion dynamique de la lumière.

Merci à tous ceux qui m'ont aidé au cours de ma thèse au sein de PM2D, que ce soit pour les formations aux outils, pour des discussions scientifiques ou pour l'ambiance générale du labo: Sylvie Ghiringhelly, pour ta gentillesse, ton aide tout au long de ma thèse et ta patience sur la thématique HSE Nano; Sandrine Rossi pour ton accueil, ta bienveillance et ton aide; Robert Stutz, Violaine Ducru et Christiane Prebet pour vos formations, vos conseils et votre bonne humeur au labo physique ; Olivier Bronchard pour la bonne ambiance qui règne dans la halle méca, Michel pour toutes tes histoires de vélo, de voile et de rando; Vincent Curtil pour tous ces bons moments passés ensemble autour d'une pétanque ou d'une bonne bière ; Fabrice Millet, Thibaut Marque, Mathieu Taban, Xavier Thierry, Thierry Gisbert et Tiffany Bergey pour ces bons moment en salle café; Olivier Andres; Olivier Gilbain ; Elisabeth Chaland ; Olivier Sanseau pour tes conseils en début de thèse; Jérôme Bikard pour toutes les discussions et ton aide sur la partie champs électriques et simulations; Rabih Al Orabi pour tes calculs DFT et ton implication en début de thèse; Anthony Bocahut pour nos discussions et ton intérêt pour mes travaux en fin de thèse.

Un grand merci au service Microscopie : Pauline Grau pour m'avoir fait confiance dès le premier jour, pour tout le temps que tu m'as consacré, les échanges très intéressants qu'on a eu et pour ton humanité ; Clémence Abadie pour ton aide ; Baptiste, tes formations étaient irréprochables mais c'est pour toute autre chose que je te remercierai plus tard.

Merci aussi à Alexandre Comment, Virginie Reynes, Haniya Ait Mourid et Thomas Lippens pour votre aide sur les thématiques HSE et notamment sur la partie Nano qui nous à donner du fil à retordre.

Merci également Alexandra Siot, Laetitia Allary, Nadia Delon-Anik pour toutes vos analyses qui ont grandement contribué à mes travaux.

Merci aux thésards, intérimaires, stagiaires qui ont contribué à apporter cette belle ambiance de travail pendant ces plus de trois ans!

Un grand merci à mon équipe de EAB, Francesco Pedroli et Julien Fernandez. Un grand merci pour toutes ces discussions scientifiques qui ont grandement façonnées ma thèse. vous avez été mes mentors. Julien, je ne te remercierais jamais assez pour toute

cette vitamine D, tous ces beaux moments qu'on a passés ensemble à Lyon, partout en France et en Europe, autour de concert, de festival, d'activité sportive ou d'une simple Tatanka. Francesco, gracie mille per tutti, pour ta bonne humeur inébranlable et la bonne ambiance que tu sais si bien créer autour de toi en toutes circonstances, pour ces deux ans de collocation et ton accueil lors de mes visites en Italie. En fait, merci pour votre amitié car c'est de ça qu'il s'agit!

Merci ensuite à mon équipe d'évadées, Eléonore Mathis et Melissa Rambo pour ces escapades créatives et leur goût de liberté, pour ces moments suspendus où le temps s'arrête, pour ces passages à la MB et toutes les bonnes soirées qu'on y a passé. Merci pour vos joies de vivre et votre bonne humeur inépuisable.

Merci Rita Martins pour ta gentillesse, ta bienveillance, et pour tous ces bons moments passés autour de notre thé de 15h. Merci Baptiste Gros pour toutes ces sessions musicales, de la simple jam session aux envolés lyriques sous les étoiles tropicales, aux airs d'apothéose et aux notes gratinées. Merci Thomas Merlette pour ton aide autour d'équations de champs électrique ou de pluie qui tombe, mais surtout pour les multiples délires qu'on a eu autour de bières et de pinceaux. Merci Agathe Charvet pour avoir partagé mon amour de la Bretagne et du Reggae et pour tous les bons moments qu'on a passé. Merci Stéphanie Djukic pour ton accueil dans le bureau 103c et ces bons moments autour de ce ficus (RIP). Merci Agathe Virfeu pour la bonne ambiance que tu as amené et tous les bons moments passés au court-circuit ou ailleurs. Merci Héloïse Willeman pour ta bonne humeur et ta bienveillance. Merci Ilan pour toutes ces sessions musicales. Merci Anne Colloigner d'avoir partagé ton amour de la montagne, pour nos discussions crochets/tricots et pour ce magnifique avocatier. Merci Anne Charlotte Le Guluche, pour ces très bonnes soirées passées lors de tes passages sur lyon. Merci Carolina Franzon pour tous les bons moments passés ensemble, les discussions sur la polarisation et ton programme matlab qui m'aura bien servi. Merci à Aurélien, pour nos belles soirées électroniques parmi les Joe. Merci à Jessica, Ludovic, Alexandre, Océane, Emmanuelle, pour ces bons moments et pour l'ambiance au labo.

Je finirai par remercier ma famille sans qui tout ça n'aurait pas été possible.

Résumé en français

Nicolas UGUEN

Effet de l'état de dispersion et de la modification de surface de particules à haute permittivité sur les propriétés diélectriques de nanocomposites à base polymère.

Dans le domaine des matériaux nanocomposites isolants électriques à base de polymères, les propriétés diélectriques peuvent être ajustées en modifiant la composition et/ou la morphologie du composite (rapport d'aspect, orientation, état de dispersion...). La modification de la chimie de surface des particules constitue également un outil de design des propriétés diélectriques des composites via la modification des propriétés à l'interfaces entre les particules et la matrice. Largement mentionnée dans la littérature, la modification de surface des particules entraîne bien souvent une modification de l'état de dispersion des particules dans les matériaux composites finaux. L'interdépendance entre les propriétés aux interfaces et l'état de dispersion complexifie la distinction de leurs effets respectifs sur les propriétés diélectriques et donc l'étude des mécanismes et phénomènes physiques impliqués dans les relations structure-propriétés. Cette étude expérimentale a pour but d'approfondir la compréhension de ces mécanismes en dissociant la modification de surface des particules de l'état de dispersion obtenu dans les composites. Pour cela, des nanocomposites à matrice Poly(vinylidene fluoride-co-hexafluoropropylene) (PVdF-HFP) chargés de nanoparticules de $BaTiO_3$ ont été choisis comme système d'étude et fabriqués par voie solvant.

La première partie de ce travail a consisté en l'étude des paramètres d'interaction via la théorie de Hansen. Cette théorie a permis la détermination expérimentale des paramètres d'interaction de Hansen du PVdF-HFP et des particules de $BaTiO_3$ et leur utilisation pour prédire leur interaction avec divers solvants. Cette approche spécifique a permis de rationaliser le procédé de fabrication par voie solvant des nanocomposites PVdF-HFP:$BaTiO_3$ et d'aboutir au contrôle de l'état de dispersion des particules au cours du procédé de fabrication et par conséquent dans les films de nanocomposites finaux. Ce contrôle, basé sur la sélection d'un solvant aux paramètres d'interactions spécifiques, a donc été réalisé sans avoir eu recours à une modification de surface des particules et donc sans avoir changé les propriétés aux interfaces particules/matrice.

La deuxième partie de cette étude a été consacrée à l'étude de l'effet de l'état de dispersion des particules sur les propriétés diélectriques de ces nanocomposites PVdF-HFP $BaTiO_3$. En utilisant le procédé par voie solvant développé en première partie, des échantillons de nanocomposites PVdF-HFP:$BaTiO_3$ présentant soit des particules relativement bien dispersées, soit des agglomérats de taille contrôlée, ont été fabriqués. Une première série de caractérisations physico-chimiques et structurales sur ces échantillons a permis de confirmer le bon contrôle de l'état de dispersion et de démontrer qu'aucune modification de la structure cristalline de la matrice PVdF-HFP n'est provoquée par la présence des particules. Les propriétés diélectriques de ces échantillons ont ensuite été caractérisées par spectroscopie diélectrique à basse (10^{-2}-10^7 Hz) et haute fréquence (10^6-10^9 Hz) entre -40 et 60 °C. Les résultats, analysés en fittant les différents processus de relaxation observés avec une équation de type Cole-Cole, ont permis de mettre en évidence deux effets distincts reliés d'une part à l'état de dispersion des particules et d'autre part aux propriétés diélectriques des nanocomposites. La première concerne l'amplification de la permittivité complexe de la matrice polymère par la forte polarisation des nanoparticules de $BaTiO_3$ dont la constante diélectrique est évaluée à environ 20 fois celle du PVdF-HFP. La plus forte amplification observée dans le cas des nanocomposites dans lesquels les particules sont agglomérées a été interprétée comme le résultat de l'augmentation du volume de polymère occlu au sein du nanocomposites En effet la percolation locale des particules à haute permittivité induit une réduction du champ électrique dans la fraction de polymère présent à l'intérieur des agglomérats, augmentant ainsi la fraction volumique effective des particules et donc la permittivité globale du nanocomposite. La modélisation de la polarisation dans le cas de systèmes 2D équivalents confirme l'interprétation proposée. La seconde relation structure-propriétés observée concerne l'augmentation de l'amplitude d'un mécanisme de polarisation de type Maxwell-Wagner-Sillar (MWS) observé à basse fréquence avec l'état d'agglomération des particules. On présume que ce mécanisme est associé à de la conduction aux interfaces entre les particules et la matrice, directement liée présence d'eau à la surface des nanoparticules. Lorsque les nanoparticules percolent localement, la migration des charges électrique s'effectue sur de plus grande distance au sein des agglomérats et contribue donc à l'augmentation de l'amplitude de la polarisation interfaciale. Après séchage des échantillons, l'amplitude de la polarisation de type MWS est considérablement réduite dans les nanocomposites.

Enfin, la modification de la chimie de surface des nanoparticules de $BaTiO_3$ a été réalisée et étudiée sous divers angles. Dans un premier temps, l'impact de la modification de surface sur les paramètres d'interaction des particules a été caractérisé. L'ajout de groupes chimiques possédant des paramètres d'interaction différents de ceux

de la particule a entraîné une modification cohérente de son comportement en suspension et donc de ses paramètres d'interaction. Trois séries de nanocomposites à matrice PVdF-HFP ont ensuite été fabriquées avec des particules de $BaTiO_3$ ayant trois chimies de surface différentes et plusieurs états de dispersion. L'étude de ces échantillons par spectroscopie diélectrique n'a néanmoins pas permis d'identifier d'effet significatif des propriétés aux interfaces sur la permittivité complexe des nanocomposites. En effet, un effet prépondérant du procédé de modification de surface a été observé sur les propriétés diélectriques.

Ces travaux constituent une approche globale prenant en compte les interactions moléculaires à l'œuvre durant le procédé de fabrication des nanocomposites, l'état de dispersion des particules, et jusqu'aux propriétés diélectriques macroscopiques qui en découlent. Ces travaux offrent une ouverture à l'approfondissement de ces relations structure-propriétés en caractérisant de manière plus poussée la structure même des agglomérats et son effet sur les propriétés diélectriques et de transport de charges dans les nanocomposites à haute permittivité. L'étude des propriétés diélectriques à fort champ de ces matériaux, et cela jusqu'au claquage, pourrait également permettre d'approfondir la compréhension des mécanismes de transport de charges et mettre en évidence l'influence des propriétés aux interfaces.

Abstract

Polymer-based nanocomposites with high-permittivity are of main interest for insulating materials for dielectric use like energy storage. Their design consists in finding the best compromise between the good electrical insulating properties of the matrix and the high permittivity of the filler. The control of the filler dispersion state, the interfacial feature and the electronic structure is essential in order to control the dielectric properties in nanocomposites.

The methodology proposed in this work has consisted in controlling the dispersion state of $BaTiO_3$ nanoparticles (NP) in Poly(vinylidene fluoride-co-hexafluoropropylene) (PVdF-HFP) matrix in order to separately study the effect of NP dispersion state, of interfacial features and of electronic structure on the dielectric properties in nanocomposites.

An extended study of the Hansen interaction parameters has allowed a rationalization of the nanocomposites solvent casting process, from the quality of the polymer matrix to the dispersion state of the NPs. The Hansen Solubility Parameters (HSPs) and Hansen Dispersibility Parameters (HDPs) of PVdF-HFP and $BaTiO_3$ NPs were experimentally determined by solubility test and sedimentation tests, respectively. Scanning Electron Microscopy (SEM) and Dynamic Light Scattering were used to characterize the NP dispersion state throughout the fabrication process. Two methodology based on the selection of a solvent with appropriate HSP values was proposed to control the NP dispersion state in nanocomposites.

The fabrication of PVdF-HFP:$BaTiO_3$ nanocomposites with either well dispersed or agglomerated particles has allowed studying the effect of NP dispersion state on dielectric properties at low electric fields. They were characterized by Broadband Dielectric Spectroscopy (BDS) and High Frequency Dielectric Spectroscopy (HFDS). Two different effects were found to depends on both the NP content and their dispersion state:

1- The amplification of the matrix permittivity by the high-permittivity fillers was found to increase with $BaTiO_3$ NP content and to be higher in nanocomposites with agglomerated NP as compared to well dispersed. The presence of occluded polymer inside the agglomerates that leads to increase the effective content of NP has been proposed to explain such effect of the dispersion state
2- An additional Maxwell-Wagner-Sillars polarization related to water-assisted charge carrier conduction at the surface of the NPs was found to have larger magnitude in nanocomposites with agglomerated NPs as compared to well

dispersed NPs. The local percolation of the interphases within the agglomerates was proposed to explain this result.

Finally, surface modifications of the NPs were performed with either Poly(Methyl-MethAcrylate) (PMMA) or alkyl chains. The modified NPs were characterized by Fourier Transformed Infra-Red (FTIR) spectroscopy and Thermogravimetric Analysis (TGA). The stability of the NP suspension in some solvents was affected by surface modification, which is interpreted as a proof that HDPs can be modified by NP functionalization to tune the interactions in nanocomposite fabrication process and control its dispersion state.

Nanocomposites were prepared with the modified NPs and BDS and HFDS were used to characterize their dielectric properties. No significant effect of the surface modification was found at low electric fields. However, the modification process is thought to have introduced impurities responsible for unexpected dielectric behaviour as compared to nanocomposites filled with as received NPs.

Table of Contents

List of Abbreviations

Abbreviations:

BDS: Broadband Dielectric Spectroscopy
BET: Brunauer, Emmett, and Teller
CCTO: $CaCu_3Ti_4O_{12}$
CED: Cohesive Energy Density
DC: Direct Current
DCM: Dichloromethane
DFT: Density Functional Theory
DLS: Dynamic Light Scattering
DMF: Dimethyl Formamide
DRIFT: Diffuse Reflectance Infrared Fourier Transform
DSC: Differential Scanning Calorimetry
FTIR: Fourier-Transformed Infrared Spectroscopy
HDP(s): Hansen Dispersibility Parameter(s)
HFDS: High Frequency Dielectric Spectroscopy
HOMO: Highest occupied molecular orbital
HSP(s): Hansen Solubility Parameter(s)
LDPE: Low Density Polyethylene
LoF: Laboratory of Future
LUMO: Lowest unoccupied molecular orbital
MEK: Methyl Ethyl Ketone
MWS: Maxwell-Wagner-Sillars
NP(s) : nanoparticle(s)
OM: Optical Microscopy
PC: polycarbonate
PDI Polydispersity Index ()
PEEK: PolyEtherEtherKetone
PMMA-co-MAA : Poly(Methyl-MethAcrylate-co-MethAcrylic Acid),
PVD: Physical Vapour Deposition
PVdF: Poly(vinylidene fluoride)
PVdF-HFP: Poly(vinylidene fluoride-co-hexafluoropropylene)
RED: Relative Energy Distance
RH: Relative Humidity
RICL: Research & Innovation centre of Lyon
RST: Relative Sedimentation Time

RT: Room temperature
SEM: Scanning Electron Microscopy
TGA: Thermogravimetric analysis
VFT: Volgel-Fulcher-Tammann

Introduction

General objectives

Synthetic polymers have attracted a wide interest as electrical insulators for a variety of applications due to their unique properties in comparison with paper, natural rubber and ceramic materials[1]. Indeed, their low conductivity, high electrical strength, low density, high flexibility, ease of processing and low cost make them essential materials in energy and electricity handling (transport, production, storage, conversion, signal transformation, telecommunication…)[2–4].

The current increasing demand for electric energy vectors comes with the growing demand for dielectric material solutions with high performances. For several applications including energy storage, high permittivity materials with good electrical insulating properties are required. However, most polymers possess a low relative permittivity (ε_r~2-3) which may limit their application range. Thus, new material solutions are found in high performance polymers such as fluoropolymers and in polymer-based (nano)composites[5].

Polymer-based composites offer the possibility of tuning the dielectric properties. Indeed, introducing inorganic fillers with high permittivity into a polymer matrix leads to increase the effective permittivity of the composites as compared to the matrix alone. Nevertheless, dielectric losses, electrical strength and thus the global dielectric properties of composites can be degraded by the presence of inorganic fillers due to heterogeneous polarization, field effects and charge carrier conduction. The design of dielectric properties in composite materials consists in finding the best compromise between effective permittivity, dielectric losses and electrical strength[6].

The miniaturization of dielectric devices has led to the emergence of nanocomposites in which inorganic fillers at the nanoscale are introduced. This leads to the large increase of the interfacial area which is increasingly considered as having a strong influence on the dielectric properties of nanocomposites[7].

The design of polymer composites with controlled dielectric properties requires a thorough understanding of the relationships between the physicochemical features of the raw materials, their structures at all scales and the final macroscopic properties of the composite.

In polymer-based nanocomposites, the effects of the filler structural and geometrical features (shape, aspect ratio, orientation...) on the effective permittivity, dielectric losses and electric strength have been widely studied over the past decades[8,9]. However, their exact influence on the above-mentioned compromise is not fully clear yet. Interfaces have been highlighted as an additional factor that has to be considered in this compromise[7]. The control of the interfaces by surface modification of the fillers has

shown promising results in improving the dielectric properties of polymer-based nanocomposites[10]. Nevertheless, the relationships between interfacial features and dielectric properties in these materials are complex: 1) interfaces are difficult to characterize directly 2) modifying the interfaces (by surface modification of the fillers for example) results in several structural modifications (dispersion state, morphology of the interfaces, electronic structure at the interface, etc) that all influence the dielectric properties of nanocomposites. This makes the discrimination of the various factors complex[7,10].

More recently, the electronic structure of nanocomposites has been introduced as a key factor influencing charge carrier dynamics and thus determining the electrical insulating properties in nanocomposites. Again, the complexity in characterizing the local electronic structure represents a technical barrier in the study of their effect on the dielectric properties in nanocomposites[11–14].

The aim of this PhD project is to further investigate the effects of structural parameters, interfacial features and electronic structure on the dielectric properties of nanocomposites. In order to discriminate these effects, PVdF-HFP-based nanocomposites filled with $BaTiO_3$ nanoparticles (NPs) were fabricated with independently controlled dispersion states and interfacial properties. First, the study of the interaction parameters during the fabrication process by solvent casting of the nanocomposites enabled the control of the NP dispersion state through the selection of a solvent with specific interactions with both PVdF-HFP and $BaTiO_3$ NPs. Then the fabrication of nanocomposites with controlled dispersion state without NP surface modification enabled the study of the relationships between dispersion state and dielectric properties in polymer-based nanocomposites. Finally, NP surface modification was carried out in order to assess the influence of the interfacial features on dielectric properties in composites with identical dispersion state.

Context

This PhD thesis was carried out in the Laboratoire Polymère et Matériaux Avancés (LPMA) UMR5268, a joint research laboratory between CNRS and Solvay. This work was performed in collaboration with the GBU Speciality Polymer of Solvay with the aim of supporting their development of polymer-based materials for dielectric uses. Scientific and technical supports were provided by Laurianne D'Alençon and Marie Plissoneau from FIM laboratory (Solvay) and Julien Laurens (PhD student at LoF) and Julien Jolly from LoF (Solvay) for particle surface characterization and modification. In this work, the relationships between structure, physicochemical features and dielectric

properties have been investigated in polymer-based nanocomposites with high permittivity.

Structure of the manuscript

The first chapter of this manuscript presents the state of the art on polymer-based nanocomposites with high effective permittivity and good dielectric properties. This section results in the methodology used in this study. The second chapter is dedicated to the presentation of the studied materials as well as the description of their fabrication process and the experimental techniques used to characterize their structural and thermal properties.

The third chapter presents the study of the interaction parameter between the constituents during the nanocomposite fabrication process and the resulting experimental method enabling the control of the NP dispersion state in the final materials. Then, the effect of the NP dispersion state on the dielectric properties is addressed in the fourth chapter. Finally, the surface modification of the $BaTiO_3$ NPs was carried out in order to assess the effect of the interfacial feature on dielectric properties in polymer-based nanocomposites (chapter 5).

Chapter 1. State of the Art

1.1 Introduction: properties of interest

In microelectronics, materials with high permittivity and good electric insulating properties are required in the design of devices such as energy storage capacitors, actuators, transistors… For capacitors the figure of merit is the electric energy density U_e (J/m^3) that can be stored in the material and is defined as follows:

$$U_e = \frac{1}{2}\varepsilon_0 \varepsilon'_r E^2 \quad (1.1)$$

with ε_0 the permittivity of the vacuum (8.85x10^{-12} F/m), ε'_r the real part of the relative permittivity of the material, and E the applied electric field (V/m).

Equation (1.1) shows that the energy density is proportional to ε'_r (in the linear regime, where ε'_r does not depend on the electric field) and to the square of the electric field. For a given material with a constant permittivity, the energy density is limited by the maximum electric field that can be applied to the material without damaging it. This value of the electric field is called electric strength (or breakdown field) and will be denoted E_{BD}. In the design of high energy density materials, both the permittivity and electric strength have to be increased as much as possible.

Another critical point is the dielectric losses ε''_r of the materials. They are due to friction or electrical conduction and result in energy consumption converted into heat within the material. These dielectric losses are detrimental for two reasons: (1) a part of the stored energy is lost and (2) the associated heat generation may significantly increase the temperature of the device and alter its functioning. Therefore, reducing the dielectric losses is also a key issue in designing polymer composites with high energy density. In the following section, these different properties will be detailed.

The physicochemical and structural features governing these properties will be presented for bulk materials and then for composites on the basis of literature data. Yet unclear points and open questions shall be then pointed out. In the last part, the methodology used in the work will be detailed.

1.2 Dielectric properties

In this part, the intrinsic properties of bulk materials and thus of each component of composite materials are considered.

1.2.1 Complex Dielectric permittivity ε^*

Polarization - ε'

The polarization of a material refers to the motion of the electrical charges it contains under an external electric field. These electrical charges can be electrons, holes, positive and negative ions, permanent and induced dipoles…

Let us first consider two parallel plate electrodes of infinite area separated by vacuum. Applying an electrical potential difference V between the two electrodes generates an electric field whose magnitude $\|\vec{E}\|$ is:

$$\|\vec{E}\| = \frac{V}{d} = \frac{\sigma_0}{\varepsilon_0} \tag{1.2}$$

where d is the distance between the two electrodes and σ_0 the absolute value of the surface charge density on the electrodes, as shown in Figure 1.1.

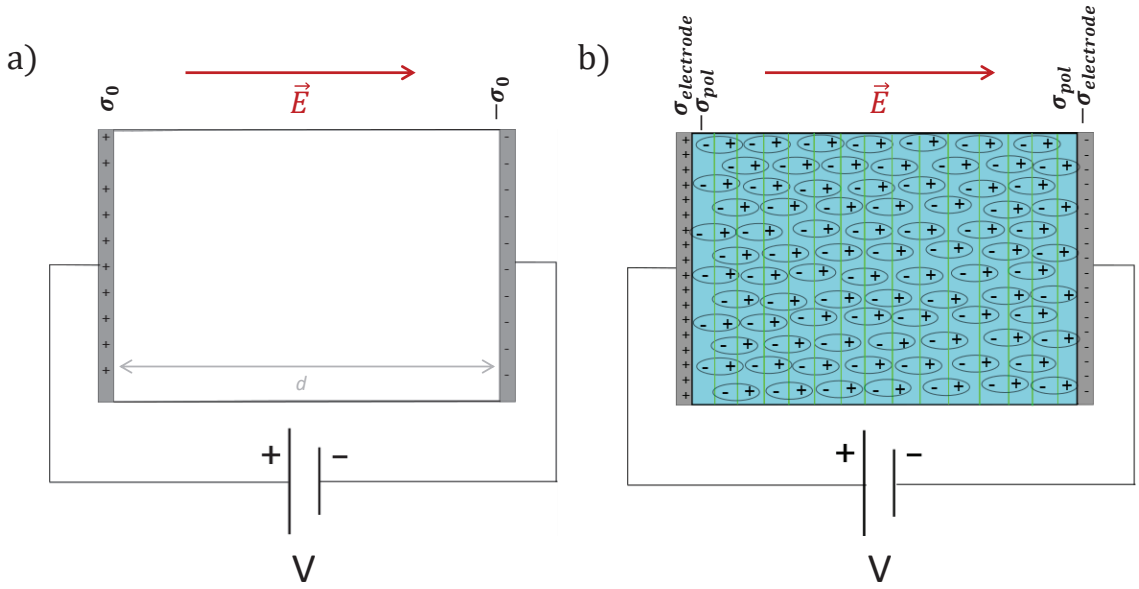

Figure 1.1: Representation of a parallel plate capacitor containing a) vacuum and b) a dielectric material between its electrodes.

Let us now introduce a perfect dielectric material between these electrodes, as presented in Figure 1.1 b). A so-called "perfect" dielectric material implies that it contains no free charges (electrons, holes or ions). Under the electric field, the bound electric charges present in the material (permanent dipoles for example) move and create surface charge densities σ_{pol} and $-\sigma_{pol}$ in the material near the electrodes (which are oppositely charged). These are called polarization charges. It follows that the total surface charge density $\sigma_{electrode}$ contained in the electrodes must increase to counterbalance the polarization of the material and maintain the magnitude of electric field now defined as:

$$\|\vec{E}\| = \frac{V}{d} = \frac{\sigma_{electrode}}{\varepsilon_0 \varepsilon'_r} \tag{1.3}$$

with

$$\sigma_{electrode} = \sigma_0 + \sigma_{pol} = \varepsilon'_r \sigma_0 \tag{1.4}$$

The electrical displacement $\vec{D}$ (C/m^2) is expressed as:

$$\vec{D} = \varepsilon_0 \vec{E} + \vec{P} = \varepsilon_0 \varepsilon'_r \vec{E} \quad (1.5)$$

Considering a supposedly homogeneous material, the polarization is more generally expressed as:

$$\vec{P} = \varepsilon_0 \chi \vec{E} = \varepsilon_0 (\varepsilon'_r - 1)\vec{E} \quad (1.6)$$

with $\vec{P}$ the polarization and χ is the dielectric susceptibility.
In a parallel plate capacitor, $\sigma_{electrode}$, σ_0, and σ_{pol} correspond to $\|\vec{D}\|$, $\varepsilon_0\|\vec{E}\|$, and $\|\vec{P}\|$.

Complex permittivity ε*(ω)

The above-mentioned consideration with a static field E is also valid for an electric field $E(\omega)$ oscillating at the angular frequency ω and defined as:

$$E(\omega) = E_0 \cos(\omega t) \quad (1.7)$$

with E_0 the magnitude of the electric field.

As well as with a static electric field, the oscillating field will induce electrical charge motions or dipole reorientation and thus polarization in the material. This polarization may be out of phase with the field which leads to use a complex permittivity ε* presented in equation (1.8)[15].

$$\varepsilon^* = \varepsilon' - j\varepsilon'' = |\varepsilon| e^{-j(\omega t + \delta)} \quad (1.8)$$

where ε' is the real part, ε'' the imaginary part of the permittivity and j the imaginary number. The real part of the permittivity corresponds to the "elastic" charge displacement (capacitive/conservative part) and the imaginary part to the "viscous" charge motion (resistive/dissipative part).

Dielectric losses ε'' and loss factor tan(δ)

The ratio between the dissipative and the conservative parts is called loss factor (or tan(δ)) and expresses the fraction of energy lost during a polarization-depolarization process. It is expressed as:

$$\tan(\delta) = \frac{\varepsilon''}{\varepsilon'} \quad (1.9)$$

In materials, both polarization mechanisms and conductivity impact dielectric losses. The polarization mechanisms observed at frequency below $10^{10\text{-}11}$ Hz are relaxation phenomena characterised by relaxation frequencies (The various polarization mechanisms are further detailed p.13). The contribution of such polarization mechanisms to dielectric losses is due to friction and can be described by

the Debye model equation (1.10) in the case of one single relaxation time τ. At frequencies well above the relaxation frequency $\tau^{-1}$of the polarization phenomena, the charges (dipoles or charge carriers) do not move fast enough to induce dielectric losses. At frequencies well below the relaxation frequency, charges/dipoles follow the field instantaneously and thus move in phase with the field. Temperature impacts the relaxation frequency of the polarization processes so that dielectric properties are temperature-dependent: increasing temperature leads to increasing the relaxation frequency. At a given temperature, a typical Debye relaxation process is illustrated in Figure 1.2.

$$\varepsilon'' = \frac{\Delta\varepsilon\omega\tau}{1+\omega^2\tau^2} - \frac{\sigma_{DC}}{\omega\varepsilon_0} \qquad (1.10)$$

The Direct Current (DC) conductivity, denoted σ_{DC}, only impacts the dielectric losses ε". Since the σ_{DC} contribution to ε" is proportional to $1/\omega$, it increases considerably as the frequency decreases. It corresponds to the electrons flux that transfers from/to the electrodes through the material. At low electric field, σ_{DC} is considered to be independent of time and can be expressed as:

$$\sigma_{DC} = \sum_k q_k \mu_k n_k \qquad (1.11)$$

where q_k, μ_k, n_k are the effective charge, mobility and charge density of each charge carrier k.

The electronic conductivity concerns the global electron and hole transport through a material and may involve different mechanisms presented in the following paragraph.

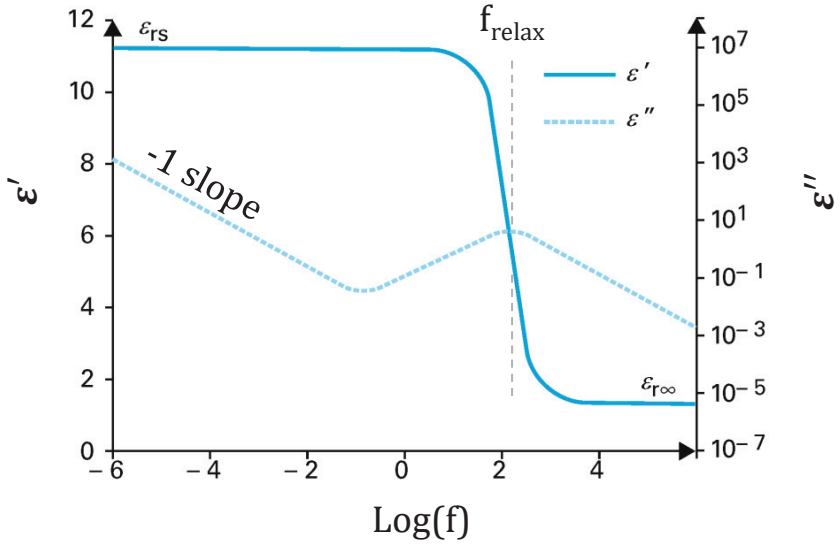

Figure 1.2: ε' and ε" related to a Debye polarization process combined with DC conductivity[16].

Energy density U_E – Nonlinear regime

At given frequency and temperature, in the linear regime, i.e. at low electric field, the polarization P and the electrical displacement $D = P + \varepsilon_0 E$ are linear functions of the electric field (blue curve in Figure 1.3). The permittivity is then constant and the energy density stored in the material is then described by equations (1.12) and corresponds to the area contained between the ordinate axis (D) and the curves (grey zones in Figure 1.3).

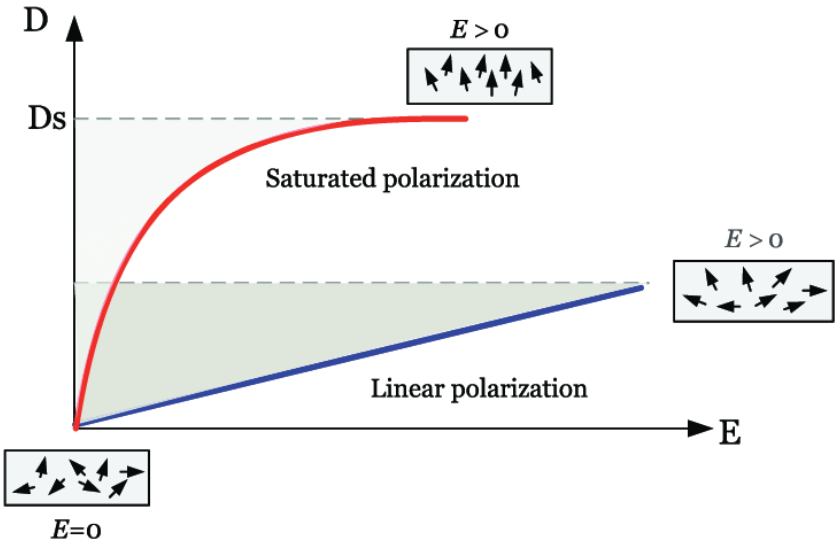

Figure 1.3: Polarization behaviour with electric field intensity[17]. The grey areas correspond to the stored energy.

If the electric field is raised above the linearity limit, which depends on the considered material, the polarization is no longer proportional to the electric field and the permittivity is not constant (for example in the case of saturation or ferroelectricity). The saturation case is illustrated by the red curve in Figure 1.3. The energy storage is expressed by equation (1.12).

$$\begin{cases} dU = EdD = \varepsilon_0 \varepsilon'_r EdE \\ U_{stored} = \int_0^{E_{max}} EdD = \int_0^{E_{max}} \varepsilon_0 \varepsilon'_r EdE \end{cases} \quad (1.12)$$

For a constant permittivity, analytic solving of equation (1.12) gives equation (1.1) presented in section 1.1.

Finally, non-linear permittivity affects the energy density of a material. For this reason, ferroelectricity and polarization saturation must be avoided in materials for energy storage applications.

In the absence of electrical conductivity, D corresponds to the cumulated electric charges brought to the electrodes by the external circuit per electrode surface unit. It may also be expressed as:

$$D(t) = \int_0^t j(t')dt' \tag{1.13}$$

where j is the current density (A/m^2) in the external circuit.

As seen before, in real materials, dielectric losses (friction during polarization and DC conductivity) generate an out of phase polarization which results in energy losses. Thus, Equation (1.13) is not valid any longer. Lissajous representations (Figure 1.4) well illustrate both the effects of non-linear ε'_r and of dielectric losses on the energy density. It consists in plotting the integral of the current density j with time as a function of the electric field. This representation is analogous to the stress-strain cycles in mechanics. Various types of dielectric response under oscillating electric field are plotted in Figure 1.4.

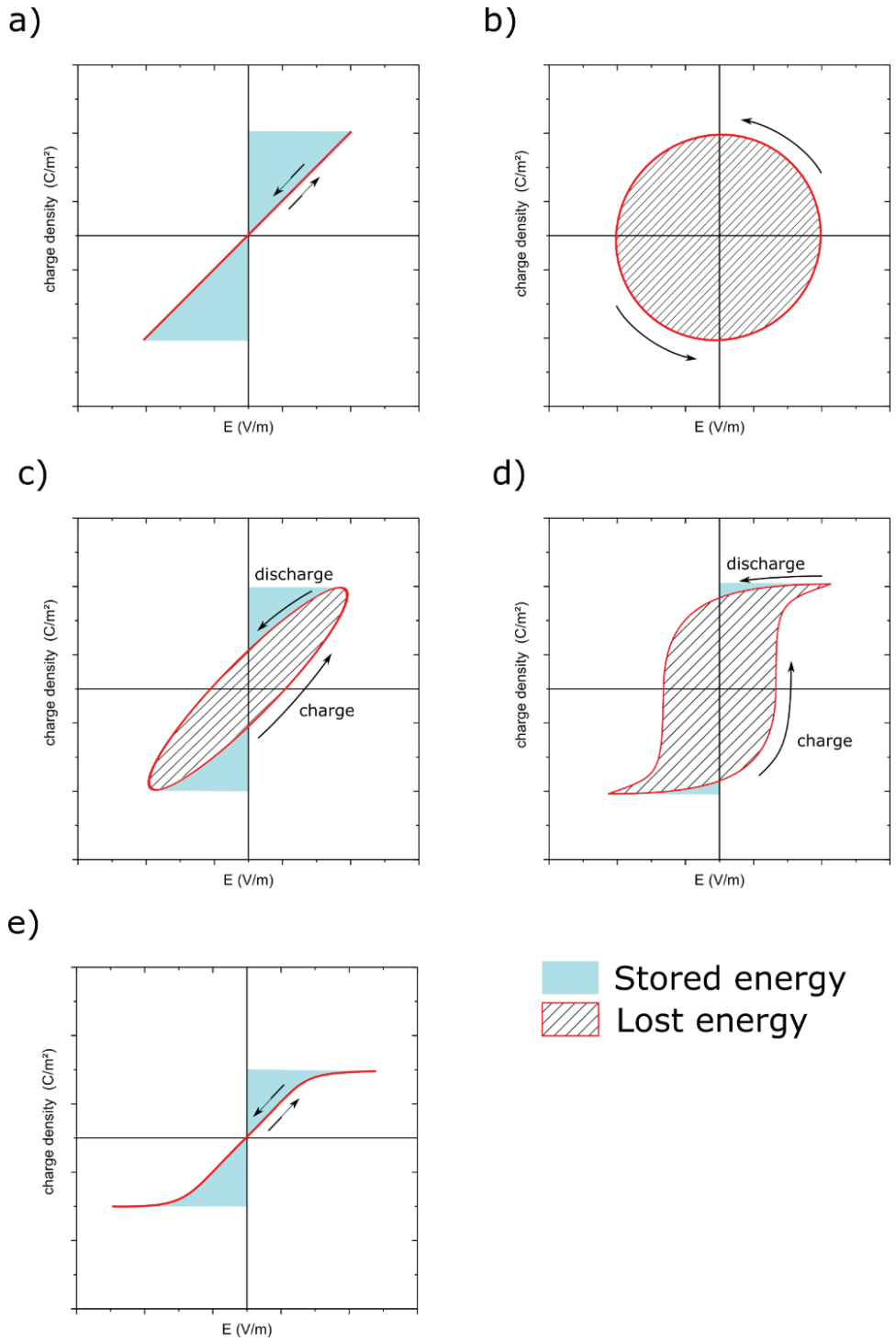

Figure 1.4: Lissajous representation of a) an ideal capacitor, b) an ideal resistance, c) a real linear dielectric material, d) a non-linear ferroelectric material, and e) a material with polarization saturation.

In Figure 1.4 a), the material is a perfect dielectric with no dielectric loss. As seen before, the energy stored is the area of the blue zone. Case b) is the behaviour of an ideal conductor having a constant conductivity (Ohmic behaviour). In this case, the energy is entirely lost by dissipation (Joule effect). In a real linear dielectric material,

both conductivity and polarization contribute to the measured current density and to the resulting charge density as presented in Figure 1.4 c). The striped area corresponds to the energy lost during one polarization cycle whereas the blue area corresponds to stored energy. Energy is lost by dissipation during the polarization (polarization out of phase with the field) or by charge conduction (DC current). It is important to note that electrical conduction in a material reduces its energy storage efficiency.

Case (d) represents the behaviour of a ferroelectric material in which a residual polarization remains after removing the electric field (at E=0). In this case, the stored energy is very low and the lost energy is very high. Case (e) represents the behaviour of a material exhibiting polarization saturation.

Microscopic mechanisms of polarization

Case of polymers

In polymers, various contributions to the permittivity can be found:

(1) The electron polarization comes from the displacement of the electrons with respect to the atom nuclei positions. This contribution is usually very small in fully saturated polymers (~1-3 for wide band gap materials) but it can go up to 10 in conjugated polymers (with low band gaps) where electron delocalization is enabled by the presence of double bonds. This increase in permittivity is correlated to a lowering of the band gap of the polymer [18–20] (See Figure 1.5 a). This trend has been explained by Baer et Zhu to be due to the increased electron polarization achieved by delocalizing electrons among conjugated molecular orbitals [21]. Electron polarization exhibits resonance frequencies around 10^{15}-10^{18} Hz (see Figure 1.6).

(2) The vibrational (or atom, ionic) contribution comes from the displacement of two atoms with different effective charges (e.g. C-O bond). This contribution (represented in Figure 1.5 b) does not depend on the band gap of the polymer. Vibrational polarization exhibits resonance frequencies around 10^{12} Hz (see Figure 1.6).

(3) The dipolar contribution comes from the orientation of the molecular dipoles present in the polymer chains. This contribution is strongly affected by the molecular dynamics and may increase after dynamic transitions (α, β, γ…). Thus, orientation polarization mechanisms have relaxation frequencies that drastically depend on both frequency and temperature and usually range between about 10^{-4} Hz for glassy polymers and 10^{6-8} Hz for rubbery polymers at room temperature (RT). Dipolar contribution of water molecules may be found up to 10^{9} Hz at RT[22].

(4) The interfacial contribution is observed in polymers with heterogeneous ionic or electronic conductivity. The migration of the ions within the more conductive phase gives rise to their accumulation at the interfaces with the less conductive phase. This mechanism is denoted Maxwell-Wagner-Sillars (MWS) polarization and will be detailed in a dedicated section. The amplitude and relaxation frequency of MWS polarization depend on the contrast in conductivity and on the structure of the material. MWS polarization is commonly observed at relatively low frequencies in rubbery semi-crystalline polymers where ions migrate through the amorphous phase and accumulate at the interfaces with the crystallites.

(5) Electrode polarization corresponds to the migration of the mobile ions from the bulk of the material to the electrodes. Electrode polarization depends on the sample thickness used for testing and usually appears at very low frequency.

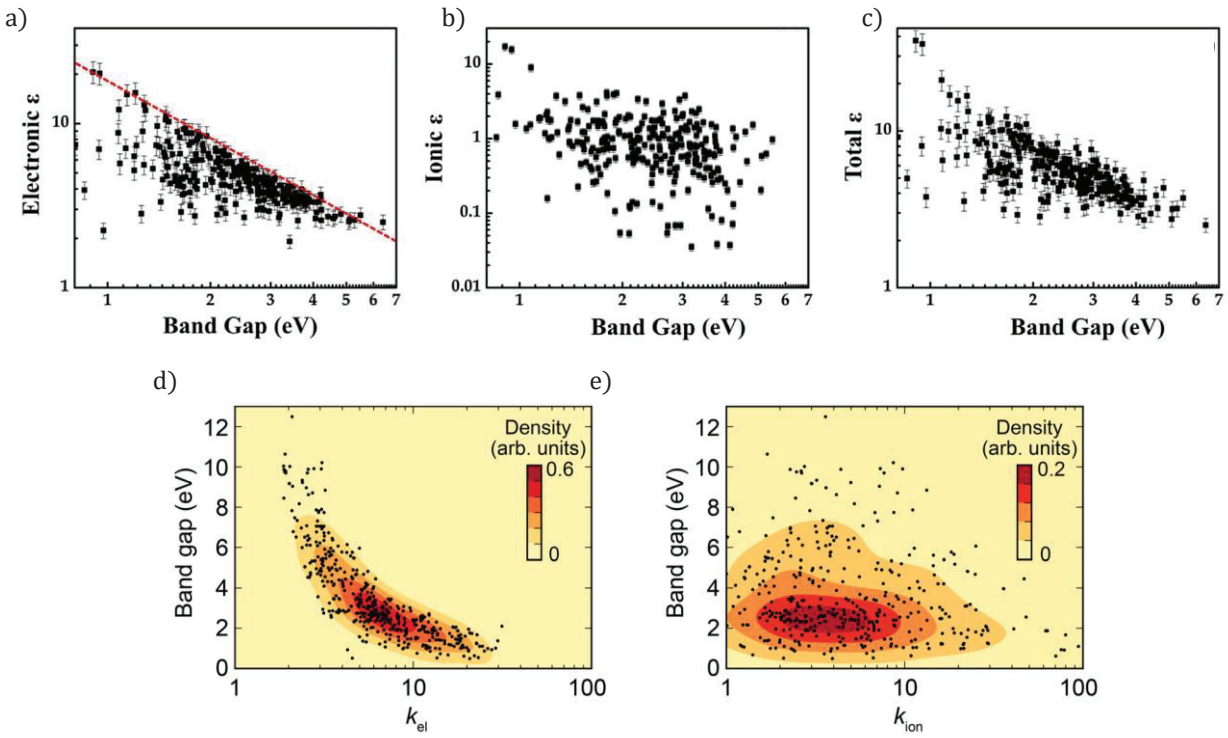

Figure 1.5: a) Electronic and b) vibrational (ionic) contribution to the permittivity and c) total dielectric permittivity as a function of the band gap for various polymers[21] and d) electronic and e) ionic contribution to the dielectric permittivity of various inorganic materials (metal oxides, etc)[19]. In d) and e), k ≡ contribution to ε.

Table 1.1: Dielectric permittivity and glass transition for polymers commonly used in the insulating layer of capacitors[23].

Type	Polymer	ε'_r (at 100Hz and RT)	T_g (°C)
Apolar	PP	2.2-2.6	-3 to -51
	PTFE	2.1 (@100Hz)	115
Polar	PA6,6	3.2-4.3 (@100Hz)	56-70
	PC	3.2 (@100Hz)	137-154
	PVdF	9-10.5 (@100Hz)	-29 to -57
	PVdF-HFP	7.6-10.6 (@100Hz)	-5 to -40
	P(VdF-CTFE-TrFE)	>45	-40

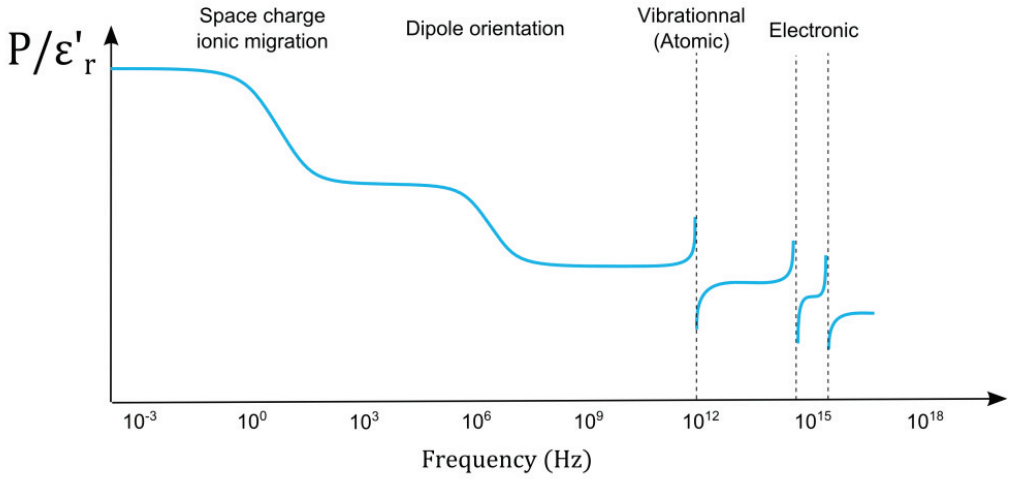

Figure 1.6: Typical evolution of the polarization/permittivity as a function of the frequency for dielectric materials. Space charge and dipole orientation exhibit relaxations whereas atomic and electron polarization exhibit resonances.

Some examples of polymer permittivity values are reported in

Table 1.1. Since the difference of electronegativity between atoms is usually low in polymers (from 2.20 for H to 3.44 for O) the permittivity is very low for glassy polymers ($\varepsilon'_r \sim$ 2-3). Polar polymers present a higher permittivity above the glass transition because of higher dipolar polarization. Fluoropolymers are exceptions and may have very large permittivity values due to the dipolar contribution of C-F bonds ($\varepsilon'_r \sim 45$ for P(VdF-TrFE-CFE)). Indeed, the electronegativity of the fluorine atom is 3.98 and such polymers usually possess a high molecular mobility due to low glass transition.

Table 1.2: Dielectric permittivity of oxides and ceramics commonly used in capacitor insulating layer[24].

Type of material	Composition	Dielectric permittivity at 100Hz
Perovskite	$BaTiO_3$	1,700
	$PbNb_2O_6$	225
	$SrTiO_3$	2,000
oxide	SiO_2	3.9
	Al_2O_3	9
	Ta_2O_5	22
	TiO_2	80
	WO_3	75
	ZrO_2	25
	HfO_2	25
	$HfSiO_4$	11
	La_2O_3	30
	Y_2O_3	15
Covalent crystal	Si (silicon)	14
	C (diamond)	5.5 - 10

Case of inorganic materials

In inorganic materials, electron and vibrational polarization mechanisms are similar to those in polymers. As well as in polymers, the electron contribution to ε'_r is limited by the material band gap and does not exceed a few tens (see Figure 1.5). Nevertheless, the vibrational contribution may reach very high levels for materials with high difference of electronegativity between the atoms and high level of mobility of the atoms around their equilibrium positions. Some examples of inorganic materials permittivity values are given in

Table 1.2. Materials made of atoms with similar electronegativity present low permittivity (e.g. SiO_2 with ε_r=3.9) whereas $BaTiO_3$ and $SrTiO_3$ possess very high permittivities (up to ε_r~ 1700-2000) because of a high vibrational contribution. As regards to its very high permittivity, $BaTiO_3$ has been widely studied and reported as a capacitor active layer in the literature. In the same way as in semi-crystalline polymers, electric charge conduction may lead to interfacial polarization in inorganic materials that exhibit heterogeneity of conductivity (e.g. at grain boundaries).

The resonance frequencies of the electronic and vibrational contributions being respectively around 10^{15} and 10^{12} Hz, the dielectric permittivity of these materials should be independent of the frequency below 10^{12} Hz in the absence of interfacial polarization due to charge carrier conduction. Nevertheless, the permittivity can be drastically affected by structural changes. Indeed, crystal phase transitions may modify the permittivity as in the case of $BaTiO_3$ crystals. Philippot et al. report the evolution of the permittivity along temperature-induced phase transitions for $BaTiO_3$ crystals as represented in Figure 1.7[25]. $BaTiO_3$ exists in a ferroelectric tetragonal phase between 0 and 120 °C. Above this temperature (called the Curie temperature), the crystal turns into a non-ferroelectric cubic phase. As the size of the particles is reduced, the Curie transition temperature decreases in such a way that below 1 µm, the structure is no longer tetragonal but cubic at RT. This effect has been explained by internal lattice stress relaxation at the nanoscale. **The evolution of the permittivity with the particle size is shown in Figure 1.8. As a result, the permittivity of $BaTiO_3$ nanoparticles (NPs) is lower than in bulk $BaTiO_3$, does not undergo drastic change with temperature and does not depend on frequency.**

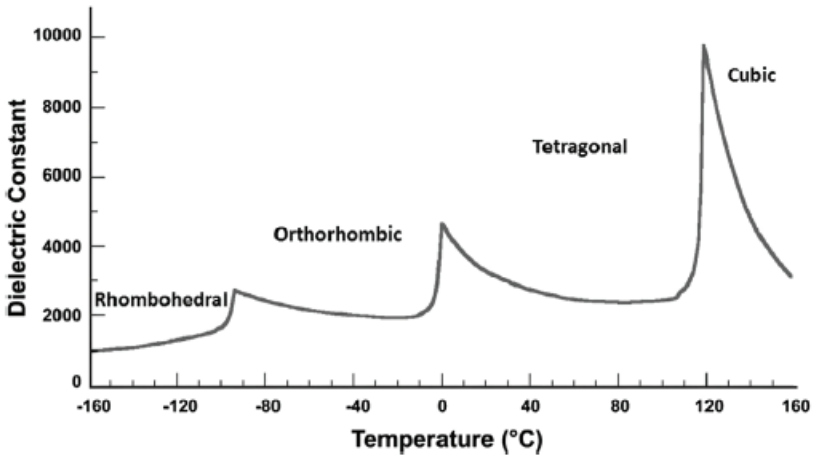

Figure 1.7: Evolution of the dielectric constant of large $BaTiO_3$ particles with the temperature induced phase transition[25].

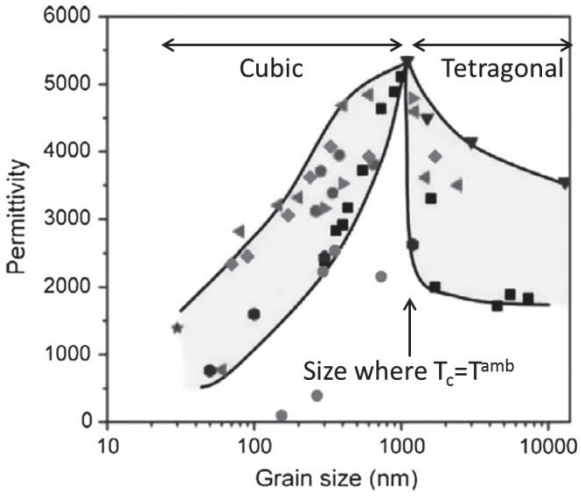

Figure 1.8: Evolution of the dielectric permittivity of $BaTiO_3$ particles as a function of the grain size (at 1 kHz, RT)[25]. The tetragonal phase is ferroelectric.

1.2.2 Charge dynamics in solids

In dielectric materials, both ions and electrons may participate to charge conduction. The electrical conductivity σ_{DC} depends on the density of the electric charge carriers and on their mobility. Charge carrier density depends on both their generation and collection whereas their mobility depends on the transport mechanisms. Thus, electrical conduction can be limited by either transport or the generation of the charge carrier depending on the electronic structure of the material, on temperature and on the electric field. There are several mechanisms that may account for electrical transport in materials. The behaviour of electrons in solids is described on the basis of the band theory. Nevertheless, this theory does not include a description of the ion behaviour. Thus, the ionic conduction will be addressed in a dedicated paragraph.

Ionic conduction

In solids, the ions polarize their surroundings. The polarized atoms and molecules rearrange themselves to reduce the potential energy of the system. This is equivalent to the creation of a potential barrier and can be considered as a charge trapping. Then, the ions have to move by a thermally activated hopping mechanism so from one potential well to another as shown in Figure 1.9 a). The potential barriers and wells are related to the local structure of the material and are modified by applying an external electric field as schematized in Figure 1.9 b)[26].

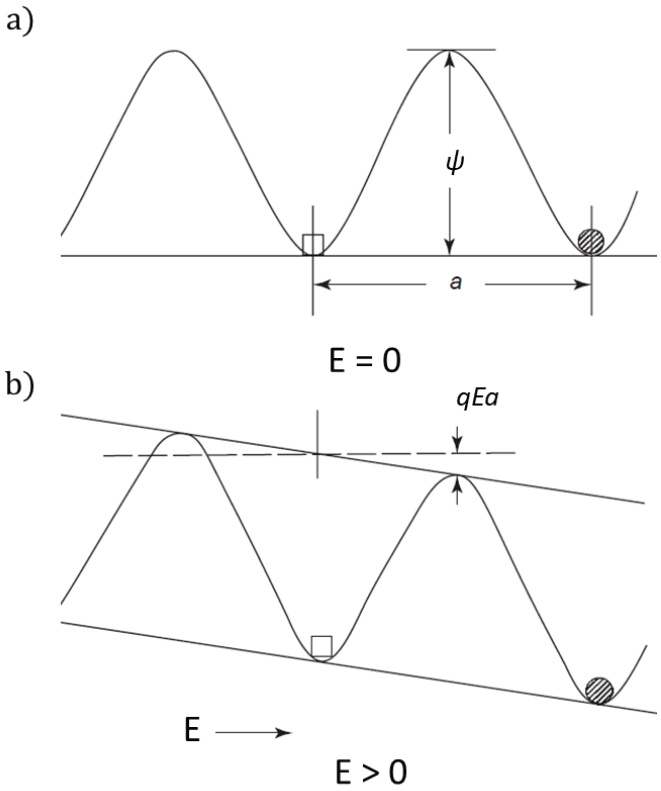

Figure 1.9: Schematic illustration of the energy barrier hindering the transport of a cation in a material: a) without electric field and b) with an applied electric field.

Ionic conduction can be classified in two categories, intrinsic and extrinsic, depending on the origin of the ions. In pure ionic crystals, the ionic conduction is called intrinsic and provided by the ions that constitute the crystal. However, in non-ionic solids, the ionic conduction is provided by impurities and called extrinsic. It depends on the nature and the concentration of the impurities. Ionic impurities are found in all dielectric materials at various concentrations. They may be due to the fabrication process, remaining fragments of polymerization catalyst, degradation and dissociation of neutral species due to radiation absorption or even from the environment such as easily dissociable water molecules. Their size generates large steric effects that justify their very low mobility compared to electrons. Their conduction is associated with matter transport[26].

It is worth noting the very important role of the relative permittivity on the dissociation of ionic species and thus on the ionic conductivity. As a result, it is reasonable to say that ionic conduction does not have a noticeable contribution in non-polar polymers.

If the ions migrating under an applied electric field are not neutralized at the electrodes, they accumulate and generate space charges near the electrodes. These space charges are oppositely charged as compared to the nearby electrode (and thus

called hetero-space charges). This leads to an increase of the electric field near the electrodes that may trigger injection of electrons from the cathode or holes from the anode.

Electronic conduction

Band theory

According to quantum mechanics, electrons in crystalline materials are allowed in certain energy levels grouped in bands, separated by forbidden energy bands (*band gaps)*. The Fermi level is the energy that separates the occupied electronic states from the non-occupied ones. Depending on the nature of the material and the structure of the crystal, the relative position of the band structure and the Fermi level can be different. Three main cases can be distinguished. They are represented in Figure 1.10.

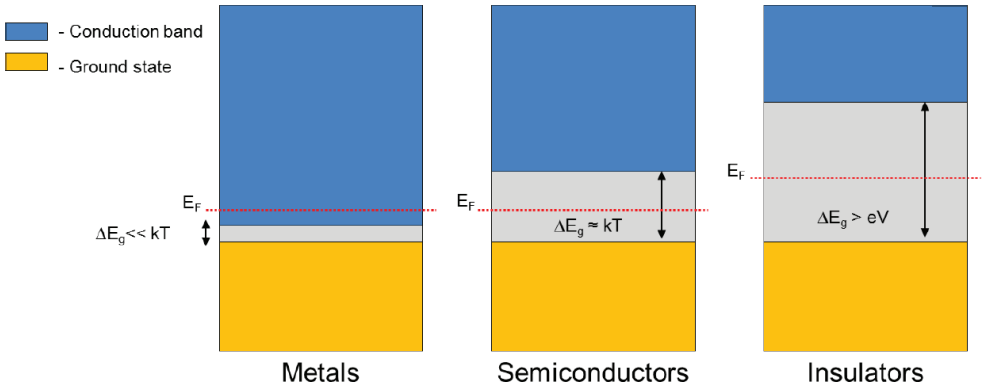

Figure 1.10: Schematic representation of the electronic band structure in metals, semiconductors, and insulators (adapted from [27])

Amorphous materials, like most insulating materials used in practice, do not exhibit long-range order, but only short-range order between atoms. This results in the presence of localized states lying in the forbidden gap, as shown in Figure 1.11 b)[11,28,29]. These localized energy states can be ranked into two categories:

(1) Localized states with an orbital extension shorter than the closest neighbour (isolated sites). These sites have low spatial density and are located deep into the forbidden gap (>0.5-1 eV). An electron trapped into such a localized state may lose energy by conventional electron transition mechanisms (photoemission, phonon…) and can be further stabilized by the surrounding medium[26] (polarization of the surrounding molecules to reduce the potential energy brought by the charge). These localized states are usually introduced by chemical defects or impurities.

(2) Localized states with an orbital overlap with neighbouring states. These states are located less deep in the forbidden band (<0.5-1 eV). They are close enough to interact (high spatial density) and to allow electron transit from one site to the other. Their spatial density decreases as their energy moves away from the conduction band. These states are called shallow traps and are usually introduced by physical disorder.

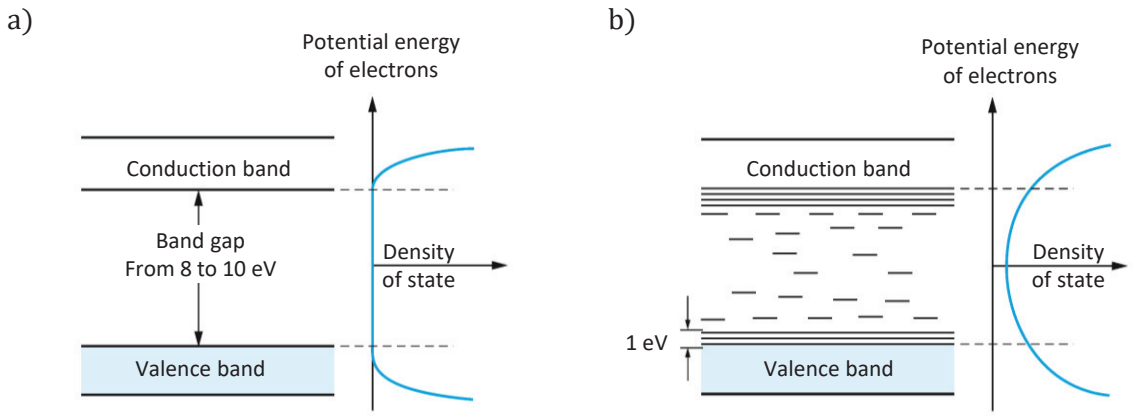

Figure 1.11: Electronic structure of a) an ideal and b) a real dielectric solid. Adapted from Laurent, 1999[28].

These two kinds of localized states may impact the charge dynamics in solids by charge transfer through shallow traps or electron trapping in deep traps. These two mechanisms will be further addressed.

Charge generation mechanisms

The basis of the charge generation is very clearly described in the work of C. Laurent[28]. This part is then widely inspired by this work.

Internal generation

Intrinsic electrical charges can be generated in the bulk of the material by the excitation of a valence electron and dissociation of the resulting electron-hole pair. These phenomena may emerge from radiation absorption, electron collision, or simply thermal motion. The minimum energy required for electron excitation corresponds to the band gap width of the material. The electronic structure of the material is thus determining the ease of electron excitation. In wide band gap materials, the probability of electron excitation is so weak that most charge carriers come from electron excitation on the impurities.

Charge generation at the interfaces

Electrons can be injected or collected (hole injection) at electrodes upon an applied voltage. The electronic structure of a metal-polymer contact is illustrated in Figure 1.12. The example of the electrons will be described in what follows but it can be transposed to hole injection by considering an opposite voltage.

In the absence of electric fields, a potential barrier of height ψ, which depends on the nature of the electrical contact, prevents conduction electrons contained in the metal to penetrate the polymer. In the presence of an electric field, the height of the potential barrier is reduced by a quantity ΔV given by equation (1.14).

$$\Delta V = \frac{e}{2}.\left(\frac{eE}{\pi\varepsilon_0\varepsilon_r}\right)^{1/2} \qquad (1.14)$$

with e the electron charge (1.6×10^{-19} C).

Then electrons (or holes) can overcome (or cross) the barrier by three different mechanisms illustrated in Figure 1.12[28]:

- The Schottky effect involves thermal activation to give enough energy to the electron to overcome the barrier (mechanism 1 in Figure 1.12).
- The Fowler-Nordheim effect in which the electron can pass through the potential barrier by tunnelling if the electron wave function is about the width of the potential barrier (mechanism 2 in Figure 1.12). This is the case only at high electric fields (around 10^8 – 10^9 V.m^{-1}). Above these values, the injection current greatly increases.
- The thermally assisted tunnelling effect combines both effects (mechanism 3 in Figure 1.12).

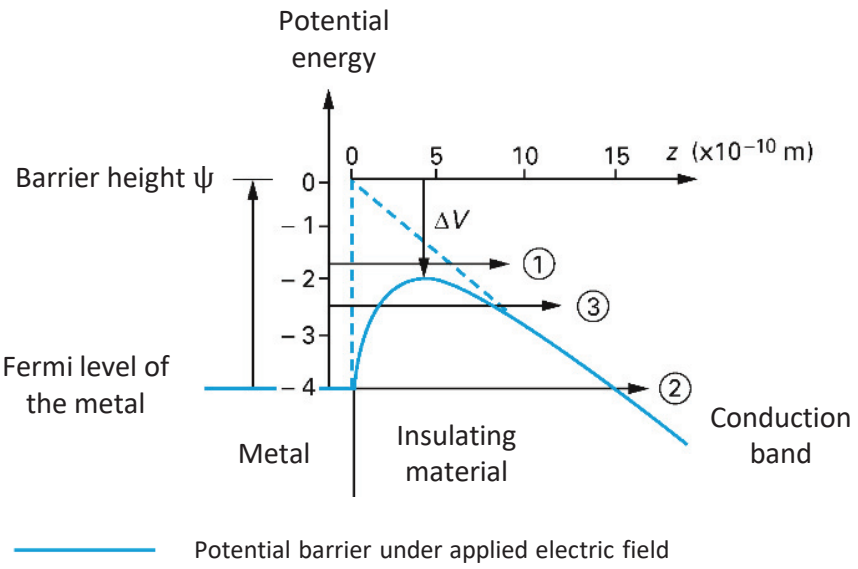

Figure 1.12: Charge injection mechanisms. Adapted from [28].

Many factors influence these injection processes. First, the surface roughness leads to local field enhancement by peak effect that reduces the potential barrier[30]. The electrode thus presents preferential injection sites heterogeneously distributed over its surface[31]. Moreover, the energy barrier depends on the crystallographic orientation of the metal and on its surface oxidation state[26,32]. Finally, the dielectric/metal interfaces usually present defects that introduce intermediate energy levels that promote a multistep injection process.[33] Indeed in general, the injection thresholds measured are much lower than those predicted by the theory.

These injection mechanisms are mainly dominating the charge carrier conduction in very thin polymer layers (10^{-8} to 10^{-7} m). In thicker film (10^{-6} to 10^{-1} m), the electrical current is mainly limited by volume transport mechanisms.

Charge transport mechanisms

Once charge carriers are generated in the materials, different phenomena may account for electrical transport in dielectric materials.

Band conduction

Band conduction is operated by mobile electrons (resp. holes) in the conduction (resp. valence) band. The probability of the presence of electrons (resp. holes) in the conduction (resp. valence) band drastically decreases with increasing the band gap. Band conduction is thus observed if no other conduction mechanisms are significant[34]. Accelerated conduction electrons may be at the origin of internal generation and material degradation[26,35].

Trapping/detrapping

Charge carrier conduction may be impacted by electron trapping. Indeed, the above-mentioned localized states in the forbidden gap present in the material act as potential wells that trap charge carriers. Charge trapping is related to various energy transfer mechanisms [26]. To leave the trap, a charge carrier has to overcome a potential barrier, by the three mechanisms mentioned above for injection.

Hopping

If the trap levels are spatially close enough the height of the potential barrier between two neighbour traps is decreased as illustrated in Figure 1.13[36,37]. Again, the same mechanisms described for injection may be involved in charge carrier transfer from one localized state to another without passing by the conduction band[38].

In polymers, electronic conduction is thought to mainly occur through these hopping mechanisms because of their high level of physical disorder in the amorphous phases and high band gap.

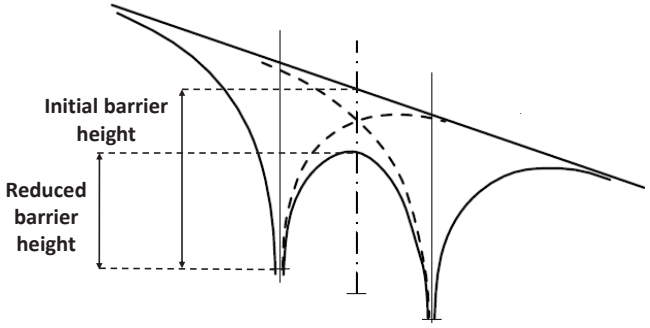

Figure 1.13: Hopping process between two traps when an electric field is applied[39].

Space charges

At high electric fields, extrinsic charge carriers (generated by injection) become predominant over intrinsic charge carriers present in the material. It follows that the injected charges may accumulate in the material. Similarly, ionic species may be dissociated and accumulate near interfaces. These "space charges" modify the electric field distribution and may affect charge injection, transport and the electrical strength of the material[40]. Charges accumulate in the material mostly under DC electric field[40].

1.2.3 Electrical degradation, Breakdown and life time

The electric strength E_{bd} (also called electric field at break or breakdown field) is defined as the electric field at which the insulating properties of a material are irreversibly destroyed.

Two kinds of breakdown may be distinguished:

- Extrinsic breakdown due to the presence of impurities or defects
- Intrinsic breakdown reflects the bulk physico-chemistry of the material.

The intrinsic electric strength is quite difficult to define in real materials such as polymers because it would require a perfectly homogeneous material without defects and impurities whose effects predominate. The extrinsic electric strength depends on three phenomena:

- Thermal breakdown
- Mechanical breakdown
- Electrical breakdown

A thermally assisted electrical breakdown is the most probable mechanism for polymers since they are strong enough to undergo high compression stress.

Electrical breakdown

In wide band gap materials, the most probable mechanism responsible for electrical breakdown is the avalanche multiplication. It happens at high electric fields, when electrons acquire enough energy to induce ionization of the matter resulting in the emission of other electrons withdrawn from their valence state. The multiplication of these hot carriers due to the bolting of this phenomena leads to electrical breakdown. The predominance of this effect in the electrical breakdown of polymer material is still controversial. Nevertheless, suitable conditions may exist because the presence of hot electrons has been proved by electroluminescence and free radical generation[11,31]. The tunnel-injection of electrons from the electrodes to polymeric film has been shown to be responsible for initiating avalanche breakdown at fields about 10^3V/µm. In that case, the electrical breakdown is governed by the electrode/polymer interfaces[31].

Thermal breakdown

Thermal breakdown occurs when the heat generated by the dielectric losses cannot be handled at macroscopic scale or, more usually, at the microscopic scale. The increase of the temperature due to power dissipation increases both charge carrier density and mobility, resulting in further heat generation by Joule effect. This retroactive loop leads to thermal breakdown through the bolting of both temperature and conductivity in the material.

Electromechanical breakdown

The electromechanical breakdown occurs due to the coulombic forces of the electrodes that squeeze the polymer which is compressed in between. The stress can reduce the thickness of the material depending on the Young's modulus and lower the electric strength. Indeed, if the electrical stress is kept constant, the reduction of the sample thickness leads to an increase of the electric field. This phenomenon is not commonly considered to occur in polymers.

Partial discharge breakdown

The partial discharge breakdown happens in the presence of cavities in the material[40]. Since they are filled with gas, they have lower permittivity than the matrix. The polarization of the surrounding matrix increases the electric field inside the cavities (described p.28) which may result in the gas ionization (breakdown of the gas induces partial discharge). The charge carriers produced by this ionization are accelerated into the cavities and may cause chemical degradation when reaching the edges of the cavity. Repeated, these partial discharges may lead to the erosion of the mater and cause macroscopic breakdown. In polymers, such cavities are commonly formed during the fabrication process.

1.2.4 Conclusion on dielectric properties

Intrinsic dielectric properties of supposedly homogeneous material have been addressed. These dielectric properties depend on the dynamics of the electrical charges. These charges can be bound charges (permanent, induced dipoles…) or free charges (electrons, holes, ions…). Free charges can effectively be considered as bound charges if they are confined at small scales.

Polarization of the permanent or induced dipoles enhances the energy density stored in the material. These polarizations are associated with dielectric losses that lead to high energy dissipation close to their relaxation frequencies. The polarization of a material is described by its complex relative permittivity ε^*_r and may depend on the frequency and on the intensity of the applied electric field. Specific phenomena such as ferroelectricity and saturation must be avoided since they considerably reduce the storage energy density at high electric fields.

The transport of free charge carriers has been shown to deteriorate insulating properties of materials. Indeed, the DC conductivity generates energy dissipation. Various mechanisms of charge transport have been introduced and they depend on the type of charge carrier (ions, electrons …), on the material electronic structure (crystalline, amorphous, presence of chemical and physical defects…) and on the applied value of the electric field. Indeed, conduction mechanisms may be triggered at high electric field and have to be considered in the design of composites where the electric field may be drastically enhanced. This aspect will be developed in what follows.

The electric strength of a material is also a property of interest for applications where high electric fields are required. Various mechanisms that may lead a material to electrical breakdown have been mentioned.

When associated in a composite, the resulting dielectric properties depend on the intrinsic dielectric properties of the various phases. In some cases, the properties of composites may be described by rules of mixture. Nevertheless, additional phenomena, specific to composites, have to be considered. The dielectric properties in composites will be addressed in what follows.

1.3 Polarization in heterogeneous materials

Designing composites is a way to obtain materials with tuned properties. This section is dedicated to the relationships between the composition and structure of a composite and its dielectric properties.

1.3.1 Rules of mixture

The effective (homogenized) permittivity ε_{eff} of a composite depends on its structure and on the volume fraction of each constituent. Various examples of either empirical or model-based rules of mixture are presented in Figure 1.15. **All of them lie between the theoretical Wiener's limits, corresponding to parallel and perpendicular multilayer configurations** presented in Figure 1.14 and described by equations (1.15) and (1.16)[41].

(1) When layers of two different materials of permittivity ε_1 and ε_2 with a volume fraction φ of material 1 are connected in parallel, the effective permittivity is described by:

$$\varepsilon'_{eff} = \varphi\varepsilon_1 + (1-\varphi)\varepsilon_2 \tag{1.15}$$

(2) In perpendicular (series) association, layers behave like capacitors connected in series:

$$\varepsilon'_{eff} = \frac{1}{\frac{\varphi}{\varepsilon_1} + \frac{(1-\varphi)}{\varepsilon_2}} \tag{1.16}$$

These rules of mixture only consider bound charge polarization of the composite constituents. They do not consider interfacial polarization due to conduction of free charge carriers within each component.

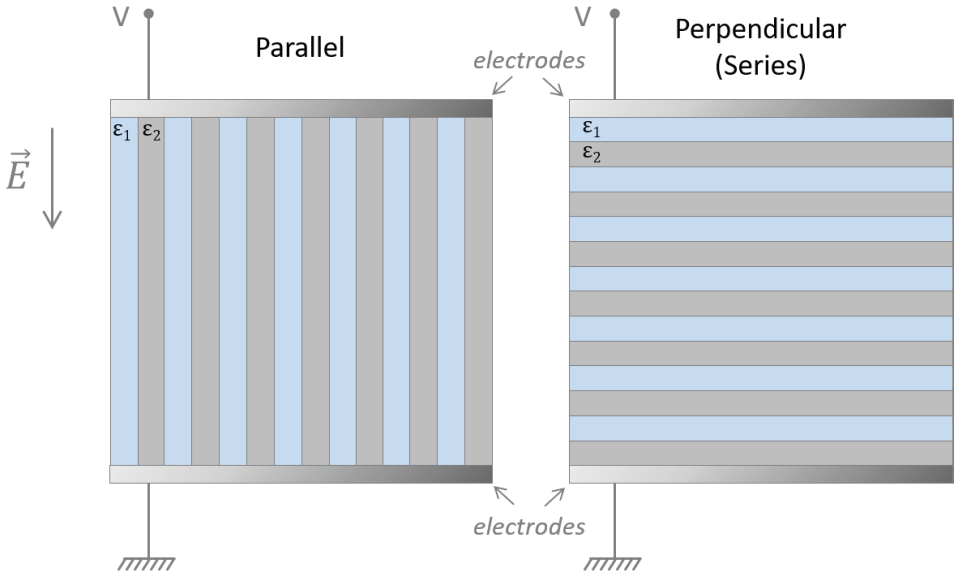

Figure 1.14: Parallel and perpendicular multilayer structures.

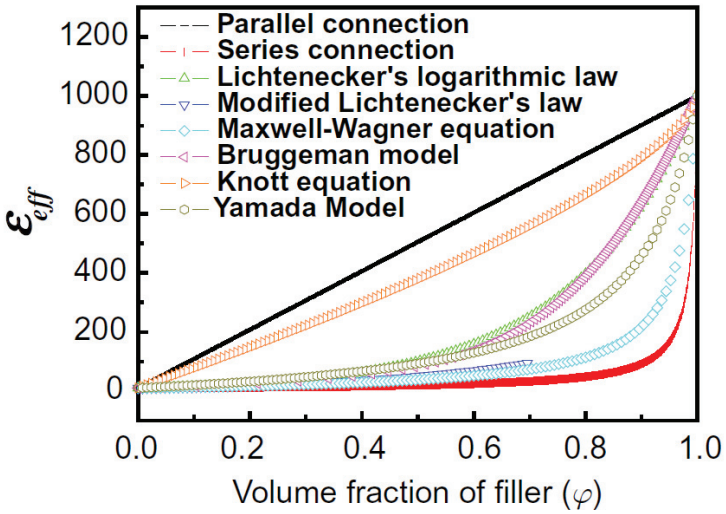

Figure 1.15: Rules of mixtures of several models for the effective permittivity. [42]

Polarization of inclusions and electric field distortion

When a composite material is placed in an external electric field, the differences of permittivity and thus of polarization will lead to a heterogeneous electric field. The polarization of a spherical dielectric inclusion (permittivity ε_i) in a matrix of different permittivity ε_h in an external electric field E_0 is first considered (see Figure 1.16). The explicit resolution of the Maxwell equations first gives, in spherical coordinates, the following expression of the surface charge distribution σ^{surf} formed at interface:

$$\sigma^{surf} = 3\varepsilon_0\varepsilon_h \frac{\varepsilon_i - \varepsilon_h}{\varepsilon_i + 2\varepsilon_h} E_0 \cos\theta \qquad (1.17)$$

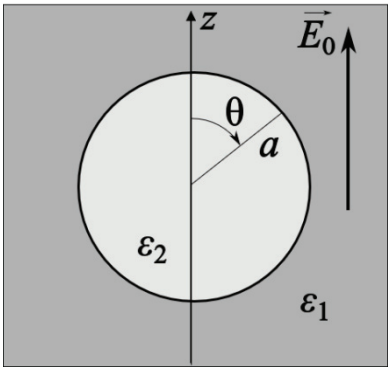

Figure 1.16: Description of the spherical inclusion in spherical coordinates.

The electric field distribution inside the inclusion and in the host medium is thus expressed by equations (1.18) and (1.19), respectively.

$$\vec{E}_i = \frac{3\varepsilon_h}{\varepsilon_i + 2\varepsilon_h} \vec{E}_0 \qquad (1.18)$$

$$\begin{cases} E_{out(r)} = \left(2\dfrac{\varepsilon_i - \varepsilon_h}{\varepsilon_i + 2\varepsilon_h}\dfrac{a^3}{r^3} + 1\right) E_0 \cos\theta \\ E_{out(\theta)} = \left(\dfrac{\varepsilon_i - \varepsilon_h}{\varepsilon_i + 2\varepsilon_h}\dfrac{a^3}{r^3} - 1\right) E_0 \sin\theta \end{cases} \quad (1.19)$$

With *a* the inclusion radius and r the distance from the inclusion centre.

First, equation (1.18) indicates that the electric field is uniform inside the inclusion. It decreases if the permittivity is higher in the inclusion than in the host medium, and conversely.

Then, equation (1.19) shows that the electric field outside of the inclusion depends on both the distance to the inclusion and the angle θ.

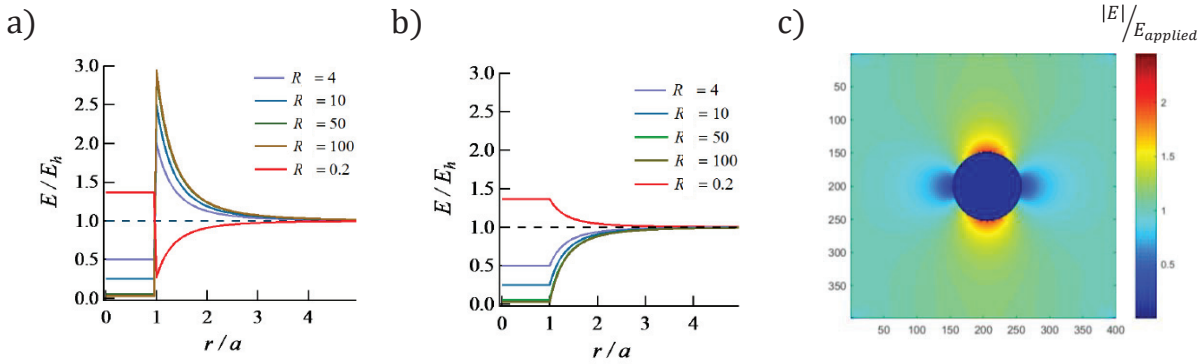

Figure 1.17: Total electric field around spherical inclusion for a) $\theta = 0$ (direction of the external electric field E_0) and b) $\theta = \pi/2$ and c) distribution of the electric field intensity around the inclusion for ε_i=10 and ε_h=1(obtained with the program described in section 4.3.3). a is the inclusion radius and r the distance to the inclusion centre. Here, the permittivity ratio between the inclusion and the matrix is denoted R.

Figure 1.17 a) and b) show the norm of the electric field, for various permittivity ratios between the inclusion and the matrix, as a function of the distance r to the inclusion centre for $\theta = 0$ and $\theta = \pi/2$, respectively. Figure 1.17 c) gives a 2D mapping of the electric field norm and direction around the inclusion.

It can be seen in Figure 1.17 that, in the case of a permittivity ratio $R = \varepsilon_i/\varepsilon_h$ higher than 1, the electric field outside the inclusion is decreased at the equators and increased at the poles (and oppositely for permittivity ratio $R < 1$). When the permittivity ratio tends to infinite value like in the case of an electrically conducting inclusion, the electric field distortion is maximum. It is given by equations (1.20) with a zero-electric field inside the inclusion and at the equator and a maximum electric field of $3E_h$ at the poles.

$$\begin{cases} E_{out(r)} = \left(2\dfrac{a^3}{r^3} + 1\right) E_h \cos\theta \\ E_{out(\theta)} = \left(\dfrac{a^3}{r^3} - 1\right) E_h \sin\theta \end{cases} \quad (1.20)$$

The local electric field enhancement induced by the polarization of the high-ε inclusions may be detrimental for the insulating properties of the composites. Two main reasons may be mentioned.

The first one concerns the impact of the electric field on the band structure of dielectric materials and its consequences on the charge carrier transfer between particle and matrix. Indeed, as discussed previously, the cumulative effect of image charge force and electric field lead to decrease the potential barrier for charge injection and even lead to injection by tunnelling effect if the electric field is too high. Similar description can be done for a particle/matrix transfer. For high-ε spherical particles, the amplification of the electric field may decrease the threshold for charge carrier transfer.

Secondly, for a host material with a homogeneous electric strength E_{BD}, as the maximum local electric field is about x3 for spherical inclusions with high permittivity, the electric field locally reaches E_{BD} when the external applied field is $E_{BD}/3$. Thus, the effective breakdown strength E_{BD}^{eff} is divided by 3 as compared to pure matrix. In this simple picture, since the energy density is proportional to the permittivity and to the square of the electric field, the decrease of the electric strength will always prevail over the increase of the effective permittivity and will lead to lower energy density [43]. However, this must be mitigated by the fact that the volume fraction in which the field is amplified may be small, thus decreasing the associated probability of homogeneous breakdown.

Homogenization theory

To calculate the effective permittivity ε_{eff} of a composite consisting of spherical inclusions dispersed in a continuous matrix of different permittivity, M. Garnett was the first author to propose an approach based on an effective medium approximation[44,45]. This approach was later generalized to include the effect of conductivity and ellipsoidal inclusions.

The complex, frequency dependent permittivity $\varepsilon_{eff}^{*}(\omega)$ of a heterogeneous mixture including dispersed inclusions in a matrix is described by[15]:

$$\varepsilon_{eff}^{*}(\omega) = \varepsilon_{h}^{*}(\omega)\frac{[n\varepsilon_{i}^{*}(\omega) + (1-n)\varepsilon_{h}^{*}(\omega)] + (1-n)[\varepsilon_{i}^{*}(\omega) - \varepsilon_{h}^{*}(\omega)]\varphi_{i}}{[n\varepsilon_{i}^{*}(\omega) + (1-n)\varepsilon_{h}^{*}(\omega)] - n[\varepsilon_{i}^{*}(\omega) - \varepsilon_{h}^{*}(\omega)]\varphi_{i}} \quad (1.21)$$

where $\varepsilon_{h}^{*}(\omega)$ and $\varepsilon_{i}^{*}(\omega)$ are the complex permittivities of the host media (matrix) and of the inclusion respectively. $\varphi_{i}$is the volume fraction of the inclusions and n is the shape factor of the dispersed inclusions in the direction of the electric field. For spherical particles, $n = 1/3$. For prolate spheroids (rod-like), $0 \leq n \leq 1/3$, with the needle, $n = 0$ as the limiting case. For oblate spheroids (disc-like), $1/3 \leq n \leq 1$, with the plate-like particle $n=1$ as the limiting case.

For spherical inclusions ($n=1/3$), equation (1.21) can be simplified as:

$$\varepsilon_{eff}^{*}(\omega) = \varepsilon_{h}^{*}(\omega)\frac{1 + 2\varphi_i \frac{\varepsilon_i^{*}(\omega) - \varepsilon_h^{*}(\omega)}{\varepsilon_i^{*}(\omega) + 2\varepsilon_h^{*}(\omega)}}{1 - \varphi_i \frac{\varepsilon_i^{*}(\omega) - \varepsilon_h^{*}(\omega)}{\varepsilon_i^{*}(\omega) + 2\varepsilon_h^{*}(\omega)}} \quad (1.22)$$

which corresponds to the Maxwell-Wagner curve in Figure 1.15.

Figure 1.18 shows the rule of mixture given by equation (1.22) for spherical inclusions as a function of the inclusion volume fraction if both constituents have a real permittivity (i.e. without dielectric losses). It predicts for example an increase of 12% of the permittivity of the matrix for a composite containing 5 vol% of inclusions with a permittivity ratio of 10, which is consistent with the literature[46]. Increasing the permittivity ratio of the system to 20 would lead to an effective permittivity increase of 14%. In the case of inclusion with an infinite permittivity such as conducting particles, the effective permittivity of the would increase by 16% at 5 vol%. This suggests that, as well as for the electric field distortion, the effect of the permittivity ratio between the inclusions and the matrix has a limit.

However, the mean field approximations used in the M. Garnett model are valid at low concentrations of inclusions since the influence of the closest neighbours are not considered. Indeed, dipole-dipole interactions cannot be ignored any longer when the inclusions get close to each other and start to feel their respective influence on the electric field. The limit concentration of this model will be estimated in section 1.3.4.

Other models, such as the Rayleigh's and Bruggeman's ones, include the interactions between the spherical inclusions and become applicable to higher concentration of inclusions[47].

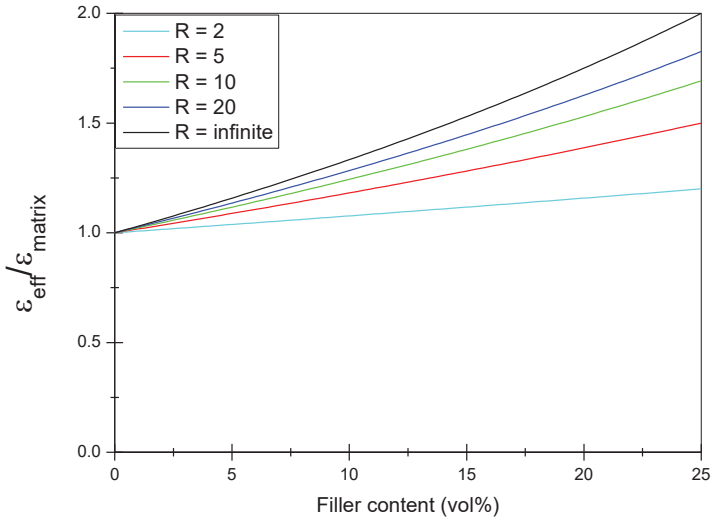

Figure 1.18: Rules of mixture obtained from equation (1.22) for spherical particles if both phases have real permittivity. The rules of mixture are plotted for different permittivity ratios (here, $R=\varepsilon_i/\varepsilon_h$ and $\varepsilon_h=1$).

1.3.2 Energy density and composite structure

Inclusion aspect ratio and orientation

Introducing particles with different shapes may have high efficiency in terms of effective permittivity enhancement [8]. The influence of both the orientation and the aspect ratio of a high-ε particle ($\varepsilon_i = \infty$) on the effective permittivity and the electric strength E_{BD} of a composite has been calculated by Roscow et al. using numerical simulation[43]. As presented in Figure 1.19 (a), the orientation of the particle with an aspect ratio of 8 has a significant influence on the field distortion. Indeed, the electric field locally reaches high values (8.8 times the applied field) when the particle is oriented in the field direction. Figure 1.19 (b), (c) and (d) shows the electrical strength E_{BD}, the Permittivity Enhancement Factor R_ε (i.e. the effective permittivity divided by the matrix permittivity), and the resulting storage energy density, respectively. The authors consider that the electrical breakdown occurs when the electric field locally reaches the electrical strength of the matrix. The electric strength of the composite is thus calculated as the electric strength of the matrix divided by $E_{local}^{max}/E_{applied}$. In Figure 1.20, these parameters are plotted as a function of the particle orientation for various particle aspect ratios between 1 and 10.

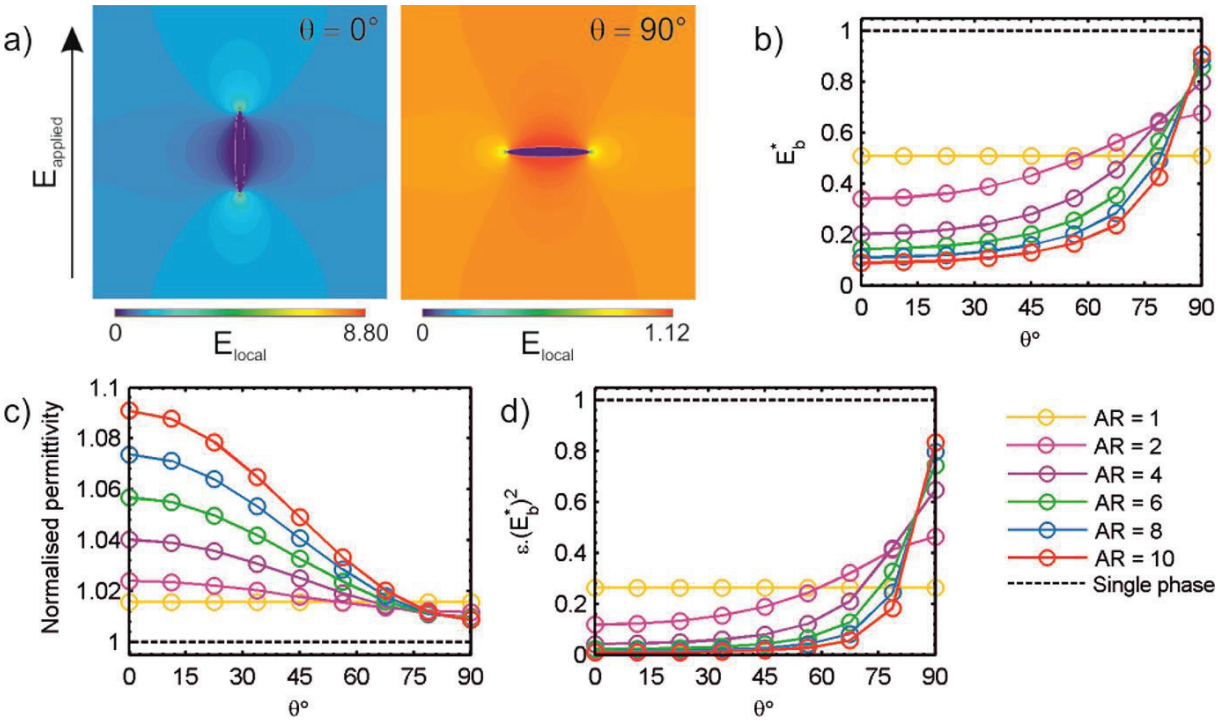

Figure 1.19: 2D modelling results with a) The electric field mappings in the cases of the polarization of a high-ε ($\varepsilon=10^6$) inclusion with an aspect ratio AR=10 oriented either parallel or perpendicular to the field direction. Evolution of b) the effective electric strength (calculated as $E_{BD}^{matrix} * (E_{applied}/E_{local}^{max})$), c) the effective permittivity (or permittivity enhancement factor)

of the composites normalized by that of the matrix, and d) the associated energy density as a function of the orientation of a particle for various aspect ratios. AR is the aspect ratio of the particles and E^*_b is the effective electric strength (denoted E_{BD} in the text). The effective surface fraction of the inclusion is 0.785%.[43]

Firstly, as the aspect ratio increases, the influence of the particle orientation on both the permittivity enhancement factor and the electric strength increases. When the particles are oriented in the electric field direction, the R_ε is at its maximum and E_{BD} at its minimum, and reversely when the particle is oriented perpendicularly to the field direction.

This result illustrates two important relationships commonly found in composites filled with ellipsoidal high-ε particles[8,43,48–54]:

- The electric field distortion is maximum (resp. minimum) when the particles are oriented parallel (resp. perpendicular) to the electric field.
- Higher is the electric field distortion, higher is the effective permittivity and the maximum local electric field

Then, from the calculated electric strength, the authors suggest that the maximum energy density cannot be increased with respect to the pure matrix (see Figure 1.19 d). However, the best case is always the composite with the particle having the highest aspect ratio and oriented perpendicularly to the electric field direction (which tends to a perpendicular multilayer structure, corresponding to the lower Wiener limit).

The divergence point found in the literature is the possibility to increase or not the energy density of the polymer matrix by introducing high-ε fillers. Indeed, even though Zhang et al. experimentally confirm[48] the above mentioned hypothesis of Roscow et al., Shen et al. suggest the opposite may be true, by proposing another model based on the growth of the breakdown path and supported by experimental studies[55]. Indeed, the authors show that orienting nanosheets or nanofibers perpendicularly to the electric field would allow increasing the energy density up to a given particle content Figure 1.20.

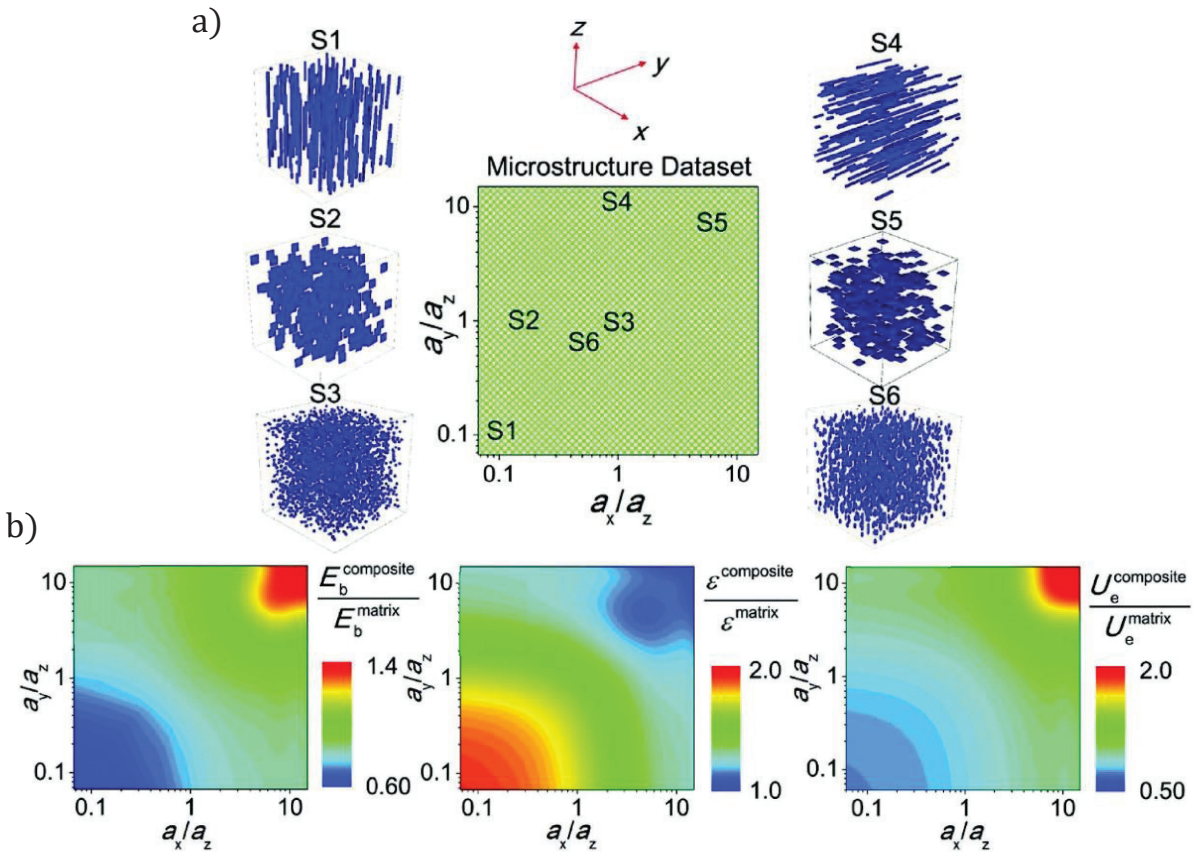

Figure 1.20: Schemes of the general relationships between dielectric properties and structural parameters in composites filled with high-ε particles. (a) Definition of the dimension factors a_x/a_z and a_y/a_z (b) enhancement factors of the Electrical strength, permittivity and energy density as a function of the filler dimension factors[55]. Electric field is along the z direction.

The results presented in Figure 1.20 (b) confirm that aligning platelet/sheet-like particles perpendicular to the electric field maximizes the energy density. Indeed, this configuration is close to the perpendicular multilayer structure and thus induces the lowest electric field distortion.

From inclusions to multi-layered structures

All these studies suggest that the best compromise is found in composite with a structure close to the perpendicular (series) multi-layer structure. Eric Baer and Lei Zhu have reviewed the possibility of tuning dielectric properties through multilayer polymer composites[21]. By increasing the number of layers in a PC:PVdF multilayer composite (and thus decreasing the layer thickness), dielectric losses may be reduced through nano-confinement of ionic species, which reduces both the conductivity and the associated MWS polarization as presented in Figure 1.21 a)[56]. Indeed, since the conductivity of PVdF is higher than that of Polycarbonate (PC), charge carriers migrating in PVdF accumulate at the interfaces with PC, leading to MWS polarization.

However, as the thickness of PVdF layers is decreased down to about 50 nm, the distance on which charge carriers migrate is decreased accordingly.

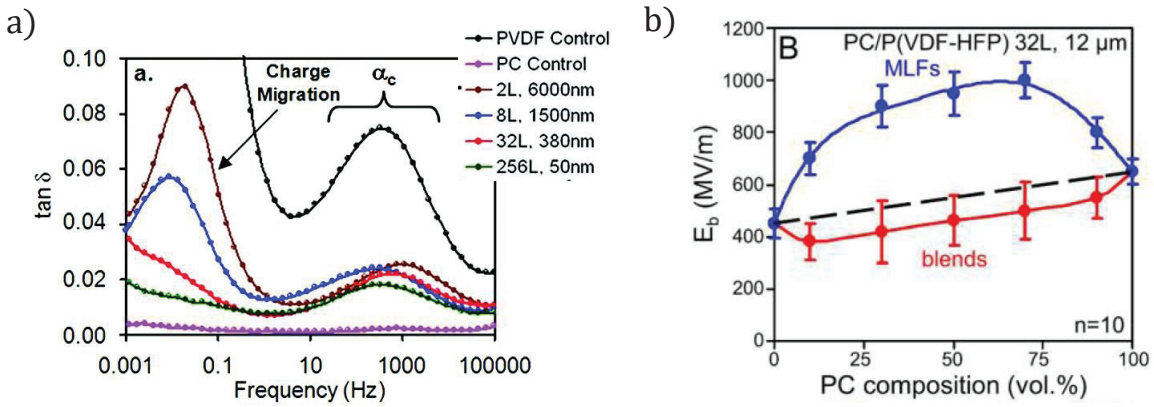

Figure 1.21: with a) Dielectric spectroscopy of PC/PVdF 50/50 multi-layered films with 2, 8, 32, 256 layers compared to pure PC and PVdF films (all films are 12 μm thick)[56] and b) breakdown strength of PC/PVdF-HFP multi-layered films with 32 layers compared to simple blends as a function of the composition[57].

Moreover, increasing the layer number considerably increases the electrical strength. Tseng et al. have reported that the effective breakdown strength of PC-PVdF-HFP multilayer films becomes higher than the respective breakdown strength of both PC and PVdF-HFP[58]. The authors explain these results as a consequence of the interfacial polarization of ions and electrons.

The results reported in the literature about multilayer associations of polymers are consistent with the general trend of the dielectric properties with the structural indicators presented before. This general trend is observed in nearly all works found in the literature.

1.3.3 MWS interfacial polarization

As seen before, when the composite phases have different conductivities, interfacial polarization mechanisms (MWS) may emerge from the accumulation of charge carriers at interfaces. In this case, the MWS polarization impacts the effective permittivity of the composite material, **which may then overcome the Wiener limits and even become higher than the permittivities of both constituents**[42].

Indeed, Polyimide-Alumina nanocomposites were found to break the Wiener limit due to an additional interfacial polarization mechanism provided by conduction phenomena, as illustrated in Figure 1.22.[59]

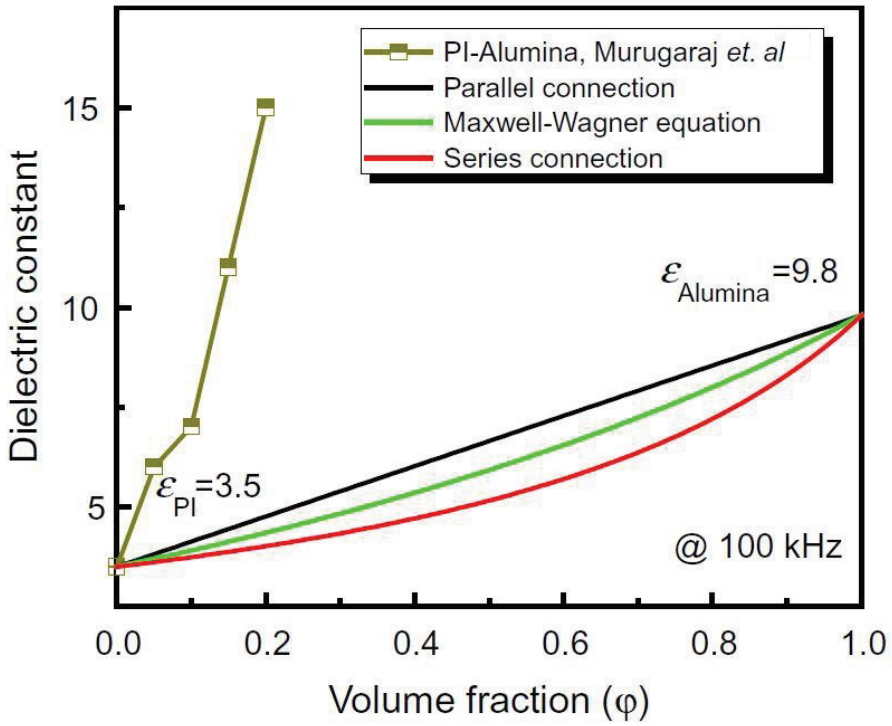

Figure 1.22: Example of a Polyimide-Alumina nanocomposites whose permittivity at 100 kHz breaks the Wiener limit (parallel connection)[42].

Similarly, Figure 1.23 presents the results of several studies reviewed by Zhang et al.[42]Figure 1.22. Conducting particles were used in the three reported cases: First, the bulk conductivity of $CaCu_3Ti_4O_{12}$ (CCTO) particles is reported to be about 10^{-7} to 10^{-5} $S.cm^{-1}$ at RT [60], which may explain the permittivity increase observed on the black square and blue triangle curves in Figure 1.23. For the red curve, the presence of conducting nickel particles is mentioned in addition to $BaTiO_3$ particles, which allows similar interpretation.

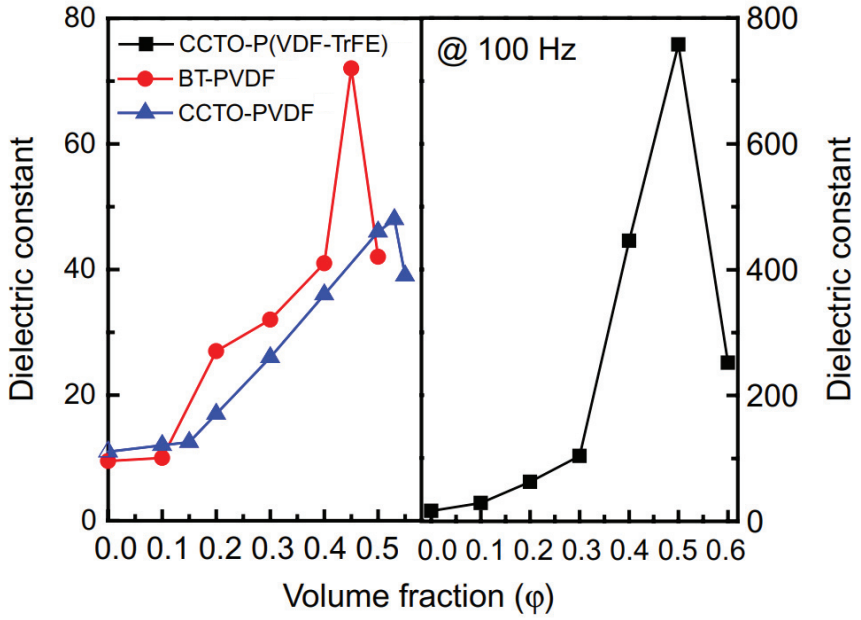

Figure 1.23: Example of systems with an effective permittivity overcoming the parallel association rule of mixing at 100Hz[42]. (Black squares: conducting CCTO ($CaCu_3Ti_4O_{12}$) particles; Red circles: $BaTiO_3$ + Ni particles; Blue triangles: conducting CCTO particles)

When conducting particles locally percolate, they can polarize on long distances, leading to drastically enhance the effective permittivity. Beyond the percolation threshold, the decrease of the permittivity is due to macroscopic percolation of the conducting particles that prevents electrical charge accumulation within the composite. This behaviour is schematized in Figure 1.24.

Polymer-based composites exhibiting giant permittivity can thus be obtained near the percolation threshold[61–64]. As a consequence, such systems usually exhibit very high dielectric losses and very low electrical strength which are detrimental for many applications including energy storage.

Nevertheless, high effective permittivity and relatively low dielectric losses may be achieved by precisely controlling the composite structure. For example, PDMS foams associated with carbonated particles were shown to exhibit permittivities of about 80 with a loss factor lower than 0.1[65].

Such MWS polarization mechanisms are also found in semi-crystalline polymers where the amorphous and the crystalline phases do not have the same conductivity, like in the case of PVdF polymers[66,67] or PolyEtherEtherKetone (PEEK)[68]. The charge carriers migrating in the phase with the highest conductivity (in most cases the amorphous phase) accumulate at the interfaces of the phase with the lowest conductivity.

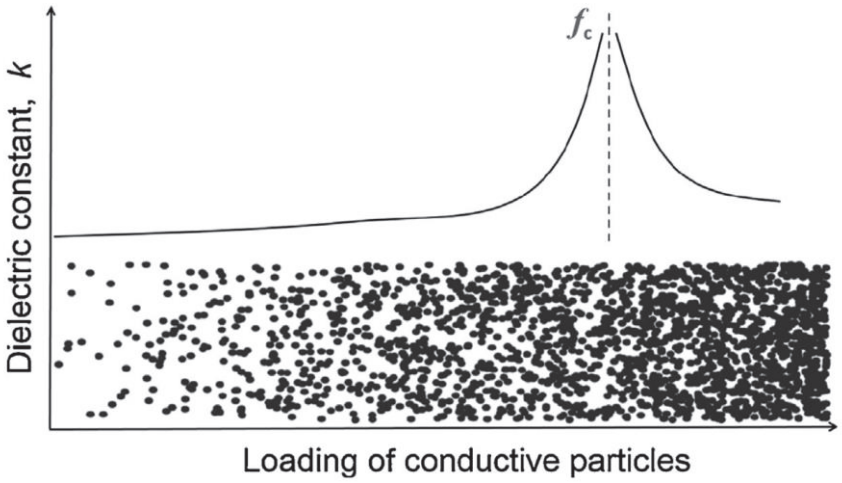

Figure 1.24: Illustration of the effective permittivity of composites filled with conducting particles. Giant permittivity is reached near percolation threshold (f_c).[61]

1.3.4 Interaction between particles

The calculated electric field and the rule of mixture presented before (see equation (1.19)) do not consider the interactions between particles. In concentrated systems, the polarized particles may modify the electric field seen by the other particles, and this may modify the effective permittivity. These interactions are called dipolar correlations. To evaluate the minimum interaction distance, an interaction radius r can be calculated arbitrarily as the limit beyond which the electric field is not modified more than 5%. The maximum values of the components $E_{out(r)}$and $E_{out(\theta)}$ can be calculated from equations (1.19) (in the case $\varepsilon_i = \infty$):

$$\begin{cases} \dfrac{E_{out(r)} - E_h}{E_h} = 2\dfrac{a^3}{r^3} = 5\% \\ \dfrac{E_{out(\theta)} + E_h}{E_h} = \dfrac{a^3}{r^3} = 5\% \end{cases} \rightarrow \begin{cases} \dfrac{r}{a} = \sqrt[3]{\dfrac{2}{0.05}} = 3.41 \\ \dfrac{r}{a} = \sqrt[3]{\dfrac{1}{0.05}} = 2.71 \end{cases} \tag{1.23}$$

We can now consider a well-dispersed system in which the centres of the particles are separated by a distance r = (3.41+1)a . In a face centred cubic structure, such inter-particle distance would correspond to a volume fraction of 7 %. As a result, one may consider the interactions between particles to be negligible and so the Maxwell Garnett model to be valid for systems with less than about 7 vol% of particles.

The interaction between neighbouring particles in concentrated systems can be constructive or destructive (i.e. leading to higher or lower permittivity) depending on the respective positions of the particles with respect to the electric field direction.

- If the two particles are aligned in the electric field direction, the particle interaction results in a higher total polarization and higher effective permittivity (Example of simulation and experimental result in Figure 1.25.)
- If the particles are aligned perpendicular to the electric field direction, the effect is opposite. Since the polarization of the particles tends to reduce the electric field at the equator, a polarized particle reduces the electric field acting on its neighbours. The effective permittivity then tends to be reduced by lateral interactions.

In their computational work, Jin et al. have shown that the interaction between two particles which are aligned in the electric field direction result in higher electrical displacement (represented by the colour mapping in Figure 1.25) and thus higher effective permittivity as the particles get closer[69]. An experimental study carried out by Bowen et al. has led to similar results[70]. The authors have shown that the effective permittivity can be increased by a factor 3 by aligning high-ε Barium Strontium Titanate particles in the electric field direction as compared to unaligned particles.

These two kinds of interactions, respectively increasing and decreasing the effective permittivity, do not necessarily cancel in a polymer composite with high particle content or agglomerated particles. Recently, Kushimoto et al. proposed a model describing the effective permittivity of composites in which part of the particles are well dispersed while the other part are randomly agglomerated at different volume ratios[71]. They show that higher is the fraction of agglomerated particles, higher is the effective permittivity. This result suggests that random interactions between particles lead to increase the effective permittivity. However, the exact effect of the agglomeration state on the permittivity is not well described yet.

Concerning the electric field distribution, a bad dispersion state tends to increase the interactions between particles which further enhances the maximum local electric field. This effect may be detrimental to the electrical strength of the composite material. Indeed, in a randomly arranged agglomerate, the electric field is inevitably enhanced between particles interacting in the electric field direction. As a result, the agglomeration of high-ε particles would both increase the effective permittivity and the maximum local electric field in composites. Thus, further investigations are required to fully elucidate the relationships between particle dispersion state and dielectric properties in polymer-based composites.

a)

b)

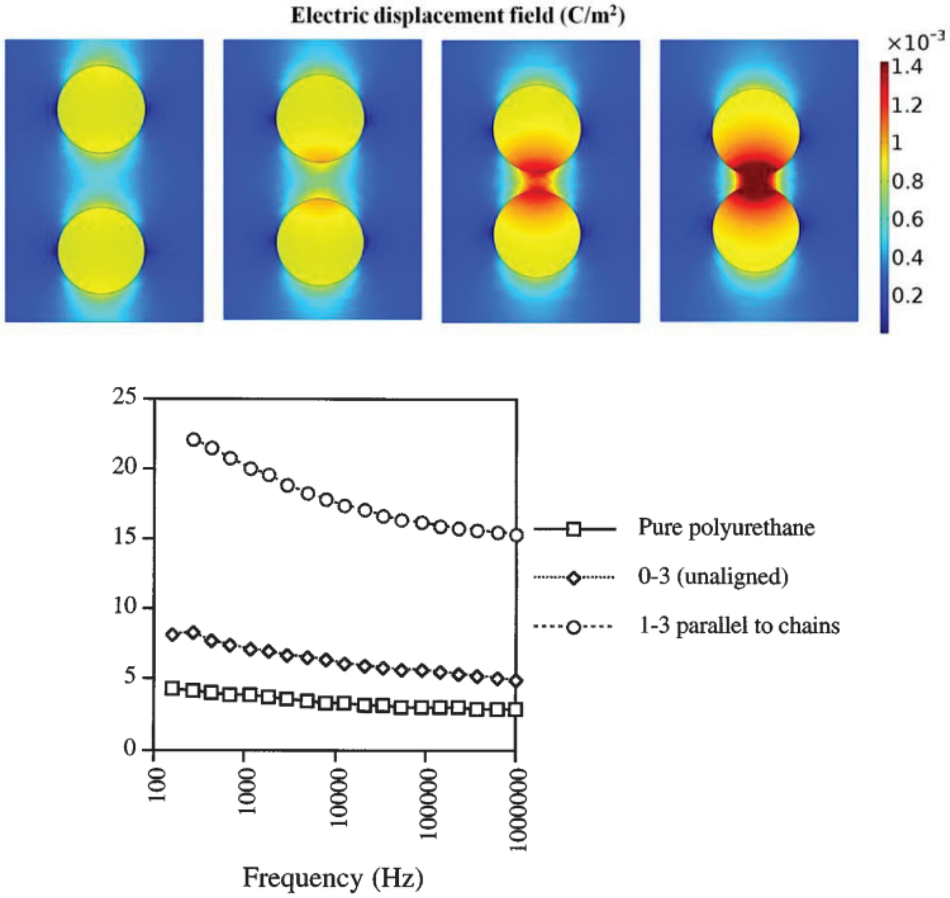

Figure 1.25: Simulation of interacting high-ε particles aligned in the electric field direction with a) a colour mapping of the electrical displacement D and b) experimental results of effective permittivity for polyurethane-based composites filled with high- NPs align either in the electric field direction or perpendicularly [69,70]. (In the legend, “parallel to chains” corresponds to “aligned parallel to the electric field”.)

1.3.5 Conclusion

When high-ε spherical inclusions are introduced in a polymer matrix, the electric field converges towards the particles and is thus amplified at the poles of the particles, as schematized in Figure 1.26.

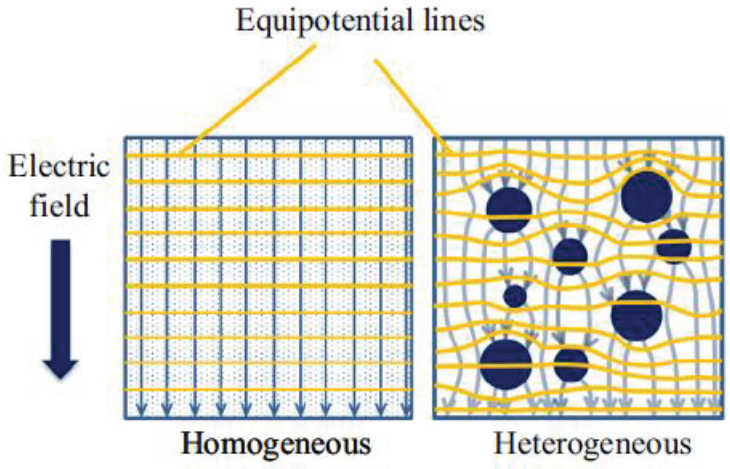

Figure 1.26: Equipotential and electric field lines for homogeneous materials and composite material filled with high permittivity fillers[71].

For anisotropic high -ε particles, this effect strongly depends on the orientation of the particles. As schematized in Figure 1.27, increasing the orientation of the composite structure in the direction parallel (resp perpendicular) to the electric field leads to increasing (resp. decreasing) the effective permittivity.

In the case of composites with heterogeneous conductivity, the effective permittivity may overcome the upper Wiener limit due to interfacial MWS polarization related to free charge carriers.

The local electric field enhancement associated with the increase of the effective permittivity is thought to reduce the electric strength. It follows that the expected trends for the effective permittivity and electric strength are opposite. As a result, a compromise between effective permittivity and electrical strength has to be found when designing the dielectric properties of composites. There is however no consensus in the experimental works.

Several points remain unclear: (1) The relationships between the particle dispersion state and complex permittivity is not fully elucidated. (2) There is no consensus about the possibility of increasing the electrical strength (or at least keeping it constant), which is key for designing a polymer-based composite with increased energy density. Somehow contradictory reported results may come from other factors, such as the non-

homogeneity of the electric strength in the volume of the material or the effect of both interfaces and material electronic structure on the electrical strength.

The role of the interfaces in the dielectric properties of polymer-based composite is increasingly considered in the literature, particularly for nanocomposites where the specific interfacial area is huge. The electric field distortion illustrated in Figure 1.26 leads the charge carriers to converge towards the particle surfaces. As a consequence, the role of NPs on the charge carrier transport in composites must be considered.

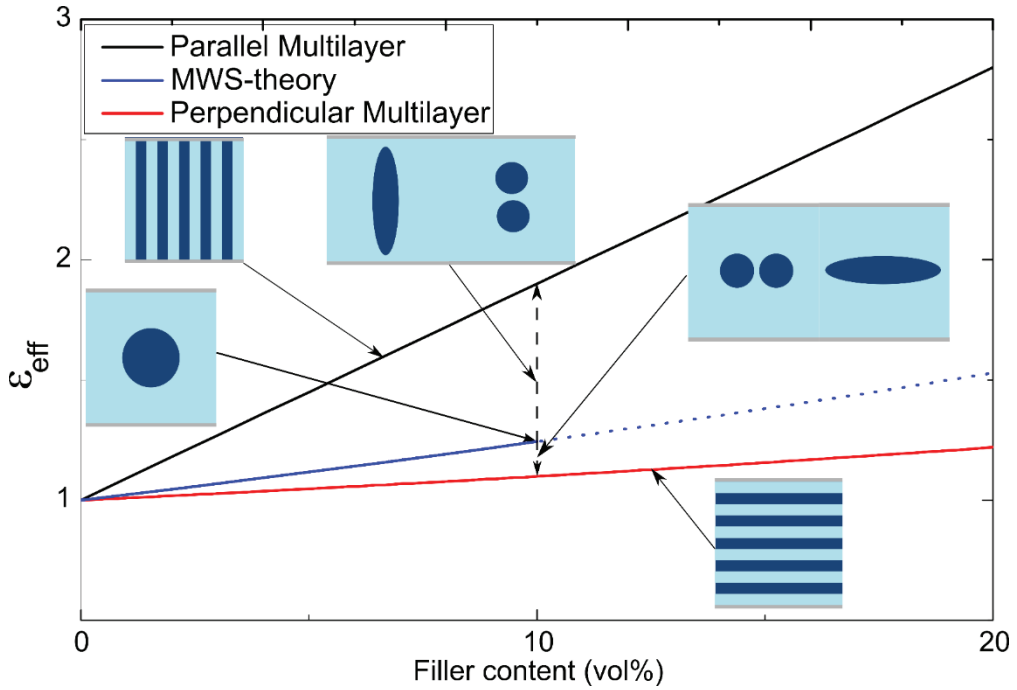

Figure 1.27: General trends of the effective permittivity rules of mixture with the structure of the composites (ε_i=10 and ε_h=1). The parallel (resp. perpendicular) cases correspond to the upper and lower Wiener limits respectively.

1.4 Interfaces and electronic structure

In the field of polymer-based composites and nanocomposites, the effect of interfacial features on global dielectric properties are generally considered to be important for several reasons: (1) interfaces may contain chemical groups that are present neither within the particle or polymer bulk. The properties of the interphase may thus be different from those of the bulk phases. (2) Real materials may exhibit structural changes at the surface, due to stress relaxation or different coordination of the surface atoms. (3) The two constituents may interact and modify their respective properties at the interface.

For these reasons, the interfaces may be the sites of physical or chemical defects (high charge density, physical disorder, unfinished bonds, free volume…). It follows that

the effects of surfaces and interfaces are more and more considered in order to understand the mechanisms involved in the determination of the final dielectric properties in nanocomposites. Altogether, interfaces may have detrimental effects on dielectric properties. On the other hand, interfaces may also offer new levers to optimize the dielectric properties of polymer-based nanocomposites.

1.4.1 Surface energy and polymer/particle interactions

Ceramics, metal oxides, metallic and carbonaceous fillers usually exhibit high surface energies as compared to the polymer matrix. This results in weak polymer-particle interfacial interactions which may have detrimental effects on dielectric properties. Two main reasons may be highlighted:

1) Particles having low interaction with the polymer matrix tend to agglomerate during the fabrication/mixing process. In the literature, the particle functionalization is widely used in order to improve their dispersion state and thus the dielectric properties of nanocomposites[72–81]. In most cases, improving the dispersion state results in a slight decrease of the permittivity, in a decrease of dielectric losses and in an increase of the electrical strength. Nevertheless, quantitative studies of the relationships between particle dispersion state and dielectric properties in polymer nanocomposites have not been carried out so far.
2) Weak affinity between particles and matrix may result in decohesion of the polymer and formation of cavities at the interface. Cavities may be detrimental to dielectric properties for several reasons: (1) they behave like low permittivity ($\varepsilon_r \sim 1$) particles and thus decrease the overall effective permittivity of composites. (2) Partial discharge in cavities may affect the electrical strength as schematized in Figure 1.28[82]. (3) The local electric field may be further enhanced inside the cavity. The combination of these two latter effects may lead to very early failure due to breakdown initiation. Moreover, the presence of cavities at the interfaces reduces thermal conduction and may trigger thermal breakdown. Improving the fillers/matrix affinity using particle surface functionalization is thought to reduce the presence of cavities at the interfaces and thus to improve the dielectric properties[83]. Indeed, Chen et al. explain the improvement of the electric strength of PVdF:$BaTiO_3$ nanocomposites with modifying the NP surface by the suppression of the cavities at interfaces[84].

The affinity between two constituents can be predicted from their surface energies (surface tension, interaction parameters). The closer their respective surface energies, the better their affinity.

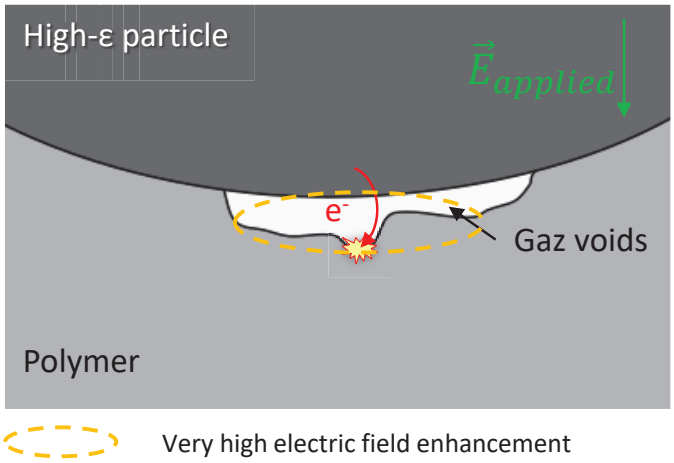

Figure 1.28: Illustration of partial discharge in an interfacial gas cavity due to very high electric field enhancement.

1.4.2 Electronic structure at the interfaces

Interfaces may be considered as a third phase (interphase) having different properties than the other phases (chemical constitution, physical order…). Indeed, several factors may impact the electronic structure at the interfaces.

Electrical double layer

When two phases presenting different Fermi levels (or electron affinity) are put in contact, the equalization of the Fermi levels (or electrochemical potential) results in the formation of an electrical double layer. It is composed of several layers of electrical charges (Stern, Gouy Chapman…) coming out from the polarization of the two phases, the dissociation of ionizable surface groups, the adsorption of ionic species onto a solid surface, and the injection of electrical charges between the two phases. This effect is involved for all the interfaces between solids and/or liquids from the synthesis of the particle to the fabrication process of the final composites. Further details about the physical mechanisms involved in the formation of this electrical double layer are given by T. J. Lewis[7]. The electrical charges contained in this electrical double layer modify the electronic structure at interfaces and introduce localized states at the interfaces.

Defect induced localized states

In addition to the electrical double layer, defects may introduce localized states[11,12,29,85] (chemical impurities, physical disorder, internal strains coming from the fabrication process[86], [32,87,88], orbital hybridation[89], etc). Some aspects of the charge carrier dynamics related to the electronic structure at the interfaces in nanocomposites are depicted in what follows

1.4.3 Charge dynamics in the interfacial region.

The electronic structure at interfaces drives the charge carrier dynamics in polymer-based composites. Various effects may be observed depending on the difference of electronic structure from the two phases and on the energy level and the spatial density of the localized states in the interfacial region.

Conduction at the interface

The dielectric properties of interfaces in polymer composites were reviewed by T. J. Lewis with a special emphasis on the potential effect of the interphase percolation on the dielectric properties[7]. Indeed, percolation of the diffuse layers may allow the charge carriers to extensively migrate through the system as shown in Figure 1.29. In this case, macroscopic percolation would result in the loss of the insulating properties in nanocomposites. This shows the importance of controlling both the interfacial features and the NP dispersion state in the design of polymer-based nanocomposites.

More recently, Ghosh et al. have developed a model in which an interfacial layer containing mobile space charges is considered in the calculation of the real part of the effective permittivity. This model well fits a set of various experimental results in which giant effective permittivities were observed at low frequencies[90]. A review of the existing models describing interfaces in polymer-based composites has been proposed by Luo et al. [82].

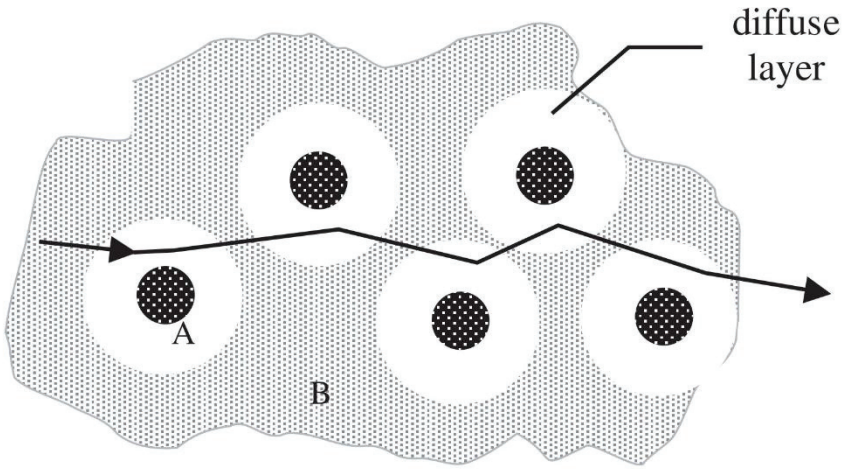

Figure 1.29: Conduction via percolation path through diffuse double layer of particle/matrix interfaces in a composite. Inter-particle distances and the size of the diffuse double layers control the conduction[7].

Charge carrier trapping

In some polymer-based nanocomposites, the NPs may act as trapping sites. Indeed, if the lowest unoccupied molecular orbital (LUMO) of the NPs is lower than that of the polymer, the electrons transferred from the polymer to the NPs and may be trapped in

the NPs because of the energy barrier that has to be overcome to transfer back to the polymer[91]. Conversely, similar trapping can happen to holes if the highest occupied molecular orbital (HOMO) of the NPs is higher than that of the polymer. These phenomena are schematized in Figure 1.30 a).

Similarly, interphases may act as trapping sites if the spatial density of localized states is low enough to prevent charge carrier hopping, as illustrated in Figure 1.30 b).

The creation of deep trapping sites using surface modification of NPs is documented in the literature[92–95]. Wang and Li have reported an improvement of the electrical strength of LDPE/TiO_2 composites by introducing deep traps at the interfaces through the functionalization of the particles with a Silane coupling agent exhibiting polar groups [96].Then, Wu et al. have reported electron trapping in TiO_2 and ZrO_2 NPs embedded in silicone and holes trapping in anthracene-type conjugated molecules grafted on the NPs[13]. This leads to improve the electrical breakdown of the nanocomposites. Finally, in their computational work, Kubyshkina et al. have reported that the chemistry present at the interfaces of a PE-MgO nanocomposite influences the charge transfer and trapping[97]. Although this approach has recently aroused interest and some works have shown encouraging results, a deep understanding of the mechanism involved in the dielectric properties enhancement is still missing.

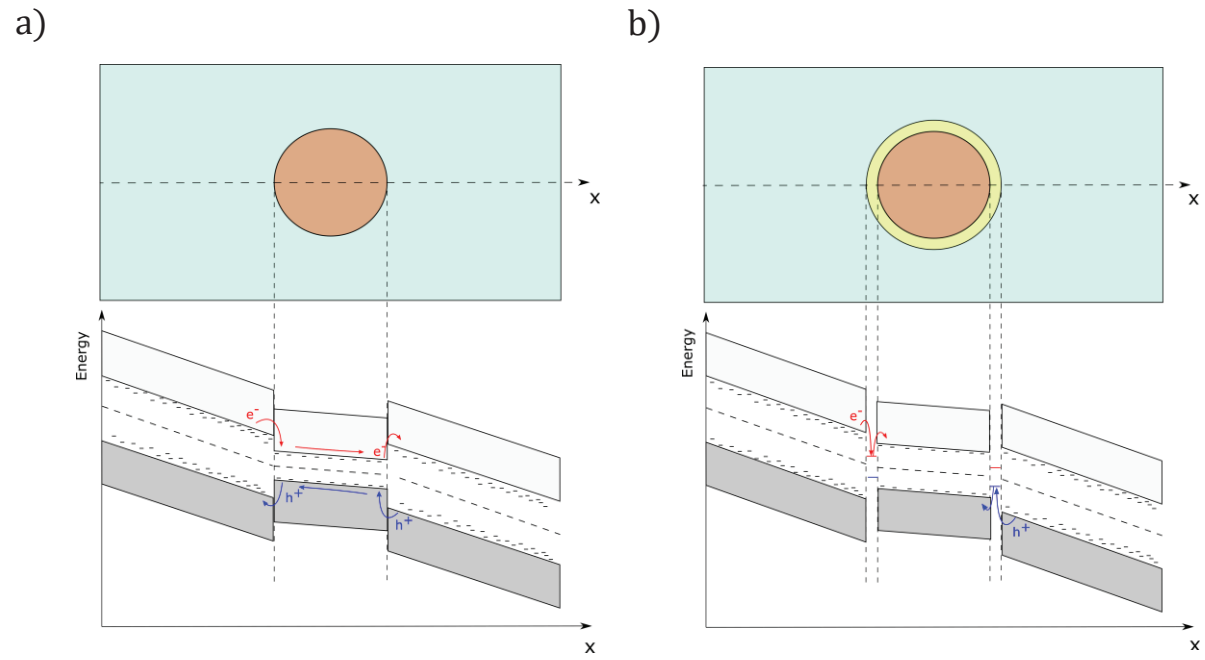

Figure 1.30: Schematization of possible nanocomposite electronic structures inducing charge trapping in a) the NPs and b) the interphase.

Barrier effect

If the LUMO (resp. HOMO) of the NPs is higher (resp. lower) than that of the polymer matrix, the electrons (resp. holes) face an energy barrier while reaching the NPs, as represented in Figure 1.31 a). This is the case where an ideal interface is considered (discontinuity between two phases with homogeneous properties). Similarly, the interphase may prevent electron (or hole) transfer from polymer to NPs if its electronic structure acts as an energy barrier as represented in Figure 1.31 b).

The design of interfaces with reduced localized state density has also shown promising results in terms of dielectric properties improvement[82,92,98–103]. For example, Alhabill et al. have demonstrated a lower electrical conductivity of SiN:epoxy nanocomposites by replacing the hydroxyl groups of the NP surface by siloxanes by performing a thermal treatment at 1050 °C under nitrogen on the NPs[99]. The authors have proposed a model considering the localized state density in the interfaces that well fits with the obtained results. Moreover, many examples of high-ε NPs covered with inorganic SiO_2 which has wide band gap, are reported in the literature as a good way to reduce dielectric losses in polymer nanocomposites[82]. Finally, Dou et al. reported the improvement of the electric strength in PVdF:$BaTiO_3$ nanocomposites by grafting alkyl chains on the surface of the $BaTiO_3$ NPs[98]. In these cases, the electrons (or holes) are stopped at the interface and have to migrate around the NPs through the polymer or the interphase. Then, the NPs constitute obstacles to the charge carrier transport.

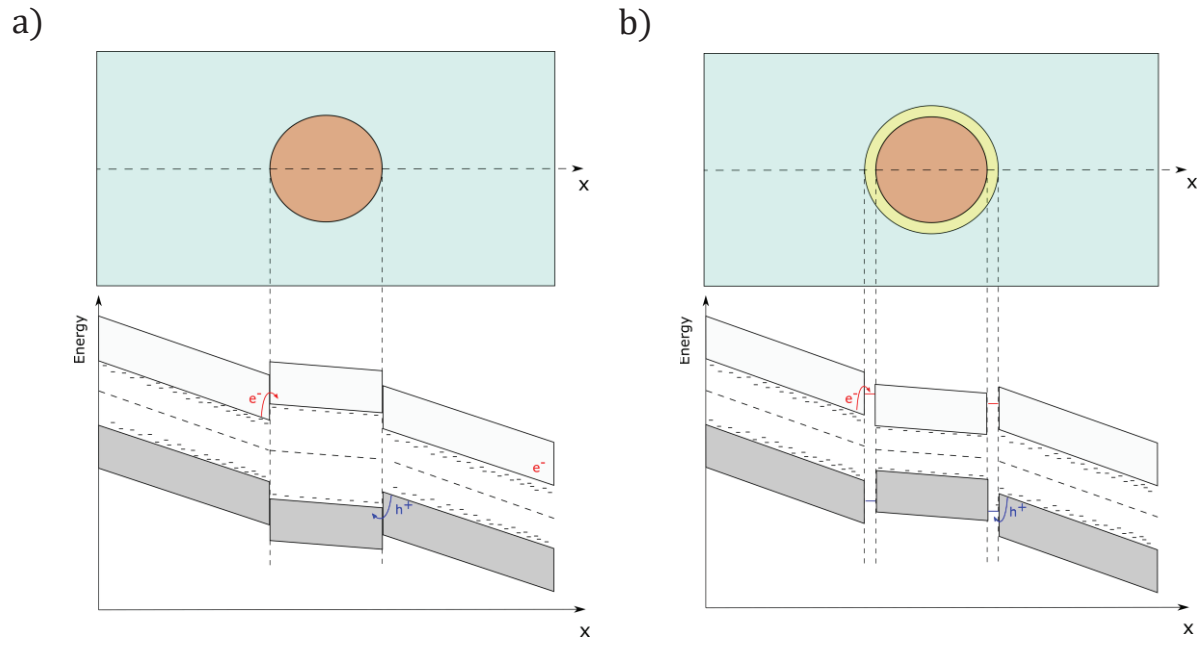

Figure 1.31: Schematization of possible nanocomposite electronic structures where a) the NPs and b) the interphase act as a barrier to the charge carrier transfer from polymer to NPs.

Impact excitation

Impact excitation corresponds to a mechanism in which the energy of a hot charge carrier is dissipated after a collision with the material structure. In this collision, the hot charge carrier transfers its energy to a valence electron which is excited to the conduction band and may then dissipate this energy by emitting a phonon or a photon when it recombines. This mechanism is increasingly considered in literature as a way to improve the electrical strength of insulating materials[11,38,40]. In their computational work, Zhang et al. consider the electronic structure of small molecules in order to find a good candidate for electron energy dissipation by impact excitation[93]. More recently, Wu et al. have proposed a mechanism of impact excitation in both TiO_2 NPs and organic additives to explain improvement of breakdown strength in silicone-based nanocomposites[13]. As a result, a molecule or a particle with a low band gap is likely to induce the dissipation of the hot electron energy by impact excitation before it could be high enough to deteriorate the polymer matrix.

Nevertheless, only few studies have reported such results and interpretations so this needs to be confirmed by additional studies.

1.4.4 Conclusion on particle surface modification

To conclude, since high-ε particles attract charge carriers that migrate within the polymer under an external electric field, controlling the interfacial features must be considered a key element in designing polymer-based nanocomposites with good dielectric properties. In the absence of control, the interfaces may contain defects (cavities, cracks, free volume, physical disorder, chemical impurities, etc) and induce particle agglomeration that are both detrimental for the insulating properties (breakdown strength and dielectric losses). Three types of approaches for particle surface modification can be considered, depending on the final objective:

1) Improve the compatibility between the particles and the matrix (leading to better cohesion, less cavities).
2) Create a strongly insulating layer at the interfaces which results in the electrical insulation of the interfacial region.
3) Create an active layer (in which electrons can be trapped for example) by grafting appropriate species on the NPs surface.

However, in general, the three approaches mentioned here are very difficult to realize separately. Indeed, the effects of surface modification of NPs on the dielectric properties in polymer composites are usually assigned to be a consequence of several chemical, physical or structural changes acting together. Moreover, the characterization of the dispersion state is usually missing or incomplete. It is thus complex to

discriminate the specific effects of interfacial features on dielectric properties in polymer-based nanocomposites.

1.5 Conclusion about the state of the art

To conclude, designing the dielectric properties of polymer-based nanocomposites involves a **complex property compromise**. While a number of factors, such as **structural features,** have a well-established effect on the dielectric properties, the specific effect of other factors on the global dielectric properties, such as the filler **dispersion state**, the **electronic structure** and the **interfacial features**, are still unclear and a general understanding is still missing. This must come from the difficulties to properly characterize the electronic structure of heterogeneous materials as well as from the fact that several mechanisms are involved in the relationship between interfacial features and dielectric properties in nanocomposites (dispersion state, charges dynamics, morphology of the interfaces…).

On the basis of the state of the art presented above, we have designed a methodology to study relationships mentioned before as precisely as possible.

1.6 Methodology

The aim of this study is focused on the relationships between physicochemical features such as the electronic structure and the interfaces, and global dielectric properties of nanocomposite materials based on a polymer matrix filled with high-ε inorganic fillers. To enable such investigation, all other parameters have to be kept as constant as possible.

1.6.1 Matrix selection

The matrices have been selected on various criteria. First, they have to present good intrinsic dielectric properties and especially good electrical strength.

First, PVdF-HFP has been chosen as a key polymer for this study because of its high dielectric constant (about 7-8 at RT and 50Hz) and high electrical strength (several hundred Volts per micron). The high permittivity arises from the high mobility of polar groups. Indeed, VdF units have CH_2 opposite to CF_2 and thus exhibit a high dipole moment. In addition, these dipoles have high mobility at RT because of the low glass transition temperature (about -40°C) of the polymer. PVdF-HFP is a semi crystalline polymer which was widely studied in the literature for energy storage and many other applications. It is a reference in the field and produced by Solvay.

In spite of these good performances, the high dielectric losses of PVdF-HFP ($\tan(\delta)\sim0.1$) may be a drawback in this study because it may mask dielectric

phenomena occurring in composites. Thus, PC was chosen as the second polymer matrix. Indeed, it is already used in microelectronics and more precisely in capacitors because of its high electrical strength and very low losses ($\tan(\delta)\sim0.005$). It presents the advantage of being amorphous. PC has a low permittivity ($\varepsilon'_r=2.9$ at RT and 50Hz), almost constant over 8 decades of frequencies because it has a glass transition temperature around 150°C.

1.6.2 Particle selection

The selection of the particles has required much attention because of the numerous structural features having an impact on the dielectric properties (see section 1.3). The objective was to find 3 particles with different band gaps in order to study their effect on the dielectric properties of nanocomposites. As a result, the following criteria has been considered for the selection of the particles.

- The particles must be spherical to avoid any effect of aspect ratio and orientation.
- The particles must all have similar diameters. On one hand, smaller will be their diameter, harder will be their dispersion in the polymer matrix. On the other hand, they have to be small enough compared to the thickness of the composite films which is usually about 10 μm.
- Safety criteria are considered.
- Their permittivity has to be high enough as compared to the matrix. Indeed, when the permittivity contrast between the particle and the matrix increases, both the complex effective permittivity and the electric field distribution in the composite converge towards those of equivalent conducting particles (infinite particle permittivity). Above a given value, increasing the permittivity contrast does not have a significant effect on the particle polarization. PVdF-HFP has a permittivity of about 7-8 so a minimum of 70-80 is required to keep a factor 10 between particle and matrix. Indeed, below 10 vol%, the difference of permittivity enhancement expected between a permittivity ratio of 10 and an infinite one is lower than 25% according to the M. Garnett theory.
- The particles must be commercially available.

Band gap in several types of particles were estimated by Density Functional Theory (DFT) calculations (performed by Rabih Al Orabi, Solvay). Three particles with different band gaps were finally selected:

1. $BaTiO_3$ NPs (from Sigma Aldrich) presenting a permittivity about 150 and a mean diameter about 50 nm. A band gap of 3.8 eV is reported in many works of the literature and matches with the DFT calculations.

2. WO_3 NPs (from Nanoamor) presenting a permittivity of 70 (obtained by DFT calculation) and a mean diameter about 30-70nm. A band gap of 2.5 eV is reported in many works of the literature and matches with the DFT calculation.
3. Ag NPs (from Nanoamor) presenting an infinite permittivity because of their high electronic conductivity and a mean diameter of 80nm. They are metallic.

1.6.3 Surface Modification selection

As presented in section 1.4.4, three main approaches can be considered in particle surface modification in order to improve dielectric properties in polymer-based composites: affinity improving, creation of an electrically passive layer and the creation of an electrically active layer. In this work, the three approaches have been considered.

1.6.4 Final methodology

The results presented and discussed in this manuscript follow a methodology that has been reshaped due to technical issues:

1) Concerning the matrices, only the PVdF-HFP is mentioned in this study. Indeed, nanocomposite films of good quality have not been achieved with PC as matrix.
2) Concerning the particles, both Ag and WO_3 NPs could not be properly dispersed in the polymer matrices.
3) Concerning NP surface modification, the creation of an electrically passive layer and the improving of the affinity between $BaTiO_3$ NPs and PVdF-HFP were prioritized since they do not require electronic structure characterization of the materials.

The main technical issues encountered are developed in the Appendix A.

As a result, PVdF-HFP-based nanocomposites filled with $BaTiO_3$ NPs have been studied. Their fabrication by solvent casting process and the study of interaction parameters enabled the control of their dispersion state. The effect of NP dispersion state on dielectric properties has then been studied. Finally, the effects of NP surface modification on both the process and the dielectric properties of nanocomposites were studied.

Chapter 2. Materials and Methods

2.1 Materials

2.1.1 Neat PVdF-HFP polymer

PVdF-HFP Solef® has been provided by SOLVAY as a white fine powder. It is a semi-crystalline fluorinated copolymer that exhibits very high polarizability due to spontaneous polarization of the highly polar C-F bonds (dipole moment of 2.1 Debye, i.e. about 7.10^{-30} C.m)[104,105]. Its chemical formula is shown in Figure 2.1, where *x* is the molar fraction of VdF monomers and *y* the molar fraction of HFP monomers. VdF and HFP monomers are randomly distributed along the chain. *y* is lower than 20 %. Like other PVdF-based polymers, it possesses a very good chemical resistance. Typical properties of PVdF-HFP Solef® are reported in Table 2.1.

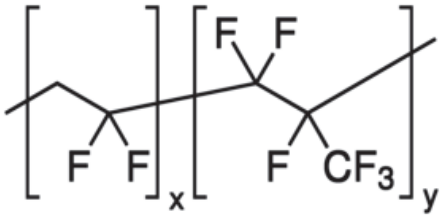

Figure 2.1: Topologic formula of the PVdF-HFP (random copolymer)

PVdF-based polymers have at least four crystalline polymorphs shown in Figure 2.2. Polymer chains in (α) and (δ) crystalline structures (Figure 2.2 A and B) are arranged in trans-gauche-trans-gauche conformation (TGTG shown in Figure 2.2.E) and their unit cells have similar dimensions. In the (α) phase, the dipoles are oppositely oriented in such a way that they cancel, making the polymorph non-polar. In contrast, the dipoles in the (δ) structure are oriented in the same direction, making the polymorph highly polar. The (γ) phase, shown in Figure 2.2.C, possess a trans-trans-trans-gauche (TTTG-TTTG shown in Figure 2.2.F) conformation and the similarly oriented dipoles make it polar. The β phase, shown in Figure 2.2.B, is the only polymorph to be ferroelectric. The all Trans (TTTT shown in Figure 2.2.G) conformation of this phase provides the highest polarity among the PVdF polymorphs.

The HFP monomer induces a lower crystallinity than in pure PVdF and prevents the formation of the β crystalline phase. The absence of ferroelectricity brings very good potential for storage energy applications to the PVdF-HFP, due to low energy losses. Large breakdown fields (up to 700 V/µm) and high energy densities, up to 25 J/cm^3, have been obtained after process optimization as reported by Zhou et al.[106].

Table 2.1: Typical properties of PVdF-HFP Solef® (Determined in this study)

Properties	Typical Value	Unit	Source
Chemical			
Number average molecular weight – M_n	175	$kg.mol^{-1}$	GPC analysis
Mass average molecular weight – M_w	310	$kg.mol^{-1}$	GPC analysis
Physical			
Density at RT	1.75-1.8	$g.cm^{-3}$	Solvay's specifications
Water Absorption 24 hrs at 23°C	<0.040	%	Solvay's specifications
Hansen solubility parameters			Solubility test p.91
δ_D	14.6	$MPa^{0.5}$	
δ_P	11.9	$MPa^{0.5}$	
δ_H	11.4	$MPa^{0.5}$	
Mechanical			
Tensile modulus	360 to 480	MPa	Solvay's specifications
Thermal			
Melting temperature	133	°C	DSC analysis on films casted from MEK p.69

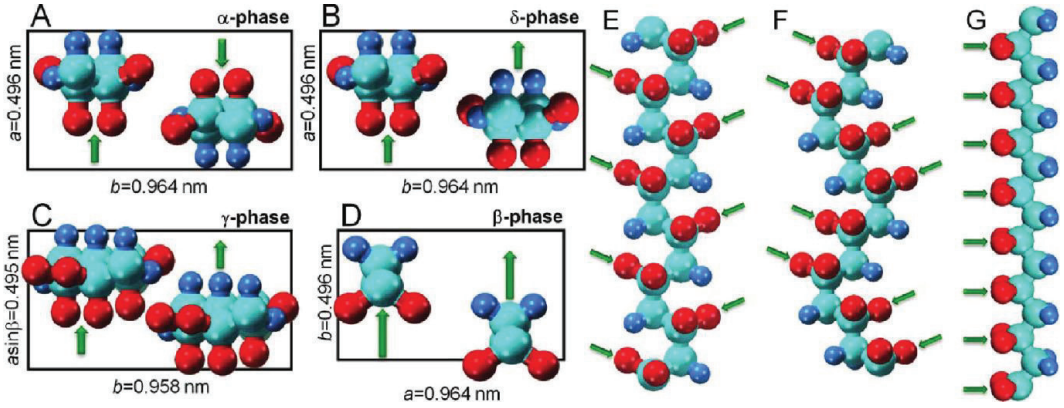

Figure 2.2: Unit cells of (A) α, (B) δ, (C) γ, and (D) β forms of PVDF crystals view along the c-axes and schematic chain conformation for (E) TGTG' (α/δ), (F) TTTGTTTG (γ), and (G) TTTT(β) phases. Red, cyan and blue spheres represent F, C, and H atoms, respectively. The projections of the dipole moment are indicated by green arrows[107].

2.1.2 Neat $BaTiO_3$ nanoparticles

$BaTiO_3$ nanoparticles (NPs) have been chosen because they have been widely studied and reported in the literature. As seen in the State-of-the-art chapter, $BaTiO_3$ NPs are perovskite materials with a particularly high dielectric constant. They are synthesized by reaction between BaOH and TiO_2 and obtained in the form of a fine powder that can be sintered to form a bulk ceramic material or used as particles embedded in a matrix.

In this work, the $BaTiO_3$ NPs were bought from Sigma Aldrich. NPs of diameter of 50 nm were selected to ensure cubic crystalline structure and prevent ferroelectricity (see section 1.2.1). Typical properties of the $BaTiO_3$ NPs are reported in Table 2.2.

Table 2.2: Typical properties of $BaTiO_3$ NPs (determined in this study)

Properties	Typical Value	Unit	Source
Physical			
Density	6.08	$g.cm^{-3}$	Supplier specifications
Crystal structure	Cubic		
Water Absorption (24 hrs, 23°C)	~0.7	wt%	TGA analysis p.68
Structural			
Mean diameter	50	nm	Gas adsorption p.57
Hydrodynamic diameter	140	nm	DLS analysis in MEK, DMF p.73
BET surface	20	$m^2.g^{-1}$	Gas adsorption p.57
Electrical			
Relative permittivity	150		Supplier specifications
Surface			
Surface chemistry	Hydroxyls + Carbonates		DRIFT analysis p.64
Hansen Dispersibility Parameters			
δ_D	20.0	$MPa^{0.5}$	Sedimentation test p.100
δ_P	13.7	$MPa^{0.5}$	
δ_H	15.5	$MPa^{0.5}$	
Isoelectric point	pH 9		Zetapotential measurement in water p.57

NP morphology

The as-received $BaTiO_3$ NPs were characterized by Scanning Electron Microscopy (SEM) following the protocol described later in section 2.3.7. SEM images, shown in Figure 2.3, show large agglomerates of about 5 to 50 µm diameter with nearly spherical shape. The size of the elementary NPs was qualitatively evaluated about 30-100 nm as shown in Figure 2.3 c). Moreover, the rounded shape of the agglomerates suggests that the cohesion energy between the NPs is quite strong.

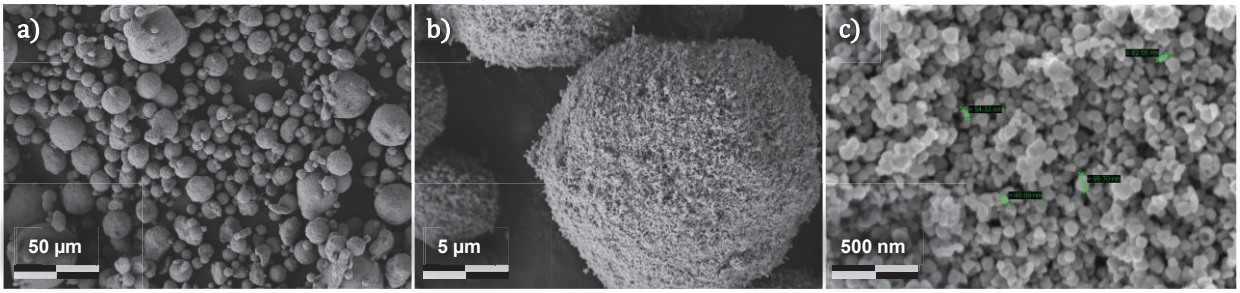

Figure 2.3: SEM analysis of the as-received $BaTiO_3$ NP powder

Specific Surface Area - BET

The specific surface area of the $BaTiO_3$ NPs was characterized by the BET (Brunauer, Emmett, and Teller) gas adsorption method[108]. This experiment has been performed at LoF (Solvay's laboratory in Pessac) with the help of Julien Jolly and Julien Laurens on a Gemini VII –Micromeritics apparatus. The results give a $BaTiO_3$ NP specific surface area of $20 m^2.g^{-1}$. This specific surface area corresponds to a diameter of 50 nm considering monodispersed NPs.

Iso-Electric Point

The isoelectric point of the $BaTiO_3$ NP suspension in water was determined by zeta potential measurements at different pH values by Marie Plissoneau from the Solvay laboratory FIM. The iso-electric point was found at around pH 9 which indicates that the hydroxyl groups are mostly bound to Barium (Ba-OH)[109]. Moreover, all measurements lead to low zeta-potential values (<5mV), which indicates a relatively low concentration of hydroxyl groups on the $BaTiO_3$ NP surface[109,110].

2.1.3 NP surface Modifiers

In order to study the relationships between interfacial features and dielectric properties the $BaTiO_3$ NP surface was modified (see chapter 5). Two types of surface modifications were carried out. The molecules and polymer used as grafting agents are Stearic Acid and Poly(Methyl-MethAcrylate-co-MethAcrylic Acid), denoted PMMA-co-MAA, which is a random copolymer composed of 1 MAA monomer (n) for 60 MMA

monomers (m). Both modifiers were bought from Sigma Aldrich. Their chemical structures are shown in Figure 2.4 and their main properties are reported in Table 2.3.

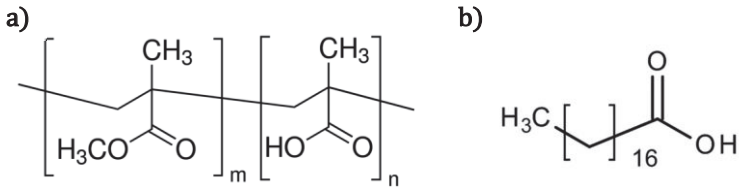

Figure 2.4: Chemical structures of a) PMMA-co-MAA (random copolymer) and b) Stearic acid.

Table 2.3: Typical properties of the PMMA-co-MAA and Stearic acid. *Data for Poly(Methyl-MethAcrylate) (PMMA) homopolymer. **Calculated by ponderation of the HSPs of neat PMMA and neat Poly(MethAcrylic Acid) (PMAA) (60:1).

Properties	Typical Value		Unit	Source
	PMMA-co-MAA	Stearic Acid		
Physical				
Density	~1.2*	0.94	$g.cm^{-3}$	Literature [23]
Melting temperature	~130-160*	68-70	°C	
Degradation temperature (at 1wt% of loss)	252	170	°C	TGA p.69
Hansen solubility parameters				Literature [111,112]
δ_D	18.1**	16.3	$MPa^{0.5}$	
δ_P	9.1**	3.3	$MPa^{0.5}$	
δ_H	6.4**	5.5	$MPa^{0.5}$	
Chemical				
Feed ratio	1:0.016	-		Supplier specifications
Number average molecular weight – M_n	60	-	$kg.mol^{-1}$	GPC analysis p.69
Mass average molecular weight – M_w	97	-	$kg.mol^{-1}$	
Average acid function per chain	10	1		

2.2 Material processing

The fabrication process of the nanocomposites has been developed based on the study of intermolecular interactions via the Hansen theory, presented in chapter 3. The general fabrication process is summarized in Figure 2.5. In this section, the various steps of the fabrication are presented.

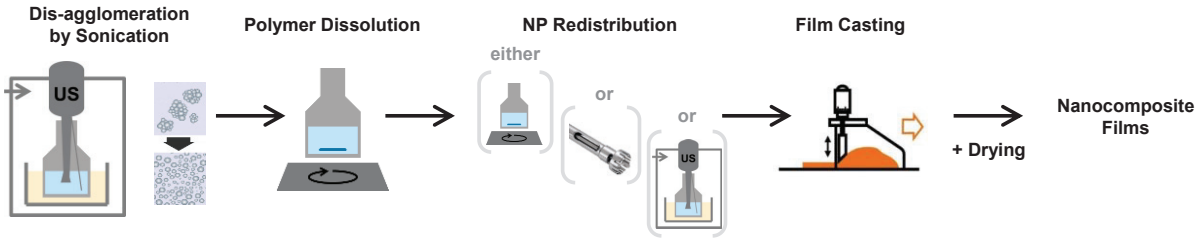

Figure 2.5: Schema of the general fabrication process of polymer and nanocomposite films

2.2.1 NP dis-agglomeration and dispersion

The very first step of the nanocomposite fabrication process is the NPs dis-agglomeration. As mentioned before, the NPs are bound together in large agglomerates in the as-received powder. In order to break these agglomerates and disperse all the NPs, they are introduced in some solvents (typically at 1 vol% of NPs) and high-power ultrasounds are applied to the suspensions. The sonication is performed with a Hieschlet UP200St-T ultrasound device. The experimental set-up is schematized in Figure 2.6. The ultrasounds are produced by the transductor and are transferred to the suspension through the sonotrode whose bottom diameter is 7mm. The acoustic energy produced by the transductor is mainly dissipated in the volume of suspension localized just below the sonotrode. In this zone, the energy density is high enough to induce cavitation. It corresponds to both the formation and the implosion of microscopic bubbles. These implosions lead to solvent jets reaching several centimetres per second and both temperature and pressure can exceed locally 4000 °C and 500 bar at the final stage of the implosion, respectively[113]. These extreme conditions induce extremely large shear stresses below the sonotrode and provide a global stirring of the suspension which are both beneficial to the dis-agglomeration of the NPs.

In the dis-agglomeration process, the maximum available power, ranging between 30 and 70 W, was applied. It depends on the sonotrode geometry, solvent viscosity and boiling point, on how deep the sonotrode is immersed... The sonication time is the main parameter considered in the process development.

The volume of the sonicated suspension being about 20-30mL, the dissipation of the sonication energy leads the temperature to increase by 1 to 5°C per minute. To prevent any problem related to temperature rise, the suspensions are placed into a cooling bath filled with a mixture of acetone and carbonic ice, so that the heat generated by

sonication can be compensated and the suspension temperature can be efficiently regulated with a thermocouple. The set-up is placed into a box which is flushed by a N_2 gas flow to avoid water uptake and for safety reasons.

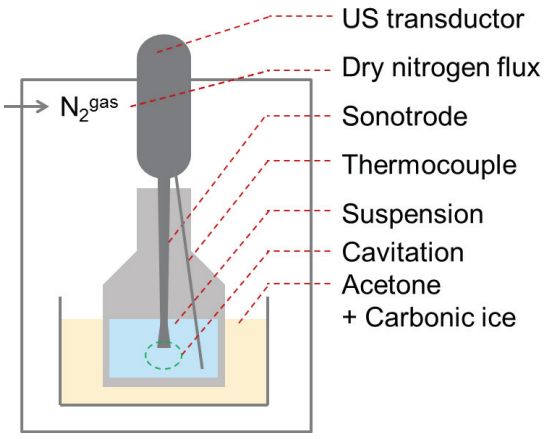

Figure 2.6: Schematic representation of the sonication set up

2.2.2 Preparation of the polymer solution

PVdF-HFP solutions are prepared by dissolving the polymer in a solvent at concentrations from 10 to 20 wt%. After polymer dissolution, the solution is filtered through a 5 µm Teflon filter to remove microgels or eventual dusts coming from the vessel or the solvent. Such impurities tend to deteriorate the dielectric properties of the polymer films[114].

In the case of Methyl Ethyl Ketone (MEK) and 2-heptanone, which are a nearly theta solvent and a poor solvent of the PVdF-HFP, respectively, the polymer solutions tend to gel within a few hrs at RT when the concentration is too high (>10 wt%). These gels melt at about 50 °C, thus PVdF-HFP solutions are always heated at 50°C and cooled down at RT just before performing solvent casting.

2.2.3 Preparation of the nanocomposite suspensions

When the $BaTiO_3$ NPs are properly dis-agglomerated (as checked by DLS, see section 2.3.7.), the suspension is mixed with the polymer solution to produce a ternary solution. Depending on the stability of the suspension, the NPs may re- agglomerate and sediment after the end of the sonication. An additional mixing step is done to homogenize the ternary solution. At this stage of the process, the NPs may have agglomerated and a stronger additional mixing step can be performed. Depending on the shear stress required in this stage of the process, magnetic stirring, mixing with an Ultraturax or an additional sonication step can be performed. The Ultraturax used in this work is an *IKA* Dispersers rotating at 10 000 rpm with a "*S 25 N - 18 G*" dispersing tool.

Degradation of the PVdF-HFP under sonication

The additional sonication step, when applied on the ternary system, may degrade the polymer. The degradation of the PVdF-HFP was characterized by GPC after applying a 20-minute sonication step at 70 W on a 20 mL solution with 15 wt% of PVdF-HFP and 1 vol% of $BaTiO_3$ NPs. These conditions were selected to be the most likely to induce degradation of the PVdF-HFP during sonication (highest concentrations, highest duration). GPC results, plotted in Figure 2.7, show that the PVdF-HFP molecular mass distribution is indeed impacted by the sonication step. The distribution is reduced at high molecular weight and increased at the centre of the distribution. This indicates that the sonication mainly breaks the longest polymer chains to form polymer chains with molecular weight close to the average molecular weight. Indeed, as reported in Table 2.4, the Polydispersity Index (PDI) of the PVdF-HFP decreases after the sonication step. No impact of this modification has been found on the film morphology observed by SEM, on their FTIR spectra nor on their dielectric properties. It is then considered that this modification has negligible or no impact on the material structure and properties.

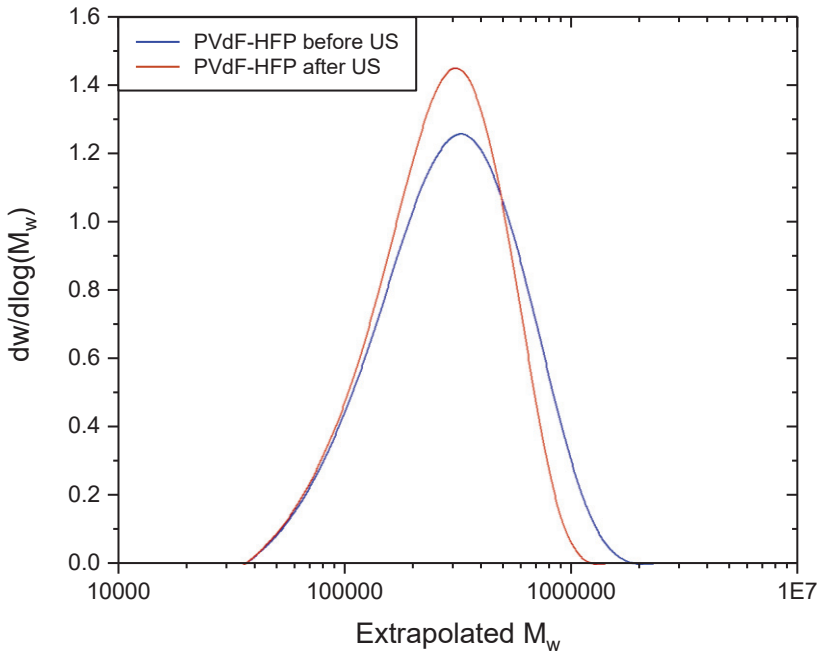

Figure 2.7: Molecular weight distribution of the PVdF-HFP obtained by GPC analysis before and after being exposed to sonication.

Table 2.4: GPC results of PVdF-HFP before and after sonication

Designation	Mn kg/mol	Mw kg/mol	PDI
PVdF-HFP before sonication	175	309	1.8
PVdF-HFP after sonication	169	242	1.4

2.2.4 Film casting process

The casting of the polymer and nanocomposite films from corresponding solutions and suspensions was performed with an *Elcometer 4340 Automatic Film Applicator*. The technique consists in placing a vertical blade at a fixed distance from the surface of a glass substrate. The substrates are first clean with soap and water and then with Acetone using a microfibre tissue. The coating formulation is then poured in front of the blade which moves at constant speed across the substrate. The blade spreads a solution/suspension layer with a thickness defined by the distance between the blade and the surface. The solvent evaporation then leaves a solid polymer or a nanocomposite film on the substrate. In addition to the thickness of the solution/suspension layer, the final thickness is determined by the solution concentration.

2.2.5 Drying process

The drying conditions depend on the boiling point of the solvent. In the case of a solvent with low boiling point (about 80 °C for MEK), the evaporation is first performed at atmospheric pressure and RT to obtain a free-standing film (about 2 hrs drying) which is then dried under primary vacuum at 80°C for 24-36 hrs. In the case of solvents with high boiling point (~150 °C for heptanone and DMF), the evaporation is directly performed under vacuum at RT, temperature being then raised to 80°C when the vacuum is low enough (primary vacuum). The total duration of the drying step is about 36-48 hrs. Polymer and nanocomposite films are then conditioned at 50 % of relative humidity (RH50) for at least 3 days.

2.3 Material characterization

2.3.1 Fourier-Transformed Infrared Spectroscopy: FTIR

Fourier-Transformed Infrared Spectroscopy (FTIR) is a non-destructive characterization technique which enables identifying chemical functions present in the analysed sample. The technique lies on the absorption of infrared radiations which induces vibration of the chemical bonds in the material structure. The wavelengths of

the absorbed radiation depend on the type of chemical bonds, on the way they vibrate (rotational, stretching…), on the atoms involved in, and on their chemical environment. In a molecule, each bond may have several vibration modes leading to several absorbed wavelengths in the infrared region. As a result, each molecule has a characteristic infrared absorption spectrum. In this work, infrared spectroscopy is used to identify unknown chemical species or crystalline structure or to detect the presence of chemical entities in a material sample. Two different methods have been used.

Attenuated total reflectance: ATR

Attenuated total reflectance (ATR) lies on the total reflection of the infrared beam by the material. The material is placed on a crystal having a high refractive index that promotes the total reflection of the beam by the sample of lower refractive index. A small part of the beam penetrates in the sample before being reflected, allowing its absorption by the material. Experimentally, a good contact between the sample and the crystal is important to ensure an optimal reflexion. In this work, ATR has been used to characterize solid polymer or nanocomposite films as well as polymer and NP powders. An illustration of the ATR principle is given in Figure 2.8. The analyses were performed at the Research & Innovation centre of Lyon (RICL) with the help of Laetitia Allary (from Solvay RICL) on a compact FTIR spectrometer *Alpha II* from *Buker* with a Platinum ATR module.

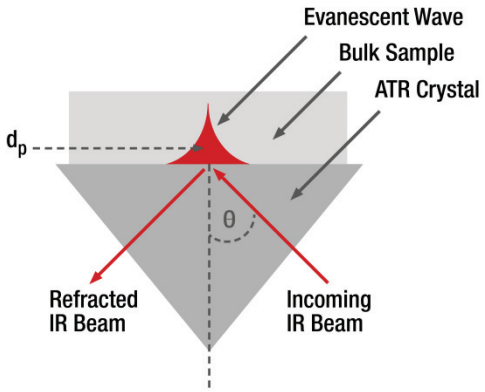

Figure 2.8: illustration of the ATR principle.

Diffuse Reflectance Infrared Fourier Transform: DRIFT

Diffuse Reflectance Infrared Fourier Transform (DRIFT) is based on the multiple scattering of the incident IR beam by a powder with high surface area and is used for the analysis of the physical and chemical structure of sample surfaces.

Figure 2.9 presents the principle of this technique. The incident IR beam is directed onto the sample and the light is scattered in all directions. Part of the incident light is

absorbed by the particles due to chemical vibrations. A concave mirror is placed above the sample in order to redirect and concentrate the scattered IR light toward the sensor. The multiple scattering of the IR beam by the powder particles provides an enhanced signal coming from the particle surface.

The experiments have been done with the help of Julien Jolly at Solvay LoF on a *Vertex 70 HTS-XT* from *Brucker*. Temperature control enables measuring IR spectra between 25 and 300 °C. The powder samples are mixed with KBr powder for the analysis and the signal of pure KBr is acquired and subtracted before each measurement.

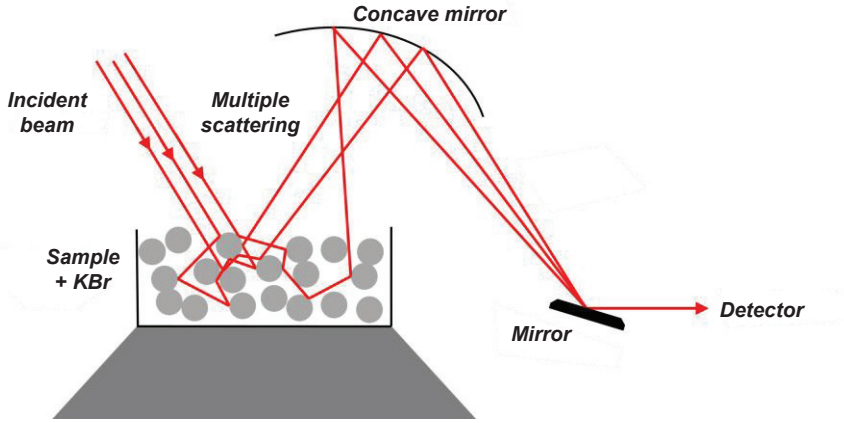

Figure 2.9: Illustration of the DRIFT principle.

$BaTiO_3$ NPs

The $BaTiO_3$ NPs were analysed by DRIFT to obtain an enhanced signal coming from their surface. 37 IR spectra were recorded from 25°C to 300°C. The IR absorption spectra of $BaTiO_3$ NPs are shown in Figure 2.10 as a function of temperature.

The IR spectra show several absorption bands. The broad band around 3500 cm^{-1} corresponds to OH stretching. This function is found in hydroxyl groups and adsorbed water. In addition, the small peak at 1632 cm^{-1} corresponds to H-O-H bending vibration mode, which confirms the presence of adsorbed water[109,115]. Indeed, $BaTiO_3$ NPs are known to present hydroxyl groups and adsorbed water on their surface due to hydrogen bonding[116,117]. Figure 2.10 also shows the decrease of the IR absorption around 3000 and 1638 cm^{-1} as temperature increases. This observation suggests that water molecules desorb from the $BaTiO_3$ NP surface and that hydroxyl groups may condensate while releasing water molecules. At 300 °C, the remaining band around 3500 cm^{-1} corresponds to OH groups still present on the $BaTiO_3$ NP surface, which may correspond to strongly adsorbed water molecules or hydroxyl groups[109,118].

The two bands at 2926 and 2855 are typical of the C-H and C-C vibrations of Alkyl chain[115]. They indicate the presence of organic molecules onto the NP surface, which may be residual surfactant molecules from the fabrication process. The negative bands around 2400 cm^{-1} come from the variation in CO_2 concentration between the background and the sample measurements.

The strong band around 1425cm^{-1}, as well as the bands at 2448 and 1749 cm^{-1} are the signature of the inorganic carbonate vibrations[115]. Note that the intensity of the band at 1425cm^{-1} increases as the temperature increases. Similar observations are done for the two other bands which show tiny increasing bands. This would indicate the formation of carbonates onto the $BaTiO_3$ NPs surface which can be expected from reaction with the CO_2 present in the atmosphere.

Finally, the very large absorption at wavenumber lower than 1000 cm^{-1} is due to crystal lattice vibrations[109].

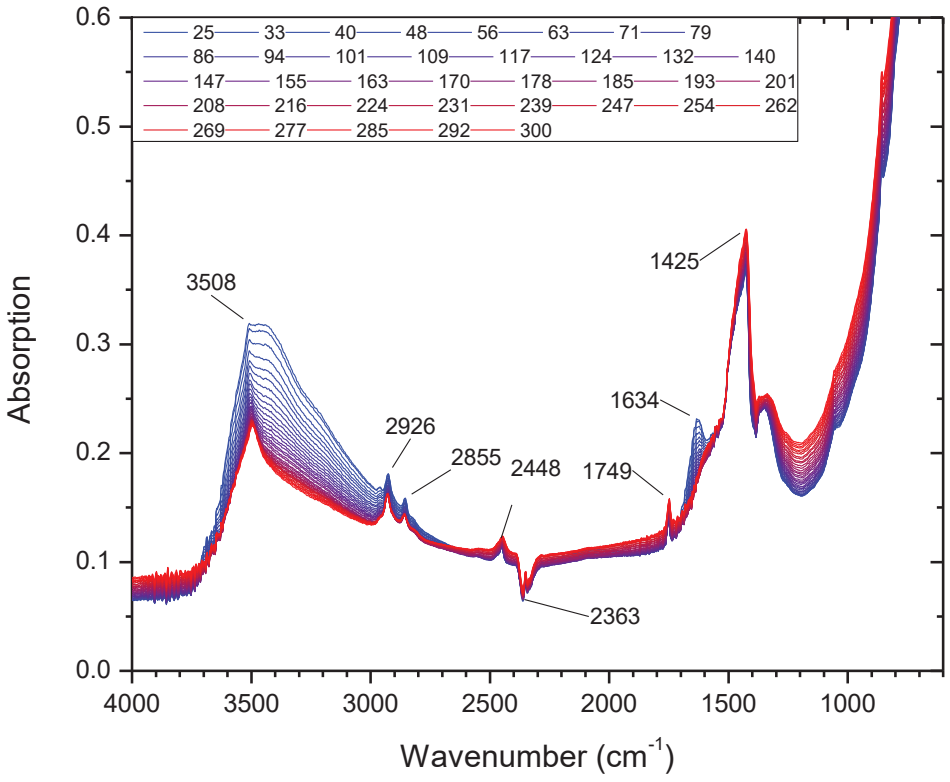

Figure 2.10: Absorption spectra of $BaTiO_3$ NP powder obtained by DRIFT analysis from 25°C to 300°C (from blue to red).

2.3.2 Karl Fischer

Karl Fischer titration is an analytical technique which allows measuring water contents in materials as low as 100 ppm. The analyses were conducted to determine the

water uptake in neat PVdF-HFP and nanocomposite films. Three blank measurements were realized prior the sample analyses. Each measurement is repeated on three samples in order to assess the repeatability of the measure. The analyses were performed at 180°C.

2.3.3 Thermogravimetric Analysis: TGA

Thermogravimetric analysis (TGA) is a destructive technique consisting in monitoring the mass of a sample being exposed to a temperature program susceptible to induce weight losses due to material degradation, chemical desorption or molecule vaporization. The sample is introduced in an aluminium cell which is placed on a nanobalance in the oven that imposes the temperature program (see Figure 2.11). In this work, TGA were performed on Netzsch TG 209 F1 Libra™ to determine the thermal stability of chemical compounds or polymers and analyse the degradation of chemical species at the surface of the $BaTiO_3$ NPs.

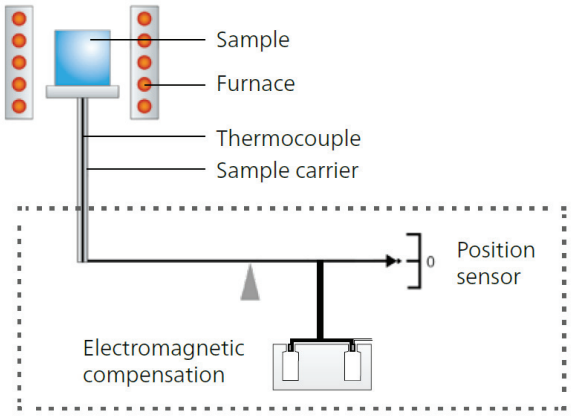

Figure 2.11: Measurement principle scheme of TGA

The temperature program used for the analysis consists in a ramp from 20°C to 600°C at 10°C/minute followed by an isotherm at 600°C maintained during 20 minutes, as shown in Figure 2.12. The experiments were conducted under a 20 $mL.min^{-1}$ flux of dried N_2/O_2 (80/20) to allow determining the organic weight content in material samples.

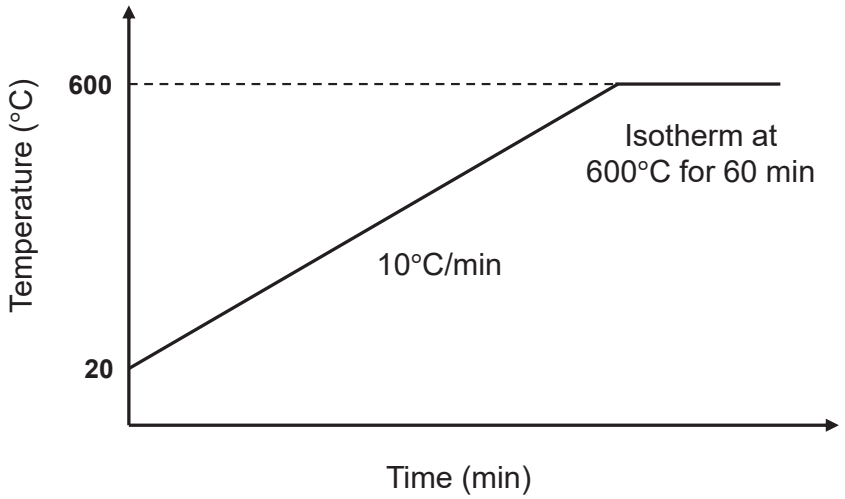

Figure 2.12: Temperature program applied in TGA measurements.

PVdF-HFP

For PVdF-HFP, TGA was performed on a film sample processed in MEK. The results are plotted in Figure 2.13. PVdF-HFP reaches 0.1% of weight loss at 340°C and 1% at 404°C. The peak of the degradation weight loss is found at 469 °C. These results show the very good thermal stability of the PVdF-HFP.

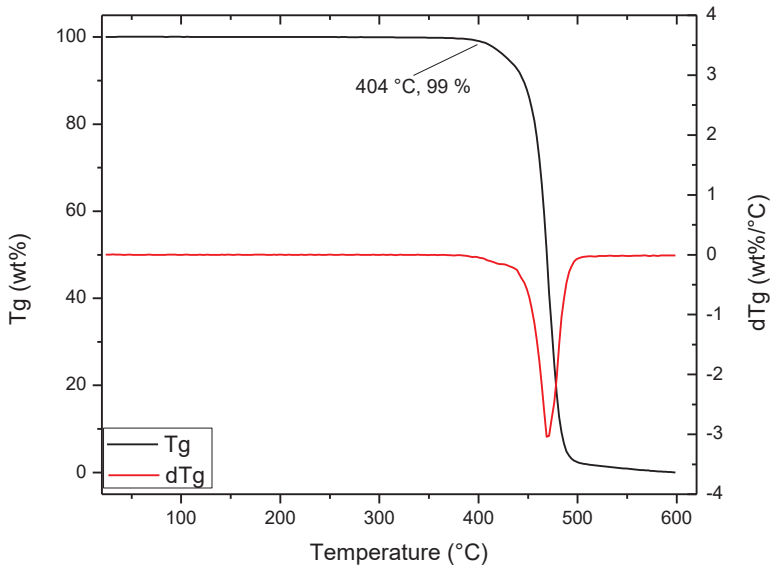

Figure 2.13: TGA thermogram and its derivative for neat PVdF-HFP under dried N_2/O_2 (80/20). Temperature ramp set at 10°C/min.

$BaTiO_3$ NPs

TGA was performed on the as-received $BaTiO_3$ NP powder. The resulting thermogram is plotted in Figure 2.14. It shows a weight loss of 1.4 wt% from 20°C to 600°C. The results show a weight loss from 20 °C to 100 °C which may correspond to water desorption.

The water desorption can be triggered at low temperature by the dry air flow lowering the H_2O partial pressure in the oven. Then, a second weight loss is probably due to the thermal degradation of the organic compound identified with the DRIFT analyses and/or water molecules resulting from the condensation of hydroxyl groups. Both peaks represent about 0.6-0.7 wt% of the total sample mass.

Finally, $BaTiO_3$ NPs are thermally stable up to 600°C, which is expected from ceramic materials.

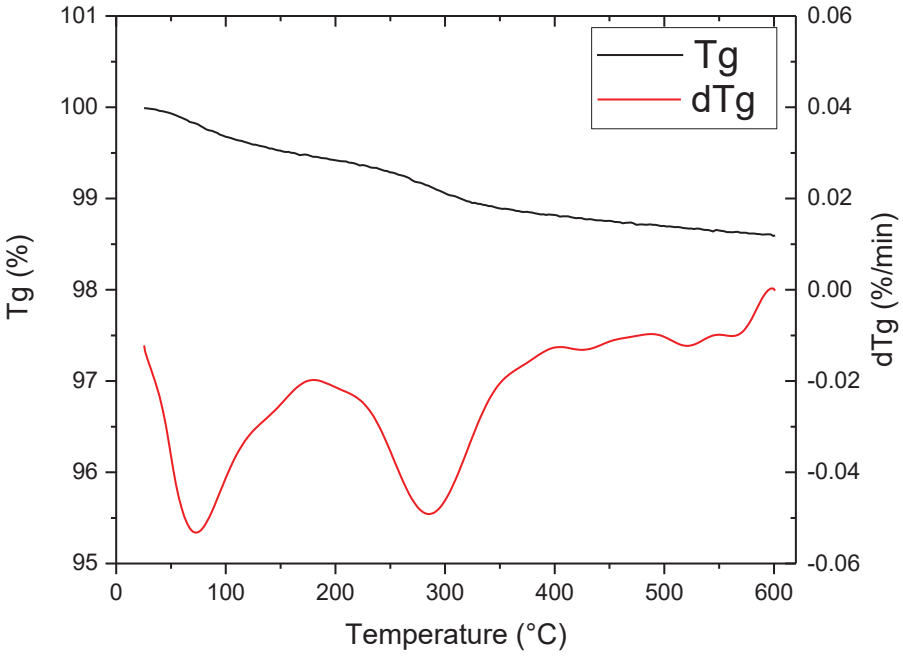

Figure 2.14: TGA thermogram and its derivative for as-received $BaTiO_3$ NPs under dried N_2/O_2 (80/20). Temperature ramp set at 10°C/min.

Modifiers

TGA was performed on the as received stearic acid and the PMMA-co-MAA. The results, shown in Figure 2.15, give temperatures at 1% of degradation of 170 and 252 °C for stearic acid and PMMA-co-MAA, respectively.

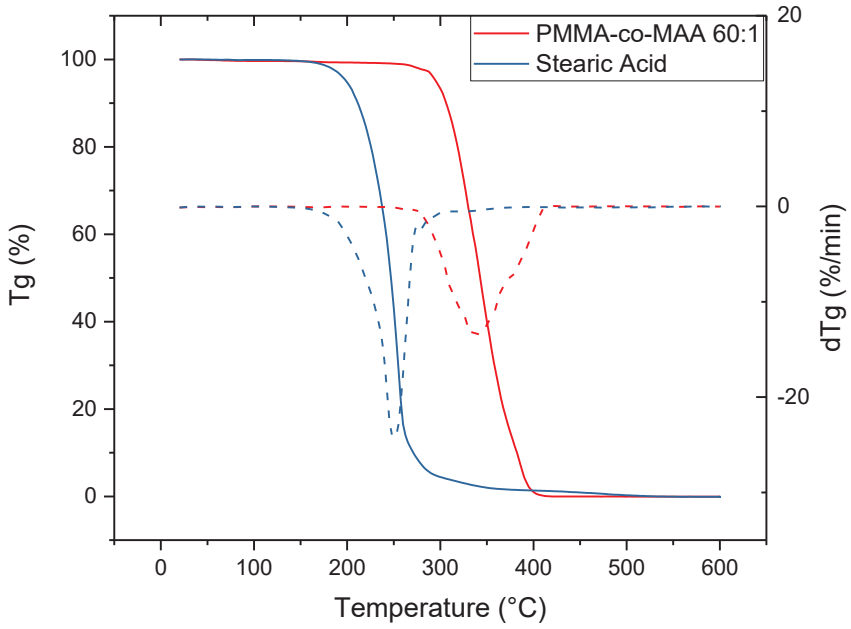

Figure 2.15: TGA thermograms (full lines) and their derivatives (dash lines) for as-received Stearic acid and PMMA-co-MAA under dried N_2/O_2 (80/20). Temperature ramp set at 10°C/min.

2.3.4 Gel Permeation Chromatography: GPC

Gel Permeation Chromatography coupled with light scattering was used to determine absolute molecular weights of polymers without truncation. The analyses were performed by Alexandra Siot (from Solvay RICL).

2.3.5 Differential Scanning Calorimetry: DSC

Differential Scanning Calorimetry (DSC) was performed to characterize the crystallinity of the polymer and nanocomposite samples. This characterization technique consists in heating and cooling down a sample with a given temperature program and measuring the heat flow difference between two pans, one containing the sample to analyse and the other being empty, used as reference. This technique enables identifying and quantifying endothermic and exothermic phenomena such as melting, crystallisation, and glass transition. Figure 2.16 presents the temperature program used for the analyses in this study.

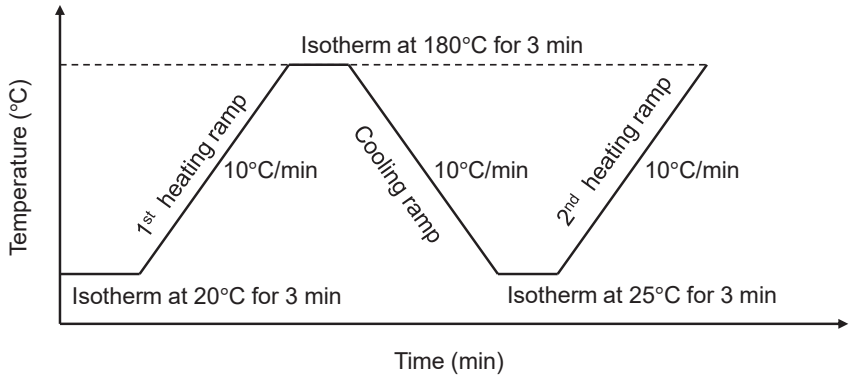

Figure 2.16: Temperature program applied for DSC analyses

Knowing the heating rate and the sample mass, the heat flow is calculated from the measured heat energy as:

$$heat\ flow\ per\ gram\ of\ sample = \frac{heat\ energy}{heating\ rate \times sample\ mass} \qquad \left[\frac{J}{K.g}\right] \qquad (2.1)$$

The mass heat flow is plotted on a thermogram where the x-axis is the sample temperature. The degree of crystallinity (χ_c) of samples is calculated as the integral of the melting peaks (ΔH_m) of the first heating ramp divided by the melting enthalpy of a hypothetical 100% crystal of PVdF (104 J/g)[119].

$$\chi_c = \frac{\Delta H_{melting}^{sample}}{\Delta H_{melting}^{\chi_c=100\%}} \qquad (2.2)$$

The phenomena observed during the first heating ramp depend on the history of the samples (thermal history, aging, fabrication process…). Since the solvent casting process used for the polymer and nanocomposites sample fabrication may affect the crystalline structure (solvent used, evaporation kinetics, drying step…), the crystallinity is determined using the first ramp. This thermal history is erased when melting the crystalline phase. Finally, the second heating ramp shows the melting of the material which has undergone a standard cooling down from the melt at 10°C/min. This information may be used as a comparative reference between the samples.

Typical DSC curves of a neat PVdF-HFP film fabricated from MEK solutions and dried at 80°C under vacuum are plotted in Figure 2.17. The obtained thermal properties of PVdF-HFP are reported in Table 2.5.

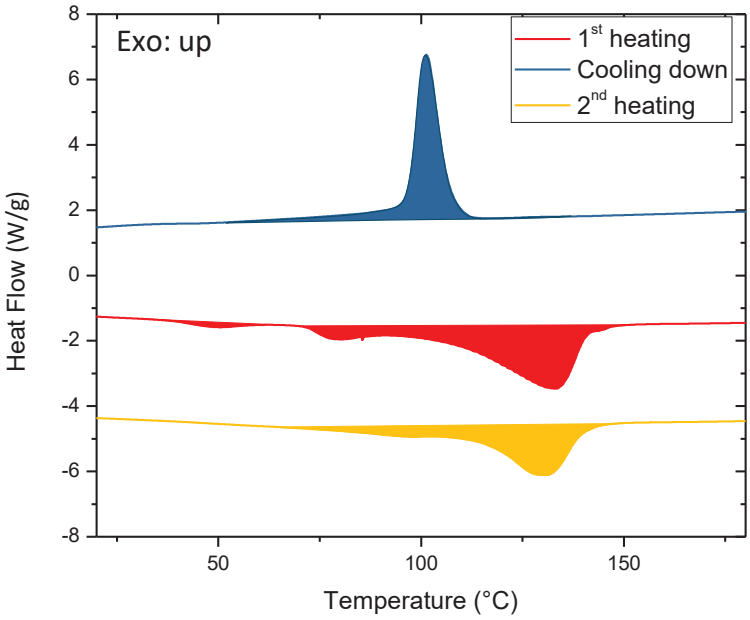

Figure 2.17: DSC thermograms of neat PVdF-HFP at 10°C/min. Integrals of melting and crystallization peaks are coloured. (Heat flow in W per gram of polymer.)

The first heating ramp (red curve) gives access to the crystalline structure of the sample which depends on the fabrication process and on the sample history. It shows three melting endotherms. Including the 3 peaks, the total enthalpy is about 39 $J.g^{-1}$ which would correspond to 38 % of crystallinity. The origin of these peaks will be discussed in the next paragraph. The crystallization peak observed during the cooling down would represent 25% of crystallinity whereas the second heating would give 26% of crystallinity. The degree of crystallinity obtained during the cooling down and the second heating are nearly identical which is consistent. Moreover, the measured enthalpy values of 26 and 27 $J.g^{-1}$ are relatively close to Solvay's specification (23 $J.g^{-1}$).

Table 2.5: Parameters of the thermal events revealed in PVdF-HFP by DSC experiments. *Corresponds to the integration of both the second and third peaks. Xtotal was calculated using $\Delta H_{melting}^{\chi_c=100\%} = 104$ $J.g^{-1}$.

Cycle	Peak Temperatures (°C)	ΔH_m ($J.g^{-1}$)	X_{total} (%)
	49 ± 1	1.3 ± 0.1	
1st heat	80 ± 2	2.3 ± 0.1	38 ± 1
	133 ± 2	38 ± 1 *	
Cooling down	104 ± 3	26 ± 1	25 ± 1
2nd heat	130 ± 1	27 ± 1	26 ± 1

The main peak at 133°C, corresponds to the melting of the main crystallites of PVdF-HFP. The first two peaks correspond to families of crystallites generated during the effective annealing periods[120]. Indeed, in their work, M. Neidhöfer et al. evidenced that an endothermic peak occurs during the first heating in DSC approximately 10°C above the annealing temperature[121]. The authors make a parallel with the secondary crystallization process observed by Marand et al. in other polymers such as PolyEtherEtherKetone and suggest that similar phenomenon takes place in PVdF regardless of the polymorph of the crystalline phase[122].

Accordingly, the peaks at 80 and 49 °C could be related to the fabrication process, which includes a drying step at 80°C followed by storage at RT. These steps can be considered as successive thermal annealing treatments. The cooling ramp exhibits only one sharp exothermic peak at 104°C that corresponds to the crystallization of the primary crystalline phase. The absence of endothermic peaks at 49°C and 80°C during the second heating confirms this interpretation.

In order to confirm this interpretation, the effect of the drying process and so of thermal annealing was investigated on neat PVdF-HFP samples dried at 23°C, 80°C and 120°C after being casted from a MEK solution (Figure 2.18). The thermograms clearly show endothermic peaks at positions correlated to the annealing temperatures.

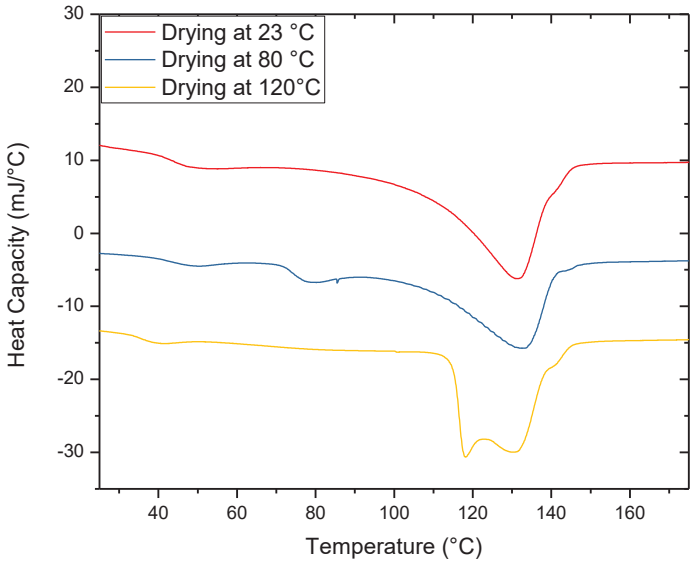

Figure 2.18: Effects of the second drying step at 80°C on the thermograms of neat PVdF-HFP samples (first heat).

Additional DSC measurements were carried out to study the impact of the process parameters on the crystalline structure. For PVdF-HFP films casted from MEK-based

solution, the solvent drying is done in two steps: The first drying is conducted under atmospheric pressure and RT and the second is conducted under primary vacuum at 80°C. DSC analyses have revealed 25% less crystallinity in PVdF-HFP if the first drying step is accelerated while being carried out under vacuum. The second drying step at 80°C under vacuum has shown to significantly modify the crystalline morphology only during the first 4 hrs of the drying process.

On the other hand, changing either the concentration of the PVdF-HFP solution in MEK from 10 to 20 wt% or the film thickness has no significant effect. Conversely, the nature of the solvent was identified to affect both the shape of the DSC melting profile and the total crystallinity.

2.3.6 Dynamic Light Scattering: DLS

Dynamic Light Scattering (DLS) is a technique that allows characterizing particle size distributions of liquid suspensions. It is based on the scattering of a laser beam by the particles (See Figure 2.19). The particles undergo a Brownian motion, which depends on their size and leads to fluctuations of the scattered light intensity. The smaller the particles, the faster the fluctuations. The autocorrelation function of the intensity $g(\Delta t)$ is computed as:

$$g(\Delta t) = \langle I(t)I(t+\Delta t)\rangle \tag{2.3}$$

where I is the intensity and t the time. $g(\Delta t)$ is expressed as:

$$g(\Delta t) \cong \exp(-Dq^2\Delta t) \tag{2.4}$$

with q the scattering vector, from which the diffusion coefficient D is deduced. The hydrodynamic radius R is obtained from the Stokes-Einstein equation:

$$D = \frac{kT}{6\pi\eta R} \tag{2.5}$$

With k the Boltzmann constant, T the temperature, and η the viscosity of the liquid medium.

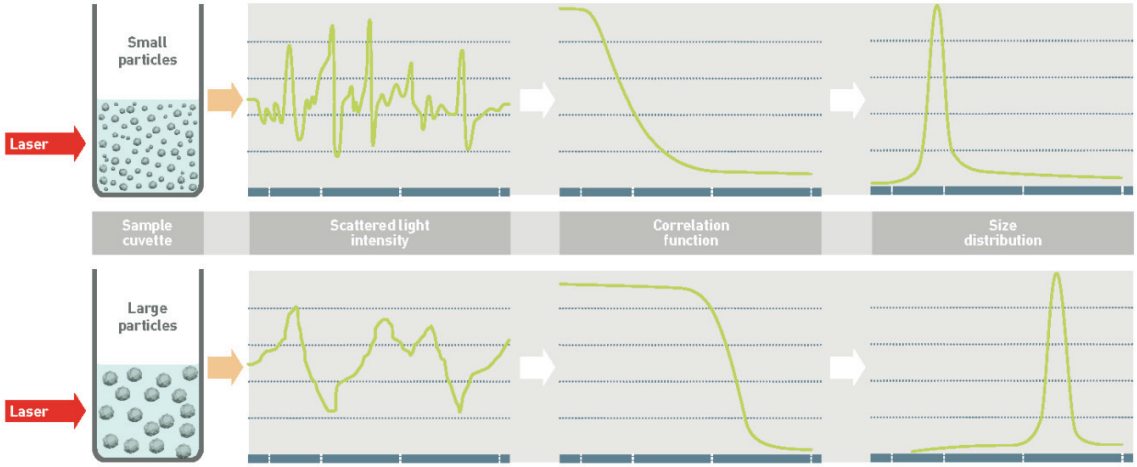

Figure 2.19: Principle of size distribution calculation of DLS measurement. Figure coming from Malvern documentation[123]

The hydrodynamic radius is a function of the real radius of the particle and of many other parameters such as the used solvent, the presence of molecules or polymers adsorbed on the particle surface, the size of the electrical double layer, etc. The size distribution determined by DLS may then be different from that determined by electron microscopy.

The experiments have been performed on a *Zetasizer Nano 90* from *Malvern* with the help of Mathieu Oullion (from Solvay RICL). In this work, DLS was used to determine whether a suspension is stable or not. Each DLS analysis consists in up to 10 successive measurements that allows assessing the stability of a suspension over 10 minutes. The first objective was to determine the concentration domain in which the analysis is relevant. Indeed, several phenomena can degrade the quality of the DLS analysis: at too high concentration, the absorption of the laser beam might be too high to detect a sufficient signal and multiple scattering may occur. Conversely, at too low concentration, the number of scattering particles might be too low to produce a sufficient signal. The concentration range for optimal analysis is typically around 25 and 100 ppm (0.0025 and 0.01 vol% of particles) for all the solvents used for the DLS analyses.

$BaTiO_3$ NP were dispersed in various solvents at several concentrations using the dis-agglomeration protocol presented in section 2.2.1. Then, some suspensions were too concentrated to be analysed directly. In this case, a sample was taken and diluted rapidly (within 10-20 seconds) after the end of sonication in order to reach the optimal concentration for the analysis. Two cases may occur:

1) The diluted sample is stable, which means that the size distribution does not shift towards higher sizes. Then, the initial suspension was considered to be stable. Even though dilution may stabilize a suspension, if not stable, the initial suspension would agglomerate within the delay (about 10 seconds) between the end of sonication and homogenization of the diluted samples. Thus, higher mean particle sizes would be obtained.
2) The diluted sample is not stable, which means that the size distribution shifts towards higher particle sizes during the DLS analysis. In this case, it is considered that the initial concentrated suspension is not stable.

The long-term stability of a suspension can be assessed by performing several samplings as a function of time. Before each sampling, the suspension must be manually stirred in order to redistribute potential agglomerates.

2.3.7 Microscopy

Scanning Electron Microscopy (SEM) and Optical Microscopy (OM) have been used to characterize the morphology and the structure of the materials (NP size, polymer film morphology, NP dispersion states…). The analyses were performed with the help of the microscopy department, Pauline Grau and her team.

OM (*Wild M420* Macroscope and *Leica DMRX* Microscope) was performed in transmission in nanocomposite films to verify the absence of very large agglomerates (>5 µm) in the samples prior to analyse the dispersion state by SEM.

SEM (*Ultra 55* by *Zeiss*) was performed to characterize the NPs (size, shape…) and then their dispersion state in nanocomposite films. As-received $BaTiO_3$ NPs were prepared by placing the powder on carbon adhesive and depositing a Platine (Pt) layer by physical vapour deposition (PVD). Polymer and nanocomposite films were prepared by cryofracture of the samples in liquid nitrogen to generate a flat cross section. The broken films were then placed on a carbon tape and metallized with Platine by PVD. This enables qualitative observation of the sample morphology and clear discrimination of NPs inside the matrix.

Secondary and backscattered electron detection were combined to provide both topographic (In Lense detector) and chemical contrast (AsB detector). Acceleration voltages between 3 and 7 kV were used. At these voltages, the electron beam is thought to penetrate the material in such a way that the NPs can be detected down to about 1 µm away from the analysed surface. Two examples of SEM images of a PVdF-HFP:$BaTiO_3$ nanocomposite taken in chemical contrast and in topological contrast are shown in Figure 2.20 a) and b) respectively. The chemical contrast is mostly based on backscattered electrons and so provides a high contrast between the $BaTiO_3$ NPs containing heavy Ti and Ba atoms and the PVdF-HFP containing lighter atoms such as C

and F. Topological contrast is mostly based on secondary electrons and so provides less contrast between the NPs and the PVdF-HFP matrix. Nevertheless, it provides very nice details about the topography. Both approaches have been combined in the SEM analyses performed in this work.

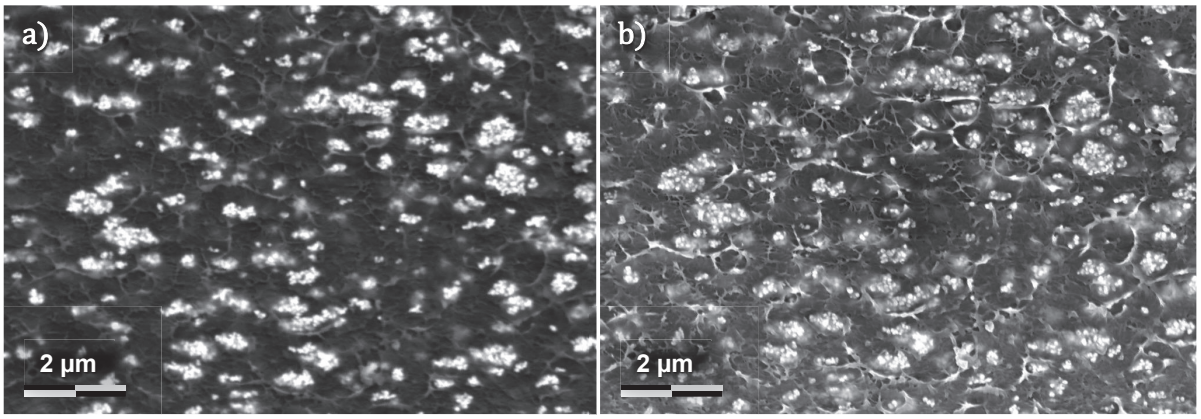

Figure 2.20: Example of SEM images of PVdF-HFP:$BaTiO_3$ nanocomposites taken a) in chemical contrast and b) in topological contrast on the same area.

2.3.8 Image analysis

In order to quantify the dispersion state and the NP/agglomerate size distribution of the nanocomposite samples, image analyses were performed with ImageJ on SEM images taken in chemical contrast. For each nanocomposite sample, the image analysis was performed on 10 SEM images at different magnifications in order to assess the reproducibility. First, the length scale was set on the SEM images. Then the image was binarized to produce a clear distinction between the matrix in black and the NPs or agglomerates in white as shown in Figure 2.21 b). It is worth to note that the binarized image corresponds to the projection of the detected NPs, which are located at less than 1 µm away from the analysed cross-section surface. Since the largest agglomerates have diameters of about 1 µm, the volume analysed is considered to be representative. Then a particle analysis is performed (see Figure 2.21 c) and gives the area for each NP or agglomerate. These areas are then converted into diameters considering disks of equivalent areas. These diameters are weighted with the corresponding sphere volume in order to produce a distribution $\Phi(D)$ defined as: $\Phi(D)dD$ is the volume fraction of particles or agglomerates with equivalent diameter between D and $D + dD$.

Figure 2.21: Example of Image analysis with a) the raw SEM image obtained in chemical contrast, b) the same image after binarization and c) the particle analysis partially overlaid on the raw images.

2.3.9 Sample Thickness

The thickness of the samples has to be determined as precisely as possible. Indeed, the complex permittivity depends on it as shown in equation (2.8). It follows that the precision of the dielectric spectroscopy mainly depends on the precision of the thickness measurements. A micrometre with a precision of 1 µm was used. For each dielectric spectroscopy measurement, the thickness of the sample was measured 10 times all over the surface of the electrode (20 mm of diameter) and the average thickness was used for dielectric permittivity calculations. All the samples had a thickness between 20 and 30 µm and the thickness heterogeneity of the films did not exceed 1 µm.

2.3.10 Broadband Dielectric Spectroscopy

The permittivity reflects the ability of a material to polarize when submitted to an electric field. This polarization can be elastic (capacitive, conservative) or non-elastic (resistive, dissipative). Broadband Dielectric Spectroscopy (BDS) is used to probe this behaviour as a function of frequency and temperature. The accessible frequency range, 10^{-2} to $10^{6\text{-}7}$ Hz, enables observing dipolar relaxations, interfacial MWS polarizations and conductivity.

Dielectric spectroscopy is based on the measurement of both the applied voltage U* and the measured current intensity I* and the detection of the phase shift δ. The complex impedance Z* is is calculated as:

$$Z^* = \frac{U^*}{I^*} = \frac{U_0\, e^{(i\omega t)}}{I_0\, e^{(i\omega t+\delta)}} \qquad (2.6)$$

where U_0 is the magnitude of the voltage, I_0 the magnitude of the current intensity and ω the angular frequency. Then, the complex permittivity is calculated as:

$$C^*(\omega) = \frac{1}{\omega Z^*(\omega)} = \varepsilon^*(\omega) C_0 \quad (2.7)$$

where C^* is the complex capacitance of the sample and C_0 the capacitance of the equivalent capacitor with vacuum between the electrodes. It is calculated as follow:

$$C_0 = \varepsilon_0 \frac{A}{d} \quad (2.8)$$

where A is the electrode surface area and d the sample thickness.
By combining equations (2.7) and (2.8) the dielectric permittivity is obtained as:

$$\varepsilon^*(\omega) = \frac{C^*(\omega) d}{\varepsilon_0 A} \quad (2.9)$$

This equation is valid in the case of a parallel plate capacitor of infinite surface. As a consequence, it is necessary to perform dielectric spectroscopy on samples with negligible thickness as compared to the diameter of the electrodes to avoid underestimating the dielectric properties[16]. In this work, the typical sample thickness (~20-30 µm) is about 1000 times smaller than the electrode diameter (20 mm) which allows neglecting edge effects. The material sample between the two electrodes can be considered as a parallel plate capacitor as schematized in Figure 2.22.

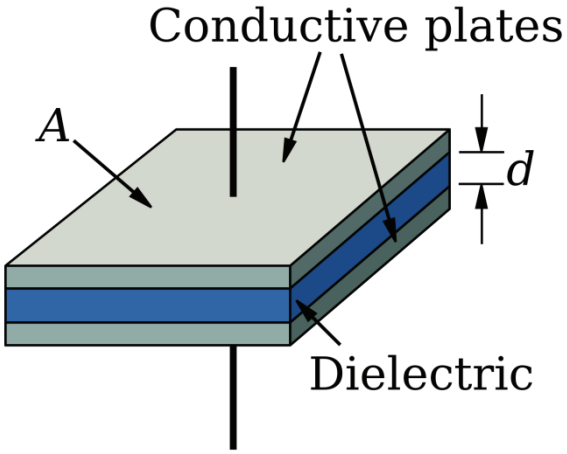

Figure 2.22: Illustration of the device used for dielectric spectroscopy measurements.

The samples are disposed between plane brass electrodes. In order to ensure a good contact between the samples and the electrodes, additional circular gold electrodes of 20 mm diameter are deposited by PVD with a Quorum Q150R S on each side of the samples. The gold deposition is carried during 120 s at 30 mA on each face. A circular mask is used to fabricate well defined electrodes. The electrode thickness is estimated to be about 50-100 nm.

The samples are placed in a sealable cell preventing the samples from drying when exposed to the nitrogen flow used for the thermal regulation or from absorbing water

from ambient humidity. This cell is composed of a bottom electrode with a diameter of 20 mm and of a top electrode with a diameter of 40 mm. The sample is then annealed at 80°C under vacuum for 36 hrs. After this thermal treatment, the samples are dry and can be directly analysed by dielectric spectroscopy. Otherwise, they are conditioned at 23 °C and RH50 for 48 hrs in the open dielectric cell which is then sealed with the upper electrode to perform dielectric spectroscopy with the initial water uptakes at RH50.

Isothermal frequency sweeps are performed between 10^{-2} to 10^{7} Hz using a temperature program going from -40°C to 60°C with a step increase of 5 °C. Two additional measurement steps are conducted at 25 °C before and after the temperature cycle in order to quantify any changes in the dielectric properties that could be due to sample drying or thermal history. The temperature program is reported in Figure 2.23. No significant differences are observed between the first measurement and the measurement at 25 °C in the cycle for all samples, which indicates that the dielectric properties of the samples are not modified by the first half of the cycle (i.e. at temperature $<$ 25°C). However, in the case of PVdF-HFP:$BaTiO_3$ nanocomposites only, the last measurement at 25 °C shows slightly lower conductivity and MWS magnitude which suggests that dielectric properties of the samples are slightly affected by the second half of the cycle (i.e. at temperature $>$ 25°C). In this case, this effect may due to drying during the experiment (even though measurements are made in a supposedly closed cell). Indeed, $BaTiO_3$ NPs contain some water at the surface (see TGA and DRIFT analyses in section 2.3.3 and 2.3.1).

All measurements were performed using a Broadband Dielectric Spectrometer from *Novocontrol*, composed of an *Alpha A analyser*, an *Alpha Active Cell*, and a *Quatro cryosystem*.

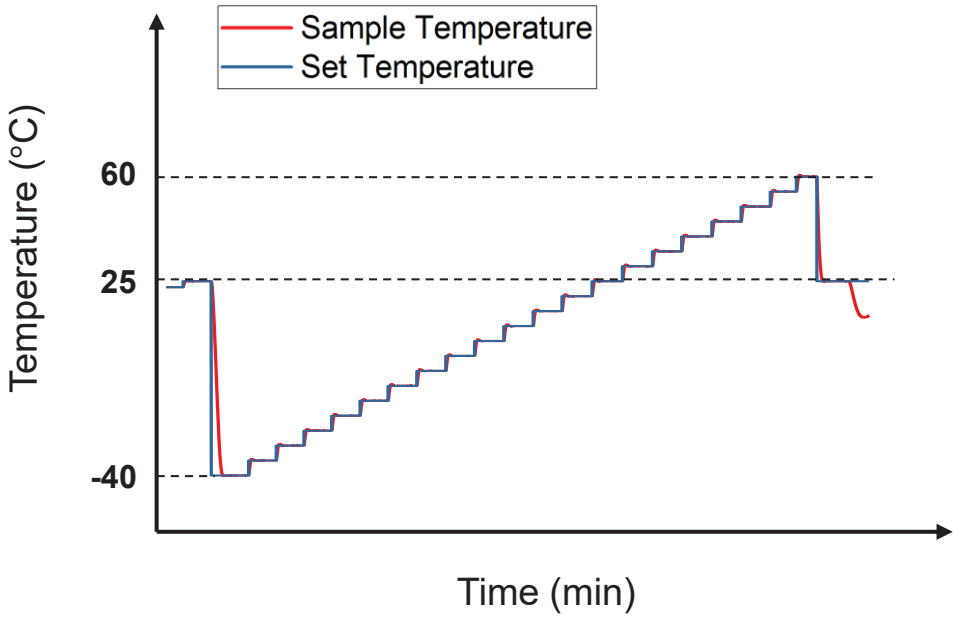

Figure 2.23: Temperature program used for the dielectric spectroscopy measurements.

Dielectric Spectra Fitting

To quantify the dielectric properties of the polymer and nanocomposite samples, the complex dielectric permittivity is fitted with the Cole-Cole equation (2.10) using *WinFit* software.

$$\varepsilon_r^*(\omega) = \sum_k \frac{\Delta\varepsilon_k}{1 + (i\omega\tau_k)^{\alpha_k}} - \frac{i\sigma_{DC}}{\varepsilon_0\omega} \qquad (2.10)$$

With $\Delta\varepsilon_k$ the magnitude of the polarization process k, τ_k its relaxation time, σ_{DC} the Ohmic conductivity and ω the pulsation. This software allows fitting together the real and the imaginary parts of the complex permittivity.

In this work, the dielectric spectra are fitted with 4 different contributions: The DC conductivity and the α_a, α_c and MWS polarization mechanisms (detailed in chapter 4). The α_a and α_c relaxations are fitted by leaving the parameters $\Delta\varepsilon$, τ, and α free to be optimized by the fitting procedure. Since the MWS contribution overlaps with the α_c relaxation and the conductivity, several sets of $\Delta\varepsilon$ and α may successfully fit the dielectric spectra. It results that the MWS parameters obtained after optimization may not be reliable. When all the parameters are left free to be optimized by the fitting procedure, the values obtained for α tend to fluctuate between 0.5 and 0.9 in most of the cases (i.e. all the samples studied in chapter 4). As a result, the α exponent was fixed at the median value 0.7 in order to obtain more stable fit results. It leads to a lower fit quality in some cases (high temperature and high MWS magnitude) but allows comparing the samples on the basis of the same mechanism. This option tends to minimize the difference observed in chapter 4 in terms of MWS magnitude.

2.3.11 High Frequency Dielectric Spectroscopy – RF reflectometry

High Frequency Dielectric Spectroscopy (HFDS) was conducted from 1MHz to 3 GHz in order to extend the frequency range of the BDS and investigate the dielectric relaxation at high frequencies. The experiments were performed in the *Centro de Fisica de Materiales* in *San Sebastian* with the help of A. Alegria under a *European Soft Matter Infrastructure* grant. A RF impedance analyzer *Keysight E4991A* (1 MHz – 3 GHz) and a nitrogen-jet stream *Quatro Cryosystem* from *Novocontrol* were used.

In this frequency range the wavelength of the electrical signal used to probe the samples starts to be comparable with the typical size of the circuit elements (sample, cables, connectors…). For this reason, HFDS differs from BDS. It consists in measuring the reflection coefficient of a field wave propagating through a precision RF air line which has the sample connected at its end. In this technique, the sample is still sandwiched between two small electrodes (10 mm of diameter) to form a parallel plate capacitor.

In order to obtain samples with the optimal capacitance to carry out HFDS (5 pC) several pieces of samples were stacked together (between 4 and 8 layers depending on the permittivity of the samples). This sample geometry allows minimizing parasite signals coming from the set up but induces an underestimation of the complex permittivity due to the presence of air between each layer. The absolute values of the complex permittivity will thus not be considered.

The samples were stored under ambient laboratory conditions (~20-25 °C and RH40-60). The HFDS experiments were performed under dry N_2 flux used for temperature regulation. No impact of water was found by repeating quick temperature cycles on all the samples. After performing an initial measurement at 25 °C, the temperature is raised up to 60°C for 5 minutes and decreased to 25°C to perform a measurement. This stage is repeated several times to check the evolution of the complex permittivity with drying.

The analyses were then performed using the temperature program previously presented in Figure 2.23 and the resulting spectra were fitted using Cole-Cole equation as presented for BDS.

Chapter 3. Interaction Parameters

3.1 Introduction

As presented in the chapter on the state of the art, the interdependence between the modification of the particle surface, dispersion state and dielectric properties of the final composite makes the study of the structure-properties relationships difficult. Indeed, the most common way to control the particle dispersion state is to implement some modification of the particle surface. This has almost systematically an effect on the interfacial morphology and electronic structure, which in turn also affects the dielectric properties of final composites. In this work, the objective was to control the dispersion state of $BaTiO_3$ nanoparticles (NPs) without changing the polymer-NP interfaces and so without modifying the surface chemistry of the NPs. As a consequence, the investigations were focused on the relationships between the fabrication process of nanocomposites and the NP dispersion state. The interactions between all the constituents mixed together during the process have been thoroughly studied using the Hansen Solubility Parameter (HSP) approach. In this chapter, this approach will be first introduced as a tool to predict the polymer solubility and the stability of the NP suspension in the chosen solvent(s). Then, a recently developed approach for the prediction of the polymer adsorption providing another tool for designing the stability of NP suspensions will be presented. Finally, based on these interaction parameters, the link between the fabrication process and the NP dispersion state in nanocomposites will be presented.

3.2 PVdF-HFP solubility

3.2.1 Polymer solution theory

Thermodynamics of mixtures

Binary and multicomponent polymer-solvent or polymer-polymer blends have been studied for many decades. When two components are mixed at the molecular scale, the uniform binary mixture is called homogeneous blend. When they do not mix at the molecular scale and the binary mixture contains two distinct phases, it is called heterogeneous blend. This ability to mix at molecular scale at equilibrium depends on the entropy and enthalpy variation, respectively ΔS_m and ΔH_m. Entropy always favours the formation of a homogeneous blend whereas the enthalpy usually prevents the mixing of the two components. The basis of thermodynamics was proposed in 1941 by Flory and Huggins[124]. The free enthalpy of mixing (Gibbs free energy) is written as:

$$\Delta G_m = \Delta H_m - T\Delta S_m \quad (3.1)$$

with ΔG_m the enthalpy of mixing and T the temperature. The entropy variation ΔS_m is always positive and tends to favour the mixing of the binary mixture. For a mixture of two components A and B, equation (3.2) can be written.

$$-T\Delta S_m = k_B T(n_A \ln \varphi_A + n_B \ln \varphi_B) \tag{3.2}$$

where k_B is the Boltzmann constant, T the temperature, φ_A and φ_B the volume fractions of the components A and B and n_A and n_B the total numbers of molecules of A and B. The total number of molecules is $n = n_A + n_B$. Equation (3.2) is based on the hypothesis that molecular volumes are identical. In the case of polymer solution where A is the polymer and B the solvent, the total entropy variation per mol, ΔS_m, should be written as:

$$-T\Delta S_m = k_B T(n_P \ln \varphi_A + n_B \ln \varphi_B) \tag{3.3}$$

where $n_P = \frac{n_a}{N}$ is the number of polymer chains, Nbeing the polymerisation degree and n_a the number of repetitive units. The enthalpy variation per mol ΔH_m resulting from the mixing of the two components A and B is written:

$$\Delta H_m = -\frac{z}{2}(\varphi_A \varphi_B)(2U_{AB} - U_{AA} - U_{BB}) \tag{3.4}$$

Where z is the number of interactions each molecule builds with its neighbours and U_{XY} is the elementary pair interaction per mol between two molecules/monomers X and Y.
The Flory parameter χ is a dimensionless number that characterizes the affinity of a binary mixture in terms of the balance of interactions[125].

$$\chi_{AB} = -\frac{z}{2}\frac{(2U_{AB} - U_{AA} - U_{BB})}{k_B T} \tag{3.5}$$

Introducing the Flory parameter in equation (3.4), the enthalpy of mixing per molecule can be written as follow:

$$\Delta h_m = k_B T \varphi_A \varphi_B \chi_{AB} \tag{3.6}$$

Finally, the Gibbs free energy (per monomer/solvent molecule) for a binary mixture polymer A solvent B can be obtained by combining equations (3.1),(3.2) and (3.6), denoting $\varphi = \varphi_A$ the volume fraction of the polymer and $(1 - \varphi) = \varphi_B$the volume fraction of the solvent:

$$\frac{\Delta g_m}{k_B T} = \chi_{AB}\phi(1 - \varphi) + (\varphi \ln(\varphi) + (1 - \varphi)\ln(1 - \varphi)) \tag{3.7}$$

As presented in equations (3.7), the Gibbs free energy is a function of the composition φ of the binary mixture and of the Flory parameter χ_{AB} that reflects the affinity between

the components A and B. Then, it is possible to plot the evolution of Δh_m, $-T\Delta s_m$and Δg_m as a function of the mixture composition.

Hildebrand interaction parameter

The thermodynamics of the mixture allows one to predict the behaviour of a system knowing its Flory parameter χ_{AB}. This illustrates the importance of determining or at least estimating this parameter for a given mixture at a given temperature. In the case of polymer solutions, χ_{AB} gives information about the solubility of the polymer into the solvent and allows predicting phase separation, i.e. the precipitation of the polymer. An estimation method of χ_{AB} has been proposed by Hildebrand and Scott[126,127] and is based on the Hildebrand parameter δ. This term is defined as the square root of the Cohesive Energy Density (CED) per unit volume as presented in equation (3.8). It is expressed in square root of J or kJ per unit volume or $MPa^{1/2}$.

$$\delta = \sqrt{CED} = \sqrt{\frac{\Delta E_v}{v_m}} \tag{3.8}$$

with ΔE_v the vaporization energy per mole and v_m the molar volume. The idea associated with this equation is the following: the dissolution of a solute is made possible by breaking the intermolecular interactions between the solvent molecules, which is analogous to boiling the solvent.

The mixing enthalpy is related to the Hildebrand solubility parameter through the Hildebrand and Scott equation (3.9). For a polymer solution where A is the polymer and B is the solvent, The Flory parameter is defined by equation (3.10).

$$\frac{\Delta H_m}{v_m} = \varphi_A \varphi_B (\delta_A - \delta_B)^2 \tag{3.9}$$

$$\chi_{AB} = \frac{v_m}{k_B T} (\delta_A - \delta_B)^2 \tag{3.10}$$

Equation (3.10) is based on the assumption that pair interaction energies per molecule/monomer (denoted U_{AB} previously) are expressed as:

$$U_{AB} = -\sqrt{v_m}\delta_A \delta_B \tag{3.11}$$

Where the – sign corresponds to the fact that pair interactions are attractive. Eq (3.11) is just another way to say that the Van der Waals interaction energy is proportional to the products of polarizability[128]

In equation (3.10), one can note that χ_{AB} is always positive. It means that theoretically, the mixing between A and B (i.e. the solvation in the case of polymer-solvent interaction) always requires energy so the phase separation is favored by the mixing enthalpy terms. In some cases, the mixing enthalpy can be negative, meaning

that the mixture is more energetically favorable than the pure constituents[129]. The resulting Gibbs free energy may exhibit different trends with the binary mixture composition depending on the χ_{AB} value compared to the critical value $\chi_c = 0.5 + 1/\sqrt{N}$. In the case of long enough macromolecules, $\chi_c \cong 0.5$.[130] Three different cases may be encountered and are presented in Figure 3.1:

(1) If $\chi_{AB} < \chi_c$, the free energy curve (green line) is concave in the whole composition range so it presents only one minimum and the mixture is miscible in all proportions. In the case of polymer-solvent mixtures, the solvent is then qualified as a good solvent. When χ_{AB} is close to zero, the solvent is said athermal and is an excellent solvent for the polymer.

(2) If $\chi_{AB} > \chi_c$, the free energy has 2 minima (orange line) so a phase separation may occur at certain compositions to reduce the total free enthalpy of the system.

(3) If $\chi_{AB} = 0.5$, the solvent is a theta solvent (yellow line).

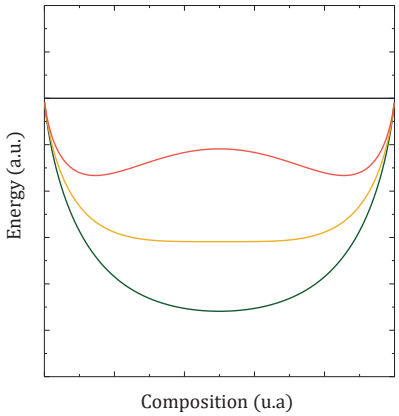

Figure 3.1: Total free energy evolution with the mixture composition

At the basis of the Flory theory, the molar volumes of A and B are hypothesized to be equal and constant during the mixing. In addition, the theory is based on the Van der Waals interactions and does not consider dipolar interactions and hydrogen bonds. As a consequence, the theory reaches its limits for polar species or species prone to form hydrogen bonding. In response to these limitations, some authors have proposed corrections to the Flory theory in order to extend its use to a larger number of chemical species[131–134].

Hansen solubility parameters

Up to 1960-70, the Hildebrand parameters have been used to predict the solubility of a polymer in a solvent. As presented previously, a good solvation is promoted when the polymer and solvent have very close Hildebrand parameters. Nevertheless, this approach is limited to non-polar species with no hydrogen bonding. Hansen has

extended this theory by splitting the total system energy E into three intermolecular contributions in order to consider polar interactions P and hydrogen bonds H in addition to dispersive interactions D into the phase equilibrium prediction, as presented in equation (3.12).

$$E = E_D + E_P + E_H \tag{3.12}$$

Accordingly, the Hildebrand solubility parameter is also split into these three intermolecular contributions:

$$\delta_{tot}{}^2 = \delta_D{}^2 + \delta_P{}^2 + \delta_H{}^2 \tag{3.13}$$

Then, the affinity between two components A and B is a function of the three intermolecular contributions $\delta_D{}^2, \delta_P{}^2$ and $\delta_H{}^2$. These contributions are the Hansen Solubility Parameters (HSPs):

- δ_D is the **Dispersive** contribution. It comes from the London forces, existing between every atom and molecule in which the electron cloud in motion may induce a temporary dipole moment that may induce attractive electrostatic forces between two atoms or molecules. The ability of the electron cloud of an atom or a molecule to be distorted is called the polarizability. This polarizability depends on the size of atoms or molecules and also on the shape of molecules. Larger and heavier is the atom or the molecules and higher are their dispersive contribution δ_D. These forces are at the origin of the Van der Waals Forces whose strength is approximately about 1 kJ.mol^{-1}.[128]
- δ_P is the **Polar** contribution. It comes from the Keesom Forces due to the interactions between permanent dipoles which are found in molecules between two atoms or groups of atoms having different electronegativity. Such permanent dipoles generate an electric field in their surroundings and interact with the electric field generated by other molecules. These forces may be attractive or repulsive and induce molecules reorientation in order to minimize their energy. This reorientation leads to mainly attractive dipole-dipole forces between polar molecules. The strength of dipolar interactions lies typically between 5 and 20 kJ.mol^{-1}.
- δ_H is the **Hydrogen bonding** contribution. It comes from the hydrogen bonds which are particular dipole-dipole interactions established in the case where a hydrogen atom is covalently bonded to a very electronegative atom (N, O, Cl, F…). Charge density on the electronegative atoms is highly negative whereas it is highly positive on the hydrogen. These dipoles give rise to

particular dipole-dipole interactions at the origin of the hydrogen bonds. The strength of most hydrogen bonds lie between 10 and 40 kJ.mol^{-1}.[128]

As with the Hildebrand parameter, the HSPs are expressed MPa$^{1/2}$, (corresponding to $(J/m^3)^{1/2}$). This unit will be used in what follows. To better describe these HSPs, Hansen has proposed a 3D view in which each coordinate represents an intermolecular contribution as shown in Figure 3.2.

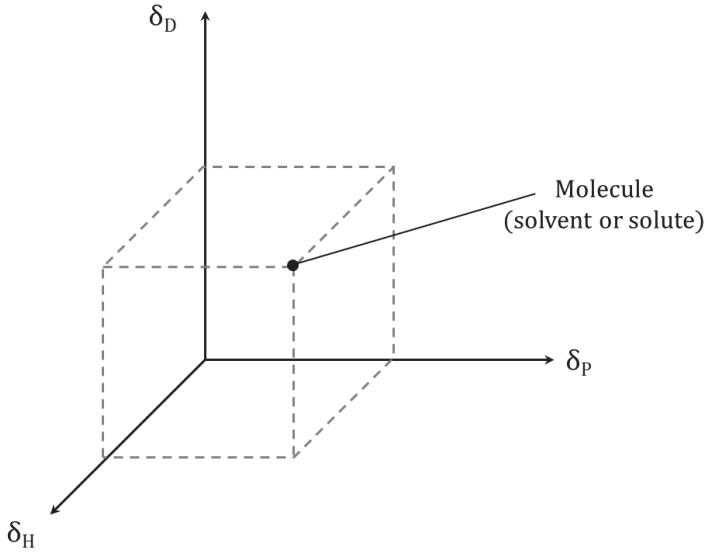

Figure 3.2: 3D representation of the Hansen Solubility Parameters

In this theory, every solvent, molecule, polymer or chemical species with defined HSP values can be represented by a point in a 3D space with its coordinate δ_D, δ_P and δ_H. The affinity between two components A and B is then determined using the following equation:

$$(Ra)^2 = 4\left(\delta_D^{(B)} - \delta_D^{(A)}\right)^2 + \left(\delta_P^{(B)} - \delta_P^{(A)}\right)^2 + \left(\delta_H^{(B)} - \delta_H^{(A)}\right)^2 \qquad (3.14)$$

where Ra is a distance between the HSP of two molecules or components. As with the Hildebrand approach, components with similar HSP will have a good affinity. Indeed, similar HSP values result in a short Ra distance in the Hansen space and then to high affinity. The term Ra corresponds to a modified distance between two components. Indeed, the factor 4 proposed by Hansen before the squared difference of the dispersive contributions on equation (3.14) is a matter of debate.

In the 3D representation, the laws of mixture are linear (which have been experimentally determined). For example, a 50:50 solvent mixture is localized at the exact centre between the HSP of the two components of the mixture as represented in Figure 3.3. A solvent with tuned HSP can be easily obtained by mixing different solvents

with selected HSP in the right proportions. This prediction lies in the convexity principle which predicts that a solvent with HSP localized in between two good solvents must be a good solvent.

In the Hansen theory, molar volumes are not considered explicitly in the determination of the affinity between two chemical species, in equation (3.14). Equations (3.12) to (3.14) rely on the assumption that contributions to the interaction energies are additives, i.e. cross terms are neglected.

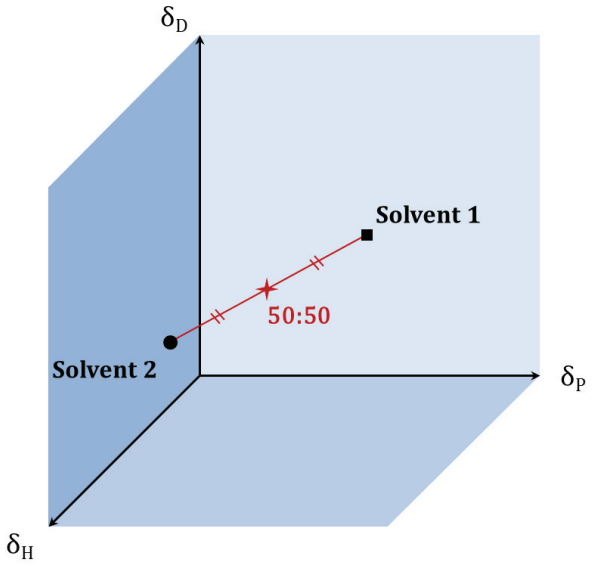

Figure 3.3: Illustration of the mixing laws for a 50:50 mixture between two solvents 1 and 2.

The HSPs depend on temperature and pressure[135]. Table 3.1 presents the equations describing the impact of both pressure and temperature on the three HSPs. In these equations, α corresponds to the thermal expansion coefficient (about 10^{-4} K^{-1}) and β corresponds to the bulk modulus (about 10^9 Pa).

Table 3.1: HSP dependency on temperature and pressure. α is the volume thermal expansion coefficient and β the bulk modulus[135].

HSP	Temperature	Pressure
δ_D	$\left(\frac{\partial \delta_D}{\partial T}\right)_P = -1.25\delta_D\alpha$	$\left(\frac{\partial \delta_D}{\partial P}\right)_D = -1.25\delta_D\beta$
δ_P	$\left(\frac{\partial \delta_P}{\partial T}\right)_P = -\delta_P\left(\frac{\alpha}{2}\right)$	$\left(\frac{\partial \delta_P}{\partial P}\right)_D = -\delta_P\left(\frac{\beta}{2}\right)$
δ_H	$\left(\frac{\partial \delta_H}{\partial T}\right)_P = \delta_H\left(1.32\times10^{-3}+\frac{\alpha}{2}\right)$	$\left(\frac{\partial \delta_H}{\partial P}\right)_D = \delta_H\left(1.32\times10^{-3}+\frac{\beta}{2}\right)$

Polymer solubility sphere

In the Hansen theory, polymers are characterized by a sphere which delimits good solvents and poor solvents. The centre of the sphere is the HSP coordinates of the polymer and its radius is denoted R_0. The solubility of a polymer into a given solvent can be predicted by comparing the solvent-polymer distance Ra to the polymer sphere radius R_0. The Relative Energy Distance (RED) is then introduced and defined by equation (3.15).

$$RED = \frac{R_a}{R_0} \tag{3.15}$$

This value directly qualifies a solvent with respect to a polymer:

- If RED<1 ($Ra < R_0$): the solvent is a good solvent of the polymer
- If RED>1 ($Ra > R_0$): the solvent is a non-solvent of the polymer

A representation of this solubility sphere is given in Figure 3.4.

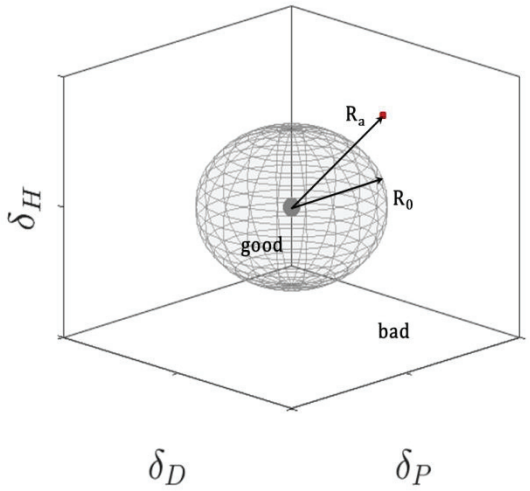

Figure 3.4: Representation of the solubility sphere of the PVdF-HFP with an arbitrary positioned solvent (■)

In the Flory theory the limit of the solubility of a polymer into a solvent (at given T and P) is given by $\chi_{AB} = 0.5$ which corresponds to a theta solvent. Similarly, the limit of the solubility in the Hansen theory is given by the surface of the polymer sphere (RED=1). A solvent with HSP localized onto the surface of a polymer sphere may be considered as a theta solvent for this polymer[136].

3.2.2 Experimental determination

Solubility tests

Solvent HSP values are known and tabulated in the literature. Semi-empirical calculation methods such as the group contribution methods can be used to estimate

the HSP for non-tabulated solvents or molecules[136]. While the HSP of monomers can be estimated easily with this method, the estimation of the HSP for macromolecules (>100000g/mol) is not accurate. For polymers, the HSP are experimentally determined by testing their solubility in a large variety of solvents covering a wide range of HSP values. The solvent selection comes from the work of Laurens et al.[137]

For the experimental determination of the PVdF-HFP HSPs, 60 solvents with particular HSPs covering a wide range of HSP values were selected to assess their ability to dissolve the polymer. In this selection, the solvents have dispersive components $\delta_D$varying from 12.9 to 21.0 $MPa^{1/2}$, polar components δ_P varying from 0 to 26.2 $MPa^{1/2}$ and hydrogen bonding components $\delta_H$varying from 0 to 42,3 $MPa^{1/2}$. In addition, solvent mixtures were used to reach particular HSP that could not be found in regular solvent, such as Glycerol-Water and Formamid-Water mixtures. The solvent selection is detailed in Table 3.2. For the solubility tests, the concentration was set to 5 wt% and the polymer was stirred on a rotating rack for 24 hrs at RT in order to ensure each system reaches thermodynamic equilibrium. These measurements were performed in LoF with the help of Julien Jolly and Julien Laurens.

Then, the evaluation of the solubility was done by visual assessment. Quotation marks between 1 and 6 were given depending on the dissolution state of the polymer. A mark of 1 corresponds to the total dissolution of the polymer and a mark of 6 to the absence of effect of the solvent on the polymer as shown in Figure 3.5. Intermediate marks were given for in-between cases.

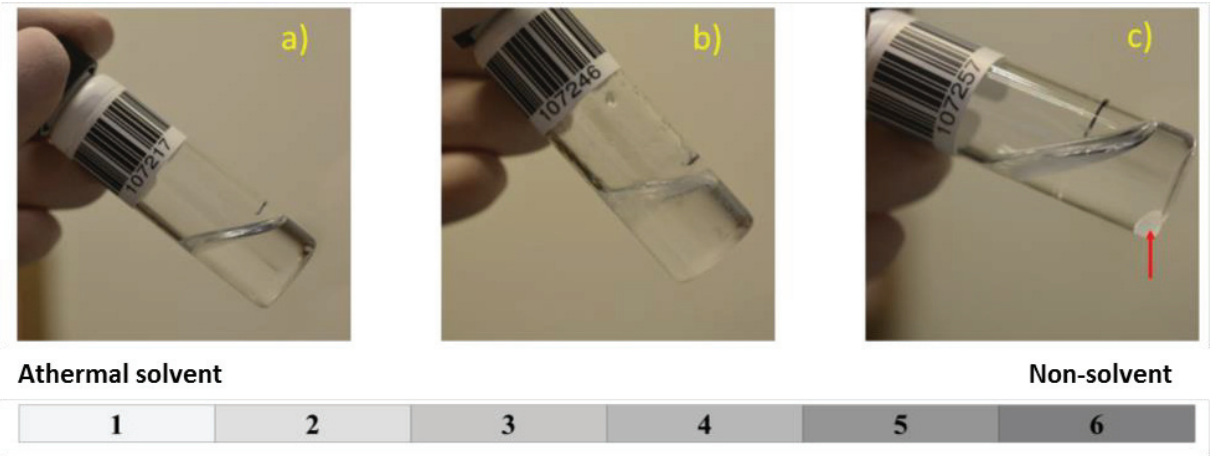

Figure 3.5: Example of solubility test and visual assessment of the polymer solubility. A) Mark A: total solubility, b) mark 2 to 5: intermediate solubility and c) mark 6: no solubility.

The marks resulting from the solubility visual assessment were then implemented in the HSPiP® software (Hansen Solubility Parameter in Practice, developed by Hansen, Abbott and Yamamoto[138]). The software was used to fit a sphere including all good

solvents and excluding all other solvents. The boundary between “good” and “poor” solvents can be adjusted in order to include enough solvents and fit a sphere accurately.

Table 3.2: Description of the selected solvents for the solubility test. Solubility parameters are expressed in $MPa^{1/2}$. The density ρ, the viscosity η and the optical index n_{20} are given at 20 °C. The solvent selection and the HSP data come from the work of Julien Laurens.[137]

N°	Solvent	δ_D	δ_P	δ_H	ρ (g/ml)	η (mPa.s)	n_{20}
1	Pentane	14.5	0	0	0.626	0.24	1.358
2	Heptane	15.3	0	0	0.684	0.45	1.385
3	Cyclohexane	16.8	0	0.2	0.778	1.2	1.427
4	Toluene	18	1.4	2	0.87	0.59	1.497
5	Tetrahydronaphthalene	19.6	2	2.9	0.97	2.02	1.541
6	Methylene Dichloride	17	7.3	7.1	1.327	0.41	1.424
7	Chloroform	17.8	3.1	5.7	1.483	0.89	1.446
8	Tetrachloroethylene	18.3	5.7	0	1.613	0.99	1.506
9	Chlorobenzene	19	4.3	2	1.11	0.8	1.524
10	1-Chlorobutane	16.2	5.5	2	0.89	0.45	1.402
11	o-Dichlorobenzene	19.2	6.3	3.3	1.3	1.32	1.551
12	1,1,2,2-Tetrabromoethane	21	7	8.2	2.967	6.45	1.637
13	Tetrahydrofuran (THF)	16.8	5.7	8	0.889	0.42	1.405
14	Diethyl Ether	14.5	2.9	4.6	0.713	0.22	1.353
15	Anisole	17.8	4.4	6.9	0.995	1.09	1.514
16	Acetone	15.5	10.4	7	0.791	0.26	1.356
17	Methyl Ethyl Ketone (MEK)	16	9	5.1	0.805	0.41	1.376
18	Methyl Isobutyl Ketone (MIBK)	15.3	6.1	4.1	0.802	0.58	1.396
19	G-Butyrolactone (GBL)	18	16.6	7.4	1.129	1.7	1.435
20	Propylene Carbonate	20	18	4.1	1.118	2.5	1.421
21	Ethyl Acetate	15.8	5.3	7.2	0.902	0.56	1.37
22	Isopropyl Acetate	14.9	4.5	8.2	0.87	0.52	1.377
23	Isobutyl Isobutyrate	15.1	2.8	5.8	0.855	0.67	1.398
24	Acetonitrile	15.3	18	6.1	0.786	0.36	1.342
25	2-Nitropropane	16.2	12.1	4.1	0.982	0.72	1.394
26	N-Methyl-2-Pyrrolidone (NMP)	18	12.3	7.2	1.028	1.65	1.479
27	Formamide	17.2	26.2	19	1.133	3.3	1.447
28	Dimethyl Formamide (DMF)	17.4	13.7	11.3	0.944	1.04	1.427
29	N,N-Dimethyl Acetamide	16.8	11.5	9.4	0.937	0.95	1.438
30	Carbon Disulfide (0 Dipole Moment)	20.2	0	0.6	1.266	0.36	1.627
31	Diméthylsulfoxyde	18.4	16.4	10.2	1.1	1.99	1.479
32	Methanol	14.7	12.3	22.3	0.791	0.77	1.327
33	Ethanol	15.8	8.8	19.4	0.789	0.98	1.359
34	1-Butanol	16	5.7	15.8	0.81	2.57	1.399
35	Benzyl Alcohol	18.4	6.3	13.7	1.044	5.47	1.539
36	Ethyl Lactate	16	7.6	12.5	1.03	2.71	1.412
37	2-Ethyl-Hexanol	15.9	3.3	11.8	0.833	10.3	1.431
38	Water	15.5	16	42.3	1	1	1.333
39	Ethylene Glycol	17	11	26	1.113	16.1	1.431
40	Diethylene Glycol	16.6	12	19	1.118	35.7	1.447
41	M1 Glycerol-Water 70/30	16.8	12.7	31.7			

N°	Solvent	δ_D	δ_P	δ_H	ρ (g/ml)	η (mPa.s)	n_{20}
42	M2 Formamide-Water 75/25	16.8	23.7	24.8			
43	M3 Formamide-Water 50/50	16.4	21.1	30.7			
44	M4 Formamide-Water 25/75	15.9	18.6	36.5			
45	Decamethylcyclopentasiloxane	12.9	1.3	1	0.958	3.74	1.396
46	Rhodiasolv AC6	16.7	6.4	5.5			
47	Rhodiasolv IRIS	16.6	8.7	5.0			
48	Rhodiasolv Polarclean	15.8	10.7	9.2			
49	Rhodiasolv Adma10	16.6	7.4	8.7			
50	Rhodiasolv LiTec2V	16.0	7.2	19.3			
51	Rhodiasolv RPDE	17.2	6.3	9.2			
52	Isosorbide dimethyl ether (Y-MB)	17.6	7.1	7.5	1.15		1.461
53	Augeo Clean Plus	17.2	17.2	8.4			
54	Rhodiasolv Green 25	17.6	9.2	6.6	6.5		
55	1-bromonaphtalene	20.6	3.1	4.1	1.48	4.45	1.657

HSP determination

The calculation of the HSP values from the solubility results includes 2 steps: First, all solvents used in solubility tests are reported in the 3D Hansen space. The solvents solubilizing the PVdF-HFP are marked by blue circles (•) and the solvents that did not solubilize it by red squares (■). The solvents for which the solution remains turbid, meaning partial solubility, are marked by orange triangles (▲). This is represented in Figure 3.6 b).

The second step consists in calculating the HSP of the PVdF-HFP by fitting a sphere that includes the "good" solvents and excludes the "poor" solvents. As shown in Figure 3.6 b) there is a clear separation between the good and the poor solvents. Additional 2D projections are given in Figure 3.6 c), d) and e).

The coordinates of the fitted sphere centre are the HSPs of the PVdF-HFP. They are found to be 14.6 $MPa^{1/2}$ for δ_D, 11.9 $MPa^{1/2}$ for δ_P and 11.4 $MPa^{1/2}$ for δ_H and the radius of the sphere is 8.1 $MPa^{1/2}$. Those values are presented in Table 3.3 together with other estimations obtained from the literature[139,140]. The obtained results slightly differ from the data found in the literature. Particularly, the dispersive contribution found for PVdF-HFP is lower than those found for PVdF and PVdF-HFP. Moreover, Akkoyun et al. have found higher δ_D for PVdF-HFP than for the homopolymer. The deviation observed on δ_D can be explained by the fact that more than half of the sphere is out of the cloud of the representation point of the solvent. Concerning, δ_p and δ_H, the results found in this work are in good agreement with the literature.

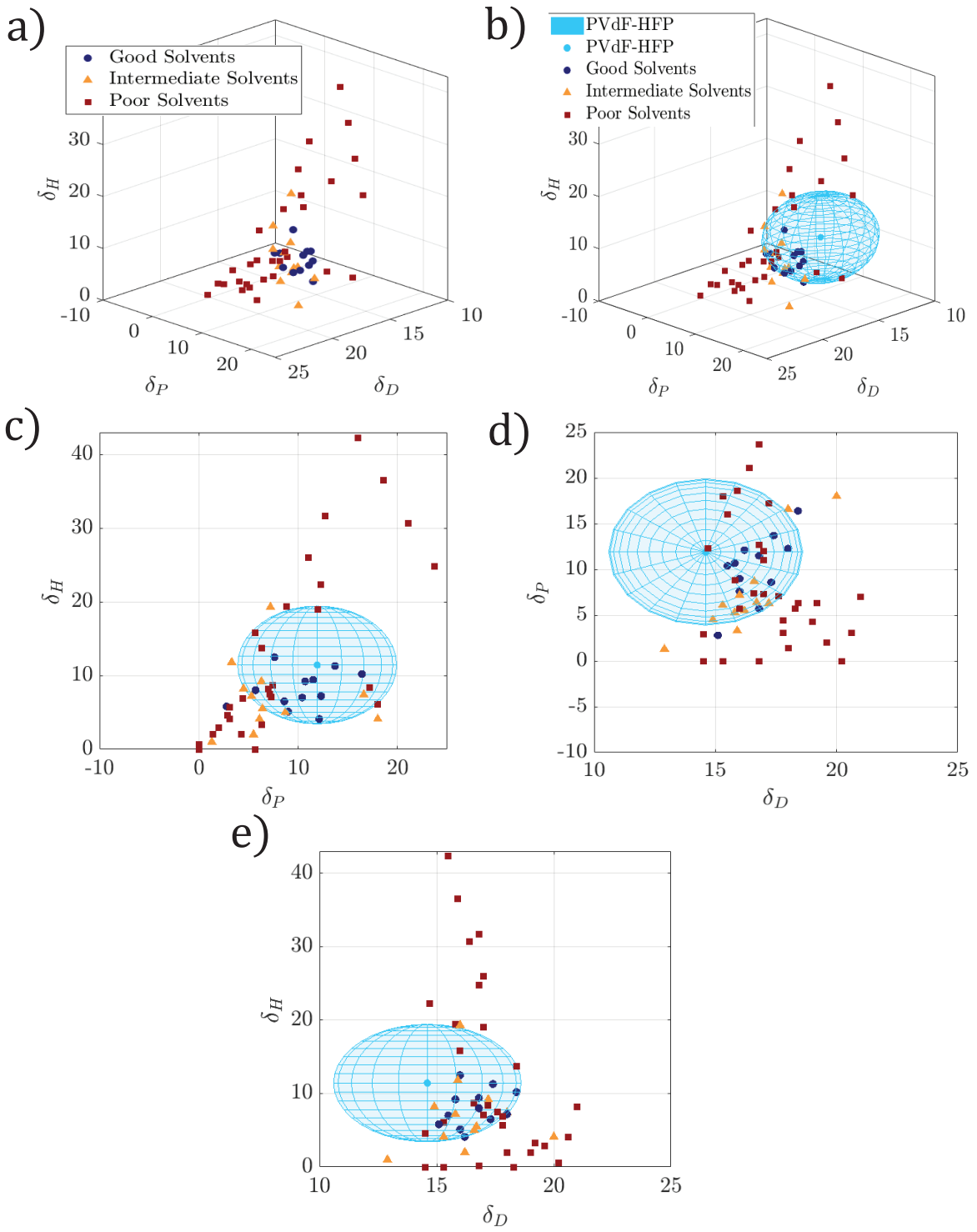

Figure 3.6: a) Representative positions of the solvents in the Hansen space with colour symbols to differentiate good, intermediate or poor solvents. b) PVdF-HFP sphere determination in 3D. The whole data are plotted in 2D following c) the δ_H/δ_P plan, d) the δ_P/δ_D plan and e) the δ_H/δ_D plan.

Table 3.3: HSP values obtained for PVdF-HFP and compared to PVdF and PVdF-HFP values from the literature.

Polymer	Authors	δ_D ($MPa^{1/2}$)	δ_P ($MPa^{1/2}$)	δ_H ($MPa^{1/2}$)	δ ($MPa^{1/2}$)
PVdF	Bottino et al. (1988) [139]	17.2	12.5	9.2	23.2
PVdF	Akkoyun et al. (2012) [140]	17.0	12.1	10.2	23.2
PVdF-HFP		19.9	12.8	11.6	26.4
PVdF-HFP	This work	14.6	11.9	11.4	22

It is worth mentioning that 5 “poor” solvents are localized into the fitted sphere (Methylene dichloride, 1 butanol, Rodiasolv Adma C10, Rhodiasolv Rpde, Rhodiasolv Augeo Clean Plus) and 3 “good” solvents are localized outside (Tetrahyfdrofuran, Isobutyle Isobutyrate, Dimethyl Sulfoxide) even though both are located close to the sphere boundary. This means that the fitted sphere does not perfectly describe whether a solvent is good or not simply based on its relative position with respect to the sphere. This uncertainty may come from the numerous hypotheses on which the Hansen theory is based (no effects of the molar volume or of some particular molecular structure, no interactions between induced and permanent dipoles…).

With these HSPs, it is possible to predict the solubility of the PVdF-HFP in any solvent for which the HSPs are available or can be estimated with the group theory calculation method mentioned before.

3.2.3 HSP results and predictions:

Solubility predictions

In the wide variety of solvents commercially available, it is now possible to carry out a screening in order to extract all solvents fulfilling expectations for the fabrication process. The expectations regarding the HSP of the solvent have then to be combined to other constraints such as the boiling and melting points.

A screening has been done with the following criteria: (1) the solvent must have a RED value lower than 1 (i.e. the solvent must be in the PVdF-HFP sphere). (2) The solvent must be a liquid at RT (i.e. must have a melting point below 20 °C) and (3) it must have a boiling point relatively low to enable a simple drying process (typically <150 °C). Out of the 1200 solvents registered in the HSPiP database, 91 fulfil these criteria. Some examples are given in Table 3.4. Note that 2-heptanone was selected as a counter example with a RED value of 1.25.

Table 3.4: Relevant physicochemical properties of the solvent selection for PVdF-HFP film fabrication.

Solvent name	δ_D ($MPa^{1/2}$)	Δ_P ($MPa^{1/2}$)	Δ_H ($MPa^{1/2}$)	RED	T^{melt} (K)	T^{boil} (K)
MEK	16	9	5.1	0.93	-87	80
DMF	17.4	13.7	11.3	0.73	-60	152
2-Heptanone	16.2	5.7	4.1	1.25	-35	151

Examples of MEK, Heptanone and DMF

PVdF-HFP films were fabricated using the solvents presented in Table 3.4. MEK is commonly found in the literature as PVdF-HFP solvent. Indeed, MEK-PVdF-HFP binary mixture exhibits a low RED value. The films were dried under atmospheric pressure and RT because of its low boiling point. In this case, flat, homogeneous and transparent films were obtained. Scanning Electron Microscopy (SEM) analysis confirmed the homogeneous structure of the PVdF-HFP films casted from MEK solutions as presented in Figure 3.7 a)

In the case of 2-heptanone, the solvent casted films are dried under primary vacuum. They exhibit a hazy white colour indicating high light scattering in the films and so probably porous structure. The porous structure can be observed directly by SEM analyses as shown in Figure 3.7 b). Such morphology can be explained by a phase separation occurring due to the low affinity between polymer and solvent as predicted by the RED which is slightly higher than 1. Indeed, the 2-heptanone is known to quickly form a PVdF-HFP gel structure due to intermediate affinity between polymer and solvent[141].

In the case of the Dimethyl Formamide (DMF), which is a heavy solvent molecule with a boiling point very close to that of the 2-heptanone, the fabricated films were dried under the same conditions. However, the fabricated films are transparent and SEM analysis shows a very homogeneous structure as shown in Figure 3.7 c). This result is consistent with the low RED of 0.73 so that DMF exhibits good affinity with the polymer.

As a result, the quality of the final PVdF-HFP films obtained by solvent casting highly depends on the RED value, and thus on the affinity between the polymer and the solvent even though the selected solvents were apparently all able to solubilize the required PVdF-HFP amount for the film casting process. The HSP theory then gives a good rationale for this observation.

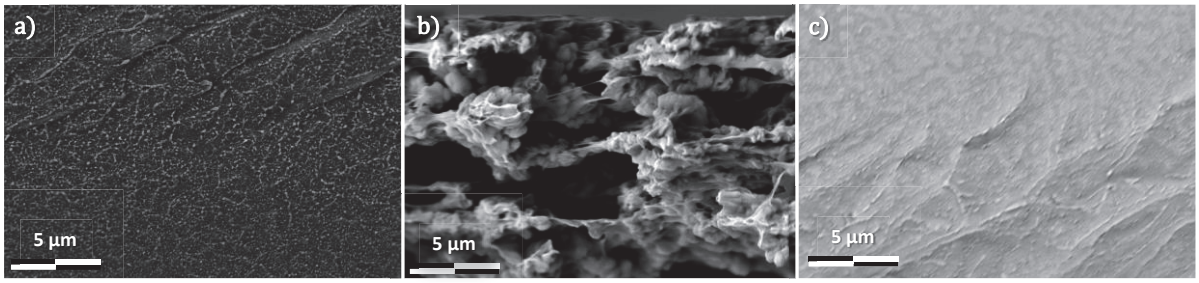

Figure 3.7: SEM pictures of PVdF-HFP film cross-sections. The films were fabricated by solvent casting in (a) MEK (b) 2-heptanone, and (c) DMF. All the cross sections were prepared by cold breaking in liquid nitrogen.

Relation to process

The previous results show that the HSP formalism can be used as a tool to find potential solvents suitable for a process. Solvents with low RED are prone to form homogeneous film structures whereas solvents with RED value slightly higher than 1 may be used to induce particular morphology in the films such as open or close porosity. Although further investigations concerning the vaporisation kinetics of the solvent would be required to control such processes, a first screening with the solvent HSPs may help in the process design and development.

3.3 Dispersibility of $BaTiO_3$ nanoparticles

In the case of a polymer solvent mixture, the HSPs provide information about the affinity between molecules and then information about the solubility of the polymer. This information is crucial in order to design the process and obtain polymer films with the expected morphology and properties. In the case of PVdF-HFP:$BaTiO_3$ nanocomposites, the NPs have to be dis-agglomerated and distributed in the polymer solutions used in the fabrication of nanocomposites. The final NP dispersion state in the nanocomposite film then depends on the stability of the suspension throughout the process. It follows that the interactions between the solvent and the NPs are also a crucial point in the development of nanocomposite fabrication processed by solvent casting.

3.3.1 Extension of the Hansen theory

To investigate the stability of NP suspensions, a similar approach can be used. An extension of the HSP theory has been developed and allows assessing the interactions between a non-soluble solid surface and a solvent[136]. Similarly to monomers/molecules, solid NPs can be represented in the Hansen space using experimental determination of

their parameters δ_D, δ_P and δ_H. In the case of solid particles, these parameters are not called Hansen Solubility Parameters but Hansen Dispersibility Parameters (HDPs).

These HDPs provide similar information as compared to polymers regarding the affinity with the solvents. The determination of the $BaTiO_3$ HDP provides tools to control the stability of NP suspensions and so to control the final nanocomposite morphology. Additional criteria can be used in the solvent selection to improve the nanocomposite fabrication process.

3.3.2 Experimental determination

Theoretical basis

The experimental methodology to determine the three HDPs is based on the following phenomenon: solvents having good affinity with the particles wet the surface, while solvent having weak interactions does not. Wetting leads to better stabilization of the particles and weaker attractive forces between the particles themselves that results in delayed sedimentation as schematized in Figure 3.8. It is precisely this aspect that Hansen uses to assess the solvent-particle affinity. To do so, he has introduced the Relative Sedimentation Time (RST) which is calculated with equation (3.16).

$$RST = \frac{t_s(\rho_p - \rho_s)}{\eta_0} \tag{3.16}$$

where t_s is the sedimentation time, ρ_s and ρ_p the densities of the solvent and particles respectively and η_0 the solvent viscosity. Higher is the wetting of the solvent onto the particle, higher is the RST. Conversely, lower is the wetting and lower is the RST. The sedimentation kinetic is also controlled by the interactions between particles, including hydrogen bonding and Van der Waals interactions[142].

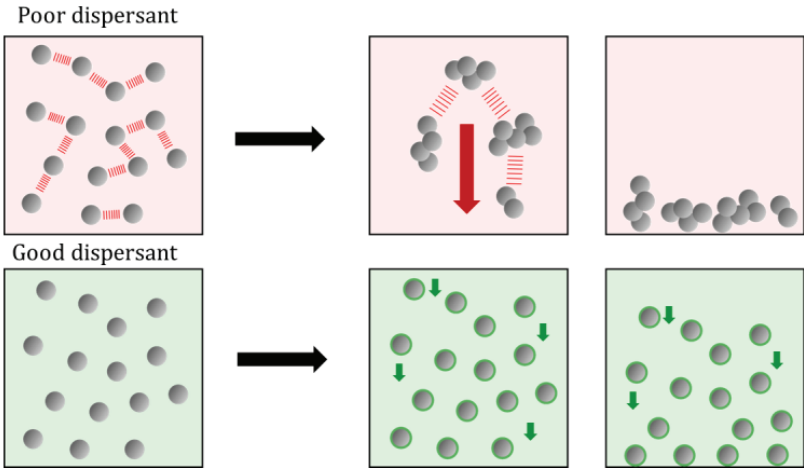

Figure 3.8: Illustration of the agglomeration-induced sedimentation of particles in poor dispersant compared to good dispersant.

Sedimentation monitoring

As with polymers, the HDP of $BaTiO_3$ NPs were studied by dispersing them into a large number of solvents with a wide HSP variety. Due to the much complex experimental procedure used for the HDPs determination, the number of solvents used in this part was reduced to 24 as compared to solubility tests previously described. The solvent selection comes from the work of Julien Laurens[137] and is defined in order to cover the largest zone possible in the Hansen space. All the solvents used for sedimentation tests are presented in Table 3.5. First, the NPs are introduced as a powder into glass vials with the solvents. The quantity of solvent is adapted to maintain the NP content at 2 wt%. Then, the NPs are dis-agglomerated and dispersed using a home-made ball milling. This dispersion process consists in adding some small silica spheres (around 2 mm of diameter) to the NP-solvent mixtures and placing the vials into a vortex for 2 hrs. The silica spheres act as mechanical stirrers as they induce large local shear and elongation stresses. Previous studies carried out on silica NPs have revealed that the particle/agglomerate size distribution after such ball milling process does not depend on the solvent used[137].

Table 3.5: Description of the solvent selected for the $BaTiO_3$ NPs HDP determination. The HSP are expressed in $MPa^{1/2}$.[136]

N°	Solvent	δ_D	δ_P	δ_H	ρ (g/ml)	η (mPa.s)	n_{20}
1	Heptane	15.3	0.0	0.0	0.684	0.451	1.385
2	Octane	15.5	0.0	0.0	0.703	0.579	1.395
3	Nonane	15.7	0.0	0.0	0.718	0.766	1.403
4	Dodecane	16.0	0.0	0.0	0.749	1.524	1.415
5	Cyclooctane	16.6	0.1	0.1	0.813	0.659	1.452
6	Acetonitrile	15.3	18.0	6.1	0.786	0.361	1.342
7	Acetone	15.5	10.4	7.0	0.791	0.296	1.356
8	THF	16.8	5.7	8.0	0.886	0.418	1.405
9	O-xylene	17.8	1	3.1	0.88	0.81	1.505
10	Dioxane	17.5	1.8	9.0	1.029	0.746	1.42
11	Chloroform	17.8	3.1	5.7	1.483	0.659	1.446
12	Methanol	14.7	12.3	22.3	0.791	0.766	1.327
13	Ethanol	15.8	8.8	19.4	0.789	0.982	1.359
14	IsoPropanol	15.8	6.1	16.4	0.785	2.04	1.375
15	MEK	16.0	9.0	5.1	0.805	0.41	1.376
16	Anisole	17.8	4.4	6.9	0.995	1.089	1.514
17	Et. Acetate	15.8	5.3	7.2	0.902	0.56	1.37
18	Bu. Acetate	15.8	3.7	6.3	0.882	0.885	1.392
19	Prp. Carbonate	20	18	4.1	1.188	2.5	1.421
20	Water	15.5	16	42.3	1	1.002	1.333

N°	Solvent	δ_D	δ_P	δ_H	ρ (g/ml)	η (mPa.s)	n_{20}
21	T.Cl.Ethylene	18.3	5.7	0	1.613	0.997	1.506
22	MIBK	15.3	6.1	4.1	0.801	0.607	1.393
23	Nitroethane	16	15.5	4.5	1.043	0.798	1.39
24	DMF	17.4	13.7	11.3	0.944	1.042	1.427

After this dispersion process, the sedimentation kinetics of the NPs are monitored using a home-made image acquisition apparatus (presented Figure 3.9) in which the vials are placed on a double stage sample holder. A white backlight is placed behind the sample vials in order to create contrast between solvent and NPs. The contrast comes from the light scattering induced by the difference of refraction index between the NPs ($n_{20} = 2.4$) and the solvents ($n_{20} = 1.3$-1.5). A camera is placed at 40 cm away from the vials and takes pictures of the vials as a function of time. The time between the end of the ball milling process and the starting of the camera is estimated to be 30 seconds. The acquisition frequency is first set at about 1 image every 5 seconds to monitor the fastest sedimentation kinetics and reduced up to 1 image per minute for slow ones. The image acquisition is stopped after 24 hrs when nearly all the suspensions have sedimented. The entire apparatus is placed in a dark box to prevent any external light pollution.

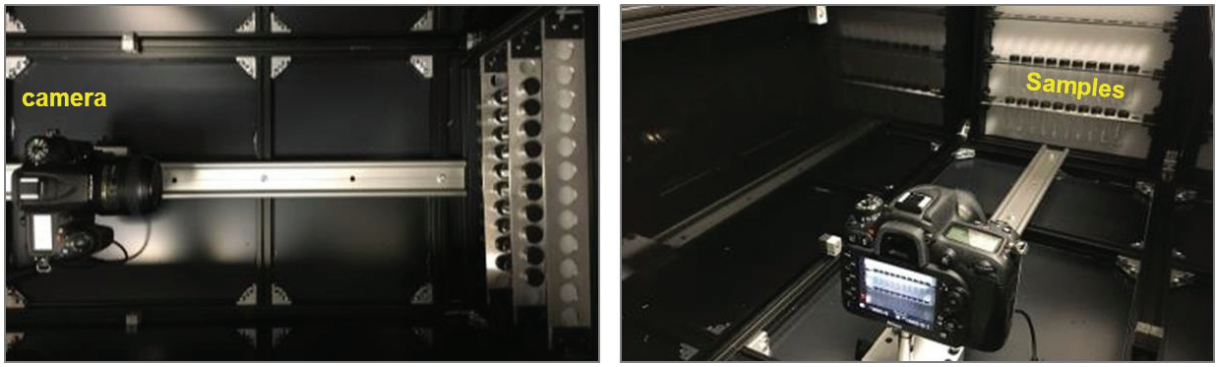

Figure 3.9: Image acquisition apparatus used for particle sedimentation monitoring.

In this way, the sedimentation kinetics of the 24 $BaTiO_3$-solvent systems are followed simultaneously. Figure 3.10 summarises the experimental approach used in this part. In most cases, the NPs sediment at once, so the parameter of interest is the sedimentation front position as a function of time. In particular cases such as for water, MEK, DMF, O-xylene or THF, a first sedimentation occurs first with a clear front while a fraction of the NPs remains in suspension in the solvent. After a longer time, the remaining NPs sediment and create a second sedimentation front. This could be explained by the presence of two NP populations of different agglomerate sizes.

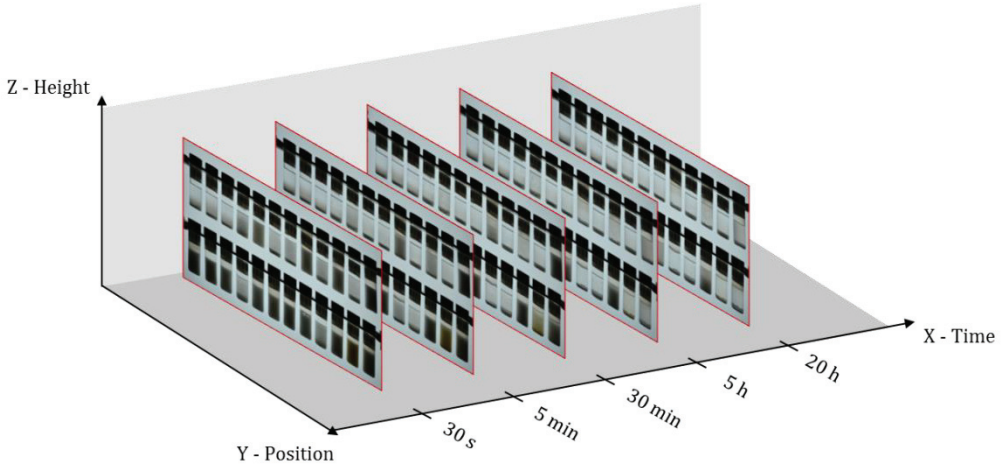

Figure 3.10: Schematized experimental approach of sedimentation kinetic monitoring based on image acquisition.

The following part is dedicated to how the sedimentation front position has been extracted from the acquired images.

Sedimentation kinetic determination

Figure 3.11 presents two parts of the pictures acquired by the camera at the initial time and after 10 hrs of sedimentation. Only the 12 bottom samples of the double stage sample holder are shown to illustrate the approach. On these images, the dark part of the liquid in the vials corresponds to the $BaTiO_3$ NP suspension. This contrast is due to light scattering induced by the NPs. First, it can be seen that in the initial step, the samples 4 and 9 seem to be already mostly agglomerated (respectively anisole and tetrachloroethylene). The reason for this is that the sedimentation in these systems is very fast and mostly occurred during the 30 seconds required to install the apparatus and start the acquisition after the ball-milling process was stopped. Such fast sedimentation indicates strong agglomeration kinetics due to very poor affinity between the $BaTiO_3$ NPs and these solvents. Nevertheless, a remaining light contrast could indicate the presence of a very low fraction of fine NPs that does not agglomerate and so does not sediment that fast. The other samples exhibit homogeneous contrast in the liquid part that suggests the absence of strong $BaTiO_3$ NPs agglomeration.

The bottom line in Figure 3.11 shows the sedimentation state 10 hrs after stopping the ball-milling process. The samples highlighted in blue squares (1, 2, 7, 10and 12) exhibit homogenous darkness in the liquid part or only a slight contrast in the very upper liquid zone. This reveals the presence of the NPs in suspension in the dark zones and so very slow sedimentation kinetics. In these cases, a good affinity between the $BaTiO_3$ NPs surface and the solvent would lead to weaker attractive interactions between the NPs themselves. As a consequence, the NPs would not strongly

agglomerate and remain in suspension with slow sedimentation kinetics due to their small sizes. These 5 solvents can be considered as good solvent for the $BaTiO_3$ NPs.

Conversely, the samples highlighted in red squares (3, 4, 5, 6, 8, 9, and 11) exhibit very weak contrast as compared to the backlight in the major upper part of the liquid, suggesting a very low NP concentration (or pure solvent) after sedimentation. The dark contrasts in the bottom part of the vials confirm the sedimentation of the NPs. For these samples, the solvents can be classified as "poor" solvents in which the weak interactions between the NPs and the solvents do not lead to strong adsorption and so no stabilization effect. The NPs then form large agglomerates that exhibit higher sedimentation kinetics.

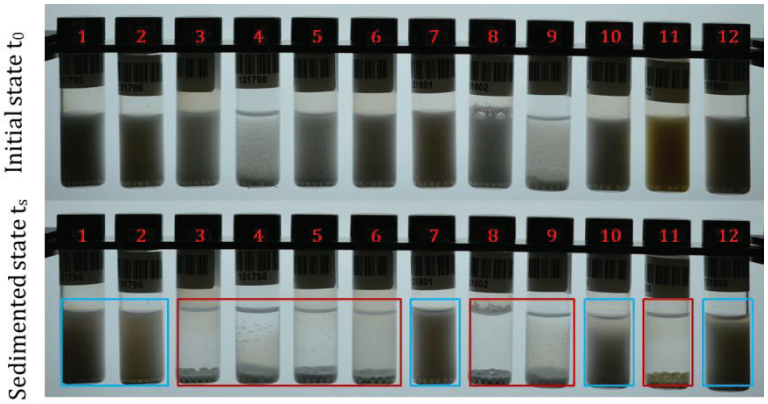

Figure 3.11: Example of 12 systems $BaTiO_3$ NPs-solvent before and after sedimentation (10 hrs). Blue squares correspond to non-sedimented samples and red squares correspond to sedimented samples.

HDP determination method

With the same approach used for the determination of the PVdF-HFP HSP, the HSPiP software was used to fit a sphere including all "good" solvents for dispersing the $BaTiO_3$ NPs and excluding all "poor" solvents. The "good" solvents that provide stable dispersions over more than 10 hrs are methanol, ethanol, 2-propanol, propylene carbonate, MIBK and DMF. With these "good" solvents, the sphere fitted with the HSPiP software provides the following HDP for $BaTiO_3$ NPs: 20.0 $MPa^{0.5}$ for δ_D, 13.7 $MPa^{0.5}$ for δ_P and 15.45 $MPa^{0.5}$ for δ_H.

Another representation consists in creating a 3D polyhedron (a 3D convex hull) including all the "good" solvent and excluding all the "poor" solvents. This approach has been proposed by Howel et al. [143] in order to better describe the affinity region of systems where the sphere is not properly delimiting "good" and "poor" solvents.

Both Hansen sphere and convex hull 3D representations with "good" and "poor" solvents are shown in Figure 3.12. As a result, it can be noted that the fitted sphere does

not include all the “good” solvents. This is due, for instance, to the close proximity in the Hansen space between the MIBK which is a “good” solvent and “poor” solvents such as Chloroform or acetone… Moreover, the fitted sphere covers a large part of the Hansen space where no solvents are represented. For example, the experimental solvent set has δ_D values between 14.7 and 20 $MPa^{1/2}$ whereas the fitted sphere extends up to 26.2 $MPa^{1/2}$. The uncertainty is then very high in the regions with no experimental information. Finally, it can be noted that the centre of the convex hull delimiting the “good” solvents does not coincide with the sphere centre.

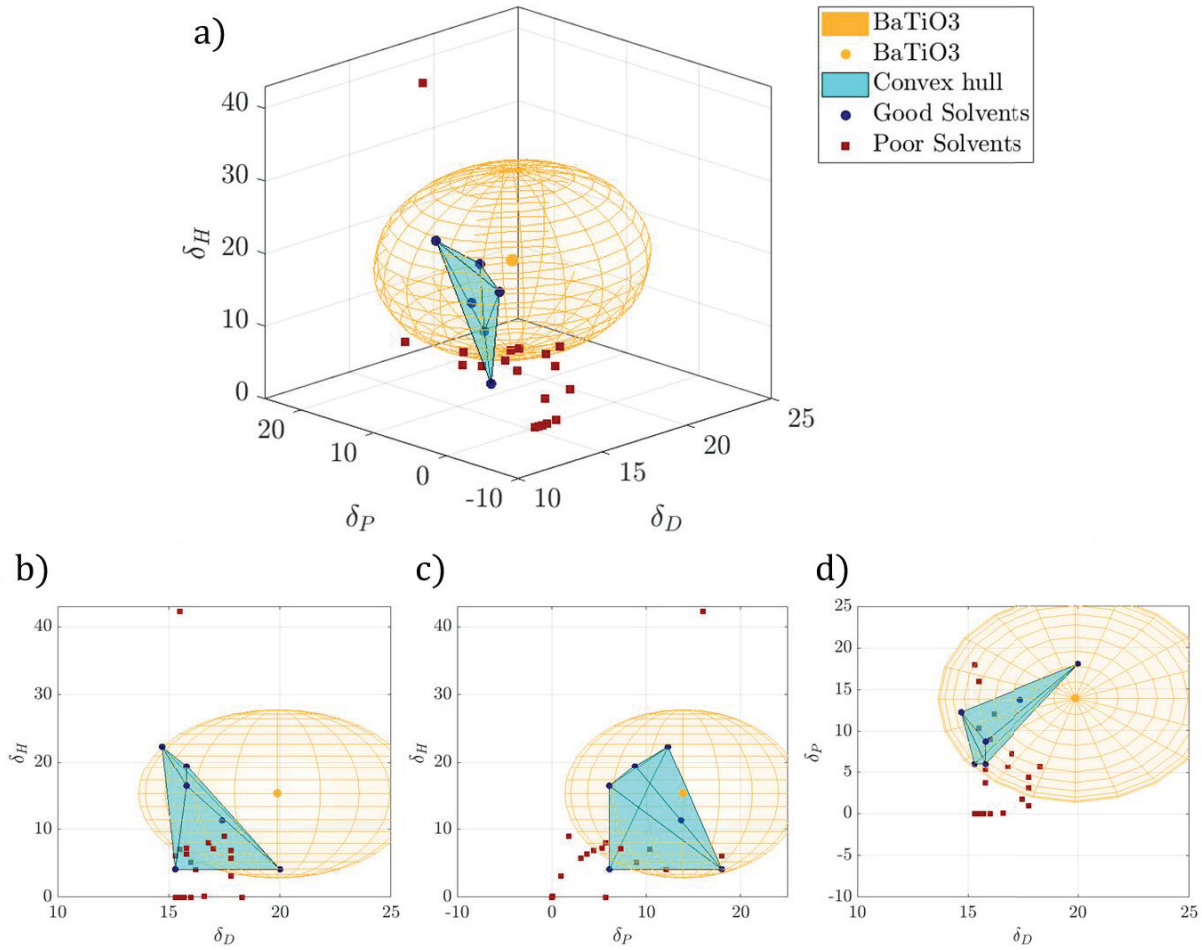

Figure 3.12: 3D representation of the $BaTiO_3$ HDP sphere and convex hull with the “good” solvents (blue circle) and the poor solvent (red square).

With the HSPiP sphere and the 3D convex hull, 4 ways of determining the HDPs of $BaTiO_3$ NPs may be used:

- Method 1: centre of the sphere

  Presented previously, this method consists in fitting a sphere including “good” solvents and excluding “poor” solvents. The HDP is then obtained with the centre coordinates of the sphere.

- Method 2: HDP convex hull 1
  Based on the 3D convex hull representation, the HDPs are calculated as the average of the coordinates of all the "good" solvents, dimension per dimension.
- Method 3: HDP convex hull 2
  Based on the 3D convex hull representation, the HDPs are calculated as the average of the coordinates of the "good" solvents located at the surface of the convex hull uniquely.
- Method 4: HDP convex hull 3
  In this method, the HDPs are calculated as the centroid of the generated 3D convex hull volume.

Note that from the first convex hull method to the third, the dependence of the $BaTiO_3$ NPs HDP on the solvent set selected for the sedimentation tests decreases.

The HDP obtained for the $BaTiO_3$ NPs with the various methods introduced above are presented in Table 3.6 and illustrated in Figure 3.13. The results show that the main difference in terms of $BaTiO_3$ NPs HDP is found between the classic sphere HDP determination method and the three convex hull methods. Indeed, as already suggested previously, the sphere and the polyhedron are not centred at the same position which leads to HDP results from 2 to 4 $MPa^{1/2}$ higher with the classic sphere method compared to convex hull methods. Nevertheless, the HDP determined with the three convex hull methods are quite similar. This can be due to the low number of "good" solvents constituting the convex hull.

The convex hull provides a supposedly more precise delimitation of the boundaries between "good" and "poor" solvents. Nevertheless, it is not compatible with the use of the RED notion in the Hansen theory anymore. In what follows, the HDPs obtained with the classic sphere method will be used while doing prediction coming from the Hansen theory. Nevertheless, the convex hull method providing a better sensitivity, it will be used in the last chapter in order to evaluate the impact of surface modification onto the HDPs of the $BaTiO_3$ NPs.

Table 3.6: HDP values of the $BaTiO_3$ NPs determined by various methods.

Method	δ_D	δ_P	δ_H	δ
		($MPa^{1/2}$)		
HDP sphere	20.0	13.7	15.5	28.7
HDP convex hull 1	16.5	10.8	13.9	23.6
HDP convex hull 2	16.3	10.3	13.3	23.4
HDP convex hull 3	16.5	10.7	12.2	23.2

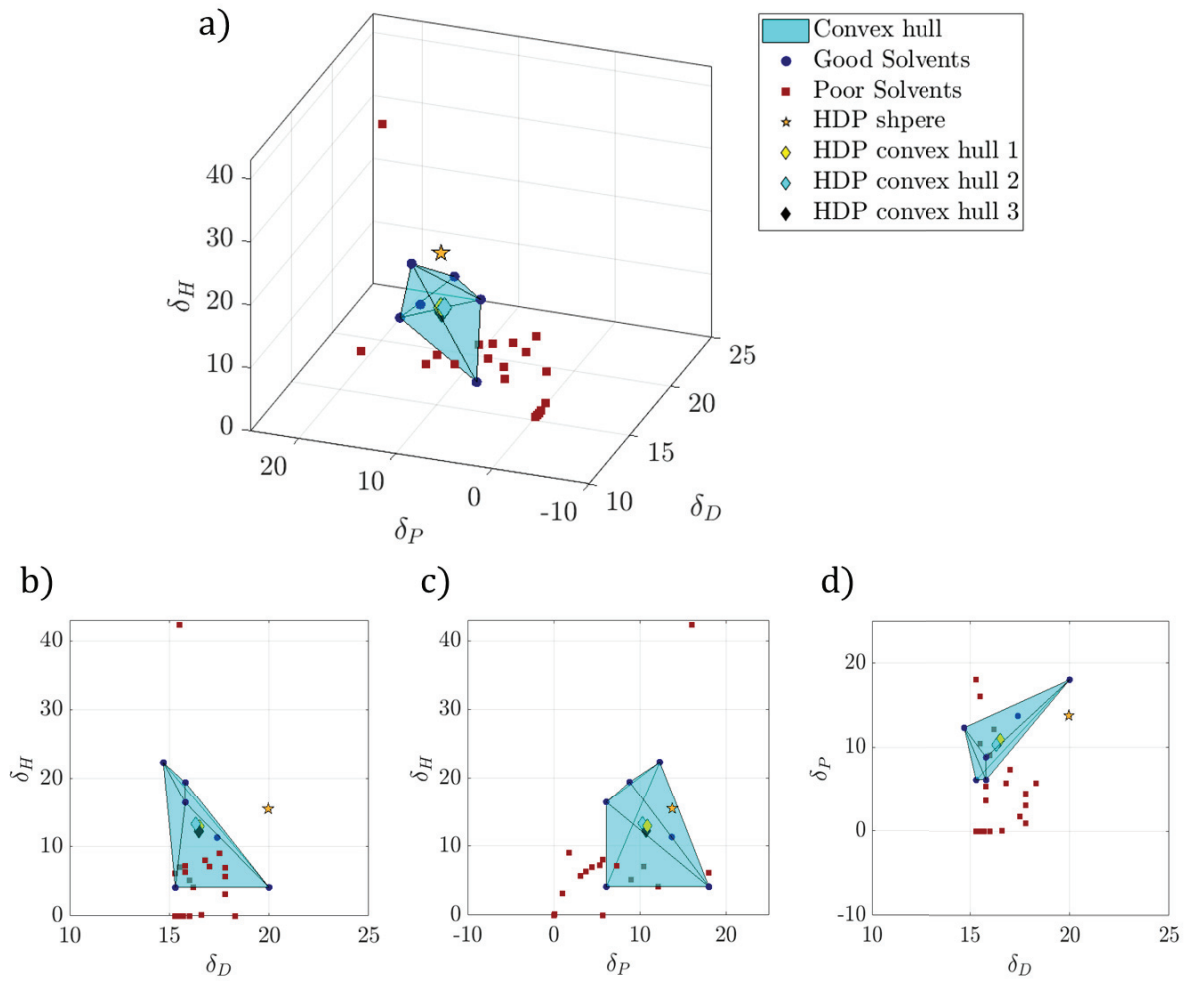

Figure 3.13: Convex hull polyhedron including "good" $BaTiO_3$ NPs solvents. The HDP calculated with the 4 methods are plotted.

3.3.3 Results and predictions:

Figure 3.14 shows the fitted sphere of the $BaTiO_3$ NPs superposed to the PVdF-HFP sphere. As we can see, the two spheres partially overlap. This overlapping volume in the Hansen space contains the solvents that should both solubilize the PVdF-HFP and stabilize the $BaTiO_3$ NPs.

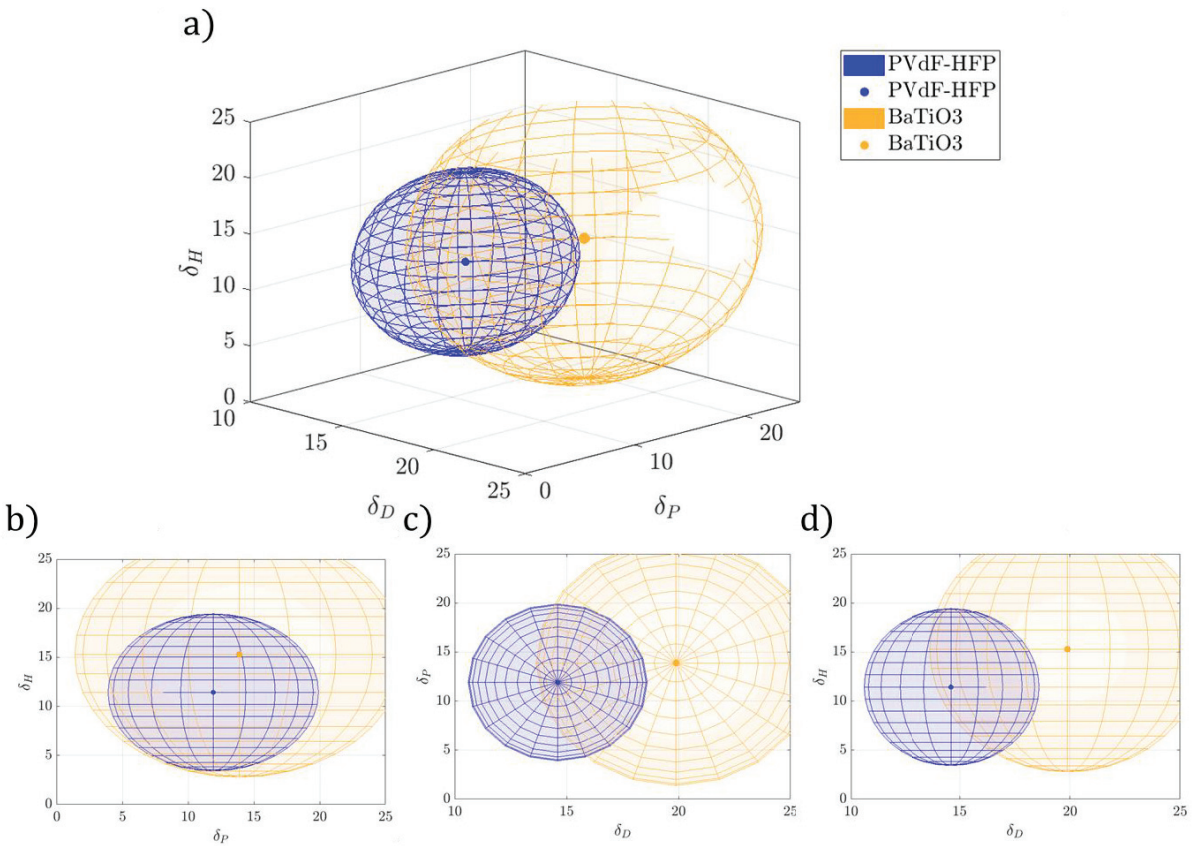

Figure 3.14: 3D representation of the PVdF-HFP and $BaTiO_3$ NPs spheres in the Hansen space and associated projections

The radius of the sphere is closely related to the experimental choices concerning the limit between "good" or "poor" solvents as well as the experimental conditions chosen in terms of polymer concentration and NP content. Conversely, the sphere centre is supposed to be independent of the experimental determination conditions. The fact that the centre of the PVdF-HFP sphere is included into the sphere of the $BaTiO_3$ NPs does not allow drawing any conclusion on the affinity between the NPs and the polymer. In the case of the $BaTiO_3$ NPs-PVdF-HFP interactions, the Ra is equal to 11.6.

Kinetics of NP agglomeration observed by DLS analysis

In order to have a better insight into the stability of the $BaTiO_3$ NP suspensions, Dynamic Light Scattering (DLS) measurements were carried out on some systems. The stability of the $BaTiO_3$ NPs was assessed in three solvents: DM), MEK and dichloromethane (DCM), which have interaction radii Ra of 6.6, 13.9 and 12.1 $MPa^{1/2}$ respectively. These values indicate a better affinity between the $BaTiO_3$ NPs surface and DMF than with the other solvents. The experiment consisted in assessing the stability domain of the suspension in terms of NPs concentration. To do so, the three

suspensions were prepared at 1 vol% in $BaTiO_3$ NPs, which is the concentration used in the fabrication process of a nanocomposites film at 10 vol% in NPs with respect to the polymer. The suspensions were then sonicated for 1 hr in order to break the NP agglomerates using the set up described in section 2.2.1. Since DLS analyses cannot be performed on too concentrated suspensions, a dilution step was required to reach a NP content around 0.01-0.0025 vol% which is the optimal concentration to perform DLS analysis. This concentration was preliminary determined. For each suspension, a sample is directly taken after stopping the sonication and diluted. If the suspension is not stable, the NPs start to agglomerate during the few seconds between the end of the sonication and the dilution. The dilution may slow down the agglomeration kinetics or even stabilize the sample in the agglomeration state at the moment of the dilution. If the suspension is stable, no effect of the dilution is expected. A series of DLS measurements is then performed on the diluted sample.

The stability of the suspension was explored at lower concentrations by diluting the suspensions and performing additional sonication steps of 5 minutes in order to redistribute the $BaTiO_3$ NPs in the solvents. After stopping the sonication, a similar procedure (sampling, dilution and analysis) was carried out to analyse the suspension stability at lower concentration. Below 0.01 vol%, no dilution of the sample was required before the DLS analyses. The determination of suspension stability after resting for a given duration is performed by manually shaking the suspension and taking a sample in the bottom of the solution in order to detect the presence of agglomerates that may sediment fast.

These DLS analyses aimed at determining the stability of the $BaTiO_3$ NP suspensions. Thus, a particular attention was paid to the evolution of the size distribution as a function of the time. As presented in section 2.3.6, the calculated sizes obtained by DLS do not correspond to the real sizes of the NPs but to their hydrodynamic radius. Thus, the mean size and the size distribution are either used as an order of magnitude or in a comparative way. The absolute value of the mean particle size is not considered.

In the case of DCM, the DLS analyses were not possible because of too fast agglomeration. For MEK and DMF, the DLS analyses were possible due to lower sedimentation kinetics. Figure 3.15 presents the principal DLS results for $BaTiO_3$ NP suspensions in MEK and DMF.

In the case of the MEK, the $BaTiO_3$ NP suspension was not stable at the concentration of 1 vol%. After stopping the sonication, the NPs agglomerate as shown in Figure 3.15 a). The dilution was observed to slow down the agglomeration kinetics. The suspension was diluted to 0.1, 0.025 and 0.01 vol%. The only concentration at which the suspension appears stable after 10 minutes is 0.01 vol% as shown in Figure 3.15 b) and c). The size distribution fluctuates but does not shift toward higher particle sizes within 10 minutes.

In Figure 3.15 d), the DLS analysis after 24 hrs resting shows the formation of large agglomerates with time, indicating the absence of long-term stability. In the case of the MEK, the interactions with the surface of the $BaTiO_3$ NPs were not sufficient to induce quantitative wetting and to significantly reduce the interactions between NPs at high volume content. Nevertheless, below 0.01 vol%, the $BaTiO_3$ NPs did not agglomerate too fast and were stable for 10 minutes.

In the case of the DMF, a different behaviour was observed on a 1 vol% suspension. After the sonication was stopped, several samples were taken as a function of time. The 1 vol% suspension was homogenised manually before each sampling and the sample was then diluted to 0.0025 vol%. As shown in Figure 3.15 e), the $BaTiO_3$ NPs were stable over 10 minutes after dilution which was not the case of similar suspension in MEK. Several samplings were carried out as a function of time and all the results were similar. Indeed, as shown in Figure 3.15 f), the DLS analysis of the last sample taken 24 hrs after the end of the sonication reveals a good stability of the 1 vol% $BaTiO_3$ NP suspension in DMF. As expected regarding the low Ra between DMF and the $BaTiO_3$ NPs, strong interactions could lead to quantitative wetting between the DMF and the NP surface leading to very low interactions between the NPs themselves and thus preventing NP agglomeration and fast sedimentation.

Table 3.7 summarizes the results obtained from the DLS analyses and the Hansen theory predictions concerning the stability of the NP suspensions (Ra). The relationship between the predicted solvent-NP affinity and the experimentally assessed suspension stability is relevant. For low Ra, illustrated by the case of DMF, the suspension exhibits a very good stability. For higher Ra values, as in the cases of MEK and DCM, the suspensions rapidly agglomerate and are not stable at the concentration of 1 vol%. Short-term stability has been found in the case of the MEK:$BaTiO_3$ NP suspension at low concentration (below 0.01 vol%)

As a result, the DLS analyses give an idea of the stability level that can be expected depending on the Ra obtained from the sedimentation tests. Knowing the prediction in terms of suspension stability, an additional criterion can be used in the solvent selection in order to generate a good NP dispersion state during the nanocomposite fabrication process.

Table 3.7: Ra affinity predictions and DLS results concerning $BaTiO_3$ NP suspensions in DCM, MEK and DMF.

Solvent/dispersant	Ra	Suspension stability	Stability concentration limit
DCM	12.1	No stable	-
MEK	13.9	Stable for 10 min	<0.01 vol%
DMF	6.6	Stable for 24 hrs	Up to 1 vol%

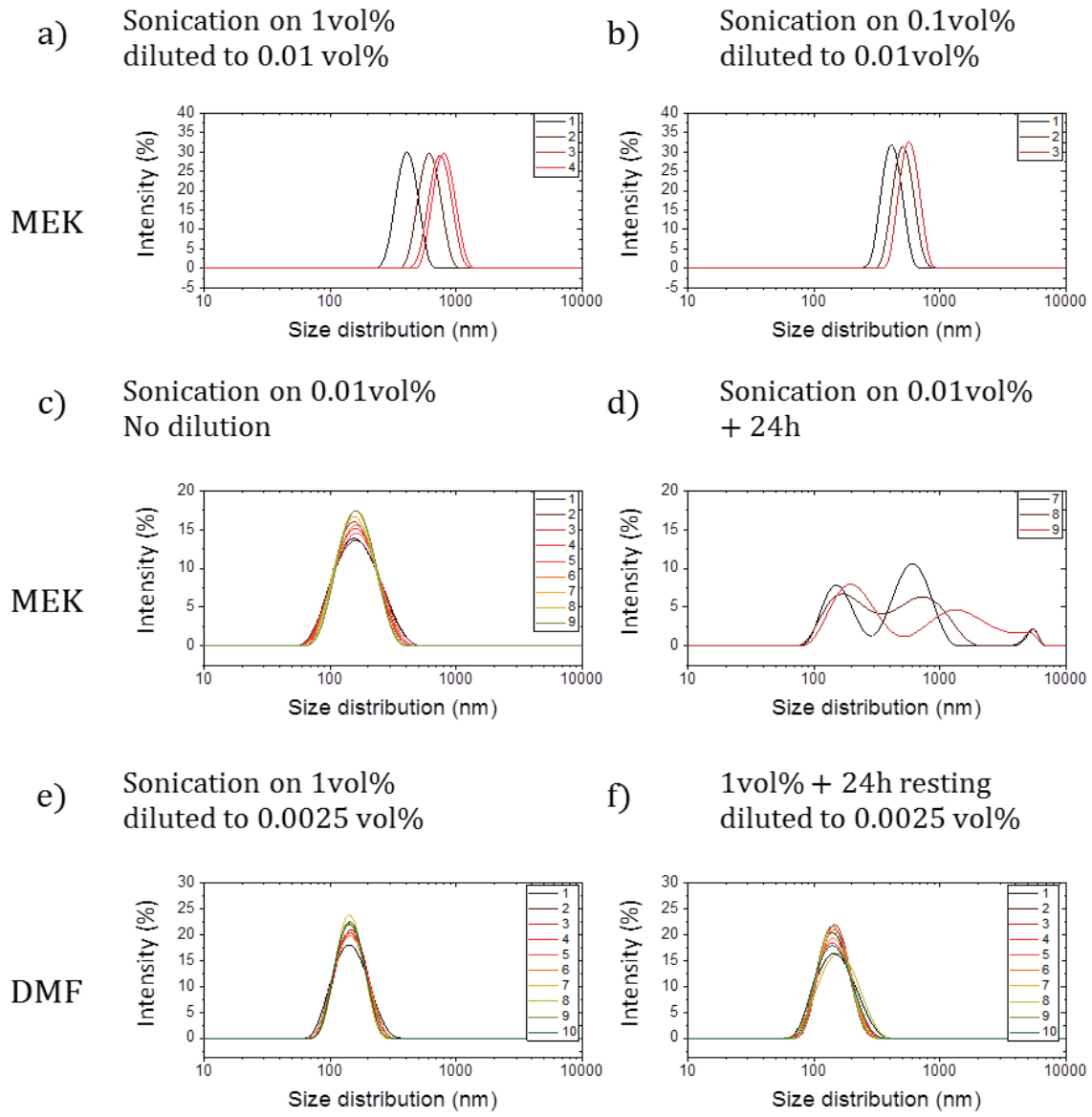

Figure 3.15: Size distribution results of DLS analysis carried out in multiple measurements with about 1 minute between each measurement. The analysed systems are MEK-based suspension sonicated at (a) 1 vol%, (b) 0.1 vol% and (c) 0.01 vol% and diluted at 0.01 vol% if necessary before analysis. (d) corresponds to the sample (c) after 24 hrs resting. (e) and (f) are DMF-based suspensions sonicated at 1 vol% and diluted just before the analysis either (e) directly after the sonication or (f) after 24 hrs of rest.

3.3.4 Link to the process

The prediction of the $BaTiO_3$ NPs stability in various solvents is useful for designing a dispersion process that would allow one to obtain polymer nanocomposites with a good NP dispersion state. In order to validate the Hansen approach from the prediction to the final material structure, three nanocomposites were fabricated at various NP content or using various solvent. All the nanocomposites were fabricated using almost similar processes and casted from polymer solutions at 20 wt% with respect to the total liquid weight (i.e. solvent and polymer). Two nanocomposite films were casted from MEK-based solution at 0.1 vol% and 10 vol% of $BaTiO_3$ NPs (0.34 wt% and 27.3 wt% respectively) with respect to the total nanocomposite volume (weight). A third nanocomposite was fabricated from DMF-based solution at 10 vol% of $BaTiO_3$ NPs. One should note that the initial suspensions prepared for the fabrication of PVdF-HFP nanocomposites at 0.1 and 10 vol% in $BaTiO_3$ NPs have a volume content in NPs of about 0.01 vol% and 1 vol% respectively. This implies that only the suspension in MEK at 1 vol% is supposed to be unstable and to rapidly agglomerate.

A first sonication step of 30 minutes was performed in order to dis-agglomerate the as-received $BaTiO_3$ NPs. Then the NP suspensions were mixed into the appropriate polymer solutions by magnetic stirring. Finally, the films were casted and dried in order to remove the solvent. Given the difference between the boiling points of the two solvents (respectively about 80 and 150 °C for MEK and DMF), the drying processes were not the same: MEK was evaporated at atmospheric pressure whereas DMF was evaporated under primary vacuum, in both cases at RT.

The cross sections of the resulting films were analysed by SEM after freeze fracture into liquid nitrogen. Figure 3.16 shows the difference of dispersion state between the three samples. First, Figure 3.16 a), b) and c) represent the cross sections of the 0.1 vol% PVdF-HFP:$BaTiO_3$ nanocomposite processed in MEK. On these images, few $BaTiO_3$ NPs embedded in the PVdF-HFP appear to be well dispersed. The absence of large agglomerates shows that the 10-minute stability of 0.01 vol% $BaTiO_3$ NP suspension in MEK is enough to provide a nanocomposite film with a good NP dispersion state.

Then, for the 10 vol% nanocomposites processed with MEK, the SEM images represented in Figure 3.16 d), e) and f) clearly show the presence of 1 µm large agglomerates in the cross section of the nanocomposites. The low affinity between MEK and the $BaTiO_3$ NPs leads particle agglomeration and sedimentation to start even before the mixing with the polymer solution. In that case the magnetic stirring used to distribute the NPs from the suspension into the polymer solution does not provide enough shear stress to break the agglomerates that remain in this form throughout the process.

Finally, the SEM images represented in Figure 3.16 g), h) and i), show the very good $BaTiO_3$ NPs dispersion state in the nanocomposite sample filled at 10 vol% and prepared in the DMF. This observation implies that the $BaTiO_3$ NP stability in DMF is sufficient to ensure a good dispersion state during all the process.

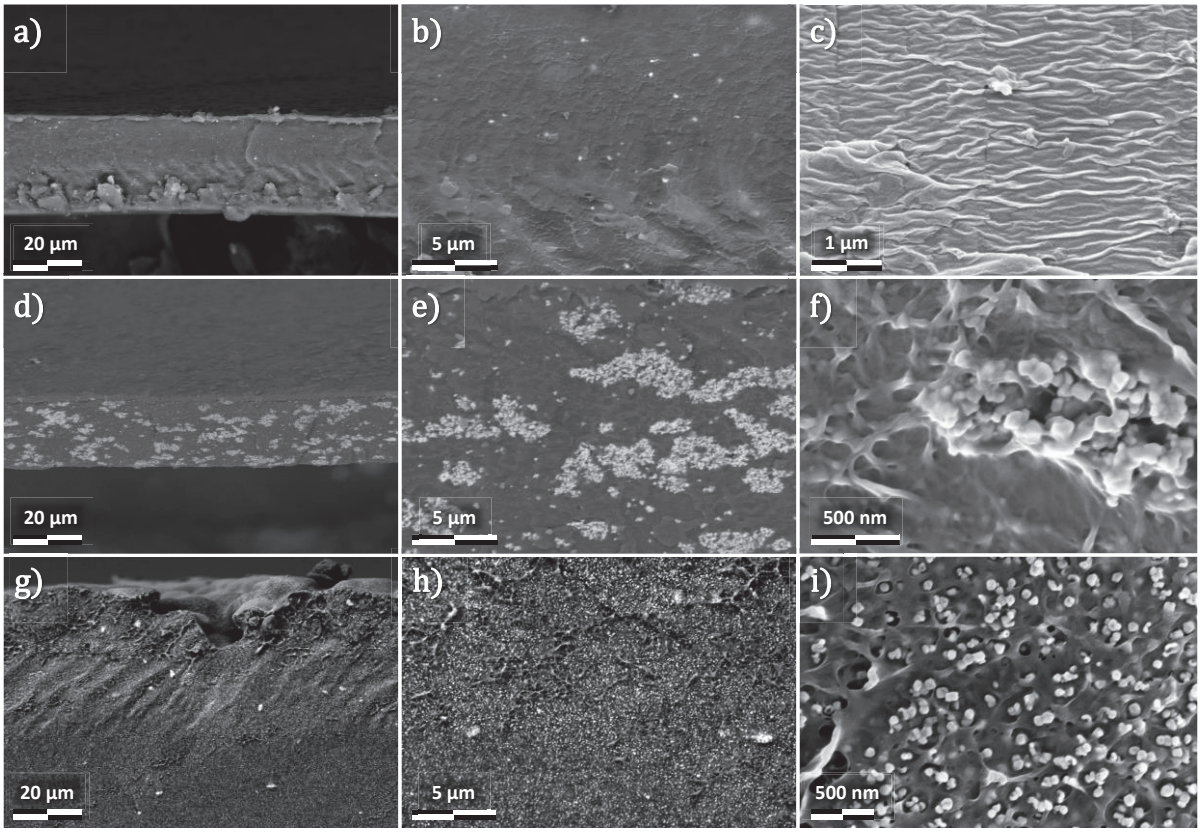

Figure 3.16: SEM images of the three fabricated nanocomposites: a), b) and c) PVdF-HFP at 0.1 vol% of $BaTiO_3$ NPs casted from a stable MEK-based suspension, d), e) and f) PVdF-HFP at 10 vol% of $BaTiO_3$ NPs casted from a non-stable MEK based suspension and g), h) and i) PVdF-HFP at 10 vol% of $BaTiO_3$ NPs casted from a stable DMF based suspension. SEM pictures acquired in chemical contrast at the magnitude of 1 kX (a, d and g) and 5 kX (b, e and h) and in topography contrast at higher magnification (c, f and i).

To conclude, the determination of the HDPs of the $BaTiO_3$ NPs using sedimentation tests has enabled the prediction of the relative suspension stabilities depending on the relative positions of the dispersant and the NPs into the Hansen space. These predictions, relative to the kinetics observed in the sedimentation tests, have been rationalized in terms of stability durations and concentration ranges by performing DLS analysis on some examples. Finally, SEM analysis of nanocomposite films has brought the confirmation of the relationship between intermolecular forces, suspension stability and final dispersion state. The Hansen approach, combined with DLS and SEM analyses, has brought crucial information about the suspension behaviour during the

nanocomposite fabrication process. It constitutes then a precious tool for designing materials with controlled structure and morphology through the selection of the proper solvent.

3.4 Polymer adsorption

3.4.1 Polymer adsorption theory

In the case of a ternary system, the HSPs of the three constituents allow predicting the most energetically favourable configuration, i.e. predicting the adsorption of the polymer onto the surface of the NP. A simple thermodynamic model, inspired by the theory proposed long ago by Silberberg[144] and using the Hansen interaction parameters has been proposed by Laurens et al[137,145]. At the basis of this theory, the energy balance between the adsorbed state and the solvated state of a monomer in a ternary polymer/solvent/particles system is considered. Let us consider one molecule of solvent B adsorbed on a particle surface A which is replaced by a monomer C taken from the bulk polymer as presented in Figure 3.17[128].

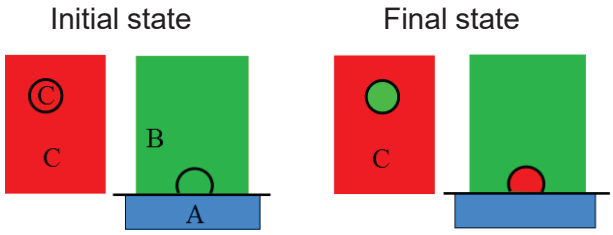

Figure 3.17: Initial and final states consider to estimate the enthalpy balance for adsorption of a monomer

.

At the basis of this theory, the pair interactions between the considered species is assumed to be $U_{XY} \propto -p_X p_Y$. The energy change between the initial and final states can be written as:

$$\Delta W = -z(p_C - p_B)(p_A - p_B) \qquad (3.17)$$

where p_A, p_B and p_C are the polarizabilities of the constituents A, B and C. As noted previously, polarizabilities p_x and Hildebrand parameters $\left|\overrightarrow{\delta_x}\right|$ are related by:

$$p_x \propto \sqrt{v_m}\left|\overrightarrow{\delta_x}\right| \qquad (3.18)$$

A negative value of ΔW indicates a favored adsorption.

In the case of inorganic oxide materials, the surface energy is high since the material is quite strongly polar and prone to form hydrogen bonds. It may thus be assumed that

the p_A parameter is larger than both p_B and p_C (in absolute values). This implies $p_A - p_B > 0$. Then two distinct cases may occur:

- If $p_C - p_B < 0$, $\Delta W < 0$ so the adsorption is favored. This case is illustrated in Figure 3.18
- If $p_C - p_B > 0$, $\Delta W > 0$ so the adsorption is not favored.

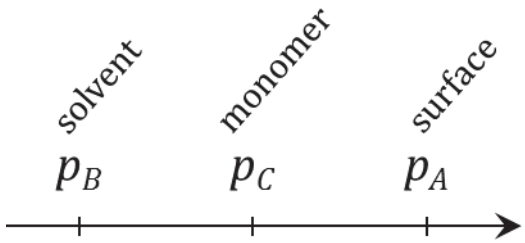

Figure 3.18: Polarizability configuration promoting monomer adsorption.

In the 3D Hansen space, the expression for the adsorption parameter χ_S is generalized as:

$$\chi_S = \frac{v_m}{k_B T}(\vec{\delta}_C - \vec{\delta}_B)(\vec{\delta}_A - \vec{\delta}_B) \quad (3.19)$$

Equation (3.19) shows that the χ_S value is proportional to the scalar product of the vectors solvent-monomer (red vector in Figure 3.19) and solvent-particle (green vector). As a result, higher is this scalar product and of course positive, stronger is the adsorption of the polymer on the particle surface. In other terms:

- The solvent must be a near theta solvent of the polymer (i.e. not too much affinity but enough to solubilize the polymer in order to fabricate nanocomposite films at the end).
- The solvent must have less affinity with the particles than the polymer.

Note that a similar theory has been developed by Faasen et al. considering the difference of Ra between the couples surfactant-particles and solvent-particles[146].

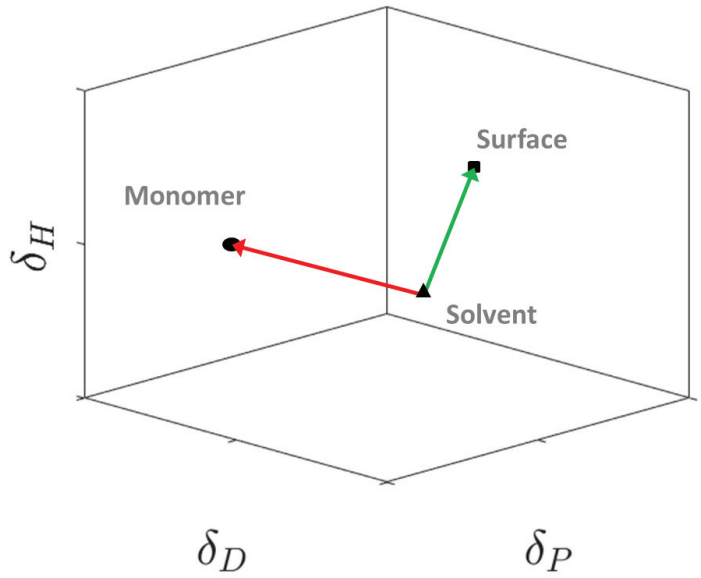

Figure 3.19: Representation of the interactions in the Hansen space for a ternary system.

3.4.2 Adsorption Prediction Examples (MEK, DMF)

Some examples of prediction have been experimentally tested. DMF and MEK were selected because of their particular HSP positions. Indeed, the respective χ_S value associated to the adsorption of the PVdF-HFP onto the surface of the $BaTiO_3$ NPs is -0.2 and 1.9 respectively for in DMF and MEK. The negative χ_S value in the case of DMF would predict the absence of quantitative polymer adsorption whereas the relatively high positive value presented in the case au MEK would suggest a strong polymer adsorption.

The adsorption of the PVdF-HFP on the $BaTiO_3$ NPs in these two solvents was then tested. Considering high molecular weight macromolecules prone to adsorb onto a solid surface, several adsorption sites are expected per polymer chain leading to a very low probability of desorbing the entire polymer chain from the NP surface[130]. In what follows, the adsorption of the PVdF-HFP onto the $BaTiO_3$ NPs surface is hypothesised as irreversible.

After having dis-agglomerated the NPs into the solvent by a 30-minute sonication step, 5 wt% of PVdF-HFP with respect to NP weight was added into the suspension. This corresponds to a 5-time excess considering the adsorption to be of the order of 1 mg/m^2.[147] A short sonication step was used to redistribute the $BaTiO_3$ NPs and allowed the adsorption of the PVdF-HFP to occur onto the NP surface. The ternary system was left under magnetic stirring overnight to reach the equilibrium before being centrifuged and rinsed several times with the same solvent using sonication-centrifugation cycles renewing the solvent each time. The final $BaTiO_3$ NPs powders were then dried under vacuum and analysed by TGA and ATR-FTIR to quantify the adsorption of the polymer.

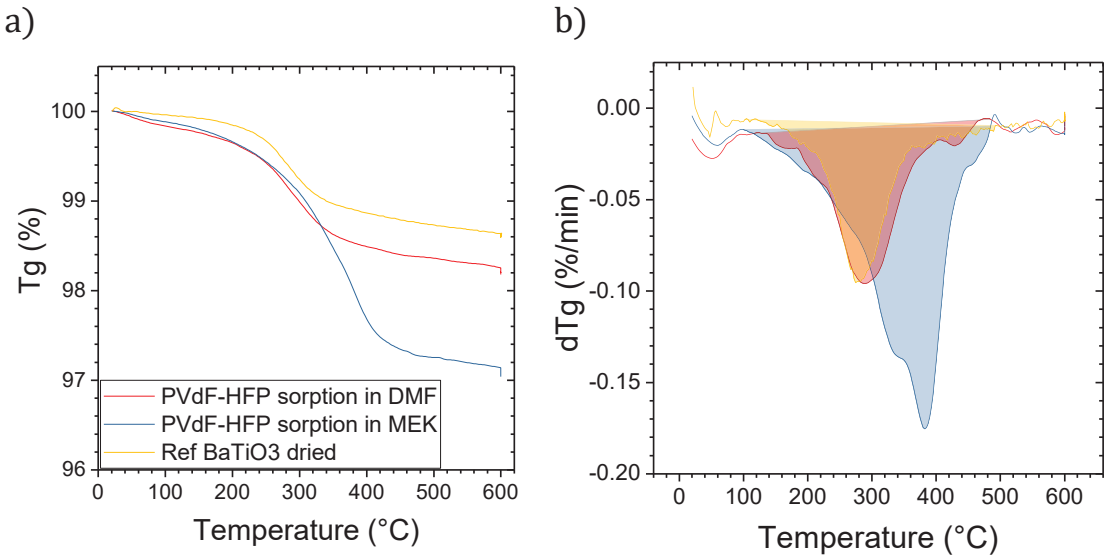

Figure 3.20: TGA analysis of the $BaTiO_3$ NPs put in presence of PVdF-HFP in MEK and DMF. a) the mass ratio Tg (%) and b) the mass loss dTg (%/min) are represented.

Figure 3.20 shows the TGA results of this adsorption test. It is clear that the two NP batches put in the presence of PVdF-HFP in DMF and MEK respectively exhibit different types of behaviour. The use of MEK led to higher weight loss (approximately + 1 wt%) as compared to DMF. The mass loss, presented in Figure 3.20 b), reveals a clear difference between the two solvent cases. Moreover, the $BaTiO_3$ NPs associated with DMF and PVdF-HFP exhibit a clear similarity with the reference neat $BaTiO_3$ NPs. The mass loss differences around 50-100 °C are coming from water desorption due to unequal drying process or water uptake in ambient air before the analysis.

The ATR-FTIR analyses are presented in Figure 3.21. As a result, the adsorption test carried out in MEK leads to the presence of an additional peak around 1200 cm^{-1} as compared to DMF. This peak is considered to be the signal of the adsorbed PVdF-HFP that exhibits, in the neat form, an absorption peak slightly below 1200 cm^{-1}. Note that both NP batches sonicated in the presence of PVdF-HFP and either MEK or DMF present a double peak at 1600-1700 cm^{-1}. This peak has been found on $BaTiO_3$ NPs after being sonicated in various solvent such as MEK, 2-heptanone and DMF. It could correspond to the vibration of double CO bonds that may either come from strongly adsorbed residual solvent or from the formation of carbonyl on the NP surface.

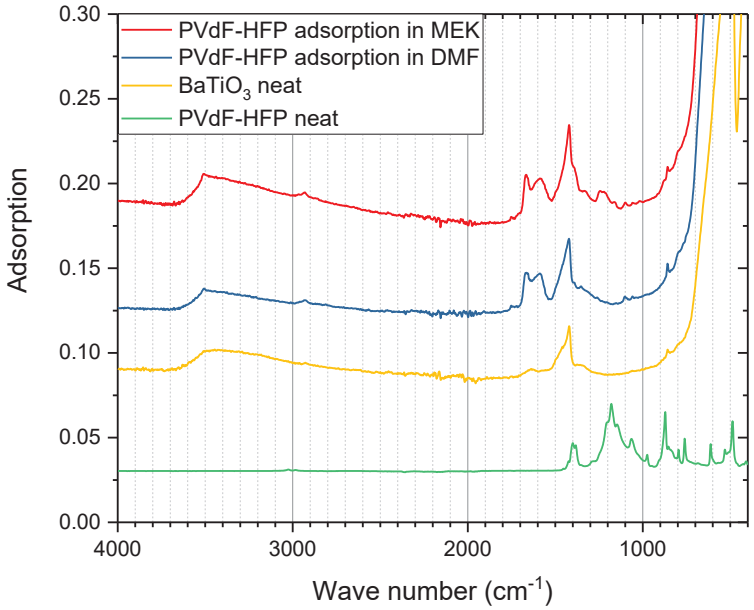

Figure 3.21: ATR-FTIR analysis of the $BaTiO_3$ NPs after the PVdF-HFP adsorption test in MEK and DMF. Both neat $BaTiO_3$ and PVdF-HFP are represented as reference.

Both TGA and ATR-FTIR results tend to indicate that PVdF-HFP adsorbs on the $BaTiO_3$ NP surface only when they are mixed together into MEK and does not adsorb in DMF. The TGA peaks associated to either thermal degradation of the NP surface only or combined with the one of the PVdF-HFP were integrated as illustrated by the coloured area in Figure 3.20. The integration results are presented in

Table 3.8. The adsorbed amount of PVdF-HFP is calculated by subtracting the integrated mass loss of the reference NPs to those of the NPs after the adsorption test. This amounts to assume that all the NP batches have the same fraction of their weight loss related to their surface chemistry (hydroxyl groups) and thus that their surface chemistry is not significantly affected by the adsorption process. It is found that 1.2 wt% of PVdF-HFP has been adsorbed onto the $BaTiO_3$ NPs surface in the presence of MEK. The observed difference in terms of PVdF-HFP adsorption onto the $BaTiO_3$ NP surface between MEK and DMF is consistent with the χ_S value being 1.9 and -0.2 respectively.

Considering the BET surface of the $BaTiO_3$ NPs, being $20 m^2/g$, it corresponds to 0.6 mg of PVdF-HFP per square meter of NP surface.

Table 3.8: Detail of the adsorption results. Percentages are expressed with respect to the total initial mass.

Samples	Integrated mass loss (wt%)	Estimated PVdF-HFP adsorption content (wt%)	Estimated adsorbed amount (mg/m^2)
$BaTiO_3$ NPs after PVdF-HFP adsorption test in MEK	2.2	1.3	0.6
$BaTiO_3$ NPs after PVdF-HFP adsorption test in DMF	1.1	0.2	0.1
$BaTiO_3^{reference}$	0.9	0	0

In this part, the HSP theory, its extension to HDP and the adsorption parameters χ_S have enabled the prediction of the PVdF-HFP adsorption on the surface of the $BaTiO_3$ NPs depending on the solvent HSPs and HDPs. The results obtained in this part are consistent with the conclusions of Laurens et al.[137,145]. In their work, they have shown a clear relationship between the χ_S value and the adsorbed amount of Polystyrene onto silica NPs in various solvents.

From polymer adsorption to NP suspension stabilization

In this paragraph, the role of the PVdF-HFP adsorption on the stability of the $BaTiO_3$ NPs is discussed. Polymer adsorption is known to improve suspension stability. A quick test was performed by monitoring the sedimentation of two $BaTiO_3$ NPs:MEK suspensions after adding 0.2 wt% of PVdF-HFP into one of the suspension and sonicating both suspensions for 5 minutes. The test revealed slower sedimentation kinetics in the presence of PVdF-HFP as compared to bare $BaTiO_3$ NPs:MEK suspension (see in Figure 3.22). Indeed, the sedimentation front of the particles without PVdF-HFP reaches half of the liquid height after 19 minutes whereas about 88 hrs are required to the system with PVdF-HFP to reach the same sedimentation level. At this concentration, the viscosity increase induced by the PVdF-HFP is negligible so the difference of sedimentation kinetics can be assigned to the reduction of the attractive interactions between NPs due to the polymer adsorption already demonstrated.

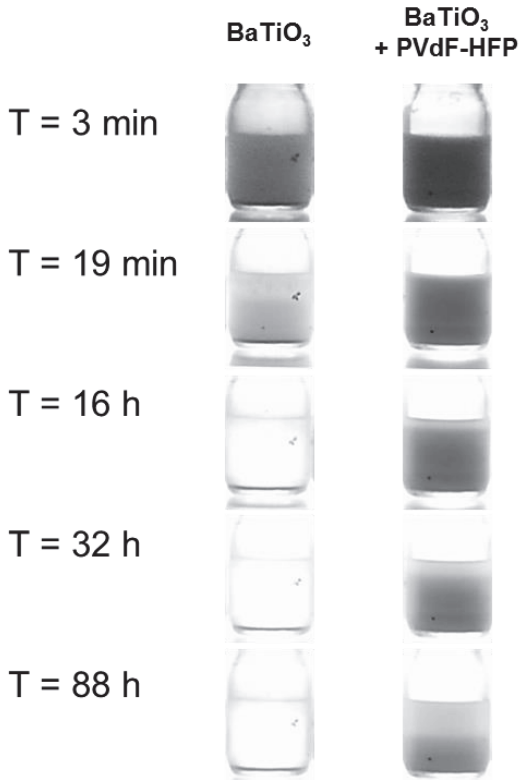

Figure 3.22: Quick sedimentation test with $BaTiO_3$ in MEK – influence of the PVdF-HFP adsorption. ($BaTiO_3$ at 0.1 vol% and PVdF-HFP at 0.2 wt% compared to MEK)

Further experimentations were performed in order to better characterize the effect of the PVdF-HFP adsorption on the stability of the $BaTiO_3$ NP suspension. In order to do so, DLS analyses were conducted on similar ternary systems. The results are presented in

Figure 3.23. A $BaTiO_3$ NP suspension was prepared at 1.2 vol% and sonicated for 1 hr to ensure a good NP dis-agglomeration. A 20 wt% PVdF-HFP solution in MEK was then added in the proportion 1:1 in volume and an additional sonication step was performed in order to redistribute the NPs into the polymer solution. The final ternary system is then composed of about 10 wt% of PVdF-HFP and 0.6 vol% of $BaTiO_3$ NPs as compared to MEK weight and volume respectively. After 20 minutes, the sonication was stopped and a first sample was taken from the suspension and directly diluted by 100 to be analyzed by DLS. The diluted suspension sample is then composed of 0.006 vol% of $BaTiO_3$ NPs covered with adsorbed PVdF-HFP and about 0.1wt% of non-adsorbed PVdF-HFP. The first result presented in

Figure 3.23 a) shows the evolution of the size distribution in intensity obtained by carrying out 10 measurements within 10 minutes. It clearly shows that the size distributions obtained within 10 minutes are centered around 100-200 nm. This indicates that the $BaTiO_3$ NPs have not agglomerated before the dilution of the sample

which suggests a good stability of the NPs in at 0.6 vol% with respect to the MEK in the presence of PVdF-HFP. After 2 hrs without stirring, the sample was homogenized manually and 3 additional measurements were performed. The results of this analysis are presented in

Figure 3.23 b). It shows equivalent size distributions and no large agglomerates were detected. This proves the stability of the $BaTiO_3$ NP suspension at 0.006 vol% upon at least 2 hrs.

2 hrs after the sonication was stopped, the concentrated solution was first manually homogenized and a second sample was taken, diluted by 100 and analyzed by DLS. The results, presented in

Figure 3.23 c) clearly show the same size distribution as the previous sample, indicating the very good stability of the concentrated MEK-based suspension. As a result, the PVdF-HFP adsorption significantly improves the stability of the $BaTiO_3$ NPs in the MEK, being stable at the concentration of 0.6 vol% for at least 2 hrs. A later use of this suspension has revealed a nice dispersion state after 1 month of rest.

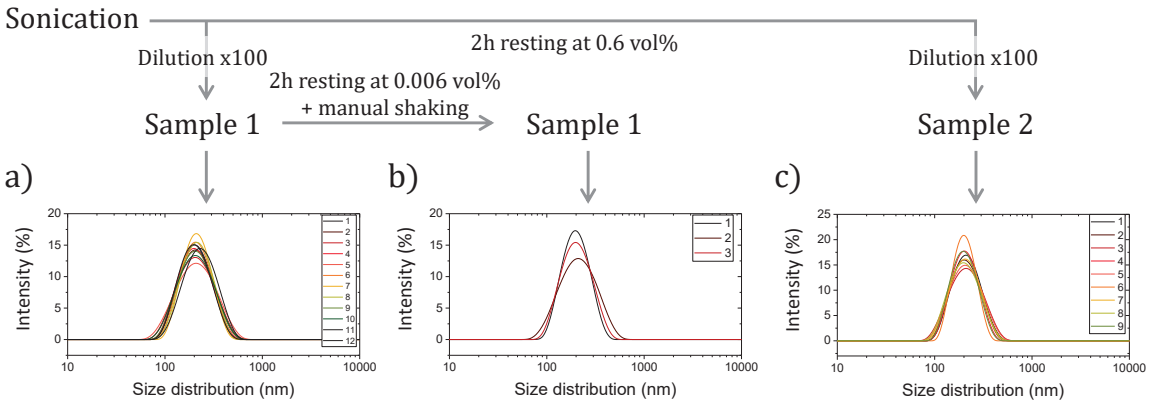

Figure 3.23: DLS results on $BaTiO_3$ suspension in MEK with PVdF-HFP adsorbed on the surface.

The adsorption of the PVdF-HFP onto the $BaTiO_3$ NPs in MEK stabilized the suspension. The $BaTiO_3$ NPs having agglomerated after the end of the first sonication step and before the polymer addition due to low affinity with the solvent are bounded together with a given strength. The application of high shear stresses on the solution with the second sonication step allowed breaking these bonds and redistributing the freshly stabilized NPs in the solution thus creating a stable suspension. DLS analyses have shown the ability of the sonication step to fully break the agglomerates by providing high shear stresses to the suspension.

3.4.3 Link to process development

The adsorption of the PVdF-HFP onto the $BaTiO_3$ NPs presented in this part has shown to efficiently stabilize the NP suspension after the NP redistribution which is enabled by breaking the agglomerates with a high shear mixing. In order to explore the possibilities of this redistribution step, PVdF-HFP:$BaTiO_3$ nanocomposites were fabricated using the MEK as solvent and several redistribution methods were used. After the dis-agglomeration of the $BaTiO_3$ NPs which tend to agglomerate rapidly in the MEK, the suspension was mixed to a PVdF-HFP solution. Then, progressive shear stresses were applied to the solution. First, low shear stresses were applied for 30 min using a magnetic stirrer rotating at 200 rpm in order to homogenize the solution. At this stage, the PVdF-HFP is expected to adsorb onto the agglomerated NPs. Then, higher shear stresses were applied by:

- Increasing the rotation speed of the magnetic stirrer to 500 rpm for 10 minutes more.
- Performing a 1 minutes mixing step using an Ultraturax with a rotation speed of 10 000 rpm
- And finally applying several sonication steps.

After each application of shear stresses, nanocomposite films were fabricated from the solution and analyzed by SEM. The results are presented in Figure 3.24.

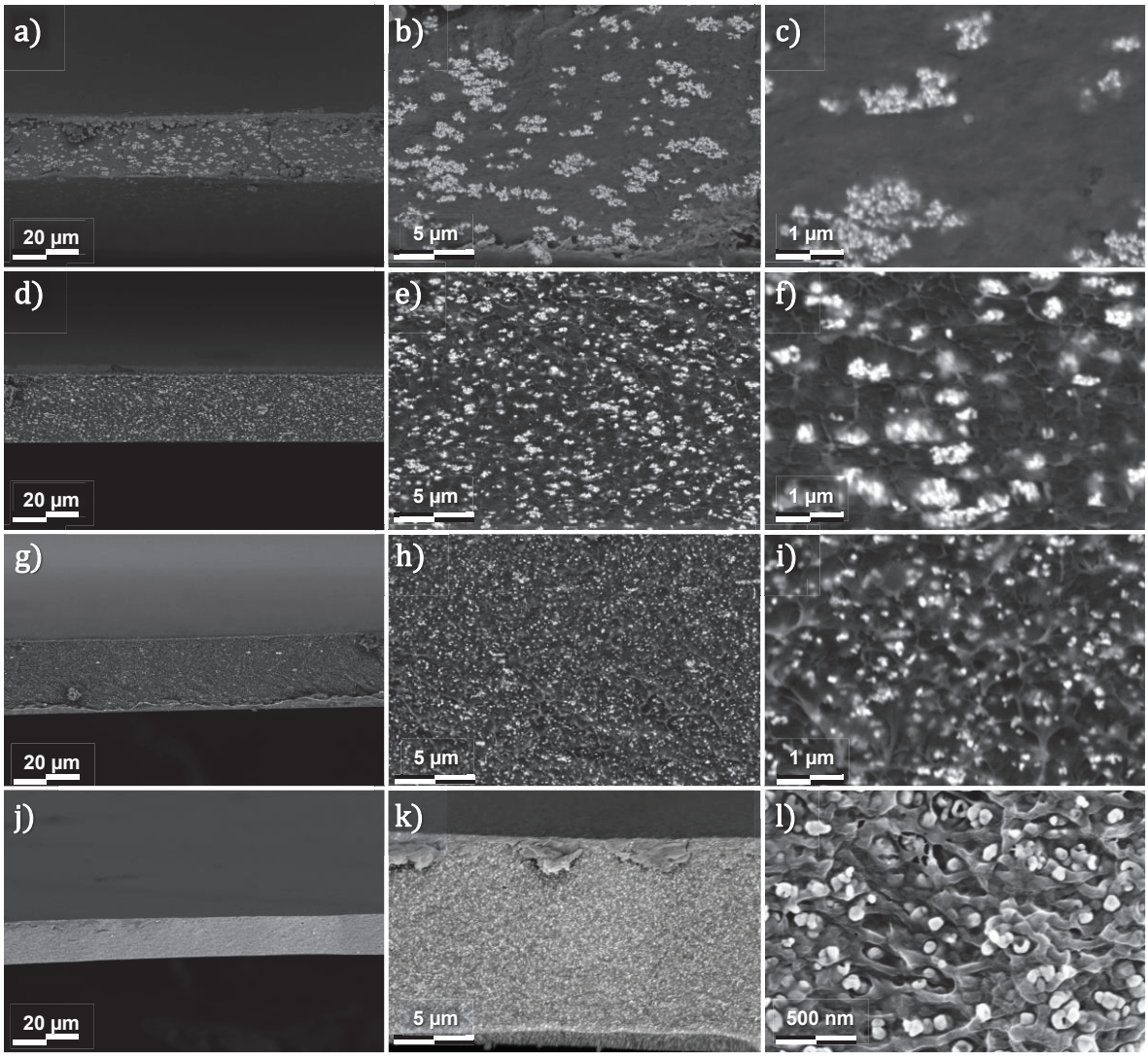

Figure 3.24: SEM images at three magnifications of a PVdF-HFP:$BaTiO_3$ nanocomposites fabricated after redistribution of the $BaTiO_3$ NPs stabilize by PVdF-HFP adsorption with a) b) and c) a magnetic stirring at 200 rpm, d) e) and f) a magnetic stirring at 500 rpm, g), h), and i) an Ultraturax with a rotation speed of 10 000 rpm and J), k), and l) a 5 minute sonication step. The observations are performed on cross-sections prepared by cold breaking.

Figure 3.24 a), b) and c) show the presence of large NP agglomerates in the polymer matrix. This is the consequence of the very low shear stresses applied by the magnetic stirring at 200 rpm. The increase of the stirring rotation speed to 500 rpm leads to smaller agglomerates as compared to 200 rpm (see Figure 3.24 d, e and f). The increase of the shear stresses applied to the solution breaks more efficiently the agglomerates. By applying further increased shear stresses by using the Ultraturax with a rotation speed of 10 000 rpm, the resulting agglomerates size was decreased in such a way that most of the NPs were well dispersed and only some agglomerates of few NPs were still present, as shown in Figure 3.24 i). Finally, the nanocomposite casted after performing a 5-minute sonication step exhibits well dispersed NPs as shown in Figure 3.24 j), k)

and l). The high magnification picture Figure 3.24 l) shows that the NPs are well separated and only some NPs are touching each other. In these cases, it is likely that the first sonication step aiming in dis-agglomerating the NPs was not sufficient

These results confirm the stabilization of the $BaTiO_3$ NPs observed by DLS and attributed to PVdF-HFP adsorption. Moreover, it shows that this stabilization remains during the entire process including the solvent evaporation. Indeed, very good NP dispersion states were obtained after applying enough shear stresses to redistribute the NPs. The intermediate dispersion states observed for 500 rpm magnetic stirring and Ultraturax mixing suggest that the interaction forces between the NPs within the agglomerates have to be overcome to break the assembly and to separate the NPs. As a consequence, the dispersion can be tuned by choosing the strength of the shear stresses applied after the adsorption of the PVdF-HFP on the $BaTiO_3$ NPs. Indeed, this result is consistent with the fact that the higher is the applied shear stress, the smaller is the scale at which the agglomerates can be broken[148].

As seen before with both the solubility of the PVdF-HFP and the very good stability of the $BaTiO_3$ NPs into the DMF, the Hansen theory can provide predictions that may be useful in the design of the fabrication processes of polymer nanocomposites. Here again, the adsorption of a polymer on the surface of NPs can be predicted using the Hansen approach and the adsorption parameter χ_S. As presented in the last paragraphs, the adsorption may be used to provide stability to a given suspension and so to improve a dispersion process.

3.5 Conclusion - process optimization and design

In this chapter, the Hansen theory was first presented as a tool predicting molecular interactions between polymer and solvent. In the design of a solvent-casting process, polymer solubility and phase separation does not constitute the only technical challenge that may be encountered. Nevertheless, the HSP theory allows a first level of prediction about polymer solubility and can be used as a designing tool. It can be used to select potential solvents to design the fabrication process of a new material as well as to replace a toxic solvent in an existing process by a less harmful one. In this work, several solvents were identified as potential solvents for the fabrication process of PVdF-HFP films.

The extension of the Hansen theory to the stability of NP suspensions was then addressed and similar conclusions were reached. The determination of the HDPs of the $BaTiO_3$ NPs allows selecting a proper solvent to ensure the good stability of the suspension. Combined with the first HSP approach, a multi-criteria solvent selection was conducted to promote both good polymer film quality and good suspension

stability. As a result, PVdF-HFP-based nanocomposites were fabricated with a good $BaTiO_3$ NPs dispersion state, i.e. without NP agglomerates.

Finally, the introduction of the adsorption parameter provided another lever in the selection of solvents potentially producing stable NP suspensions by promoting the polymer adsorption. In the case of MEK, the adsorption of the PVdF-HFP has allowed the control of the dispersion by tuning the level of the shear stresses applied to the solution. Finally, very well dispersed NPs were obtained in nanocomposites by performing a high shearing sonication step after polymer addition.

As summarized in Figure 3.25, two routes have been found to fabricate polymer-based nanocomposites with good NP dispersion state by solvent casting: (1) the selection of a solvent with good affinity with both the polymer and the NPs and (2) the selection of a solvent with special affinities with the polymer and the NPs in order to promote the adsorption of the polymer onto the NPs. The second route allows controlling the dispersion state with the shear stress intensity which is applied to the solution after polymer adsorption.

However, the complete dis-agglomeration of the NPs must be achieved at first to enable the use of the above approaches (see Appendix A). Moreover, the Hansen theory and its extension for NP suspensions are based on numerous approximations and must thus be considered as a screening tool more than as a quantitative approach.

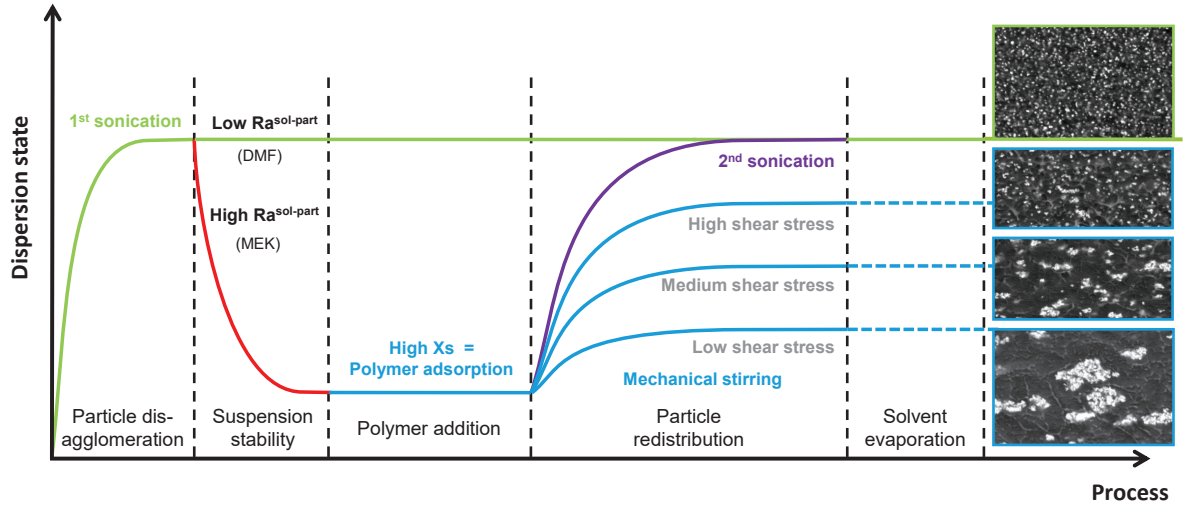

Figure 3.25: Schematized NP dispersion state along the nanocomposite fabrication process by solvent casting. Various routes to design the final NP dispersion state in the nanocomposite are presented.

Chapter 4. Dispersion State and Dielectric Properties.

As described in the State-of-the-art chapter, the dispersion state in polymer-based composites has an important impact on the final dielectric properties. Since the dispersion state of the nanoparticles (NPs) is almost systematically changed after performing surface modifications, the exact effect of the dispersion state on the dielectric properties cannot be easily discriminated from the effect of the interfacial properties.

In this chapter, the innovative way to control the dispersion state presented in the previous chapter is applied in order to produce two series of materials with distinct dispersion states. The dielectric properties of these materials are investigated by broadband dielectric spectroscopy. It is essential to verify that the $BaTiO_3$ NPs do not change the matrix, so that changes in dielectric properties can be attributed to the NPs only.

4.1 Nanocomposite film fabrication with controlled dispersion state

4.1.1 Dispersion protocols

To produce two series of PVdF-HFP:$BaTiO_3$ nanocomposite films with different dispersion states, a protocol based on the NPs stabilization by adsorption of the polymer was used, as presented in chapter 3. A first sonication step of 1 hr was performed on the $BaTiO_3$ NPs in suspension in MEK resulting in the complete NP dis-agglomeration. Since MEK is not a very good dispersant for the $BaTiO_3$ NPs, the obtained suspension is not stable and the NPs tend to re-agglomerate and sediment rapidly. Then, PVdF-HFP solution is added into the suspension. The use of mechanical stirring with a magnetic stirrer produces a macroscopic homogenization of the solution that becomes turbid and white. Nevertheless, as explained in chapter 3, the shear stress applied in the system by the magnetic stirrer is too low to redistribute perfectly all the NPs into the PVdF-HFP solution. The NPs are spread into the polymer solution in the form of agglomerates with low interaction between them. At this point, the solution was divided into two parts which are submitted to two different protocols:

(A) – In protocol A, for the preparation of *Agglomerated NPs*: the composite solution is casted after 2 hrs of mechanical stirring provided by the magnetic stirrer. In this case, the NPs are expected to be in the form of agglomerates into the polymer solution.

(S) – In protocol S, for the preparation of *Sonicated NPs:* the composite solution is exposed to an additional sonication step. This step, shorter than the initial one, aims at redistributing the NPs into the polymer solution.

As seen in the previous chapter, the NPs are stabilized by the adsorption of the PVdF-HFP in both cases. Then, no fast sedimentation of the NPs or the agglomerates is expected.

Prior to be casted, both solutions are again divided in two parts. One is used for the fabrication of nanocomposites at 10 vol% in NPs referred to the total volume of nanocomposite (PVdF-HFP + $BaTiO_3$ NPs), denoted A10 and S10 with agglomerated and well dispersed (Sonicated) NPs, respectively. The other one is diluted with a neat PVdF-HFP solution in MEK in order to produce a composite solution with 5 vol% of NPs. The same procedure is used to produce nanocomposite films A5, S5, A2.5, S2.5, A1, and S1, at 5, 2.5 and finally 1 vol%. A pure PVdF-HFP solution is used to fabricate neat unfilled PVdF-HFP films that are used as reference. All the film samples are casted with a Doctor Blade with a targeted final thickness of 20-30 μm. Then, the fabricated films are dried at 80 °C for 60 hrs under primary vacuum to ensure the removal of MEK. Further details about the fabrication process are presented in section 2.2.

4.1.2 Samples presentation

The fabricated samples are presented in

Table 4.1. The neat PVdF-HFP films are transparent and colourless. A slight transparency with an orange colour is observed on the nanocomposite samples of the series S whereas a white opaque aspect was found on the nanocomposite samples of the series A. This difference indicates a better dispersion state of the NPs in series S. Indeed, the scattering of visible light is very low in the case of well dispersed NPs. In that case the white light penetrates the sample and a part of the light is absorbed. The orange colour may come from the absorption of the visible light near the violet part of the spectra which would be consistent with the theoretical band gap of $BaTiO_3$ NPs (3.7 eV) which correspond to a light wavelength about 335 nm. Conversely, the formation of NP agglomerates with typical sizes larger than the visible light wavelength increases the light scattering, making the films turbid.

Table 4.1: Details of the fabricated sample of PVdF-HFP and PVdF-HFP:$BaTiO_3$ nanocomposites

Sample name	Theoretical $BaTiO_3$ content (vol%)	Dispersion state
PVdF-HFP neat	0	-
A1	1	Agglomerated NPs
A2.5	2.5	
A5	5	
A10	10	
S1	1	Well dispersed NPs
S2.5	2.5	
S5	5	
S10	10	

4.2 Characterization of the nanocomposite films

4.2.1 Nanocomposite morphology and NP dispersion state

This section is dedicated to the morphological characterization of the neat PVdF-HFP and nanocomposite films. The thickness of the films was first controlled using a micrometre as described in section 2.3.9. All the fabricated films were found to be about 20-25 μm thick. Then, the samples were characterized by optical microscopy in order to ensure the absence of big agglomerates (>5 μm) or air bubbles in the film samples. No particular heterogeneity was found by optical microscopy in all the samples. The observations of the sample morphologies and dispersion states at a smaller scale were carried out by SEM. For each sample, two pieces were cut in different zones of the film to assess the reproducibility of the observations. These sample pieces were then cryofractured, i.e. immersed into liquid nitrogen and broken in order to produce brittle breaks and so flat cross-section profiles. This allows assessing the dispersion state in the volume of the materials. All the nanocomposite films lead to reproducible observations in both pieces of a given sample. The obtained Scanning Electron Microscopy (SEM) images are presented in Figure 4.1.

In Figure 4.1 a), b), c) and d), that correspond to samples prepared with protocol A, the SEM images show distinct agglomerates (in white) in the PVdF-HFP matrix (in dark). Their typical diameter reaches about 1-2 micrometres. In Figure 4.1 e), f), g) and h), that correspond to samples prepared with protocol S, the SEM pictures show both the good dispersion and distribution of the agglomerates. In both cases A and S, it can be noted that the number of the agglomerates or NPs visible on the images seems to decrease with decreasing the $BaTiO_3$ NPs content.

In order to better quantify the dispersion state of the $BaTiO_3$ NPs in the nanocomposite samples, image analysis was carried out on the SEM images using the software ImageJ®. The image analysis protocol has been presented in chapter 2.

Figure 4.2 presents the volume average distribution of the equivalent diameter of the particles/agglomerates in the nanocomposite samples. A clear difference is found between the samples depending on the used fabrication protocol (A or S). Indeed, the samples of series S exhibit mean equivalent diameters around 100 nm whereas the samples of the series A exhibit mean equivalent diameters of 400-800 nm. This result indicates that the distributions of particle/agglomerate size and so the dispersion states in the nanocomposite samples do not depend on the particle content but only on the used protocol.

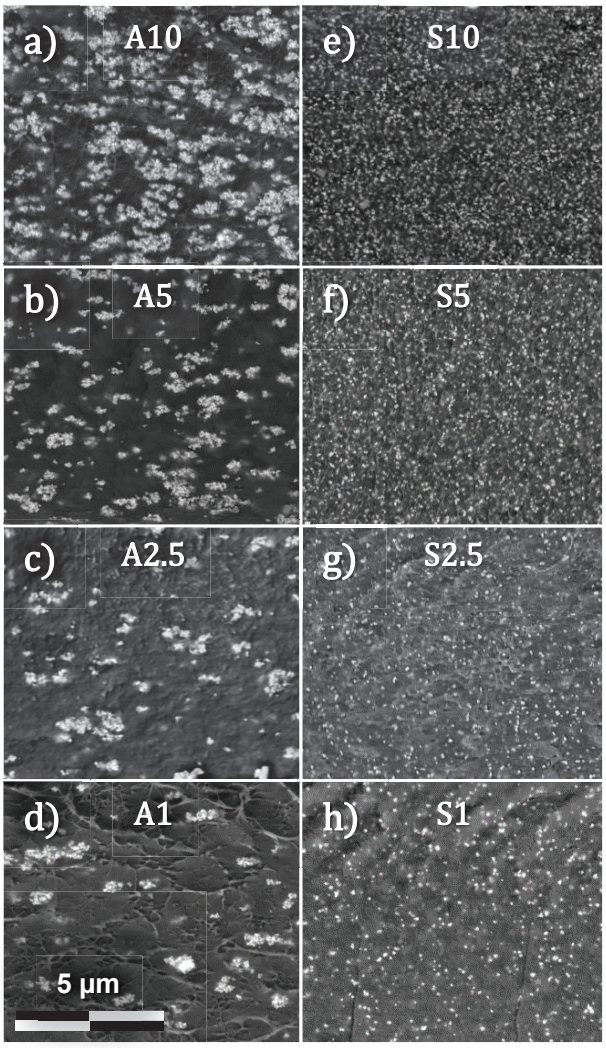

Figure 4.1: SEM images of the sample cross section obtained by cryofracture at magnification of 5 k for a) A10, b) A5, c) A2.5, d) A1, e) S10, f) S5, g) S2.5, and f) S1. The bright zones correspond to the NPs and the dark zones to the polymer. The name of each sample is written on the corresponding picture.

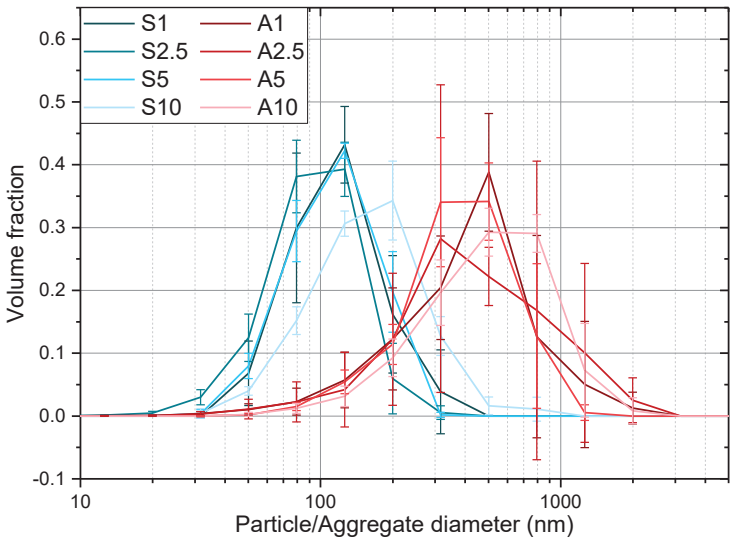

Figure 4.2: Equivalent diameter distribution for both agglomerated (A1 to A10) and well dispersed (S1 to S10) PVdF-HFP:$BaTiO_3$ nanocomposites.

4.2.2 Influence of the $BaTiO_3$ NPs on crystallinity

The impact of the NPs on the crystallinity of PVdF-HFP was studied by DSC. The resulting thermograms are presented in Figure 4.3 and the associated crystalline fractions obtained by integration of the peaks are reported in Table 4.2.

First, all DSC thermograms exhibit the 3 endothermic peaks at 49, 80 and 133 °C described in the section 2.3.5. The first two peaks at 80 and 49 °C would correspond to the melting of a secondary crystalline phase formed during thermal annealing at 80 °C (drying step) and at RT (during the storage), respectively. The last peak at 133 °C corresponds to the melting of the primary crystalline phase.

Secondly, Figure 4.3 b) shows that the thermograms of all nanocomposites exhibit the same shape as compared to neat PVdF-HFP, which suggests that the $BaTiO_3$ NPs have no significant impact on the crystalline structure. Moreover, the integration of the melting peaks indicates a similar crystalline fraction in all the samples.

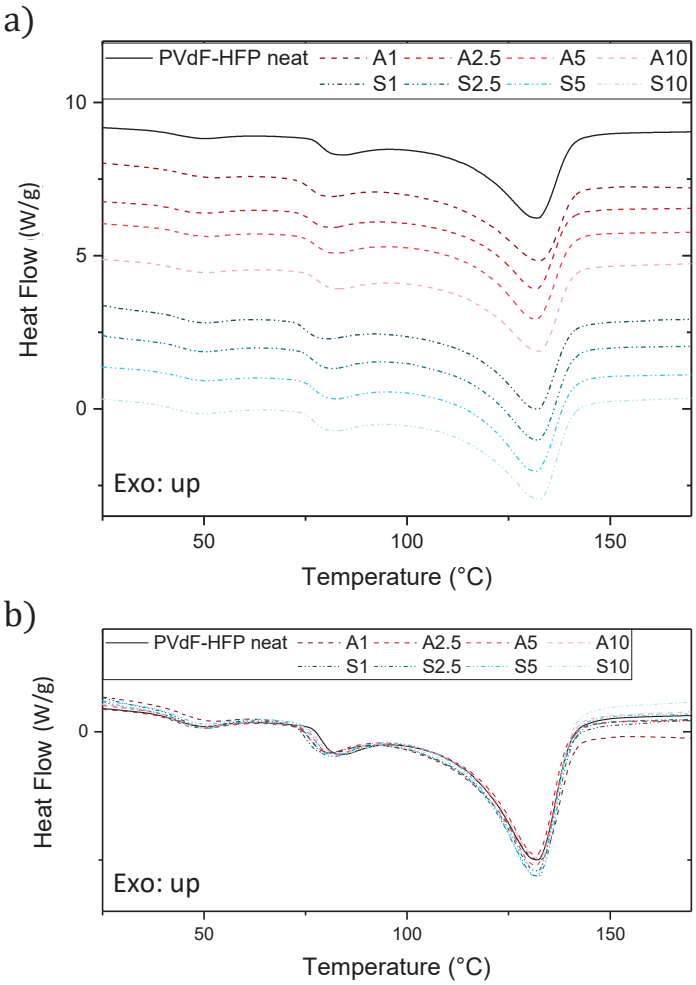

Figure 4.3: First ramp of the DSC thermograms of neat PVdF-HFP (full line) and of the nanocomposite samples having well dispersed (dotted lines) and agglomerated (dash lines) NPs. a) expanded and b) overlapped view. (Heat flow in W per gram of polymer.)

Table 4.2: Crystallinity of neat PVdF-HFP and nanocomposite samples determined by DSC. (Calculated with the theoretical melting enthalpy of 100% crystalline PVdF homopolymer, $\Delta H_m^0 = 104.7\ J.g^{-1}$)

Sample name	Crystalline fraction (wt%)
PVdF-HFP	38 ± 1 %
A1	36 ± 1 %
A2.5	39 ± 1 %
A5	38 ± 1 %
A10	40 ± 1 %
S1	39 ± 1 %
S2.5	38 ± 1 %
S5	38 ± 1 %
S10	40 ± 1 %

4.2.3 Impact of $BaTiO_3$ NPs on crystalline structure

In order to check whether $BaTiO_3$ NPs impact the nature of the crystalline phase present in the material, ATR-FTIR characterizations were carried out and the characteristic IR absorption signature of the PVdF-HFP film and the nanocomposite samples were analysed. As presented in Figure 4.4 a), similar signatures of the PVdF-HFP crystal lattice vibration are observed in neat polymer and in nanocomposites. The IR spectra exhibit the typical bands of the α phase at 763 and 614 cm^{-1}, whereas the typical bands of the β and γ phases, respectively located at 1275 and 1234 cm^{-1}, are not present or are very tiny. According to Cai et al., these results suggest that the PVdF-HFP is in the form of the α phase in all the samples[149]. Figure 4.4 b) shows the FTIR spectra of all nanocomposites and neat PVdF-HFP superimposed to the IR spectrum of the neat $BaTiO_3$ NPs. One can see that the major variation between the samples is found between 500 and 600 cm^{-1} and is due to the IR footprint of the $BaTiO_3$ NPs. As expected, the contribution to the nanocomposite IR spectra in this region as compared to neat PVdF-HFP increases as the NP content increases.

Therefore, by combining the results obtained by FTIR and by DSC, it can be concluded that the presence of $BaTiO_3$ NPs neither significantly affects the crystalline structure nor the crystallinity of the PVdF-HFP matrix.

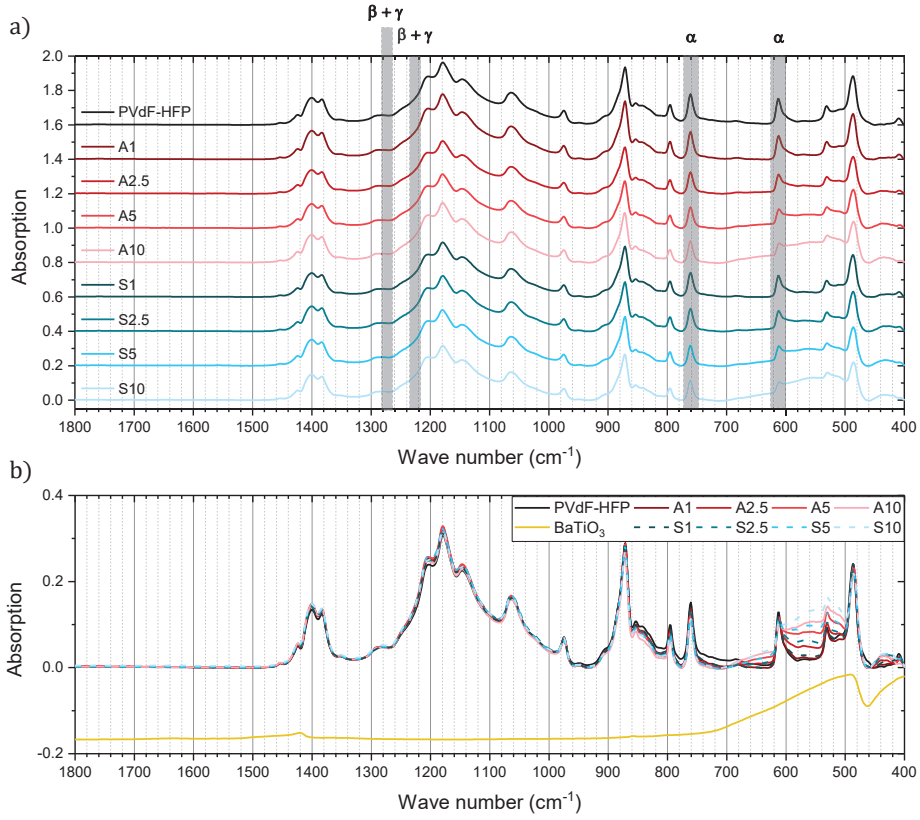

Figure 4.4: FTIR spectra of the neat PVdF-HFP and the nanocomposite samples of the series A and S a) reported and compared to typical IR absorption bands of the polymorph α, β, and γ[149] and b) superposed and compared to the $BaTiO_3$ NPs spectrum measured on powder.

4.3 Dielectric properties

The dielectric properties of the neat PVdF-HFP and the nanocomposite films were investigated by performing dielectric spectroscopy in large temperature and frequency ranges using standard Broadband Dielectric Spectroscopy (BDS – 10^{-2} - 10^{7} Hz) and High Frequency Dielectric Spectroscopy (HFDS – 10^{6}-10^{9} Hz) following the procedures described in sections 2.3.10 and 2.3.11. In the case of standard BDS, the samples were conditioned at 23 °C and RH50 before the analysis and analysed in a closed sample cell. Dielectric spectroscopies were also performed on dry samples to evaluate the effect of humidity. For HFDS, the samples were conditioned in the ambient conditions of the lab (T~20-25°C and RH40-60) before being analysed in an open sample cell.

4.3.1 Dielectric spectroscopy of neat PVdF-HFP film

The dielectric spectra of neat PVdF-HFP obtained from -40 °C to 60 °C by BDS are presented in Figure 4.5 a) and b). Figure 4.5 clearly shows the evolutions of several relaxation processes with frequency and temperature. Each relaxation process is characterized by an increasing step Δε on ε'(ω) (from high frequency to low frequency) and a relaxation peak on ε"(ω), as seen in section 1.2.1. All relaxation processes shift towards higher frequencies when temperature increases, which is consistent with thermally activated processes. As a result, ε'(ω) increases with increasing the temperature on the whole frequency range studied. The high ε"(ω) values observed at high temperatures and low frequencies correspond to the DC conductivity σ_{DC} and does not affect ε'(ω). It is characterized by $\sigma_{DC}/i\omega$ behaviour in ε"(ω) that is a -1 slope in the log-log plot in case of Ohmic conductivity.

The dielectric spectra of ε"(ω) obtained by HFDS are presented in Figure 4.6. The values of ε"(ω) lower than 0.01 obtained at high frequencies (i.e. above the limit schematized by the dash lines in Figure 4.6) are due to artefacts coming from the measurement set up and from the deviation of the sample capacitance with respect to the optimal capacitance of the measurements.

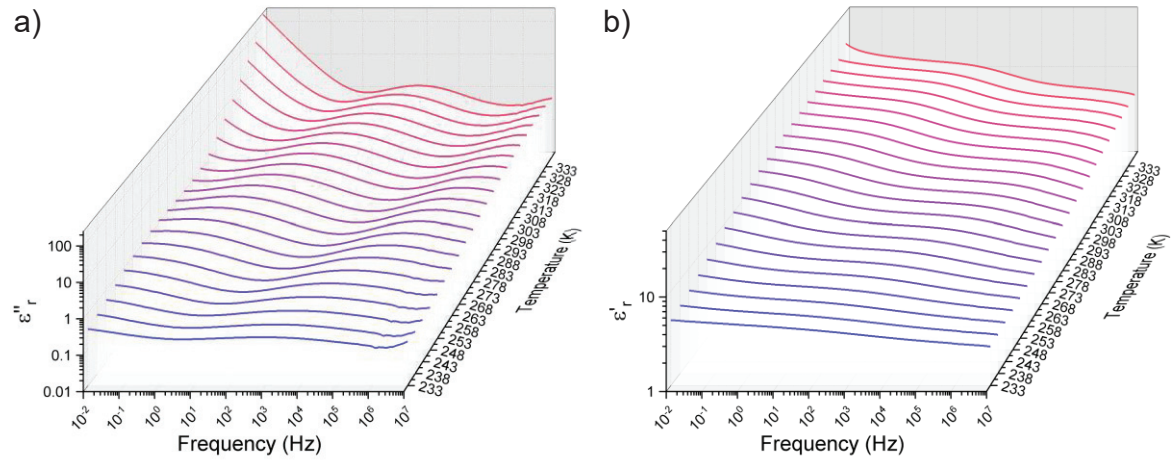

Figure 4.5: a) ε''_r and b) ε'_r as a function of frequency plotted for neat PVdF-HFP from -40 °C and 60 °C by BDS.

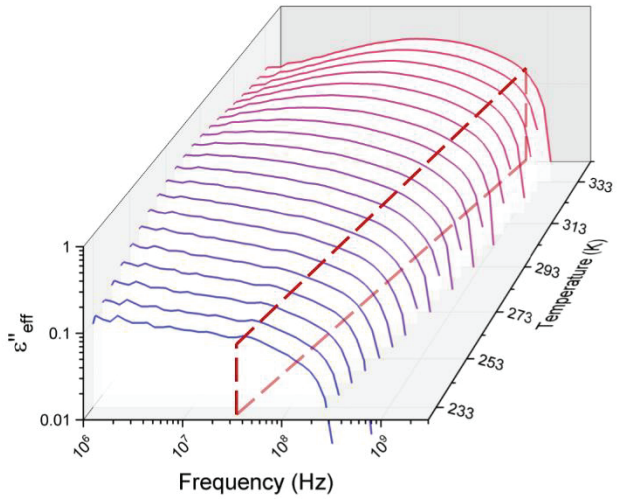

Figure 4.6: ε''_r as a function of frequency for neat PVdF-HFP at high frequency from -40 °C and 60 °C by HFDS. The red dash lines correspond to the limit above which the results are not relevant anymore.

Some examples of dielectric spectra plotted with both BDS and HFDS results are presented in Figure 4.7. The dielectric results obtained by HFDS were corrected by a factor 1.4 in order to get rid of the impact of air layers between all the stacks on the measured complex permittivity as mentioned in section 2.3.11. One can observe that the ε"(ω) spectra obtained by BDS and HFDS superpose quite well on the common frequency range 10^6-10^7 Hz and give a relevant behaviour of the full dielectric spectra.

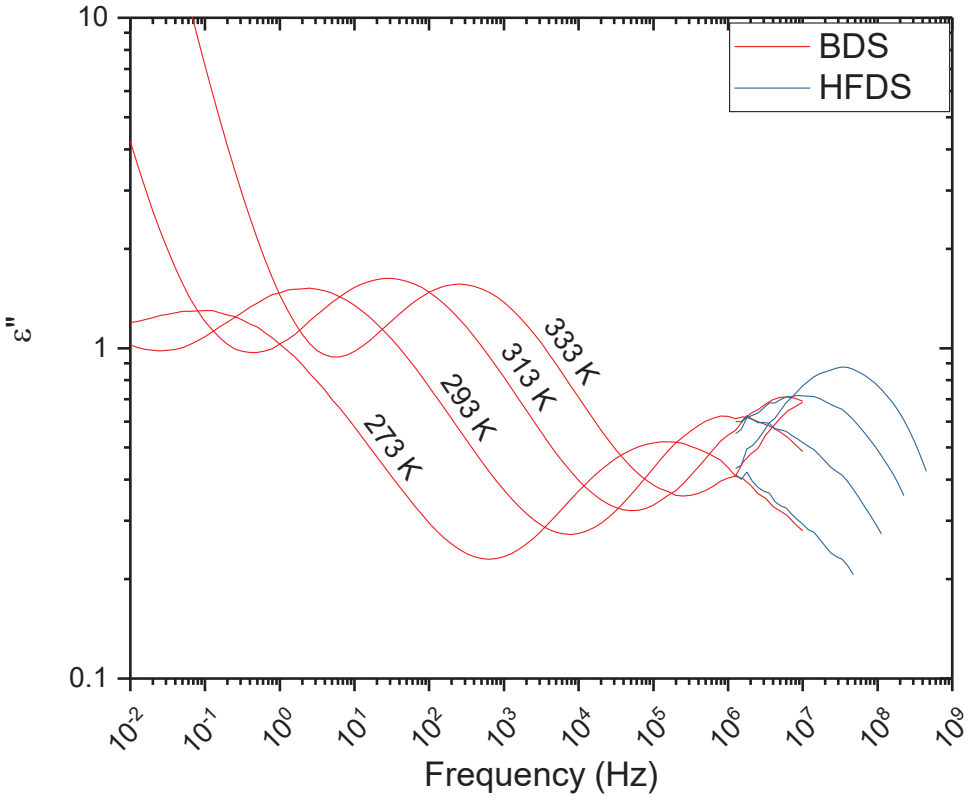

Figure 4.7: Examples of dielectric spectra including results from both BDS and HFDS at 273, 293, 313, and 333 K.

A more quantitative analysis was conducted by fitting the various polarization mechanisms present in the dielectric spectra. Both the real and the imaginary parts of the complex permittivity were fitted as a function of frequency with the Cole-Cole equation (cf. section 2.3.10) for each temperature.

First, the polarization mechanism related to the α_a relaxation is found at low temperature (from 10^3 to 10^7 Hz) in the BDS results and high temperature in the HFDS results. This relaxation is associated with the glass transition.

Secondly, a polarization mechanism denoted α_c is observed at higher temperature or lower frequencies. The exact origin of this polarization process is still not fully understood today. Most of the studies performed on both PVdF and PVdF-HFP seem to show a relationship between this polarization mechanism and the crystalline phase of PVdF. Its molecular origins must be found in various forms of imperfection including chain loops at the lamellar surface, chain twisting within the crystal structure, discontinuities, etc.[150] Indeed, some authors make a correlation between this polarization mechanism and the secondary crystalline phase mentioned before and appearing during thermal annealing[121,122]. Teyssedre et al. correlate this polarization

mechanism to an "ordered layer" at the crystal-amorphous interphase[151]. Other research groups reported an ultraslow chain motion reorienting the CH_2 bonds along the chain direction in the crystal lattice. This change in conformation with internal rotation could be promoted by defects in the crystal structure[152–154].

Finally, the DC conductivity σ_{DC} appears at low frequency and high temperature on $\varepsilon''(\omega)$ only with a -1 slope. However, the addition of a 3rd relaxation process between the conductivity and the α_c process is required to properly fit both the real and the imaginary parts of the permittivity, as shown in the case of $\varepsilon''(\omega)$ in Figure 4.8. This contribution is attributed to a Maxwell-Wagner-Sillar polarization mechanism that has already been described for PVdF[155]. It is commonly found in semi-crystalline polymers in which the crystalline and the amorphous phases do not possess the same conductivity[66–68,155]. As presented in the State-of-the-art section the electrical charges migrating in the high conductivity phase reach the interfaces with the low conductivity phase and accumulate. These electrical charges are introduced in the material during the fabrication process (ion from the solvent, impurities…). They are trapped in the material at low temperature and may participate in the conduction at high enough temperature.

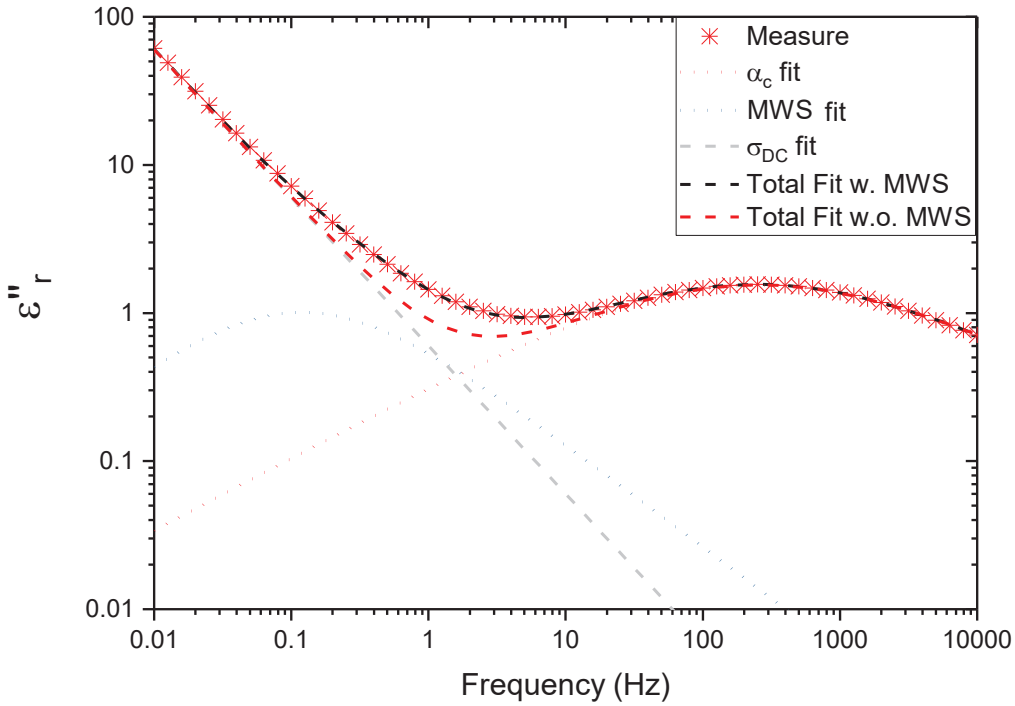

Figure 4.8: Example PVdF-HFP dielectric spectrum at 333 K with the fitted contributions α_c, MWS, and σ_{DC} and the global fitted curve with (w.) and without (w.o.) the MWS contribution.

The analysis and fit allow extracting the various parameters of the Cole-Cole equations. In addition to the conductivity, the characteristic relaxation time τ, the magnitude of the polarization $\Delta\varepsilon_r$ and the exponent α are extracted for each relaxation process.

The relaxation map of the neat PVdF-HFP, plotted in Figure, shows the evolution of the characteristic relaxation time of each process as a function of 1000/T.

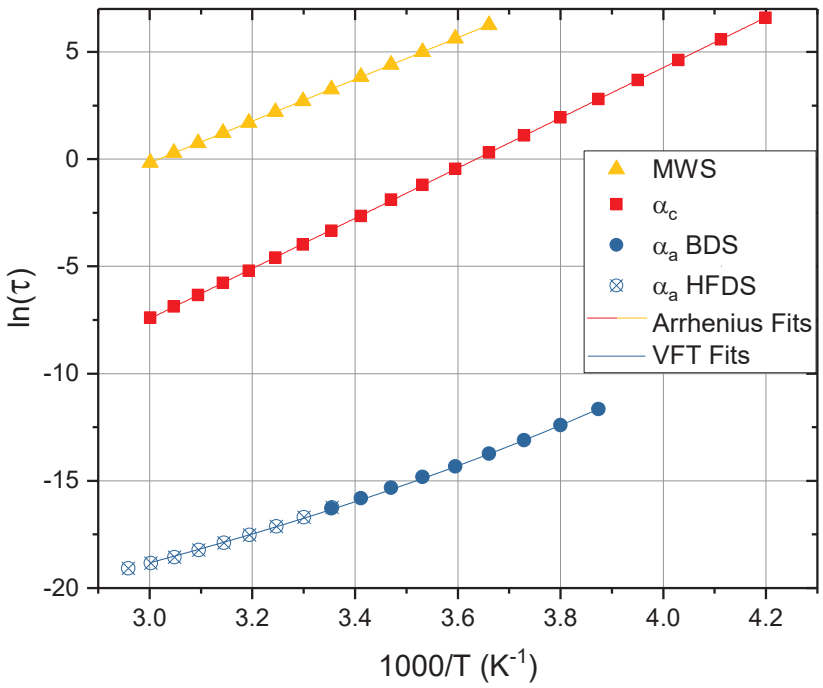

Figure 4.9: Relaxation map of the neat PVdF-HFP.

The characteristic times of the α_a relaxation are obtained by fitting both the BDS and the HFDS dielectric spectra. As a result, Figure 4.9 shows the good agreement between BDS and HFDS results. The evolution of the α_a relaxation times with temperature were fitted with a Volgel-Fulcher-Tammann (VFT) equation:

$$\tau = \tau_0 exp\left(\frac{B}{T - T_V}\right) \tag{4.1}$$

Where B is the activation temperature which is equal to E_a/k_b and T_V the Vogel Temperature.

The temperature dependence of the α_c and MWS relaxations were described by the Arrhenius equation:

$$\tau = \tau_0 exp\left(\frac{E_a}{k_b T}\right) \tag{4.2}$$

where E_a is the activation energy and τ_0 the pre-exponential time. The fact that the α_c and MWS relaxations could not be fitted with the VFT parameter used for α_a relaxation indicates that they are not directly, or not only related to the polymer mobility. The choice of the models is consistent with the literature[155,156].

The results of the fit analysis are reported in Table 4.3. The relaxation time at infinite temperature of the MWS relaxation is very low compared to the Debye time ($\sim 10^{-13}$s) but it is consistent with the values reported in the literature for PVdF homopolymer. The associated activation energy of 81 kJ.mol^{-1} is consistent with the value reported by Rekik et al. on PVdF. The α_c polarization shows similar relaxation time as compared to literature. In the case of the α_a relaxation, τ_0 is very close to the expected Debye time.

Table 4.3: Result of the fit analysis of the neat PVdF-HFP relaxations compared to similar studies reported in the literature.

Reference	MWS		α_c		α_a		
	τ_0 (s)	E_a (kJ.mol^{-1})	τ_0 (s)	E_a (kJ.mol^{-1})	τ_0 (s)	B (K)	T_v (K)
This Work	$10^{-18.5}$	81	$10^{-17.7}$	97	10^{-12}	577	163
Rekik et al. (PVdF) [155]	10^{-18}	92	10^{-17}	88	$10^{-12.7}$	1296	175
Chanmal et al. (PVdF)[157]	$10^{-23.5}$	174	10^{-16}	41	-	-	-

In addition to the characteristic times related to each relaxation, the fit analysis provides other parameters such as the magnitude of the relaxation processes, denoted $\Delta\varepsilon$, and the conductivity.

The magnitude of the α_c relaxation, denoted $\Delta\varepsilon^{\alpha_c}$, is plotted in Figure 4.10 a) as a function of temperature. One can note that $\Delta\varepsilon^{\alpha_c}$ increases with temperature up to 300K before decreasing with further increase of temperature. The first increase could be explained by the increase of thermal motion in the PVdF-HFP crystal with temperature. The decrease of $\Delta\varepsilon^{\alpha_c}$ above 300K is likely to be related to the melting of the crystalline phase formed by annealing 30 °C, following the hypothesis formulated by Neidhöfer et al.[121]. Indeed, the partial melting of the secondary phase could lower the fraction of the crystalline phase or the amount of interfacial material involved in this polarization mechanism. Moreover, such decrease in magnitude has also been evidenced by Mijovic et al. in PVdF at higher temperature[150].

The magnitude of the MWS relaxation, plotted in Figure 4.10 b), increases as temperature increases. This must be related to the increase of the charge carrier density due to higher ion dissociation at high temperature. Part of the ions do not accumulate at

the interfaces and migrate through the thickness of the sample. These ions participate to σ_{DC}. The conductivity is described by an Arrhenius equation as follow:

$$\sigma_{DC} = \sigma_0 exp\left(\frac{-E_a}{k_b T}\right) \quad (4.3)$$

where σ_0 is the conductivity at infinite temperature. Figure 4.10: c) presents $\ln(\sigma_{DC})$ as a function of 1000/T. As expected from the increase of molecular mobility while increasing the temperature, $\ln(\sigma_{DC})$ decreases with 1000/T. The activation energy related to the evolution of σ_{DC} is 133 kJ.mol^{-1}.

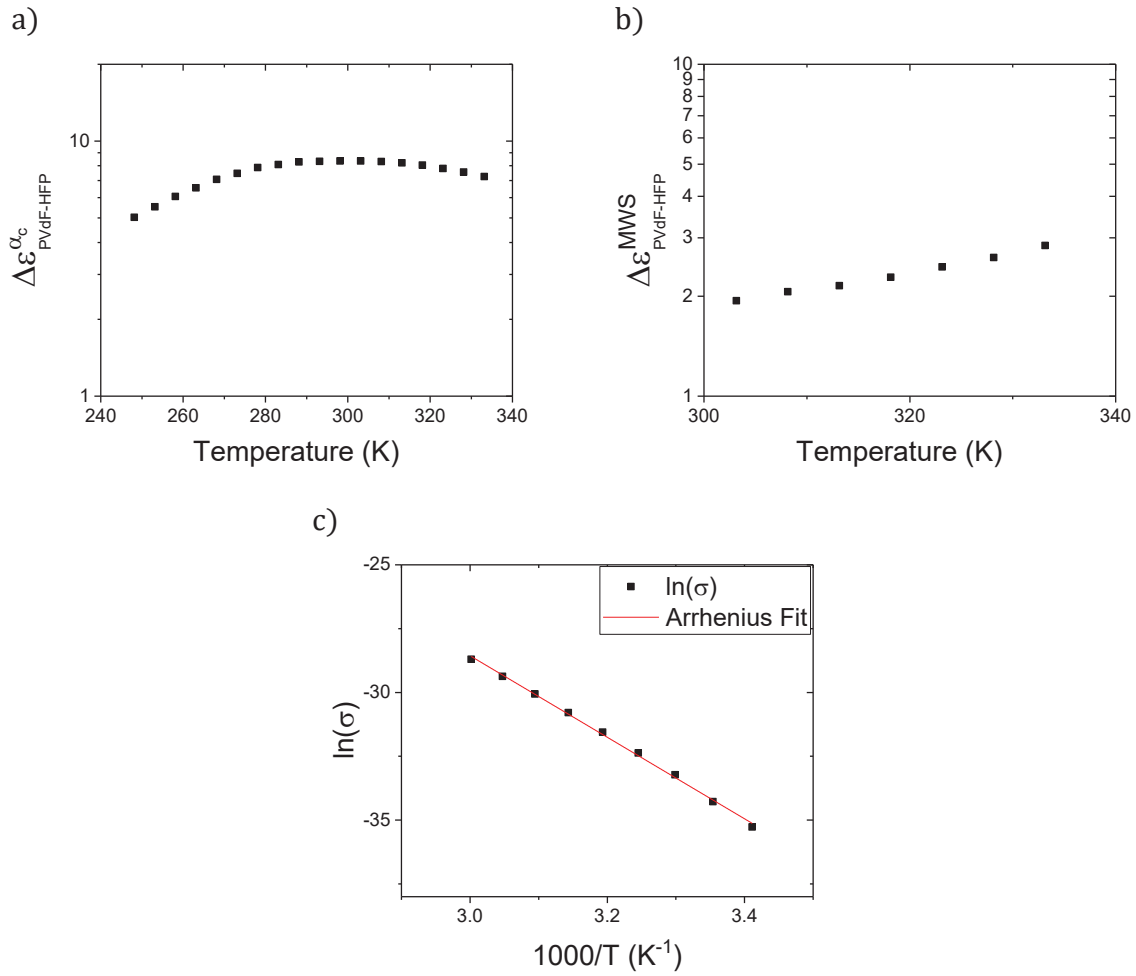

Figure 4.10: Evolution of a) $\Delta\varepsilon^{\alpha_c}$ and b) $\Delta\varepsilon^{MWS}$ with the temperature and of c) ln(σ) with 1000/T for the neat PVdF-HFP sample

4.3.2 Dielectric spectroscopy of PVdF-HFP:$BaTiO_3$ nanocomposite films

In order to assess the impact of the high permittivity $BaTiO_3$ NPs on dielectric properties of the PVdF-HFP-based nanocomposites, BDS and HFDS were conducted on the nanocomposite samples following the same protocol as for the neat PVdF-HFP. BDS was performed on all samples whereas HFDS was only performed on the neat PVdF-HFP, A5, A10, S5, and S10 samples, which represent the extreme behaviours investigated in this section. The resulting dielectric spectra obtained by BDS at 25 °C are presented in Figure 4.11 between 10^{-2} Hz and 10^5 Hz. Indeed, the presence of contact impedance in some BDS measurements prevents any consideration of the dielectric spectra between 10^5 and 10^7 Hz.

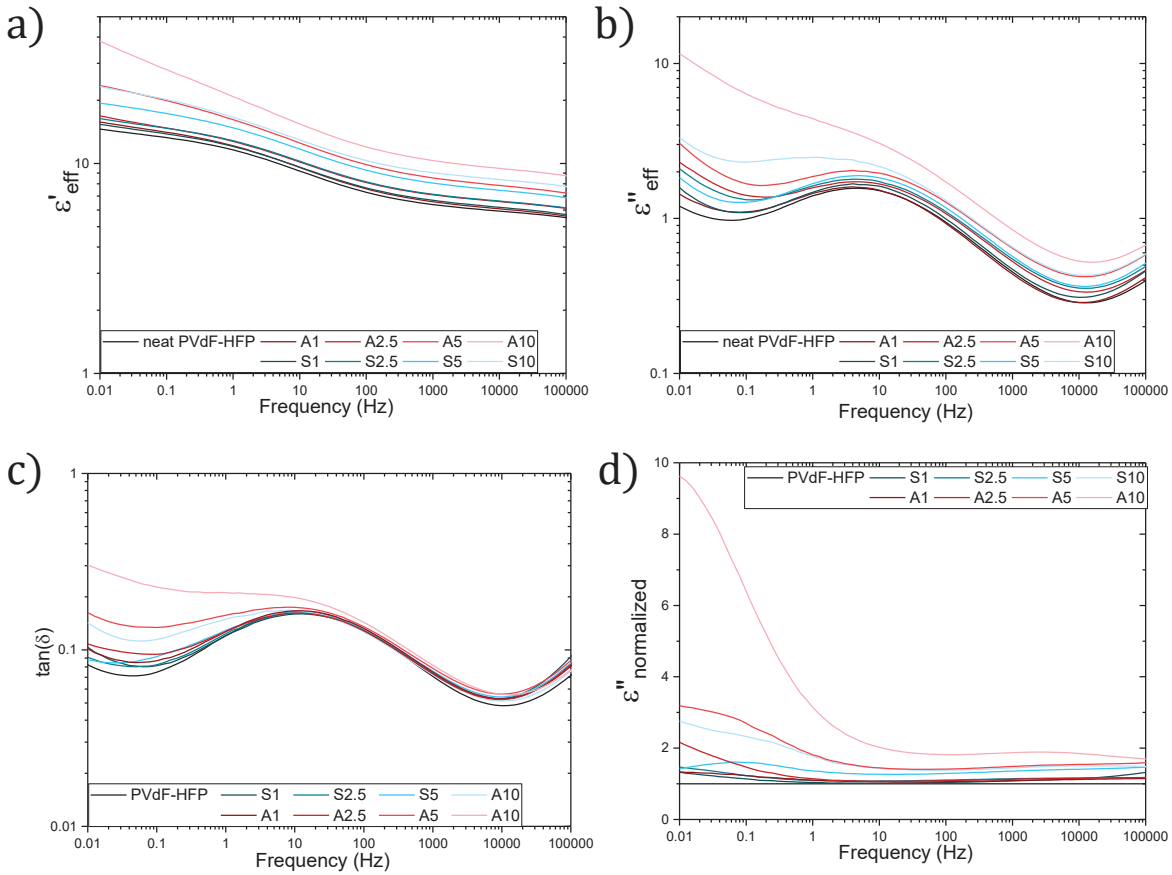

Figure 4.11: Dielectric properties of the PVdF-HFP:$BaTiO_3$ nanocomposite samples and neat PVdF-HFP: a) ε'_{eff}, b) ε''_{eff}, c) tan(δ), and d) $\varepsilon''_{norm} = \varepsilon''_{eff}/\varepsilon''_{PVdF\text{-}HFP}$.

One can see in Figure 4.11 a) and b) that both ε'(ω) and ε"(ω) are higher for nanocomposites than for the neat PVdF-HFP. This indicates that the $BaTiO_3$ NPs increase the complex effective permittivity in the nanocomposites, which is expected from their high permittivity. Indeed, the curves seem to indicate that the higher the $BaTiO_3$ NPs content, the higher the effective permittivity of the nanocomposites.

First, the ε'(ω) and ε"(ω) curves of the nanocomposites, plotted in Figure 4.11 a) and b), exhibit a very similar trend at frequencies higher than 50 Hz. In this frequency region, the ε'(ω) and ε"(ω) curves of the nanocomposites look as if they could be superimposed on the PVdF-HFP curves by a simple vertical shift in log-log scale. In other words, the dielectric spectra of the nanocomposites can be obtained by multiplying the spectra of the neat PVdF-HFP sample by a factor which does not depend on frequency. This observation is valid at high frequencies for all the nanocomposites regardless of their dispersion state or of their NPs content.

Secondly, the ε'(ω) and ε"(ω) of the nanocomposites are higher than expected from the simple shift behaviour mentioned previously at frequencies below 50 Hz. This deviation is larger for the nanocomposites with 5 and 10 vol% of NPs as compared to those with only 1 and 2.5 vol%. It suggests that the $BaTiO_3$ NPs may be responsible for this behaviour. Moreover, this deviation is larger for A10 as compared to S10 and larger for A5 as compared to S5 which would suggest an impact of the dispersion state of the $BaTiO_3$ NPs.

Equivalently, the same observation can be done on the tan(δ) curves of the nanocomposites, plotted in Figure 4.11 c). At low frequency tan(δ) increases with the $BaTiO_3$ NPs content and is higher for agglomerated NPs as compared to well dispersed NPs. Conversely, at high frequencies, only small differences are observed in tan(δ) curves of the nanocomposites as compared to the neat PVdF-HFP curve.

In order to well visualize this effect, all the ε"(ω) curves have been normalized by that of PVdF-HFP. The results are plotted in Figure 4.11 d). Nearly flat curves are obtained at high frequency (above 100 Hz roughly) whereas high increases of normalized ε"(ω) are observed at low frequencies. This indicates that the permittivity enhancement at high frequency does not depend on the frequency. As a result, the dielectric properties of the nanocomposites seem to reveal two distinct trends:

- At high frequency (50 to 10^5 Hz), all ε' and ε'' curves follow the same trend: The ε' and ε'' curves of the nanocomposites correspond to multiplication of the PVdF-HFP curves toward higher values by a constant factor (independent of frequency). This behaviour is consistent with the superposition of the tan(δ) curves and by the constant values exhibited by $\varepsilon''_{normalized}$.
- At lower frequency (0.01 Hz to 50 Hz), the nanocomposite spectra exhibit a different behaviour. Indeed, a strong increase of the imaginary part of the permittivity is clearly visible on the high loaded nanocomposites curves and particularly on the A samples with agglomerated dispersion state (A5, A10 and S10).

To better understand and quantify these differences, the same analysis and fitting as done previously for neat PVdF-HFP was done on the dielectric spectra of the

nanocomposites. In addition to σ_{DC}, the signals of the nanocomposites were analysed with three polarization mechanisms. The high frequency ones α_a and α_c correspond to those of neat PVdF-HFP. The third one at low frequency is found in a similar frequency range as the MWS polarization of neat PVdF-HFP matrix. However, this relaxation may not be of the same nature.

Figure 4.12 presents the relaxation maps with the evolution of the relaxation times of the 3 polarization mechanisms fitted for all the samples. Two observations can be done:

- $BaTiO_3$ NP content and dispersion state have no significant influence on the evolution of the relaxation times with temperature of α_a and α_c relaxation processes (see Figure 4.12 c) and d)).
- The evolution of relaxation time corresponding to the MWS polarization is modified by $BaTiO_3$ NPs and depends both on $BaTiO_3$ NP content and dispersion state (see Figure 4.12 b)).

Like in the case of neat PVdF-HFP, the evolutions of the relaxation times were fitted with the Arrhenius equation for the MWS and α_c relaxations and with the VFT equation for the α_a relaxation. The resulting VFT parameters and activation energies are reported in Table 4.4.

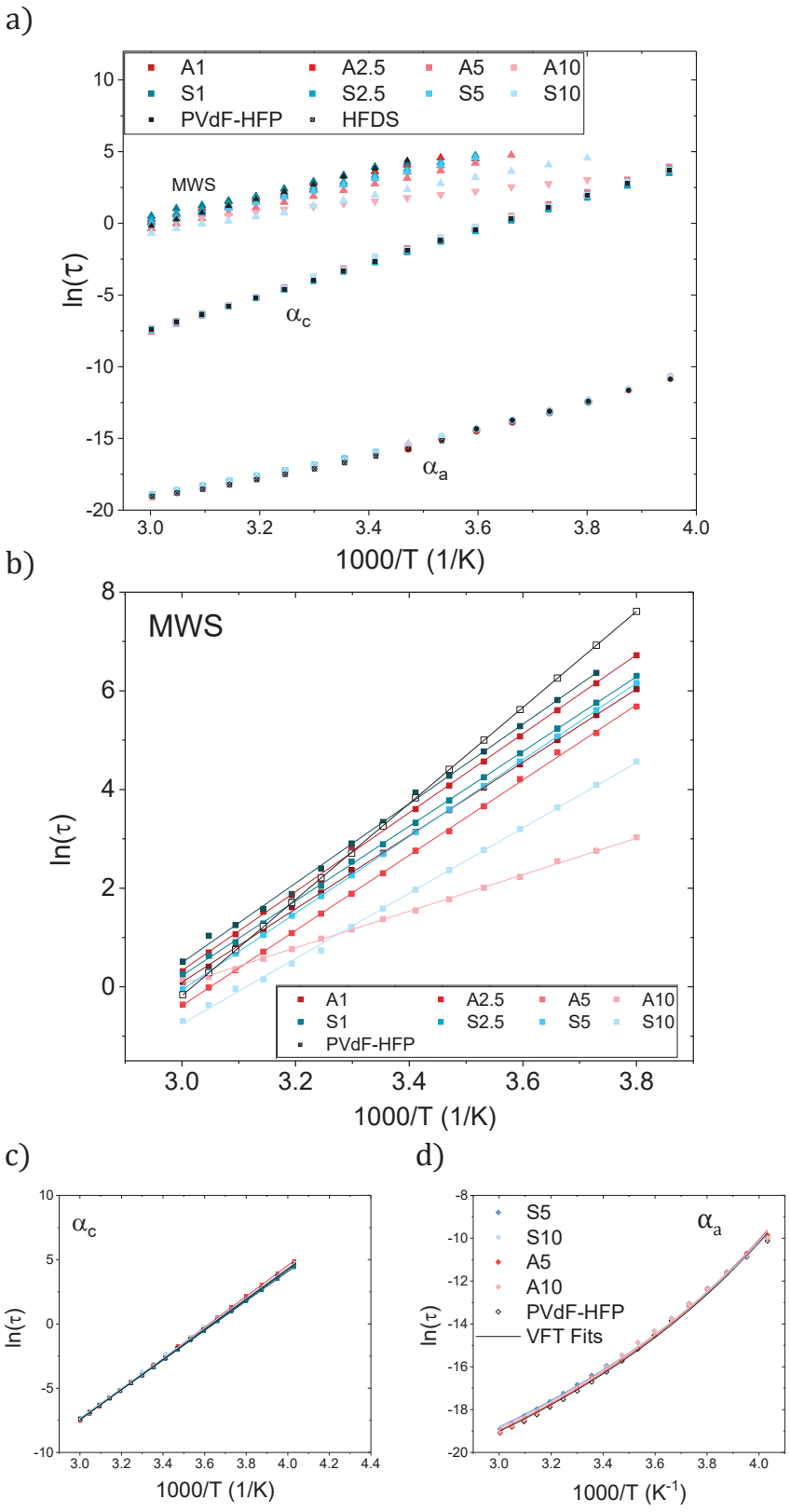

Figure 4.12: a) Global relaxation map of the PVdF-HFP:$BaTiO_3$ nanocomposites and their linear fits for the b) MWS, c) α_c, and d)α_a relaxation processes. (HFDS: High Frequency Dielectric Spectroscopy)

Table 4.4: Parameters of the various polarization mechanisms obtained from the fits of the dielectric spectra of the PVdF-HFP-based nanocomposites as compared to the neat PVdF-HFP.

Sample	α_a			α_c		MWS	
	τ_0 (s)	B (K)	T_v (K)	τ_0 (s)	E_a (kJ.mol^{-1})	τ_0 (s)	E_a (kJ.mol^{-1})
PVdF-HFP	10^{-12}	1419	169	10^{-18}	97	10^{-13}	81
A1	-	-	-	10^{-19}	97	10^{-10}	62
A2.5	-	-	-	10^{-18}	96	10^{-10}	67
A5	10^{-12}	1420	169	10^{-19}	100	10^{-10}	63
A10	10^{-12}	1456	167	10^{-18}	97	10^{-5}	31
S1	-	-	-	10^{-19}	97	10^{-10}	67
S2.5	-	-	-	10^{-18}	96	10^{-10}	63
S5	10^{-12}	1492	164	10^{-18}	98	10^{-10}	65
S10	10^{-12}	1448	168	10^{-19}	97	10^{-10}	55

As a result, the VFT parameters of the α_a relaxation are relatively close to each other for all the nanocomposites characterized by high frequency dielectric spectroscopy. The obtained T_V values are lower than the value expected from the VFT model which is approximately $T_V \sim T_g - 40$ K (i.e. about 193 K considering Tg = 233 K)[15]. Nakagawa et al. obtained similar results and interpreted qualitatively this behaviour on the basis of the Adam-Gibbs theory. Indeed, in amorphous polymers, the size of the cooperatively rearranging region increases with decreasing temperature. In semi-crystalline polymers, the crystallites limit this size by separating the amorphous regions. As the size increases with decreasing temperature, the segmental motions are suppressed by the boundary between amorphous and crystalline phases. This effect gives rise to the deviation from the VFT theory near the glass transition temperature of semi-crystalline polymers[156].

Similarly, the α_c polarization is characterized by activation energies about 96-100 kJ.mol^{-1} for all the nanocomposites as well as for the neat PVdF-HFP. The relaxation times at infinite temperature of the order of 10^{-18}-10^{-19} are consistent with that of neat PVdF-HFP. These results suggest no significant effect of the introduction of $BaTiO_3$ NPs on the dynamic of the α_a and α_c relaxations.

Conversely, the activation energy of the MWS relaxation seems to be affected by the introduction of the $BaTiO_3$ NPs. Indeed, while initially at 81 kj.mol^{-1} for neat PVdF-HFP, the activation energy decreases down to 62-67 kJ.mol^{-1} for the nanocomposite filled with 1 to 5 vol% of $BaTiO_3$ NPs regardless of their dispersion states and further decreases to 30 and 57 kJ.mol^{-1} respectively for A10 and S10.

Thus, the detailed study of the relaxation dynamics shows that the dynamics of the MWS relaxation is impacted by the incorporation of the $BaTiO_3$ NPs whereas the α_a and the α_c relaxations are not affected by the presence of the NPs. However, the dielectric properties of nanocomposites are affected by both the $BaTiO_3$ NP content and their dispersion state. Two different effects related to the addition of the $BaTiO_3$ NPs have been separately observed at low and high frequencies on the dielectric properties of the nanocomposites. In what follows, a thorough investigation of these two effects (whose delimitations are given in Figure 4.13) is conducted using the parameters extracted from the fit analysis.

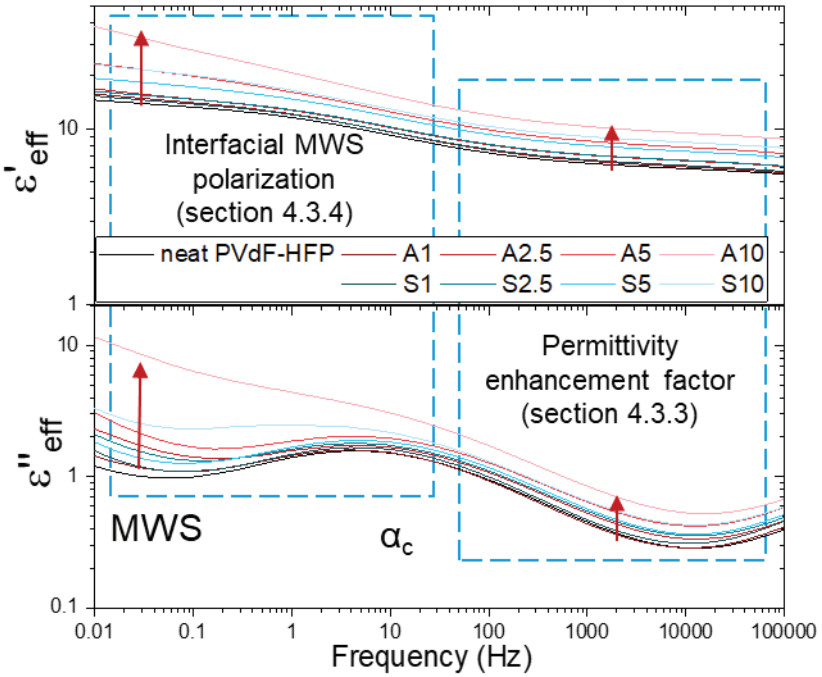

Figure 4.13: Illustration of the frequency range used for analysing the two different effects of $BaTiO_3$ NP content and dispersion state observed on the effective complex permittivity of nanocomposites. The associated effects are schematized by the red arrows and the corresponding sections are mentioned.

4.3.3 Permittivity enhancement factor

It has been shown that the addition of the $BaTiO_3$ NPs leads to increase the permittivity of the PVdF-HFP, as expected from high permittivity NPs. As mentioned previously, this increase is visible on $\varepsilon'(\omega)$ and $\varepsilon''(\omega)$ at high frequency (50 - 10^5 Hz) and looks like multiplication of the matrix permittivity by a factor that does not depend on frequency. This would consist, in log-log scale, in a vertical shift of the neat PVdF-HFP curve. This can be expected from the high permittivity of the $BaTiO_3$ NPs and it would imply the following statements:

- The permittivity contrast between the $BaTiO_3$ NPs and the PVdF-HFP matrix is high enough to consider that its effect on the composite dielectric properties will not change significantly with the frequency (section 1.3).
- The $BaTiO_3$ NPs do not possess significant dielectric losses as compared to the polymer matrix on the studied frequency range.

In this part, the theoretical basis of the permittivity enhancement will be introduced on the basis of the above-mentioned statements. Then, the relationship between the dispersion state and the enhancement of the permittivity will be discussed with the help of modelling before to conclude.

Mixing rules theory

In the case of polymer-based composites filled with particles having permittivity different from the matrix, the Maxwell Garnett theory allows describing the complex permittivity of a composite $\varepsilon_c^*(\omega)$ as a function of the dielectric properties of the pure components and the composite structural parameters (see also eq. (1.21)):

$$\varepsilon_c^*(\omega) = \varepsilon_m^*(\omega)\frac{\left[n\varepsilon_f^*(\omega) + (1-n)\varepsilon_m^*(\omega)\right] + (1-n)[\varepsilon_f^*(\omega) - \varepsilon_m^*(\omega)]\varphi_f}{\left[n\varepsilon_f^*(\omega) + (1-n)\varepsilon_m^*(\omega)\right] - n[\varepsilon_f^*(\omega) - \varepsilon_m^*(\omega)]\varphi_f} \quad (4.4)$$

in which $\varepsilon_f^*(\omega)$ and $\varepsilon_m^*(\omega)$ are the complex permittivities of the fillers and the matrix respectively and n, with $0 \leqslant n \leqslant 1$, the shape factor of the fillers which are all oriented in the same way (anisotropy axis in the same direction). This equation is based on the hypothesis of diluted systems because the interactions between the fillers are neglected. In our case, the $BaTiO_3$ NPs are assimilated to perfect spheres so that the n value is 1/3 and equation (3.1) becomes:

$$\varepsilon_c^*(\omega) = \varepsilon_m^*(\omega)\frac{\left[\varepsilon_f^*(\omega) + 2\varepsilon_m^*(\omega)\right] + 2[\varepsilon_f^*(\omega) - \varepsilon_m^*(\omega)]\varphi_f}{\left[\varepsilon_f^*(\omega) + 2\varepsilon_m^*(\omega)\right] - [\varepsilon_f^*(\omega) - \varepsilon_m^*(\omega)]\varphi_f} \quad (4.5)$$

and can be written as follows (see also eq. (1.22)):

$$\varepsilon_c^*(\omega) = \varepsilon_m^*(\omega)\frac{1 + 2\varphi_f\dfrac{[\varepsilon_f^*(\omega) - \varepsilon_m^*(\omega)]}{\left[\varepsilon_f^*(\omega) + 2\varepsilon_m^*(\omega)\right]}}{1 - \varphi_f\dfrac{[\varepsilon_f^*(\omega) - \varepsilon_m^*(\omega)]}{\left[\varepsilon_f^*(\omega) + 2\varepsilon_m^*(\omega)\right]}} \quad (4.6)$$

Now, by considering $\varepsilon_f^*(\omega)$ to be real and very high as compared to $\varepsilon_m^*(\omega)$, equation (4.7) is obtained

$$\varepsilon_c^*(\omega) = \varepsilon_m^*(\omega)\frac{1 + 2\varphi_f}{1 - \varphi_f} \quad (4.7)$$

Equation (4.7) corresponds to the permittivity homogenization of spherical and conducting particles embedded in an insulating matrix. However, this equation is also valid in the case of spherical particles of high permittivity that strongly polarize in such

a way that almost no electric field remains inside the particles. In that case, a dielectric permittivity enhancement factor R_ε can be introduced such as:

$$R_\varepsilon = \frac{\varepsilon_c^*(\omega)}{\varepsilon_m^*(\omega)} = \frac{1+2\varphi_f}{1-\varphi_f} \tag{4.8}$$

Then, we may hypothesize that each polarization mechanism ($\varepsilon_{\alpha_a}^*$, $\varepsilon_{\alpha_c}^*$, ε_{MWS}^*) is separated and independent from the other ones in both the pure polymer and the nanocomposite.

$$\begin{cases} \varepsilon_m^*(\omega) = {\varepsilon_m^*}^{\alpha_a}(\omega) + {\varepsilon_m^*}^{\alpha_c}(\omega) + {\varepsilon_m^*}^{MWS}(\omega) \\ \varepsilon_c^*(\omega) = {\varepsilon_c^*}^{\alpha_a}(\omega) + {\varepsilon_c^*}^{\alpha_c}(\omega) + {\varepsilon_c^*}^{MWS}(\omega) \end{cases} \tag{4.9}$$

Where ${\varepsilon_m^*}^{\alpha_a}(\omega)$, ${\varepsilon_m^*}^{\alpha_c}(\omega)$, ${\varepsilon_m^*}^{MWS}(\omega)$ are the contributions of the α_a, α_c, and MWS relaxations to the total complex permittivity of the matrix and ${\varepsilon_c^*}^{\alpha_a}(\omega)$, ${\varepsilon_c^*}^{\alpha_c}(\omega)$, ${\varepsilon_c^*}^{MWS}(\omega)$ are those of the nanocomposite. If the permittivity of the particles ε_f^* is constant in the considered frequency range, the factor R_ε may be considered to be the same for all relaxation processes. As a result, each polarization contributions to the effective permittivity of the nanocomposites can be extracted from equation (4.8) and expanded as:

$$\Delta\varepsilon_c^k \frac{1}{1+i\omega\tau^k} = R_\varepsilon \Delta\varepsilon_m^k \frac{1}{1+i\omega\tau^k} \tag{4.10}$$

Where $\Delta\varepsilon_c^k(T)$ and $\Delta\varepsilon_m^k(T)$ are the magnitudes of the polarization mechanism k in the nanocomposites and in the neat polymer respectively and $\tau^k(T)$ is their characteristic relaxation time which is intrinsic to the matrix. Thus $R_\varepsilon(T)$ can be expressed as:

$$R_\varepsilon(T) = \frac{\Delta\varepsilon_c^k(T)}{\Delta\varepsilon_m^k(T)} \tag{4.11}$$

This expression gives us the opportunity to determine R_ε with the fit parameters obtained for each nanocomposite as a function of temperature as compared to PVdF-HFP.

Experimental results - α_c relaxation process

To evaluate the effect of the polarization of the high-ε NPs on the nanocomposite permittivity, any relaxation process intrinsic to the PVdF-HFP matrix can be used since the permittivity of the NPs has been assumed to be constant. The α_c relaxation represents the best choice as it is well defined in the frequency and temperature windows of the BDS. Indeed, the previous analyses have shown that this polarization mechanism, likely coming from the amorphous-crystalline interphases, is not affected by the incorporation of the $BaTiO_3$ NPs in terms of dynamics. Moreover, the DSC and FTIR analyses have shown no significant modification of the crystalline phase of the PVdF-HFP matrix (polymorph, fraction, and morphology) upon addition of the $BaTiO_3$

NPs. Thus, if the dielectric properties of the nanocomposites result from the multiplication of those of the PVdF-HFP, the magnitude of the relaxation, $\Delta\varepsilon^{\alpha_c}$, is supposed to be enhanced as well.

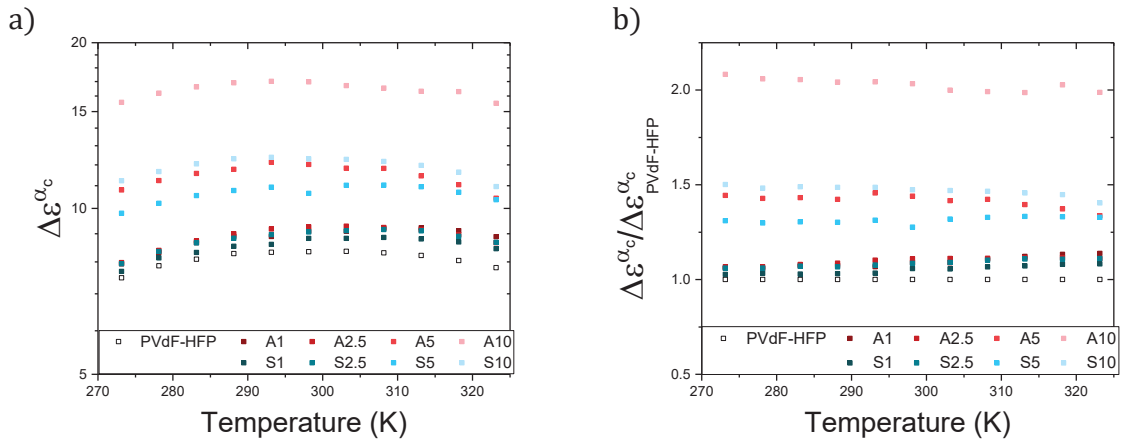

Figure 4.14: a) the magnitude $\Delta\varepsilon^{\alpha_c}$ of the α_c relaxation and b) $\Delta\varepsilon^{\alpha_c}$ normalized with respect to the neat PVdF-HFP for all the nanocomposites and the neat PVdF-HFP.

Figure 4.14 a) shows the evolution of $\Delta\varepsilon^{\alpha_c}$ with the temperature for all the samples of this study. As a first observation, the evolution trend of $\Delta\varepsilon^{\alpha_c}$ for the nanocomposites is very similar as for neat PVdF-HFP. This observation tends to confirm that the enhancement of the PVdF-HFP permittivity by the high-ε $BaTiO_3$ NPs is independent of temperature. The magnitude of $\Delta\varepsilon^{\alpha_c}$ of the nanocomposites normalized by those of the neat PVdF-HFP ($\Delta\varepsilon^{\alpha_c}_{normalized}(T) = \Delta\varepsilon^{\alpha_c}{}_c(T)/\Delta\varepsilon^{\alpha_c}{}_m(T)$), is plotted in Figure 4.14 b). The normalized magnitude of the α_c polarization does not show significant temperature dependency for all the samples. Thus, the permittivity enhancement factor R_ε defined by the equation (4.11) can safely be calculated as the average value of $\Delta\varepsilon^{\alpha_c}_{normalized}$ between 273 K and 323 K for all the samples.

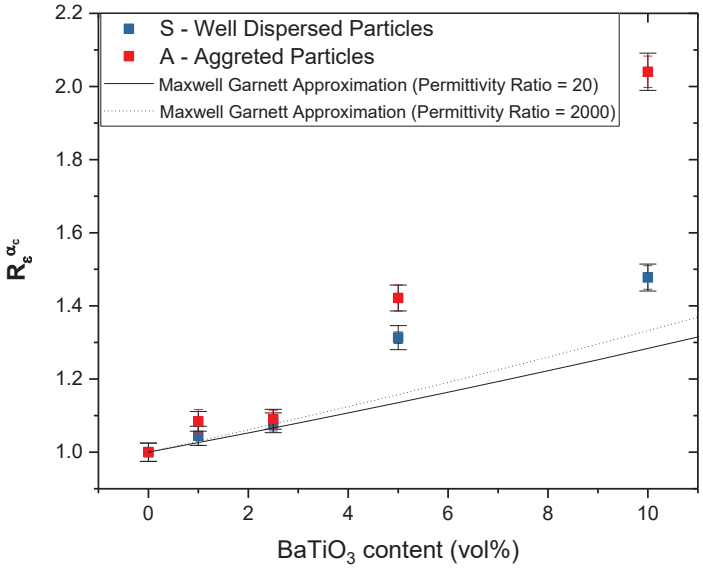

Figure 4.15: Evolution of $R_\varepsilon$values as a function of the $BaTiO_3$ NPs content

Figure 4.15 shows the $R_\varepsilon$value evolution with $BaTiO_3$ NPs content in both well dispersed and agglomerated samples. The theoretical R_ε evolution calculated with equation (4.5) is plotted for permittivity ratios between the NPs and the matrix of 20 and 2000. One should note that the permittivity ratio between the $BaTiO_3$ NPs and the PVdF-HFP is expected to be about twenty ($\sim 150/7$). First, the experimental results confirm that R_ε increases as the $BaTiO_3$ NPs content increases for all the nanocomposite samples regardless of their dispersion states.

At 1 and 2.5 vol%, the experimental data does not significantly deviate from the theoretical evolution. However, at 5 and 10 vol% R_ε starts to show different trends and the theoretical values of R_ε are lower than the experimental ones. This is expected from the fact that equation (4.5) does not consider the interactions between NPs that increase as the $BaTiO_3$ NPs content increases and leads to higher permittivity as described in section 1.3. Moreover, R_ε exhibit higher values in the case of the nanocomposites A with agglomerated $BaTiO_3$ NPs as compared to the nanocomposites S with well dispersed NPs. **This result suggests a clear effect of the dispersion state on the effective permittivity of the nanocomposites.** The higher R_ε values in the nanocomposites A compared to nanocomposites S and its relationship with the interactions between NPs in the agglomerates will be discussed in what follows.

Maxwell equation modelling

Since the permittivity enhancement experimentally observed is thought to arise from the polarization of the high permittivity $BaTiO_3$ NPs, the differences observed between the nanocomposite samples with agglomerated and well dispersed NPs could be related to this polarization effect as well. To discuss this hypothesis in a more quantitative way, we have performed some simple modelling of dispersed and agglomerated systems

To do so, a Matlab program developed by Carolina Franzon, Jérôme Bikard and Mathieu Tauban was used (Solvay proprietary). It allows modelling the polarisation of biphasic materials with heterogeneous permittivity (ε_1 and ε_2) and thus calculating the electric potential and electric field distributions in these materials. It is based on the resolution of the Maxwell equations on 2D systems when an electric potential difference ϕ is applied between the upper and lower sides, respectively considered as the upper and lower electrodes as represented in Figure 4.17 a). The resulting distributions of electric potential and electric field allow calculating the effective permittivity ε'_{eff} of the heterogeneous systems. A description of the program and its numeric method is presented in what follows.

The set of Maxwell equations is:

$$\nabla . D = \rho_f \tag{4.12}$$

$$\nabla \times E = -\frac{\partial B}{\partial t} \tag{4.13}$$

$$\nabla . B = 0 \tag{4.14}$$

$$\nabla \times H = J_f + \frac{\partial D}{\partial t} \tag{4.15}$$

Where E is the electric field, H is the magnetic field, D is the electric displacement, B is the magnetic induction, J_f is the current density vector and ρ_f the free charge density. The magnetic effects are neglected (B=H=0). In addition, two hypotheses are done: (1) the dielectric behavior of the material is assumed to be linear, and (2) the conductive behavior of the material is assumed to be linear. Both hypotheses are valid at low electric fields which are the conditions used for dielectric spectroscopy. They may become false at high electric fields where both the permittivity and the conductivity may depend on the electric field. For further simplifications, the program is here applied to simulate the behavior of perfect dielectric materials, implying (no conductivity) $\rho_f = 0, \sigma = 0$ and so $J_f = 0$, which is consistent with the negligible conductivity in this frequency range (from 50 to 10^5 Hz).

In the case of linear dielectric, the electric displacement is given by:

$$\vec{D} = \varepsilon_0 \varepsilon_r \vec{E} \tag{4.16}$$

where ε_r is independent of the electric field E. As a result, the equation to solve is:

$$\nabla.(\varepsilon_0 \varepsilon_r \nabla\phi) = 0 \tag{4.17}$$

where ϕ is the electric potential.

The numeric method used in this program is the finite difference method. It requires the discretization of the 2D system using a mesh grid. In this work, a homogeneous, periodic discretization is used as shown in Figure 4.17 b). A permittivity value ε_1 (matrix) or ε_2 (high permittivity inclusion) is attributed to each point of the grid. Inclusions can be designed manually to yield well dispersed or agglomerated inclusions with various morphologies as shown in Figure 4.16.

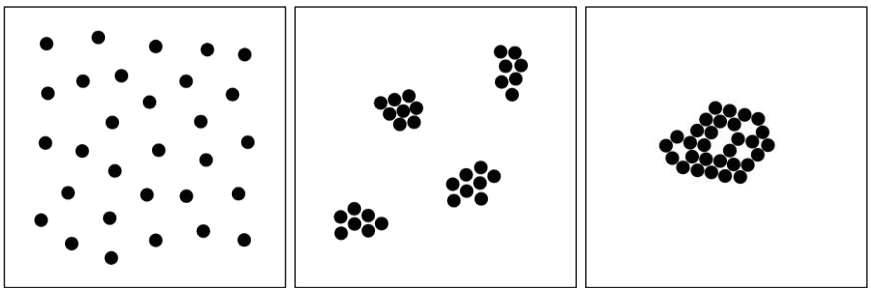

Figure 4.16: Examples of designed systems composed of particles (in black) embedded in a matrix (in white) of different permittivity.

To perform the finite difference calculation, boundary conditions are set. Concerning the upper and lower electrodes the boundary conditions, a potential difference ϕ is imposed. Periodic boundary conditions are applied on lateral sides.

In the initial state, the potential difference is set between the upper and the lower electrodes, separated by a distance h. The resulting homogeneous electric field is $E_0 = \phi/h$, which corresponds to the fact that the material polarization is not yet considered. Then, the potential in each point (i, j) of the system is iteratively calculated based on equation (4.17) depending on both the potential and the permittivity of the neighbour discretised points as represented on the Figure 4.17 c). The iterative calculation continues up to converge to the final potential distribution at equilibrium.

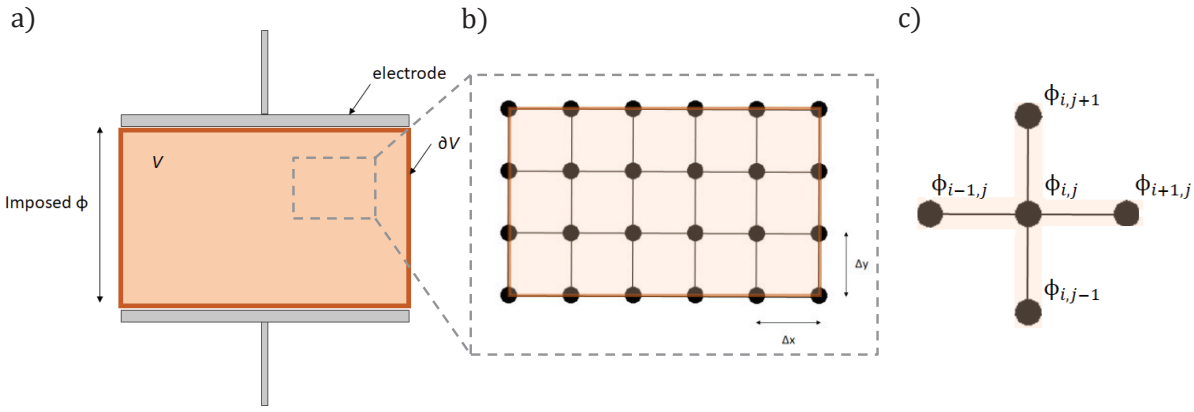

Figure 4.17: a) scheme of the 2D system representing a material between two electrodes, b) mesh grid used for finite difference method and c) mesh points considered in the determination of $\phi_{i,j}$.[158]

Then, the distribution of the electric field in the system can be calculated by derivation of the determined potential distribution. The effective (homogenized) permittivity of the modelled system can be calculated knowing both the permittivity and the electric field in each point. Indeed, as already described in the State-of-the-art chapter the total electric energy of homogenized material is defined as:

$$U_e = \frac{V}{2}\varepsilon_0 \varepsilon'_{eff} {E_0}^2 \tag{4.18}$$

where V is the volume (surface in 2D) of the material. In the Matlab program, the total electric energy of the system is calculated as the sum of the electric energies in each point of the grid:

$$U_e = \sum_{i,j} \frac{v}{2}\varepsilon_0 \varepsilon'_{i,j} {E_{i,j}}^2 \tag{4.19}$$

where v is the representative volume (surface in 2D) of each discrete element and $\varepsilon'_{i,j}$ and $E_{i,j}$ are the permittivity and the electric field at the mesh point (i, j), respectively. Reversely, the effective permittivity of the system is obtained as the permittivity of a homogeneous system having the same total electric energy ${U_e}^{system}$ and a homogeneous electric field defined by the initial potential difference applied and the system geometry:

$$\varepsilon'_{effective} = \frac{2{U_e}^{system}}{\varepsilon_0 {E_0}^2} \tag{4.20}$$

Finally, the electric field distribution is returned in the form of a 2D colour mapping. The calculated maximal electric field and effective permittivity are returned as well.

In this study, 20 images were edited in order to represent composites filled with 5 vol% of agglomerated or well dispersed NPs. In this calculation, the permittivities were

set at 7 for the matrix and 150 for the particles leading to a permittivity ratio slightly higher than 20. The results of these simulations are presented in Figure 4.18 and Table 4.5.

In a first hand, the resulting distributions of the electric field presented in Figure 4.18 show that the electric field is enhanced at the pole of the particles (i.e. in the direction of the electric field) and reduced at their equators (i.e. perpendicularly to the electric field direction), as expected[159]. The maximum values of electric field reached in the composites are reported in Table 4.5. It shows that the intensification of the electric field is higher in the case of agglomerated NPs as compared to well dispersed NPs. The associated standard deviation is also higher in the case of agglomerated particles. This may come from the fact that the agglomerate size gets close to the total size of the system. Each agglomerate has a particular structure and then a different effect on the resulting effective permittivity. Agglomerated systems are then less representative of a macroscopic system. Nevertheless, the standard deviation remains well below the difference in maximum normalized electric field values observed between well dispersed and agglomerated systems.

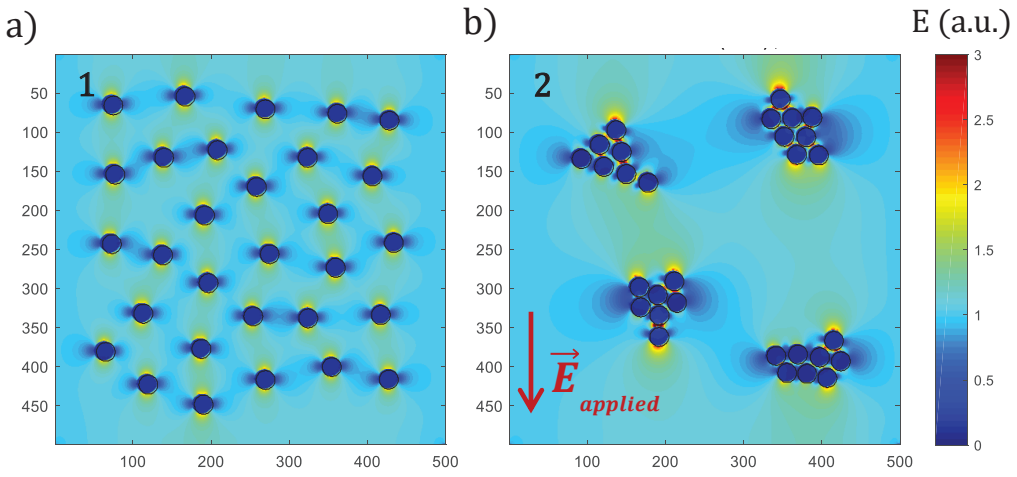

Figure 4.18: Mapping of the electric field intensification of polarized equivalent 2D composites with agglomerated and well dispersed particles obtained by 2D modelling

In another hand, the modelling results show also a higher effective permittivity and thus a higher permittivity enhancement factor for the composites with agglomerated particles ($R_\varepsilon = 1.16$) as compared to composites with well dispersed particles ($R_\varepsilon = 1.14$). These results are consistent with the previous experimental observations. Nevertheless, the permittivity enhancement factors experimentally found are 1.31 and 1.42 respectively for the composites S5 and A5 and so higher than the modelling results. This likely comes from the fact that the modelling is performed in 2D, which attenuates such effects as compared to 3D. A 3D modelling would provide much larger permittivity enhancement factors and strengthen the observed trend.

Table 4.5: Result of the modelling of the resolution of the Maxwell equation for composites with 5 vol% of well dispersed and agglomerated high-ε particles. ($\varphi_{particle} = 5$ vol%, $\varepsilon_{matrix} = 7$ and $\varepsilon_{particle} = 150$)

Composites	$\varepsilon'_{effective}$		R_ε	$E_{max}/E_{applied}$	
Well dispersed NPs	7.87	$\pm$ 0.002	1.12	2.26	$\pm$ 0.02
Agglomerated NPs	8.00	$\pm$ 0.05	1.14	4.7	$\pm$ 0.7

As a result, the 2D modelling results show a similar trend as the experimental result concerning the dependency of the permittivity enhancement factor with the dispersion state. These results tend to confirm the impact of the dispersion state on R_ε which was experimentally evidenced.

It is important to note that the electrodynamic equations which describe the system do not contain any length scale. Therefore, the results must be independent of the size, and agglomerates should give the same result as isolated particles. Thus, the previous results must be discussed and interpreted.

Interpretation

One interpretation is illustrated in Figure 4.19. When high permittivity particles are subjected to an external electric field, their strong polarization leads to reduce the electric field in their volume. As a consequence, they tend to be at isopotential. If the particles form an agglomerate and locally percolate, the isopotential region is extended to all the agglomerates and no electric field remains inside the agglomerates. The polymer which is contained in the agglomerates is then exposed to no electric field. This volume of polymer is called occluded volume. Thus, the whole agglomerates can be assimilated to particles of equivalent shape and volume. As a consequence, the effective content of particles is higher in a composite with agglomerated particles as compared to a composite with the same content of well-dispersed particles. This behaviour must be correlated to percolation theory[160].

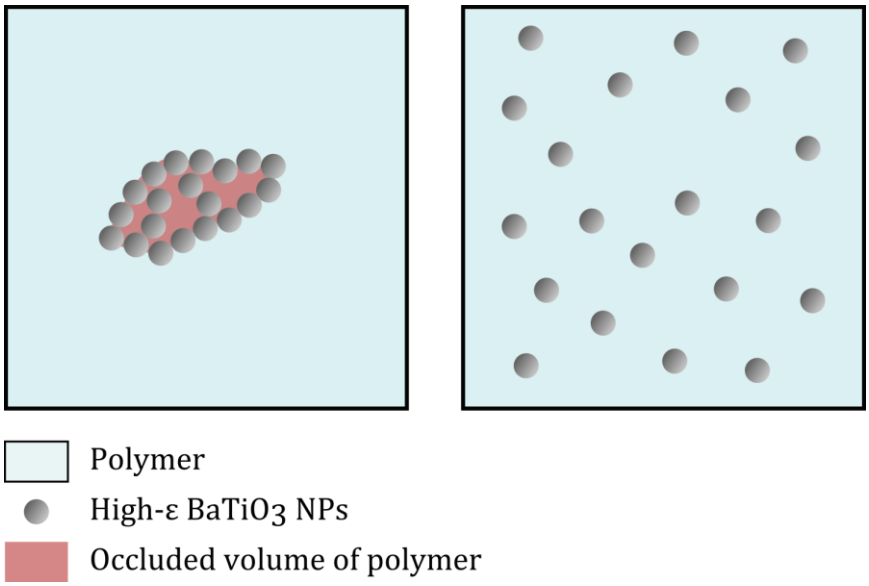

Figure 4.19: Illustration of the interpretation for higher permittivity in the composites with agglomerated $BaTiO_3$ NPs as compared to well dispersed.

Validation of the interpretation

In order to validate this hypothesis, the behaviour of various systems with different agglomerates compactness was modelled. Four 2D systems were edited at 5 vol%, as presented in Figure 4.20 a). As expected, the volume of polymer surrounded by the particles qualitatively increases from the systems 1 to 4. The resulting mappings of the electric field presented in Figure 4.20 b) clearly show an attenuation of the electric field in the polymer zones inside the agglomerates for the systems 2 to 4. The percolating particles tend to create a shell at isopotential surrounding the polymer. In this case, the permittivity ratio between the particles and the polymer has a crucial role. Indeed, higher is the difference of polarization between the particles and the matrix, lower the electric field inside the agglomerate. This observation strengthens the notion of occluded polymer inside agglomerates if they are not compact.

The effective permittivity, the associated R_ε and the maximum electric field are reported in Table 4.6 for all the considered systems. First, the effective permittivity and the associated R_ε of the most compact system 1 are very close to those of well dispersed particles obtained previously (ε'_{eff} of 7.87 and 7.88, respectively). This may come from the fact that even well-dispersed particles are surrounded by effectively occluded polymer, since the electric field is strongly attenuated at the vicinity of the equator. In compact agglomerates, the total occluded volume can be compensated by particles in contact at their equators and leading thus to less occluded polymer.

Then, the results indicate that the permittivity enhancement factor R_ε increases with the volume of polymer inside the agglomerates. These results confirm the effect of

occluded polymer on effective permittivity in composites. As a result, system 4 behaves like a compact system having a higher content of particles.

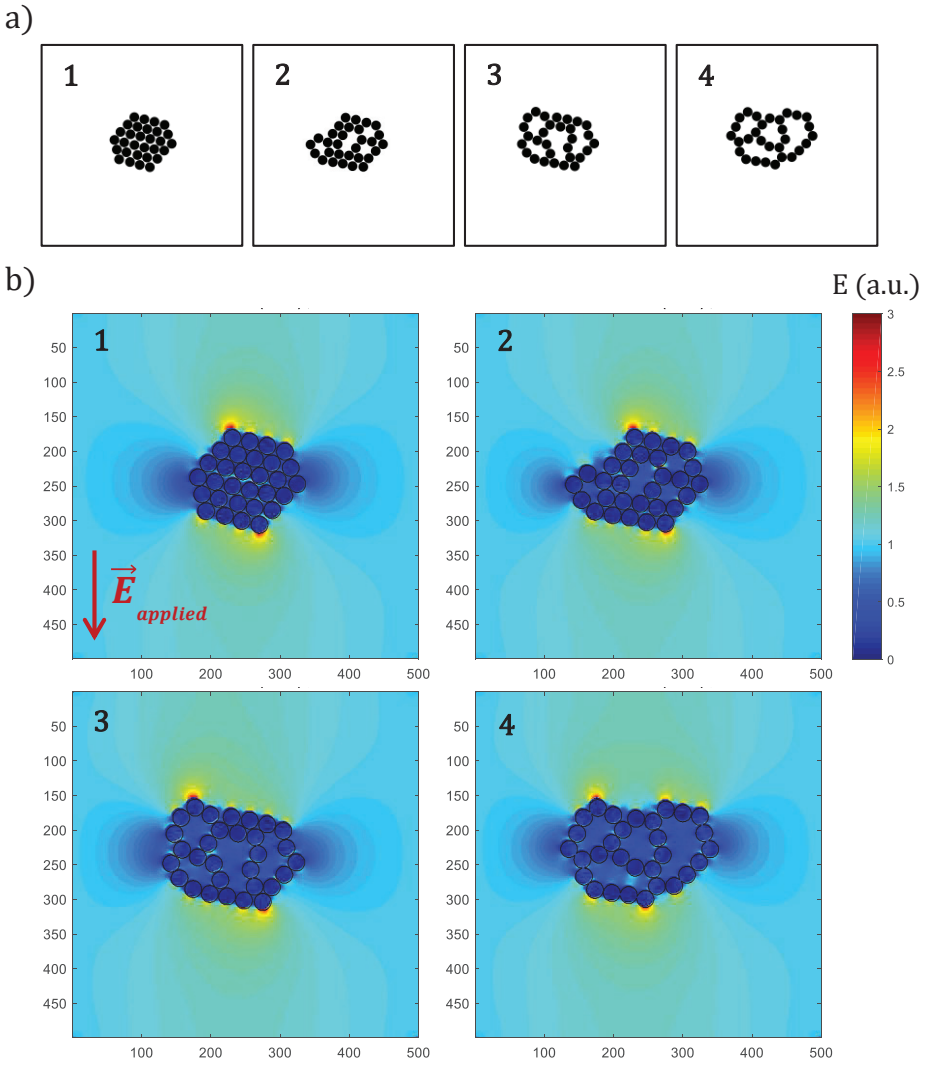

Figure 4.20: Presentation of the 2D systems and their related electric field mapping resulting from the modelling.

Table 4.6: Resolution of the Maxwell equations for composites with 5 vol% of particles with various compactness of agglomerates. ($\varphi_{particle} = 5$ vol%, $\varepsilon_{matrix} = 7$ and $\varepsilon_{particle} = 150$)

Composites	$\varepsilon'_{effective}$	R_ε	$E_{max}/E_{applied}$
1	7.88	1.12	3.0
2	7.91	1.13	4.7
3	8.04	1.15	2.92
4	8.06	1.15	2.94

The results indicate that the compactness of the agglomerates impacts the dielectric properties of composites through the presence of occluded polymer, which increases the effective content of particles and hence the effective permittivity. Considering the strong effect of particle shape factor and orientation on the dielectric properties of composites reported in the literature, the shape and the orientation of the agglomerates must have a large impact as well on the effective permittivity of composites[8,43,53]. In all these works, similar consideration of the occluded polymer volume could be done.

To conclude, the experimental results and modelling tend to validate the concept of amplification of the matrix permittivity by the high-ε particles, presented in equation (4.8). No significant dependence on temperature and frequency was observed in the frequency range studied (50 – 10^5 Hz).

In the absence of dielectric losses of the $BaTiO_3$ NPs on the whole frequency range, this amplification behaviour would be extended to low frequencies (10^{-2} - 50 Hz). This would correspond to the dash lines in Figure 4.21, that were obtained by multiplying the imaginary part of the neat PVdF-HFP permittivity by the R_ε of the sample S10 and A10. Nevertheless, higher ε" are observed at low frequency in the nanocomposites spectra as compared to the dash line.

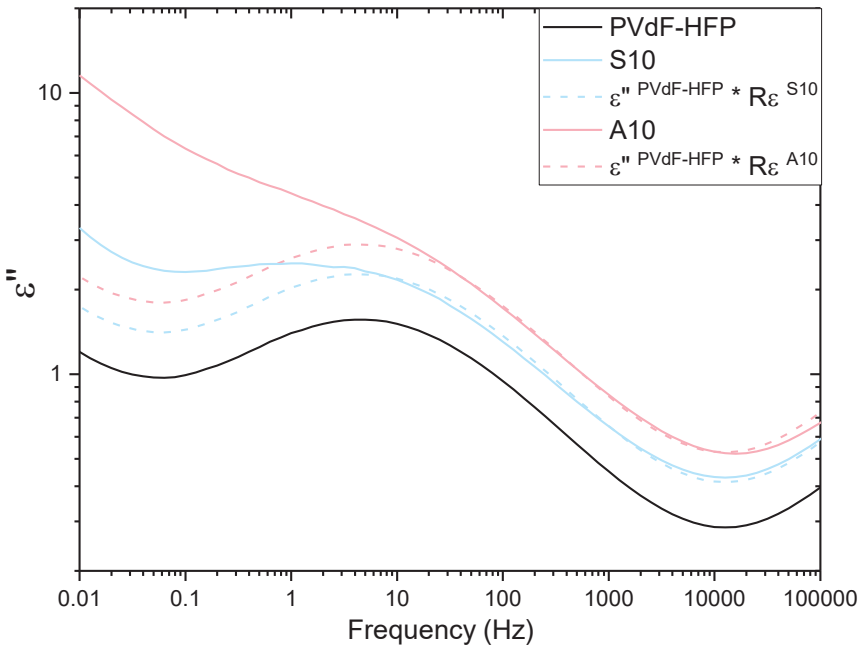

Figure 4.21: Illustration of the shift between the PVdF-HFP curves and those of A10 and S10.

4.3.4 MWS interfacial polarization

In nanocomposites, the contribution observed at low frequency and which cannot be explained by the permittivity enhancement factor only is contained within the fitted relaxation mechanism denoted MWS. We have shown previously that, conversely to the α_a and α_c relaxation processes, the dynamics of the MWS polarization is significantly impacted by the addition of the $BaTiO_3$ NPs. Moreover, the MWS magnitude seems to be much larger in the case of nanocomposites as compared to neat PVdF-HFP (as seen in Figure 4.21). As previously, the magnitude of the fitted MWS polarization $\Delta\varepsilon_c^{MWS}$ is used to investigate its origin in the case of nanocomposites.

The values of $\Delta\varepsilon_c^{MWS}$ are plotted as a function of temperature in Figure 4.22 a) for all the samples. It can be observed that $\Delta\varepsilon^{MWS}$ increases almost linearly as T increases for all the samples. The normalization of these values by those of neat PVdF-HFP, plotted in Figure 4.22 b), shows that $\Delta\varepsilon_{normalized}^{MWS}$ slightly depends on temperature. Both Figure 4.22 a) and b) suggest that $\Delta\varepsilon^{MWS}$ increases with the $BaTiO_3$ NPs content and is higher for nanocomposites with agglomerated NPs as compared to well dispersed.

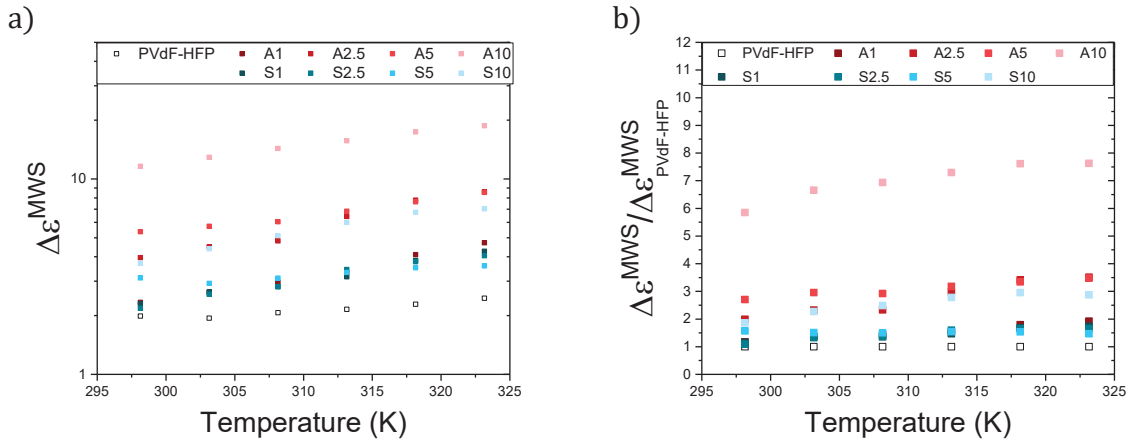

Figure 4.22: Evolution of a) $\Delta\varepsilon^{MWS}$ and b) its equivalent values normalized by the neat PVdF-HFP for all the samples studied.

To better compare the relationship between $\Delta\varepsilon^{MWS}$ and $BaTiO_3$ NPs, $\Delta\varepsilon_{normalized}^{MWS}$ has been averaged between 298 and 323 K to give an average MWS enhancement factor, denoted R_{MWS}, which is plotted in Figure 4.23 a). It shows that R_{MWS} increases as the $BaTiO_3$ NPs content increases and is higher in the case of agglomerated NPs as compared to well dispersed NPs between 2.5 and 10 vol%. Indeed, at 10 vol% of NPs, the nanocomposite A10 exhibits a R_{MWS} of almost 7 whereas it is about 2.5 in S10. Thus, the presence of the $BaTiO_3$ NPs induces an increase of the magnitude of the MWS relaxation. It is important to remind that, while the MWS polarization is homogeneous in the polymer matrix, it is also subject to the amplification provided by the large polarization of the $BaTiO_3$ NPs observed on the α_c relaxation at higher frequencies (50 –

10^5 Hz). In this case, R_{MWS} should include R_ε. To consider these potential cumulative effects, a modified MWS enhancement factor R'_{MWS} has been introduced. It is defined as R_{MWS} divided by the R_ε value related to each sample, as defined in section 4.3.2 (see equation (4.21)).

$$R'_{MWS}(\varphi,\gamma) = \frac{R_{MWS}(\varphi,\gamma)}{R_\varepsilon(\varphi,\gamma)} = \frac{< \Delta\varepsilon^{MWS}(\varphi,\gamma) >}{< \Delta\varepsilon^{MWS}_{PVdF-HFP} > R_\varepsilon(\varphi,\gamma)} \qquad (4.21)$$

where φ is the $BaTiO_3$ NPs content, γ a structural parameter associated to the NPs dispersion state, $< \Delta\varepsilon^{MWS} >$ and $< \Delta\varepsilon^{MWS}_{PVdF-HFP} >$ are the average values of $\Delta\varepsilon^{MWS}$ and $\Delta\varepsilon^{MWS}_{PVdF-HFP}$ between 298 and 323 K respectively.

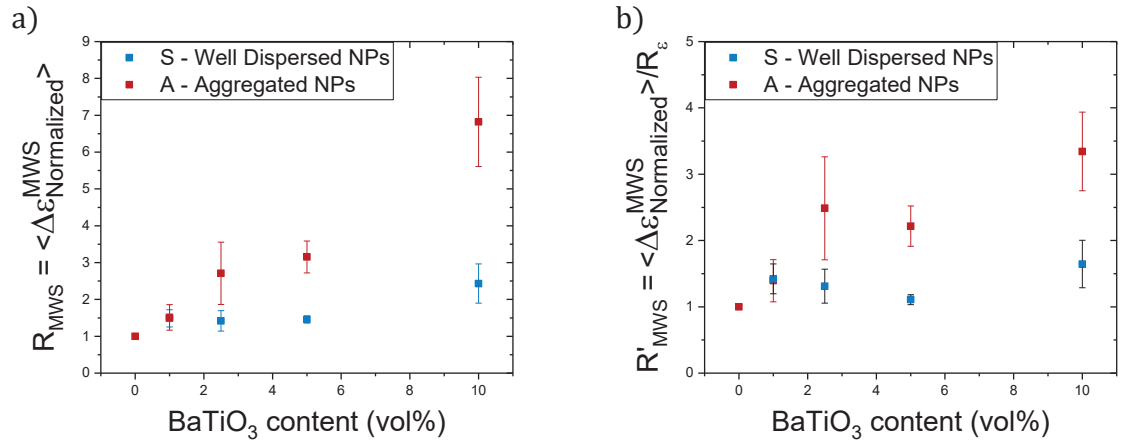

Figure 4.23: Evolution of a) R_{MWS} and b) R'_{MWS} as a function of the $BaTiO_3$ NPs content for both well dispersed and agglomerated systems.

The evolution of R'_{MWS} as a function of the $BaTiO_3$ NP content is plotted in Figure 4.23 b). Although $R'_{MWS}(\varphi,\gamma)$ is attenuated with respect to R_{MWS} when the factor R_ε is considered, its evolutions with both the $BaTiO_3$ NPs content and the dispersion state exhibit similar trend as compared to R_{MWS}.

This observation confirms that another effect is involved in the magnitude enhancement of the MWS polarization in nanocomposites. The origin of this effect cannot be attributed to impurities introduced in the samples during the fabrication process: neat PVdF-HFP films having followed the same process as used for nanocomposites (i.e. sonication) have shown similar dielectric properties as neat PVdF-HFP films obtained with a standard fabrication process. As a consequence, this effect is likely to come from the presence of $BaTiO_3$ NPs. Moreover, the dynamics of the MWS polarization being different between the PVdF-HFP and nanocomposite samples, the enhancement of the MWS magnitude cannot be simply the result of the amplification of the neat PVdF-HFP MWS polarization.

Since MWS polarization mechanisms are closely related to the local heterogeneity of the conductivity in the materials, the fitted conductivity must be analysed to further investigate the origin of the MWS polarization in the nanocomposites. In Figure 4.24, the conductivity is plotted as a function of temperature for all the samples. As expected from thermally activated processes, the conductivity increases as temperature increases for all the samples. Since the conductivity is likely to be impacted by both the EP polarization and the drying of the samples at high temperature, it is only considered around RT where it reflects the conductivity of charge carriers in the bulk of the samples. Thus, near RT, PVdF-HFP has the lowest conductivity among all the samples and the conductivity of the nanocomposites increases as the $BaTiO_3$ NP content increases. This result shows that the $BaTiO_3$ NPs increase the conductivity in the nanocomposites as compared to the neat PVdF-HFP.

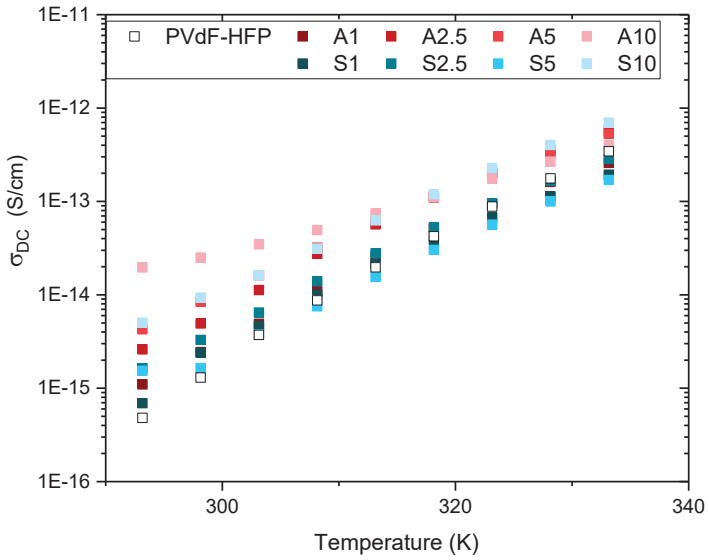

Figure 4.24: Fitted conductivity of the PVdF-HFP:$BaTiO_3$ NPs nanocomposites and neat PVdF-HFP as a function of temperature.

The influence of drying the samples on the dielectric properties have been studied by BDS on the neat PVdF-HFP, S10 and A10 samples which are the extreme cases. Figure 4.25 a) presents the R_{MWS} values as a function of the $BaTiO_3$ NP content for dried samples. The normalization was done with neat PVdF-HFP data obtained at RH50. It is observed that $\Delta\varepsilon^{MWS}_{PVdF-HFP}$ is not impacted by the relative humidity (RH). However, R_{MWS} values are much lower for the dried A10 and S10 nanocomposites as compared to those at RH50.

The evolution of the conductivity as a function of temperature is plotted in Figure 4.25 b). In PVdF-HFP, the conductivity is higher near RT after the drying process. This

observation is counterintuitive. It could be related perhaps to the partial melting of the secondary crystalline phase during the drying process, leading to easier charge carrier migration and so to higher conductivity. Indeed, the conductivity of the neat PVdF-HFP conditioned at RH50 increases up to the conductivity of the dried PVdF-HFP with increasing temperature. This could be related to the partial melting of the secondary crystalline phase during the BDS analysis (see Figure 2.18 and Figure 4.4).

Then, Figure 4.25 b) shows that drying slightly decreases the conductivity of the nanocomposite S10. In the case of the nanocomposite A10, the conductivity decreases about one order of magnitude after drying.

Finally, Figure 4.25 c) shows the evolution of the relaxation time as a function of temperature. In neat PVdF-HFP, drying does not affect the dynamics of the MWS relaxation. Conversely, in samples A10 and S10, the dynamics of their MWS relaxations are significantly modified by drying. Moreover, these dynamics exhibit almost identical behaviour after drying.

The water uptakes in neat PVdF-HFP, A10 and S10 samples were checked by Karl Fisher measurements. Water contents of 0.15 and 0.14 wt% were found for S10 and A10 respectively with an uncertainty of 0.03%. The water uptake of neat PVdF-HFP was found to be very similar to those of blank samples used to calibrate the measurements which indicates a water uptake lower than about 0.03 wt%. This indicates that the water uptake in nanocomposites comes from the $BaTiO_3$ NPs.

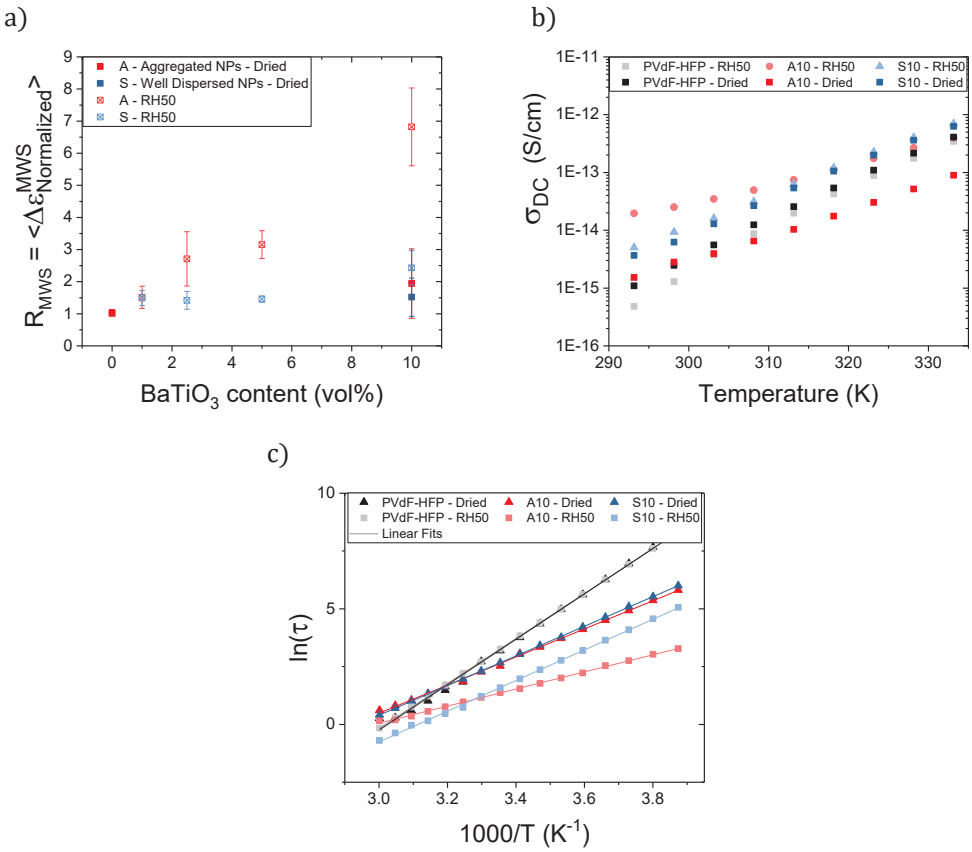

Figure 4.25: Effect of the relative humidity (RH) on a) $\Delta\varepsilon^{MWS}_{Normalized}$ as a function of the $BaTiO_3$ NP content, b) the conductivity as a function of T, and c) τ^{MWS}as a function of 1000/T, for the neat PVdF-HFP, A10 and S10 samples measured after being dried.

Discussion

Considering the above-mentioned results, several relationships can be highlighted:

First, the relatively high water uptake (about 0.14 wt% at RH50) of the nanocomposites A10 and S10 as compared to neat PVdF-HFP indicates that water is provided by the $BaTiO_3$ NPs in A10 and S10. This may be expected from the hydrophilic surface (see section 2.3.1) of the $BaTiO_3$ NPs that tend to adsorb water from ambient air.

Concerning the dielectric properties, the drying step has no significant effects on the MWS polarization and the DC conductivity of neat PVdF-HFP which is consistent with its very low water uptake. However, the drying step significantly affects the MWS polarization of the nanocomposites A10 and S10. Since MWS polarization is related to heterogeneous conductivity in materials, these results suggest the presence of water assisted conduction phenomena in nanocomposites.

As mentioned before, both the conductivity and the MWS magnitude observed at RH50 in nanocomposites increases with the $BaTiO_3$ NP content increases. Moreover, these two parameters are also found to be higher in nanocomposites with aggregated NPs as compared to well dispersed, at RH50. Thus, both MWS magnitude and the

conductivity are related to these water-assisted conduction phenomena taking place at the interfaces between the $BaTiO_3$ NPs and the PVdF-HFP matrix. These conduction phenomena would be enhanced by the local percolation of the NPs.

From the mentioned-above elements, the most probable origin of the MWS polarization observed in nanocomposites is the presence of water on the surface of the NPs.

Interpretation

Thus these results can be interpreted as follows (illustrated in Figure 4.26):

Water-assisted conduction phenomena take place at the surface of the $BaTiO_3$ NPs. The particles thus have a higher conductivity than the PVdF-HFP matrix. In that case, the polarization mechanism fitted as "MWS polarization" would contain two different contributions: the intrinsic MWS polarization of the polymer matrix (denoted MWS_1) and a new polarization mechanism (denoted MWS_2), taking place at the interfaces between the NPs and the polymer. This would explain that the dynamic of the global MWS polarization is different in nanocomposites as compared to neat PVdF-HFP. Then two case may be considered:

- In nanocomposites at RH50, the dynamics of the MWS relaxation is driven by the MWS_2 relaxation (polarization at the interface between the $BaTiO_3$ NPs and the PVdF-HFP matrix) whose magnitude is high due to the presence of water at the interfaces. Thus, $\Delta\varepsilon_c^{MWS}$ increases as the $BaTiO_3$ NP content increases. Moreover, the higher $\Delta\varepsilon_c^{MWS}$ and σ_{DC} observed in the nanocomposites with agglomerated $BaTiO_3$ NPs as compared to well dispersed NPs would be related to the local percolation of the NPs. This percolation would enable charge carrier conduction upon longer distances, thus providing a larger polarization.
- When water is removed by drying, the MWS_2 contribution gets very small due to the strong decrease in the surface conductivity of $BaTiO_3$ NPs. As a result, the MWS is no longer driven by the MWS_2 relaxation: MWS_1 magnitude (polarization within the PVdF-HFP matrix at the interface between amorphous and crystalline phase in the PVdF-HFP) might become comparable to that of MWS_2. This would be consistent with the fact that the dispersion state does not significantly impact the magnitude and dynamics of the MWS polarization any longer. Moreover, the lower conductivity observed in the dried sample A10 would suggest that the conductivity of the NPs in the dried nanocomposites would be lower than the conductivity of the matrix. In this case, in sample A10, agglomerates could represent barriers to electrical charge migration. This barrier effect should be present in sample S10 as well, to a lower extent however, and its conductivity should be intermediate between dried neat PVdF-HFP and dried A10 sample.

However, the conductivity of the dried S10 sample is higher than the conductivity of neat PVdF-HFP.

In addition to this water assisted effect impacting MWS_1, the $BaTiO_3$ NPs may affect the MWS_1 relaxation for three reasons:

(i) The amplification of the electric field is maximum near the NPs where a higher density of ionic impurities is expected. The effect of these impurities might be further enhanced because of field heterogeneity.

(ii) NPs may bring additional ionic impurities (ionisable groups, surfactants, etc) in the PVdF-HFP matrix;

(iii) The increase in the local permittivity would enhance ion dissociation, leading to larger charge carrier density[26].

Such effects could explain the higher conductivity observed in S10 after drying as compared to neat PVdF-HFP as well as the different MWS dynamics observed in dry nanocomposite as compared to neat PVdF-HFP.

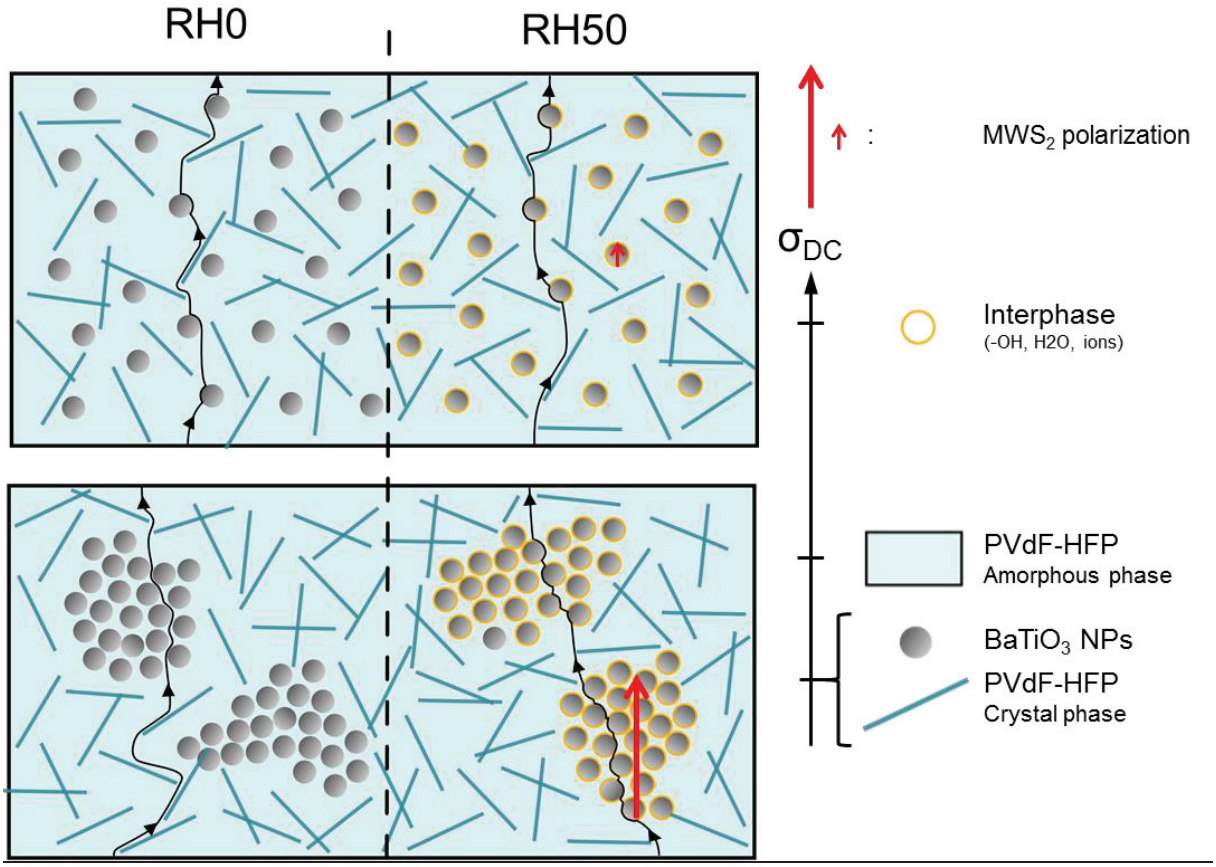

Figure 4.26: Illustration of the interpretation of the low frequency behaviour of $BaTiO_3$:PVdF-HFP nanocomposites as a function of the dispersion state and the Relative humidity (RH). Legend: the size of the red arrows illustrates both the length scale of the charge carrier migration and the magnitude of the related MWS_2 polarization. The conductivity scale shows the qualitative order of the conductivity of all the constituting elements of the nanocomposites.

Conclusion

The fabrication of PVdF-HFP: $BaTiO_3$ nanocomposites with controlled dispersion states have allowed studying the impact of the dispersion state on dielectric properties. Detailed analysis of the dielectric spectra has evidenced a first relationship between the dispersion state of the $BaTiO_3$ NPs and the enhancement of the matrix permittivity by a constant factor R_ε at high frequency (50 - 10^5 Hz) in the case of nanocomposites (Figure). This phenomenon has been attributed to the large and elastic polarization of the $BaTiO_3$ NPs. A clear impact of the $BaTiO_3$ NP dispersion state on the permittivity enhancement ratio R_ε has been evidenced (Figure 4.15). The presence of occluded polymer inside the agglomerates, leading to an increased effective volume fraction of NPs, has been proposed to explain the higher complex permittivity found in the nanocomposites with agglomerated NPs as compared to well-dispersed one. At low frequency (10^{-2} – 50 Hz), the surface conductivity of the $BaTiO_3$ NPs has been identified as the main cause of the interfacial MWS relaxation observed in the nanocomposites at RH50. The agglomeration state of the $BaTiO_3$ NPs has been shown to drastically impact the magnitude and the dynamics of the MWS polarization as well as the DC conductivity of the nanocomposites due to local percolation within the agglomerates.

Chapter 5. Nanoparticle Surface Modification

The initial purpose of this chapter is to study the relationships between the interfacial properties (morphology, electronic structure…) and the dielectric properties in PVdF-HFP:$BaTiO_3$ nanocomposites. As seen in the state-of-the-art chapter, the existence of such a relationship is now recognized by the scientific community and is increasingly investigated. Nevertheless, the modification of the interfacial features often goes along with a modification of the nanoparticle (NP) dispersion state, which has been shown in chapter 4 to also impact the dielectric properties of polymer-based nanocomposites. With the processing method developed in chapter 3, which enables controlling the dispersion state in the final nanocomposite without changing the interfacial properties, the study of the relationships between interfacial features and dielectric properties at equivalent dispersion state should be facilitated.

The modification of the interfacial properties was performed by chemical functionalization of the NP surface. However, the surface modifications are likely to change the Hansen Dispersibility Parameters (HDPs) of the $BaTiO_3$ NPs, which are at the basis of the developed process. This effect will also be discussed in this chapter.

In the first part, the chemical process used to modify the NP surface and the characterization of the new NP surface will be presented. Then, the impact of the surface modification on the HDPs of $BaTiO_3$ NPs will be presented. A third part will be dedicated to the fabrication process and characterization of the nanocomposites. Finally, the dielectric properties of the samples will be presented.

5.1 Particle functionalisation and characterization

5.1.1 Surface modification methods and processes.

The modification of the particle surface is well documented in the literature. In their review, Luo, H. et al draw three main modification routes: (1) physical adsorption, (2) covalent functionalization and (3) inorganic processes such as sol-gel or hydrothermal[82]. These three routes are illustrated in Figure 5.1 and aim to fabricate a core shell structure. In this section, the description will be focused on the fabrication of an organic core-shell structure.

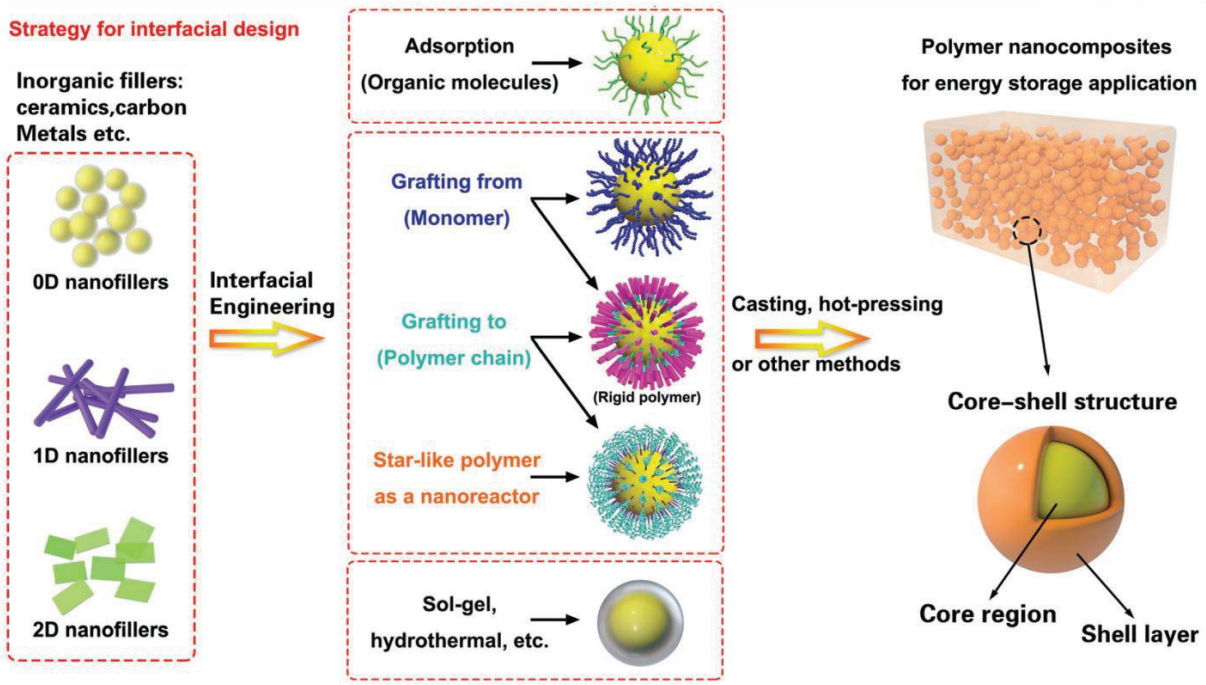

Figure 5.1: General methods to design and control core-shell structured fillers for dielectric capacitor applications[82].

Physical adsorption is easily achieved by dissolution of the modifier into the particle dispersion. The drawback of this technique is that the modifier may be desorbed during the fabrication process and released in the polymer matrix leading to high leakage current.

This drawback may be hindered by covalent grafting of the modifier onto the surface. Different grafting methods exist: (1) the "Grafting to" methods consist in the direct grafting of the modifiers via their reaction with functional groups present on the particle surface that leads to the formation of covalent bonds. (2) The "Grafting from" methods consist in the grafting of initiators using the previous methods followed by a heterogeneous polymerization of a polymer chain onto the initiator by conventional polymerization methods. (3) The creation of an inorganic shell around the particles (sol-gel, hydrothermal, hydrolysis reaction…).

5.1.2 Selection of the modifiers / Grafting method and modifier

As described in the State-of-the-art chapter, three main mechanisms likely to affect interfacial features and dielectric properties in high-permittivity polymer-based nanocomposites have been identified in the literature: (1) passivation of the interface, (2) activation of the interface, and (3) improvement of the affinity (morphology/quality). Due to the difficulty of evaluating the electronic properties (Electron Affinity, Ionization Energy…) of the $BaTiO_3$ NPs and the PVdF-HFP, activating

the interface was difficult. The study was thus focused on the other mechanisms: electrical passivation of the interfaces and improvement of the affinity between NPs and matrix.

Concerning the passivation, the objective is to create a barrier layer to prevent the transfer of electrical charge carriers from the polymer to the NPs and reversely. Thus, the modifier should possess a high band gap. In the wide variety of organic molecules, alkyl chains are among the ones with the highest bandgap. On the other hand, for improving the affinity between PVdF-HFP and $BaTiO_3$ NPs, PMMA seems to be a good candidate. Indeed, some authors report negative mixing enthalpy between PMMA and PVdF, which indicates higher affinity between PVdF and PMMA chains than between two PMMA chains and between two PVdF chains[161].

A grafting-to method was used to modify the surface chemistry of $BaTiO_3$ NPs. It consists in grafting a molecule or a polymer chain on the NPs surface through the formation of covalent bonds. The characterization of the surface of as-received $BaTiO_3$ NPs presented in chapter 2 revealed the presence of surface hydroxyl groups linked to Ti or Ba atoms. These hydroxyl groups were used as functional groups to produce the desired covalent bonds. Thus, the surface modifications of the $BaTiO_3$ NPs were performed using an esterification reaction, which is the reaction between a hydroxyl function and a carboxylic acid function as presented in Figure 5.2. The advantage of this option is the simplicity of the reaction and the easy access to a wide variety of commercially available molecules or polymers with carboxylic acid functions.

Stearic acid was used to graft alkyl chains onto the $BaTiO_3$ NPs surface. In the case of PMMA, a copolymer of PMMA containing carboxylic acid units, Poly(Methyl MethAcrylate-co-MethAcrylic Acid) (PMMA-co-MAA), was selected. Its structure is presented in Figure 5.2. It contains 60 MMA monomers for 1 MAA monomer.

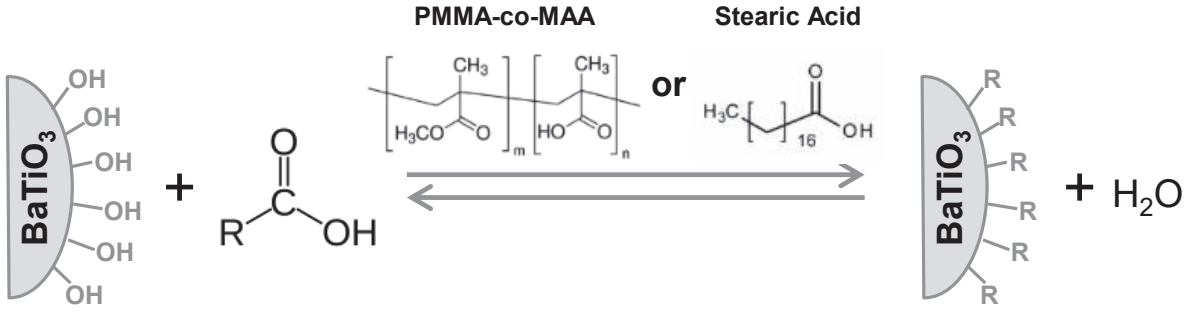

Figure 5.2: Chemical grafting process used for the $BaTiO_3$ NPs surface modifications.

5.1.3 Surface modification assisted by sonication

Several conditions have to be fulfilled to ensure a surface modification of the $BaTiO_3$ NPs of good quality. First, the esterification requires energy to be promoted. Then, the water content has to be kept as low as possible: as it is a product of the esterification

reaction, it promotes the inverse hydrolysis reaction. Heating the reaction media above 100 °C is an efficient way to remove the water produced by esterification. Finally, the dispersion state of the NPs has to be good enough to ensure the grafting reaction occurs on the whole NP surface, thus creating a homogeneous layer of alkyl chain or PMMA. To fulfil these conditions, 2-heptanone was chosen as solvent. Indeed, its boiling point at 150 °C allows heating the reacting media to remove water. A grade of 2-heptanone with a low water content (<0.3%) was chosen. Moreover, the χ_s values associated with the adsorption of stearic acid and of PMMA-co-MAA onto the $BaTiO_3$ NPs surface are 0.1 and 3 respectively in 2-heptanone. χ_s values are calculated from Hansen Solubility Parameters (HSPs) available in the literature. For PMMA-co-MAA, a pondered average of the PMMA and PMAA HSPs was used). Although the Hansen theory predicts a Ra value of 16 between as-received $BaTiO_3$ NPs and 2-heptanone, the high adsorption parameter χ_s of PMMA-co-MAA should provide stable suspension. For stearic acid, which has a χ_s of 0.1, no adsorption is expected, and the suspension stability might thus be a problem. This issue was solved by using sonochemistry to perform the reaction. It consists in sonicating the reacting media to promote the reaction. Such a process presents the advantages to both stir the reacting media, provide local heating and break the electrical double layer which surrounds the NPs and may act as a barrier to functionalization[113,162]. Moreover, it allows maintaining a good dispersion state throughout the chemical reaction.

Three batches of NPs were fabricated: the first one is a reference, denoted $BaTiO_3^{ref}$, which follows all the functionalization process steps without any modifier addition, from the NPs dispersion up to the rinsing and drying process. The second and third ones are $BaTiO_3$ NPs functionalized with PMMA-co-MAA and stearic acid, denoted PMMA@$BaTiO_3$ NPs and alkyl@$BaTiO_3$ NPs respectively.

First, three $BaTiO_3$ NPs suspensions were prepared in 2-heptanone at 1 vol%. The suspensions were then sonicated for 1 hr in order to dis-agglomerate the NPs and 10 wt% of PMMA-co-MAA and stearic acid (referred to the NP content) were separately introduced in two of the prepared suspensions. This would correspond to about 5 $mg.m^{-2}$ considering a NP specific surface of 20 $m^2.g^{-1}$ (see chapter 2) and thus to an excess of modifier considering a target of 1-2 $mg.m^{-2}$. The suspensions were stirred for 2 hrs in order to solubilize the modifiers. Additional sonication steps of 10 minutes were performed in order to promote esterification.

The NP suspensions were then left under stirring for 1 hr and centrifuged. The modified and reference $BaTiO_3$ NPs were then rinsed twice with 2-heptanone, once with MEK, once with Ethanol and finally once with Acetone. Each rinsing step consists in centrifuging the mixture in order to remove the excess of modifier solubilized in the

solvent, followed by replacing the solvent and performing a short sonication step (30s) at low (gradually decreased from 30 W to 10 W) power to redistribute the NPs. After each of the last three centrifugations, control samples were taken in order to assess that the unreacted modifier initially introduced in excess was removed. The resulting modified $BaTiO_3$ NPs, the reference and the control samples were then dried under vacuum at 80 °C for 60 hrs and stored in glass vials.

5.1.4 Characterization of the modified nanoparticles

The three $BaTiO_3$ NPs batches were analysed by TGA and ATR-FTIR after drying. The mass contents of the modifier were determined by integrating the weight loss peaks from TGA. After 6 rinsing steps, the mass losses measured in TGA do not change significantly any longer.

Figure 5.3 presents the TGA results of the three final NP batches. Both modified NPs exhibit larger weight losses around 300-350 °C as compared to $BaTiO_3^{ref}$. As mentioned in chapter 3, these weight losses include the degradation of both the modifier and the chemical groups present on the NP surface (mainly hydroxyl groups). Considering that the three batches have followed very similar processes, it can be hypothesized that the weight loss observed for $BaTiO_3^{ref}$ at 300-350 °C is also present in the two modified batches. Then, the weight fraction of the modifier layer can be calculated by subtracting the weight loss of the $BaTiO_3^{ref}$ NPs to the total weight loss of the PMMA@$BaTiO_3$ and Alkyl@$BaTiO_3$ NPs. The weight losses determined by integration of the peak and the corresponding modifier weight content are reported Table 5.1.

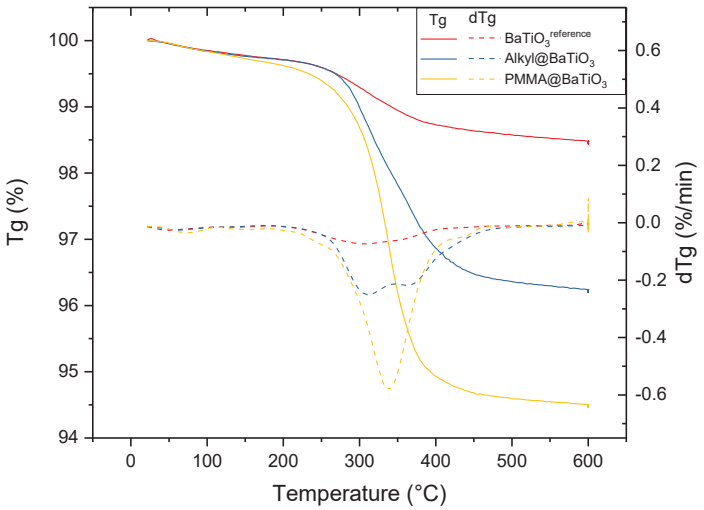

Figure 5.3: TGA of the $BaTiO_3$ NPs modified with stearic acid and PMMA-co-MAA compared to the reference batch of $BaTiO_3$ NPs. Analyses carried out under dried N_2/O_2 (80/20). Temperature ramp set at 10 °C/min (Tg denotes the relative mass loss).

Table 5.1: TGA result of the three $BaTiO_3$ NPs batches after the functionalization process. *The adsorbed amount in $mg.m^{-2}$ is calculated with a specific surface of 20 $m^2.g^{-1}$ (measured in section 2.1.2).

Sample	Integrated mass loss (%)	Estimated modifier content (%)	Estimated adsorbed amount* (mg/m^2)	Density of functionalization (function/nm^2)	Theoretical thickness (nm)
$BaTiO_3^{reference}$ NPs	0.7	0	0	-	-
PMMA@$BaTiO_3$ NPs	4.5	3.8	1.9	0.2	1.6
Alkyl@$BaTiO_3$ NPs	2.9	2.2	1.1	2.3	1.2

The TGA clearly indicates the presence of the modifier onto the surface of the NPs. No irreversible adsorption of Stearic acid on the NPs is expected because of its low molecular mass that does not ensure multiple adsorption sites per molecule. Moreover, the adsorption parameterχ_s of 0.1 predicts no significant adsorption of acid stearic on the $BaTiO_3$ NP surface. As a result, its presence onto the surface of the $BaTiO_3$ NPs highly suggests the formation of covalent bonds, as expected from the esterification reaction.

Considering 1.1 $mg.m^{-2}$ of modifier grafted onto the surface, the density of functionalization would be of 2.3 ester function per nm^2. This value is rather high considering the low density of hydroxyl groups expected on the as-received $BaTiO_3$ NPs (from zeta potential analysis in section 2.1.2) and the maximum density which should be about 10 hydroxyl groups per nm^2 (supposed from the number of atoms of Ti or Ba present in 1 nm^2 of a cubic (001) surface and susceptible to form hydroxyl groups). This would correspond to a homogeneous layer of about 1.2 nm considering NPs of average diameter 50 nm.

In the case of PMMA-co-MAA, the high adsorption parameter suggests that a large amount of modifier should be adsorbed onto the $BaTiO_3$ NPs surface. It follows that its presence onto the NP surface does not necessarily imply that the covalent bonds are formed. Considering 1.9 $mg.m^{-2}$ of PMMA-co-MAA deposited onto the surface, the density of functionalization would be about 0.2 ester function per nm^2 (coming from the reaction of the methacrylic acid with the hydroxyl groups of the NP surface) which would correspond to about 10 grafting points per PMMA-co-MAA chain. This value is rather low as compared to Alkyl@$BaTiO_3$ NPs. This is due to the low fraction of acid functions (MAA) per PMMA-co-MAA chain (about 1 acid function for 60 MMA monomers). For PMMA@$BaTiO_3$ NPs, the deposited PMMA-co-MAA would correspond to a homogeneous layer of 1.6 nm considering NPs of average diameter 50 nm. Thus, in addition to TGA, FTIR was performed to identify the chemical species and the formation of ester functions.

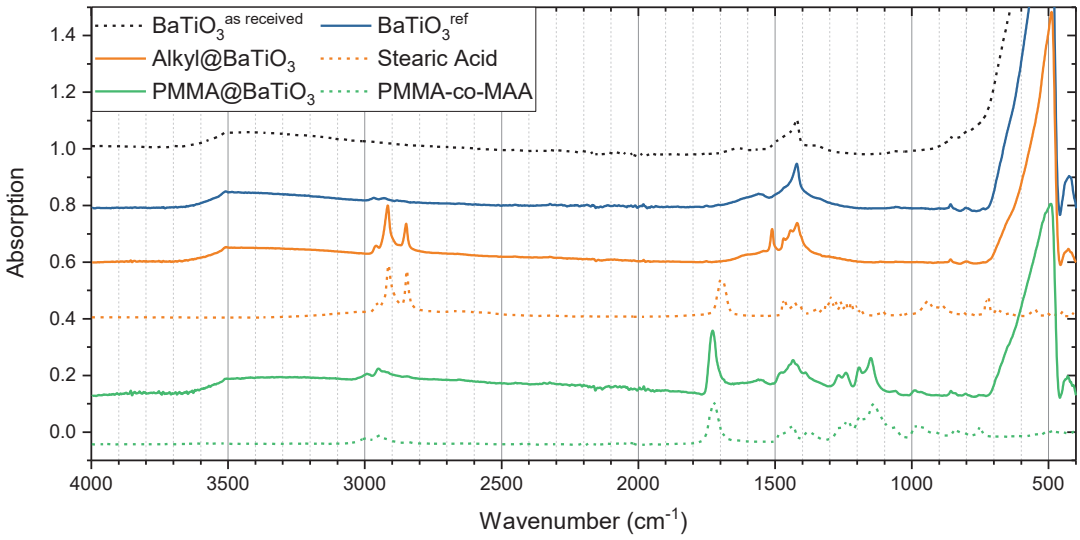

Figure 5.4: ATR-FTIR spectra of the $BaTiO_3$ NPs modified with stearic acid and PMMA-co-MAA compared to the reference $BaTiO_3$ NPs batch and the pure modifier spectra.

Figure 5.4 presents the FTIR spectra of the three $BaTiO_3$ NPs batches and of the as-received modifiers. By comparing the IR spectrum of Alkyl@$BaTiO_3$ NPs to the reference and to the neat stearic acid, the appearance of the typical signature of the alkyl chain around 2900cm^{-1} clearly demonstrates the presence of the alkyl chains on the NP surface. In addition, the Alkyl@$BaTiO_3$ NPs spectrum does not exhibit the band at 1700 cm^{-1} which is present in the neat stearic acid spectra. This band corresponds to the C=O vibrations of the carboxylic acid. However, the formation of aliphatic ester functions should produce an absorption band at a similar wavenumber. Instead of this, a band appears at 1550 cm^{-1}. It may correspond to the carbonyl whose frequency was decreased by the chemical environment. Indeed, the formation of hydrogen bonds tends to lower the C=O frequencies of ester. Moreover, the presence of an electronegative atom directly bonded to the alcoholic oxygen of the ester tends to increase the frequency[115]. In our case, the inverse effect could be expected since the atom on which the ester is formed can be either Ba or Ti and both of them are highly electropositive (0.9 and 1.5 respectively, compared to 2.5 for the C and 3.5 for the O). Thus, this shift of the carbonyl band may be considered as an indirect proof that carbonyl functions have been grafted onto $BaTiO_3$ NPs.

In the case of PMMA@$BaTiO_3$ NPs, Figure 5.4 clearly shows the presence of the four characteristic bands of the as-received PMMA-co-MAA around 1150-1270 cm^{-1} in the IR spectrum of PMMA@$BaTiO_3$ NPs. This observation confirms the presence of PMMA onto their surface. Nevertheless, the presence of ester function in the MMA unit does not allow assessing the reduction of the characteristic absorption band of the carboxylic acid, similarly positioned. The FTIR analyses indicate the presence of PMMA-co-MAA but do not directly confirm the formation of the covalent bonds expected from the esterification reaction. Nevertheless, it can be supposed that the multiple rinsing steps in various solvents including the acetone which is a good solvent of the PMMA (Ra ~ 6) would have led to the desorption of the PMMA-co-MAA if no reaction happened. In addition, the quantitative formation of the ester functions in the case of Stearic acid supports this hypothesis.

As a result, the two functionalization reactions have shown good results. From TGA analysis, it was found that 1.9 and 1.1 $mg.m^{-2}$ of modifiers were deposited for the PMMA@$BaTiO_3$ and the Alkyl@$BaTiO_3$ NPs, respectively. The FTIR have revealed the formation of the ester function in the case of the Alkyl@$BaTiO_3$ NPs, whereas the presence of ester function in the MMA unit combined to the very low grafting density calculated do not allow identifying the formation of the expected ester functions. However, the PMMA-co-MAA deposited on the surface of the PMMA@$BaTiO_3$ is well attached since it resists acetone which is a rather good solvent. It is hypothesised that the adsorption/grafting of the PMMA-co-MAA is irreversible.

5.2 Affinity of modified nanoparticles and Hansen Theory

As described in chapter 3, the interaction between a particle and a chemical species can be described by the Hansen theory through the HDPs (δ_D, δ_P, and δ_H). Indeed, particles in a solvent with similar HDPs as compared to the surface of a particle will be likely to produce a stable suspension. As shown in the State-of-the-art chapter, the surface modification of particles is widely used to improve their affinity with polymers. By modifying the HDPs, surface modification affects the affinity between a particle and a solvent or a polymer. In this section, the impact of the surface modification on the dispersibility of the modified $BaTiO_3$ NPs in various solvents is studied. The results are then used to qualitatively estimate the modification of the HDPs of the $BaTiO_3$ NPs after surface modification.

5.2.1 Dispersibility of the nanoparticles

The dispersibility of the modified $BaTiO_3$ NPs was first assessed through sedimentation tests in MEK and Ethanol. To do so, six suspensions were prepared by introducing the two modified $BaTiO_3$ NPs and the unmodified reference in the two solvents. The suspensions were stirred with a magnetic stirrer for 2 hrs and a sonication step of 5 minutes was performed in order to dis-agglomerate the $BaTiO_3$ NPs. The suspensions were then manually stirred before being placed between a back light and a camera to allow the monitoring of the sedimentation.

Figure 5.5 presents the pictures taken after different sedimentation times. The sedimentation progress can be estimated by following the position of the sedimentation front marked by the bright/dark limit. In MEK, the unmodified NPs are fully sedimented after 23h. Conversely, complete sedimentation requires about 90 hrs for modified NPs. This difference in sedimentation kinetics illustrates the better affinity between the modified $BaTiO_3$ NPs and MEK. Both modified NPs seem to have turned from “poor” solvents into “good” solvents after surface modifications. In ethanol, the alkyl@$BaTiO_3$ NPs exhibit very fast sedimentation so that most of the NPs have already sedimented after 2 minutes. Conversely, the unmodified $BaTiO_3$ and the PMMA@$BaTiO_3$ NPs are not fully sedimented after 95h. This indicates that the surface grafting of the alkyl chains shifts ethanol from “good” to “poor” solvent.

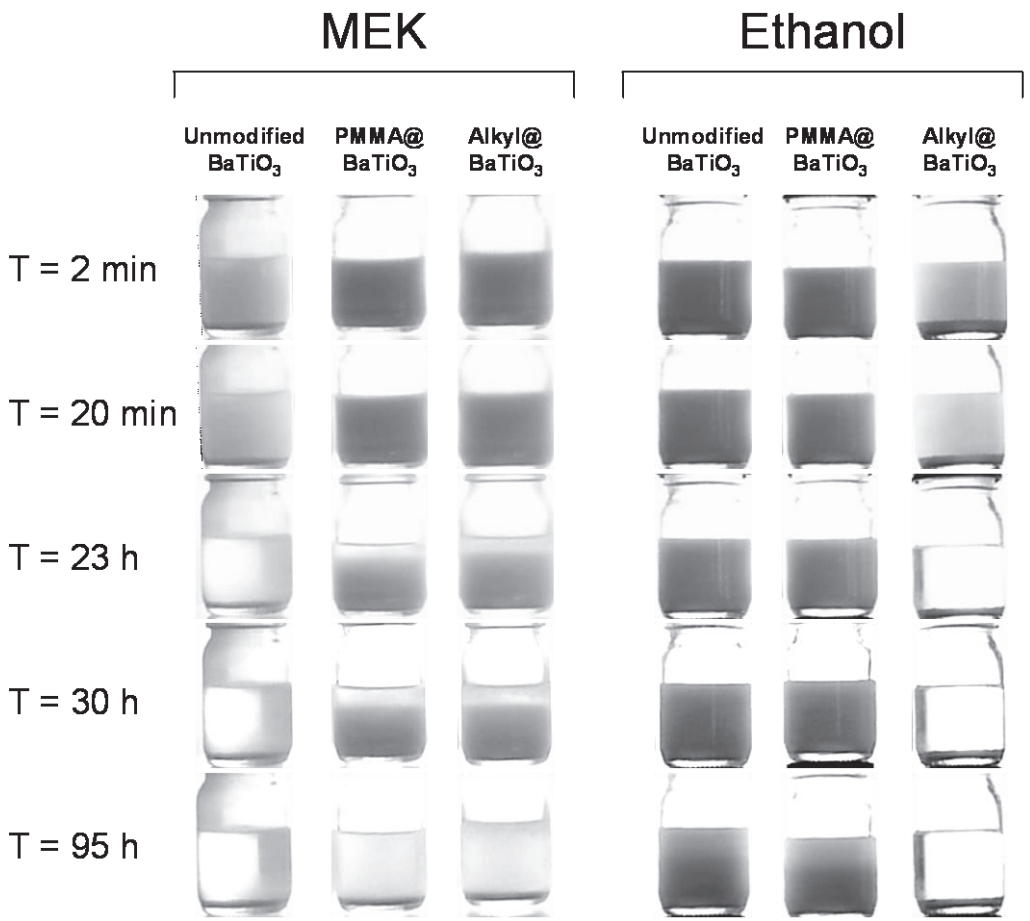

Figure 5.5: Sedimentation test with unmodified $BaTiO_3$ NPs, PMMA@$BaTiO_3$, and Alkyl@$BaTiO_3$ in suspension in MEK, and ethanol. ($BaTiO_3$ 0.1 vol% as compared to MEK or ethanol)

The results of these sedimentation tests suggest that the surface modifications performed onto the $BaTiO_3$ NPs changed the interactions between the NP surface and the chemical environment. Although the non-stability of the ethanol:Alkyl@$BaTiO_3$ NP suspension is clear, the slower sedimentation kinetics observed in MEK for both Alkyl@$BaTiO_3$ and PMMA@$BaTiO_3$NPs only shows an affinity improvement after these modifications. No conclusion can be done on the dispersion state of the suspensions and its associated stability from short term to long term.

The suspension stability of the two modified NPs and the unmodified $BaTiO_3^{ref}$ NPs in MEK were studied by Dynamic Light Scattering (DLS) in order to quantify the improvement in terms of dispersion state and suspension stability. The three suspensions were prepared at 0.1 vol%, sonicated for 10 minutes and then diluted by 10 in order to perform the DLS analyses.

The unmodified $BaTiO_3^{ref}$ NPs exhibit the same stability in MEK as observed in chapter 3.

Although the sedimentation tests have shown a slower sedimentation kinetics in the case of Alkyl@$BaTiO_3$ NPs in MEK as compared to $BaTiO_3^{ref}$ NPs, no significant improvement was revealed by the DLS analysis.

However, an improvement was found in the case of the PMMA@$BaTiO_3$ NP suspension as compared to unmodified NPs: the DLS results presented in Figure 5.6 a) show that the PMMA@$BaTiO_3$ NP suspension at 0.1 vol% in MEK is stable over 10 minutes after the dilution. A second sample was taken in the sonicated suspension which was left 24 hrs resting. The suspension was manually stirred before the sampling to disperse the potentially sedimented agglomerates and then the sample was diluted for the DLS analysis. The result shows similar stability as presented in Figure 5.6 b). It indicates the good stability of the suspension after 24 hrs, meaning that the NPs remain well dispersed (i.e. size distribution centred on 140 nm). Although the sedimentation is not fully prevented, as indicated by the sedimentation test, two hypotheses can be formulated: (1) the PMMA@$BaTiO_3$ NPs do not agglomerate and slowly sediment, or (2) the NPs agglomerate and sediment but simple manual shaking allows the total redistribution of the NPs. This result confirms the improvement of the affinity between the $BaTiO_3$ NPs and MEK after the surface modification with the PMMA-co-MAA.

Similar experiments were performed on the $BaTiO_3^{ref}$ and PMMA@$BaTiO_3$ NP suspensions in dichloromethane (DCM). As observed in section 3.3.3, the $BaTiO_3^{ref}$ NPs quickly sediment and no DLS analysis is possible. Nevertheless, the PMMA@$BaTiO_3$ NP suspension exhibits the same behaviour as observed in MEK, as shown in Figure 5.6 c) and d). Indeed, the suspension was found to be stable after sonication and dilution as well as after 24 hrs of rest and being manually stirred before the dilution for the DLS analysis. This result shows that surface modification with PMMA-co-MAA turns the $BaTiO_3$ NP suspension from completely unstable to very stable in DCM, thus indicating its effect on the affinity between the $BaTiO_3$ NPs and DCM.

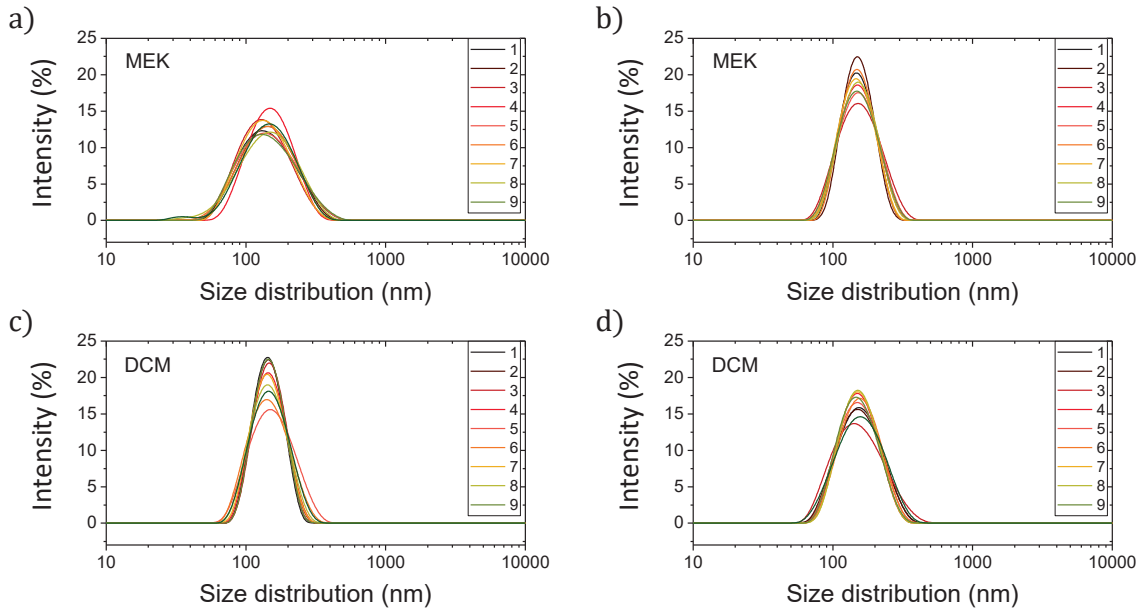

Figure 5.6: DLS analysis of PMMA@$BaTiO_3$ NP suspension in MEK (a and b) and DCM (c and d) after 10 minutes of sonication (a and c) and after 24 hrs of rest following the end of the sonication (b and d).

Finally, by combining sedimentation tests and DLS analyses, the following conclusions can be given on the effect of the NP surface modification processes on the dispersibility of $BaTiO_3$ NPs:

- **First, unmodified $BaTiO_3^{ref}$ NPs and as-received NPs have similar behaviour in suspension in MEK. This suggests that the process has no significant effect on the surface chemistry of the NPs and thus does not change HDPs. This confirms the previous FTIR observations.**
- **The grafting of alkyl chains on the NP surface strongly modifies the dispersibility of the NPs which are not stable any longer in ethanol. This indicates very weak affinity between the NPs surface and ethanol and thus confirms the modification of the $BaTiO_3$ NP surface chemistry.**
- **Conversely, the surface modification with PMMA-co-MAA, which provides a NP surface covered with PMMA, strongly improves the stability of the $BaTiO_3$ NPs in both MEK and DCM. Indeed, PMMA@$BaTiO_3$ NPs are stable on the long term while poor or no stability were found on the suspension with unmodified NPs.**

5.2.2 HDPs of the modified nanoparticles

The drastic changes in the interactions between the modified $BaTiO_3$ NPs and some solvents, as compared to unmodified NPs, constitute clues that can be implemented in the Hansen theory in order to qualitatively assess the evolution of the NPs HDPs after

surface modification. The new HDPs of the surface modified NPs could be determined quantitatively by repeating the complete set of sedimentation tests in 24 solvents, as presented in section 3.3.2.

However, the complete experiment was not reproduced, so that only a qualitative evaluation of the new HDPs of the $BaTiO_3$ NPs is possible. Indeed, one way to qualitatively estimate this evolution is to use the Hull method (see section 3.3.2) after adding or removing solvents from the list of the "good" solvents according to the previous observation concerning ethanol, DCM and MEK. This amounts to assume that all other solvents did not change from "good" to "poor" or reversely. This is, of course, a very strong assumption. The Hull-3 method, which is less impacted by the addition (or removal) of a solvent in (or from) the convex hull, was used to estimate the HDPs of the modified NPs. The HDPs were calculated by removing ethanol from the list of the "good" solvents for Alkyl@$BaTiO_3$ NPs and by adding MEK and DCM for PMMA@$BaTiO_3$ NPs.

The resulting HDPs are reported in Table 5.2 and plotted in Figure 5.7. Table 5.2 shows that no significant modifications are observed on δ_D and δ_p, which stay around 16.5 and 10.6 respectively. Nevertheless, δ_H tends to slightly decrease after both surface modifications:

- **The addition of MEK and DCM (with δ_H of 5.1 and 7.1, respectively) in the "good" solvents of the PMMA@$BaTiO_3$ NPs pulls the HDPs towards the low δ_H values. This result is consistent with the low δ_H of the grafted PMMA and the fact that the hydroxyl groups remaining on the NPs surface are partially or completely covered with PMMA.**
- **The removal of the ethanol (with a δ_H of 19.4) from the "good" solvents of the Alkyl@$BaTiO_3$ NPs moves δ_H towards lower values. This result is consistent with the very low δ_H of the alkyl chains and the lower amount of hydroxyl groups on NP surface after the esterification**

Figure 5.7 illustrates the qualitative evolution of the $BaTiO_3$ NP HDPs after surface modification. Only the trend can be commented on. The displacement of the NP HDP representative point must not be considered to be quantitative at all.

The trends observed for both the positions of Alkyl@$BaTiO_3$ and PMMA@$BaTiO_3$ NPs are consistent with the expected evolution toward the modifier HSPs, which are illustrated by the grey and green arrows on the Figure 5.7.

These results are consistent with the results of Laurens et al. In this work, the evolution of the HDPs was well correlated to the grafting density of the silica NPs[163]**. As a consequence, both works demonstrate that the combined use of NP surface modification and the Hansen theory is an efficient tool to design the interactions involved in a system, to rationalize a nanocomposite fabrication process and thus to tune the final properties of the nanocomposites.**

Table 5.2: New HDPs of the NPs with modified surface as compared to unmodified NPs.

NPs type	δ_D	δ_P $MPa^{1/2}$	δ_H
Unmodified $BaTiO_3$	16.47	10.72	12.24
PMMA@$BaTiO_3$	16.57	10.51	11.2
Alkyl@$BaTiO_3$	16.45	10.62	11.73

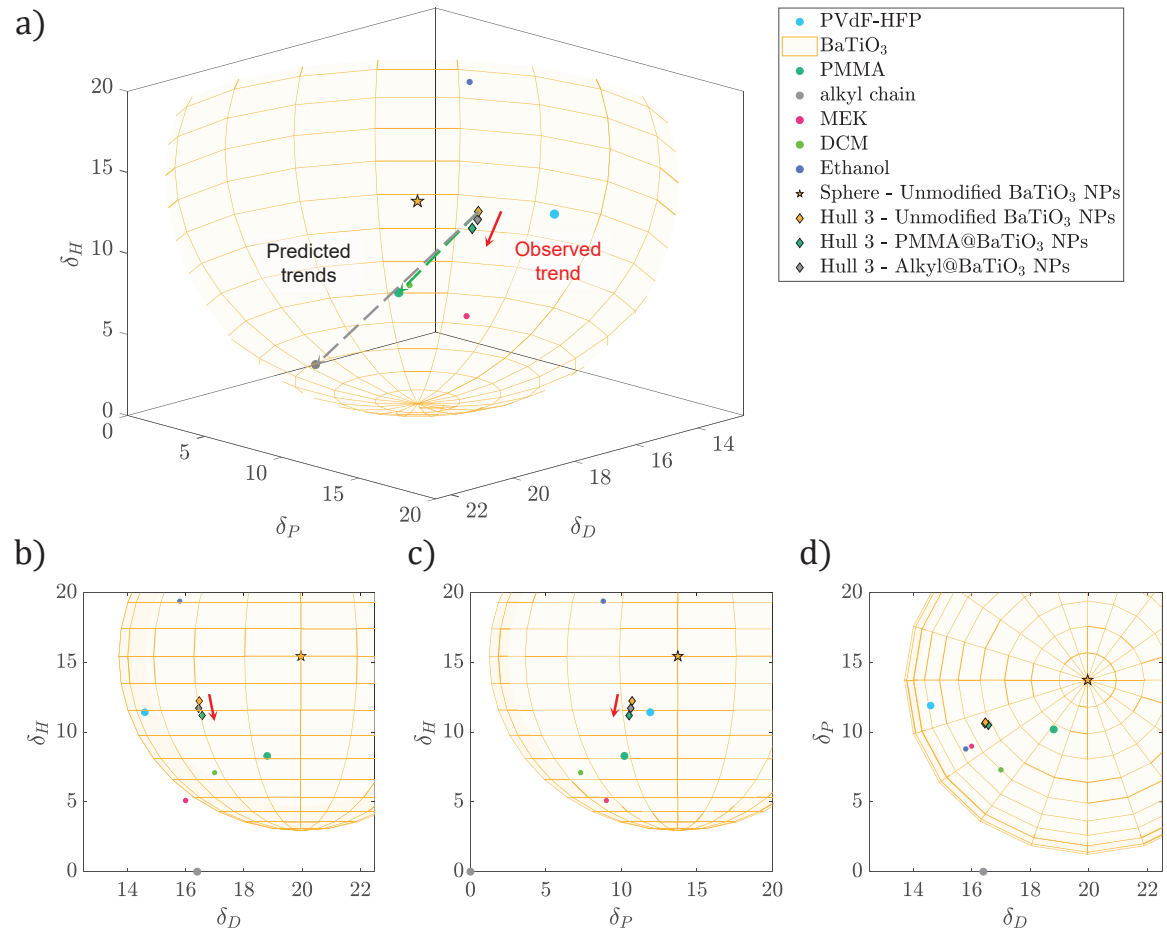

Figure 5.7: Representation of the qualitative evolution of the $BaTiO_3$ NP HDPs after surface modification determined using the *Hull-3* method. The HSPs of PVdF-HFP, PMMA, alkyl chain, MEK, DCM and ethanol are also represented.

5.3 Effect of NP surface modification on nanocomposite dielectric properties

In this section, the effect of the surface modification of the $BaTiO_3$ NPs on the dielectric properties of nanocomposites is studied, using the same methodology as in chapter 4. PVdF-HFP based nanocomposites were fabricated with 5 vol% of surface modified $BaTiO_3$ NPs. These nanocomposites are compared to the equivalent S5 sample introduced in chapter 4 and used here as a second reference fabricated with as-received $BaTiO_3$ NPs. The dispersion states of the NPs in the nanocomposites were characterized by Scanning Electron Microscopy (SEM) and image analysis and the crystalline

structure of the PVdF-HFP matrix was characterized by FTIR and DSC. Finally, the dielectric properties of the nanocomposites were studied by dielectric spectroscopy over a wide temperature range.

5.3.1 Dispersion protocols and sample fabrication

Three different nanocomposites were fabricated by filling the PVdF-HFP matrix with 5 vol% of the three types of $BaTiO_3$ NPs described previously in this chapter. The best dispersion state as possible was targeted for all the nanocomposites.

The solutions used for the solvent casting of the nanocomposite samples were prepared using the protocol described in section 2.2. The modified and unmodified $BaTiO_3$ NPs were introduced in MEK and a 30-minute sonication step was applied in order to disperse the NPs. After this sonication step, both the suspensions with the unmodified $BaTiO_3^{ref}$ and the Alkyl@$BaTiO_3$ NPs exhibited relatively fast sedimentation. Conversely, the PMMA@$BaTiO_3$ NP suspension was quite stable, as already observed previously. Then, PVdF-HFP was added into the three suspensions and the solutions were stirred for 2 minutes at 200 rpm with a magnetic stirrer. However, it is not obvious that PVdF-HFP will adsorb on modified $BaTiO_3$ NPs in the same way as on as-received NPs. For each type of nanocomposites, the suspension was sonicated for 20 minutes after adding PVdF-HFP. As a result, 3 types of nanocomposites were fabricated with various modified $BaTiO_3$ NPs, as detailed in Table 5.3.

Table 5.3: Presentation and nomenclature of the nanocomposite samples.

Sample name	$BaTiO_3$ NP type	Redistribution methods	Dispersion state
S5_ref	Unmodified $BaTiO_3^{ref}$ NPs	20 minutes sonication	Well dispersed $BaTiO_3$ NPs
S5_PMMA	PMMA@$BaTiO_3$ NPs		
S5_Alkyl	Alkyl@$BaTiO_3$ NPs		

5.3.2 Composite morphology and NP dispersion state

This section is dedicated to the morphological characterization of the nanocomposite films. The thickness of the films was first controlled using a micrometre as described in section 2.3.9. All fabricated films were found to be about 20-25 µm thick. Then, the samples were characterized by optical microscopy in order to ensure the absence of large agglomerates (>5 µm) or air bubbles. All samples were found to be optically homogeneous. The sample morphologies and dispersion states at a smaller scale were observed by SEM. For each sample, two pieces were cut in different zones of the film to assess the reproducibility of the observations in the film. These sample pieces were then cryo-fractured, i.e. immersed into liquid nitrogen and broken, in order

to produce brittle fractures and thus smooth cross-section profiles. This procedure allows assessing the dispersion state in the bulk of the materials. All nanocomposite films give reproducible observations in both pieces.

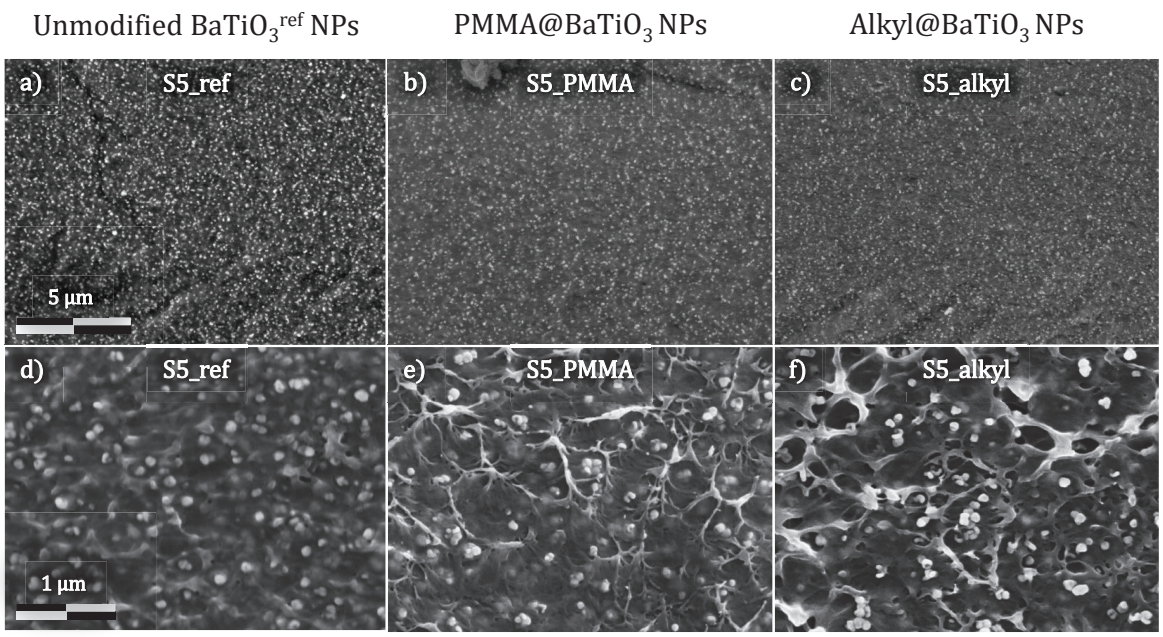

Figure 5.8: SEM images of the nanocomposites fabricated with a) and d) unmodified $BaTiO_3^{ref}$ NPs, b) and e) PMMA@$BaTiO_3$ NPs and c) and f) Alkyl@$BaTiO_3$ NPs. SEM pictures are taken in chemical contrast at magnification of x10k (a, b and c) and in chemical contrast at magnification of x20k (d, e, and f).

Typical SEM images of the nanocomposite samples are presented in Figure 5.8. The first, second and third columns correspond to the nanocomposite samples with unmodified $BaTiO_3^{ref}$, PMMA@$BaTiO_3$ and Alkyl@$BaTiO_3$ NPs respectively. In the first row, Figure 5.8 a), b), and c), SEM images were acquired in chemical contrast at magnification 10k in order to create a good contrast and to well distinguish the $BaTiO_3$ NPs inside the PVdF-HFP matrix. They show homogeneous dispersion states for all the nanocomposite samples. In the second row, Figure 5.8 d), e), and f), SEM images were taken in topographic contrast at 20k in order to observe each $BaTiO_3$ NPs. One can note the presence of many well-separated NPs as well as the presence of some small agglomerates of 3-5 NPs for all the nanocomposites.

In order to better quantify the dispersion state, SEM images were treated by image analysis following the procedure presented in section 2.3.8. The results of these image analyses are presented in Figure 5.9 and compared to the size distribution obtained for sample S5 in chapter 4. The size distributions determined for all nanocomposites show similar narrow bands centred at around 100 nm for the four samples S5_ref, S5_PMMA, S5_alkyl and S5. One can note that the size distribution of the S5_Alkyl sample shows the

presence of a few large agglomerates around 500-800 nm. However, these results indicate that the dispersion states of these samples are nearly identical.

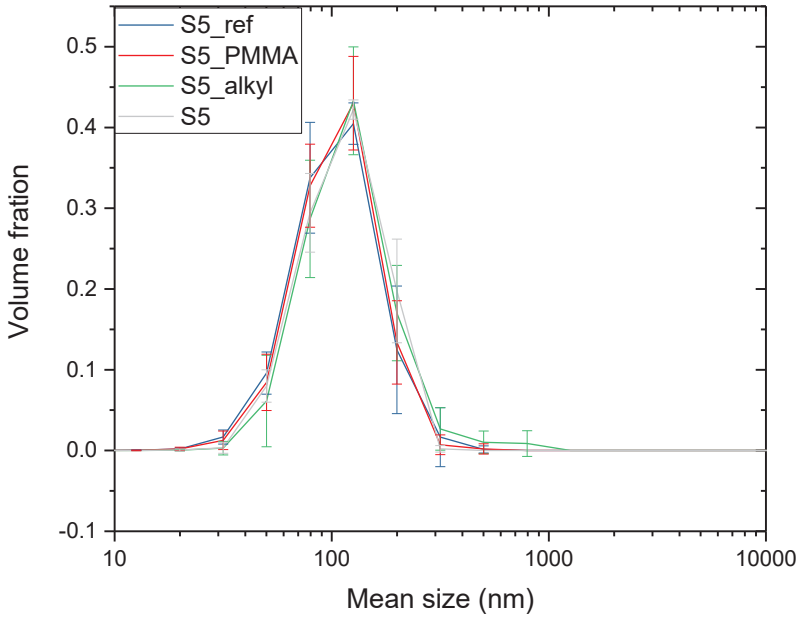

Figure 5.9: Size distribution of the $BaTiO_3$ NPs/agglomerates obtained by image analysis.

5.3.3 Impact of the modified $BaTiO_3$ NPs on crystallinity

The crystallinity of PVdF-HFP in the samples was studied by DSC in order to estimate the impact of the NPs on the crystalline phase. The resulting thermograms are presented in Figure 5.10 and the associated crystalline fractions obtained by integrating the peaks are reported in Table 5.4.

As observed in section 4.2.2, the DSC thermograms exhibit the 3 endothermic melting peaks corresponding to secondary crystalline phases formed during thermal annealing at RT (storage condition) and at 80 °C (drying step at the end of the solvent casting process), and to the primary crystalline phase (peak about 130 °C). However, Figure 5.10 shows a difference of melting temperature of the second melting peak between the samples S5_ref, S5_PMMA and S5_Alkyl and the samples S5 and neat PVdF-HFP. Indeed, the second melting peak of the nanocomposite samples filled with the modified $BaTiO_3$ NPs and their reference is observed at 90 °C. This result was correlated to a suspected temperature deviation of the oven used in the present chapter to dry the samples after the fabrication process. This difference of melting temperature suggests a difference of crystalline morphology. Indeed, it is usually admitted that the melting temperature of the crystalline phase increases with the thickness of the crystalline lamellae[164].

Nevertheless, one can note that the thermograms of S5_ref, S5_PMMA and S5_Alkyl, which were dried in the same conditions, are quite similar and are thus independent of the surface modification. **This indicates that the surface modification of the $BaTiO_3$ NPs has no significant impact on the crystalline morphology. Moreover, the crystalline fractions of the samples, reported in Table 5.4, are all about 37-38%, which suggests that the surface modifications have no effect on the crystallinity of the samples. It also suggests that changing the drying temperature by 10 °C does not significantly affect the crystallinity. To conclude, surface modification of $BaTiO_3$ NPs has no effect on the crystallization of the PVdF-HFP matrix in nanocomposites as determined by DSC.**

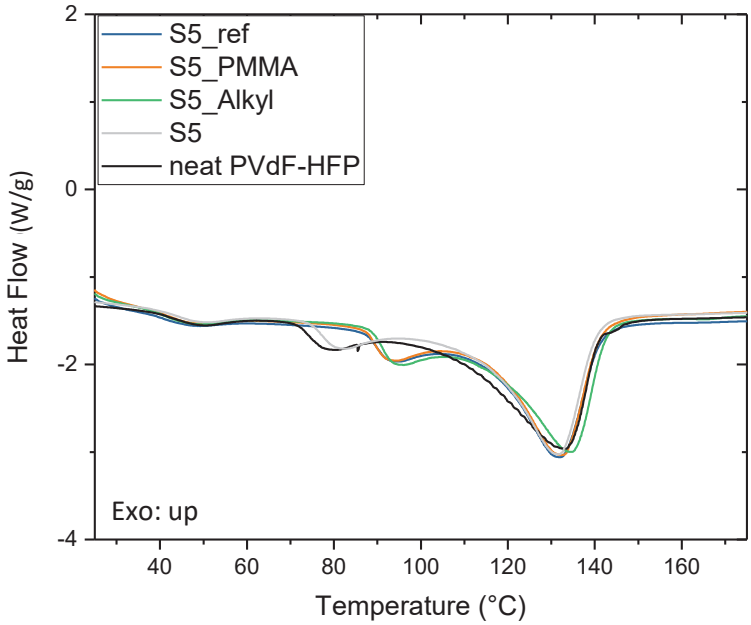

Figure 5.10: First heating ramp of the DSC thermograms of the nanocomposite samples S5_ref, S5_PMMA and S5_Alkyl having well dispersed NPs. (Heat flow in W per gram of polymer.)

Table 5.4: Crystallinity of the nanocomposite samples determined by DSC. (Calculated using the melting enthalpy of the PVdF homopolymer, $\Delta H_m^0 = 104.7\ J.g^{-1}$)

Sample name	Crystalline fraction (wt%)
S5_ref	38± 1 %
S5_PMMA	37 ± 1 %
S5_alkyl	38 ± 1 %
S5	38 ± 1 %
Neat PVdF-HFP	38 ± 1 %

5.3.4 Impact of $BaTiO_3$ NPs on crystalline structure

The crystalline structure of the PVdF-HFP matrix in the nanocomposites S5_ref, S5_PMMA, and S5_alkyl was characterized by FTIR analysis using the method described in section 4.2.3. As presented in Figure 5.11, identical PVdF-HFP signatures are observed in neat PVdF-HFP and in nanocomposites, indicating similar crystalline structures. The method proposed by Cai et al. indicates that the PVdF-HFP is predominantly in the form of the α phase for all the nanocomposites[149]. **These results suggest that the surface modification of the $BaTiO_3$ NPs has no significant effect on the crystalline structure of the PVdF-HFP matrix.**

Therefore, by combining the results obtained by FTIR and by DSC, it can be concluded that the surface modification of the $BaTiO_3$ NPs does not affect the crystalline structure nor the overall crystallinity of the PVdF-HFP matrix significantly.

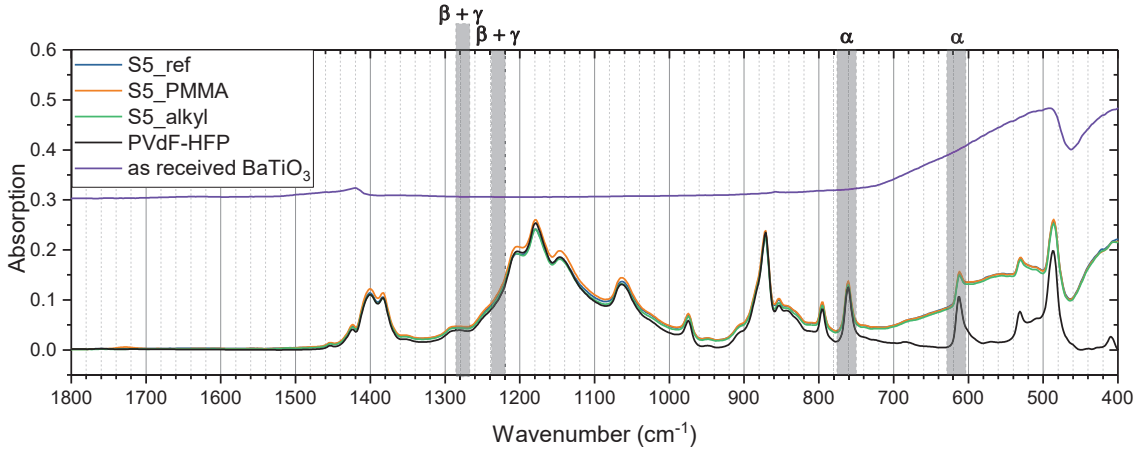

Figure 5.11: FTIR spectra of the nanocomposite samples of S5_ref, S5_PMMA and S5_alkyl compared to neat PVdF-HFP and $BaTiO_3$ NP spectra measured on powder. Typical IR absorption bands of the polymorph α, β, and γ are indicated by the grey rectangles[149].

5.4 Electrical characterization - dielectric spectroscopy

The dielectric properties of the three nanocomposite samples were investigated by performing dielectric spectroscopy in large temperature and frequency ranges. Standard Broadband Dielectric Spectroscopy (BDS – 10^{-2}-10^{7} Hz) was performed on S5_ref, S5_Alkyl and S5_PMMA and High Frequency Dielectric Spectroscopy (HFDS – 10^{6}-10^{9} Hz) was only performed on S5_PMMA and S5_Alkyl following the procedures described in sections 2.3.10 and 2.3.11. In the case of standard BDS, the samples were conditioned at 23 °C and 50% of relative humidity (RH50) before the analysis and analysed in a closed sample cell. For HFDS, the samples were conditioned in the laboratory (20-25 °C and RH40-60).

The dielectric spectra ε'(ω) and ε"(ω) obtained at 25 °C for the three nanocomposites S5_ref, S5_PMMA and S5_alkyl are reported in Figure 5.12. The

dielectric spectra are plotted between 10^{-2} and 10^4 Hz because of a strong contact impedance which alters the dielectric spectra above 10^4 Hz. The onset of this phenomenon is even visible slightly below 10^4 Hz for S5_PMMA.

The three nanocomposites S5_ref, S5_Alkyl and S5_PMMA exhibit higher ε'(ω) and ε"(ω) as compared to neat PVdF-HFP on the whole frequency range considered here (10^{-2} to 10^4Hz). This is consistent with the expected effect of high-ε $BaTiO_3$ NPs.

However, S5_ref exhibits lower ε'(ω) and ε"(ω) than S5. At equivalent dispersion state and volume content in $BaTiO_3$ NPs, more similar dielectric spectra would be expected between 50 and 10^4 Hz.

Finally, only very slight differences are observed between the nanocomposite S5_ref, S5_alkyl and S5_PMMA which suggests that the type of surface modifications does not have a significant impact on the dielectric properties of the nanocomposites at RT.

As previously observed, the dielectric spectra of the nanocomposites exhibit two distinct changes with respect to neat PVdF-HFP. First, between 10 and 10^4 Hz, ε'(ω) and ε"(ω) can be obtained by multiplying the spectra of the neat PVdF-HFP by a factor which does not depend on the frequency. At lower frequencies, between 10^{-2} and 10 Hz, the dielectric spectra of the nanocomposites deviate from the previous trend and exhibit higher values of both ε'(ω) and ε"(ω). In chapter 4, this trend was attributed to an additional MWS polarization mechanism due to water-assisted conduction phenomena on the surface of the $BaTiO_3$ NPs. A similar phenomenon could be expected S5_ref, S5_PMMA and S5_Alkyl.

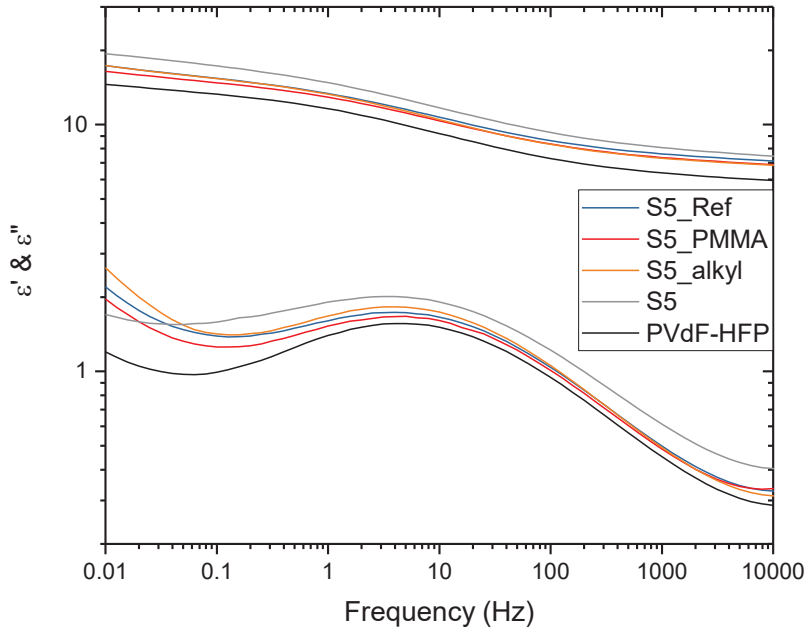

Figure 5.12: Dielectric spectra ε'(ω) and ε"(ω) obtained at 298 K for the three nanocomposites S5_ref, S5_PMMA and S5_alkyl and compared to neat PVdF-HFP. The samples were conditioned at RH50 before the analysis.

The dielectric spectra obtained between 233 and 333 K for the three nanocomposites S5_ref, S5_PMMA and S5_Alkyl were fitted following the procedure described in section 2.3.10. As a result, the magnitudes and characteristic times of the fitted relaxations were obtained as a function of temperature.

Figure 5.13 a) shows the relaxation map with the evolution of the characteristic relaxation times (ln(τ)) of the three polarization mechanisms MWS, α_c, and α_a as a function of 1000/T. They were fitted with the Arrhenius equation for the MWS and α_c relaxations and with the VFT equation for the α_a relaxation. The resulting fits are presented in Figure 5.13 b), c) and d) for the MWS, α_c, and α_a relaxation respectively.

The results show that all the samples exhibit α_c and α_a relaxations with similar dynamics. For the α_a relaxation, VFT parameters of the nanocomposites S5_ref, S5_PMMA, S5_Alkyl are similar to those of neat PVdF-HFP and sample S5 obtained in chapter 4. Concerning the α_c relaxation, the activation energies obtained for the three nanocomposites S5_ref, S5_PMMA, S5_Alkyl are found to be 76 or 77 kJ.mol^{-1}, which is similar to neat PVdF-HFP and sample S5.

These results show that the surface modification of the $BaTiO_3$ NPs does not impact the dynamic of the α_c and α_a relaxation processes of the PVdF-HFP matrix in nanocomposites. Thus, this confirms that NP surface modifications neither affect the crystalline structure, the crystallinity nor the dynamics of the amorphous phase in the

matrix. However, the MWS relaxation of the neat PVdF-HFP and the nanocomposite samples exhibit different dynamics.

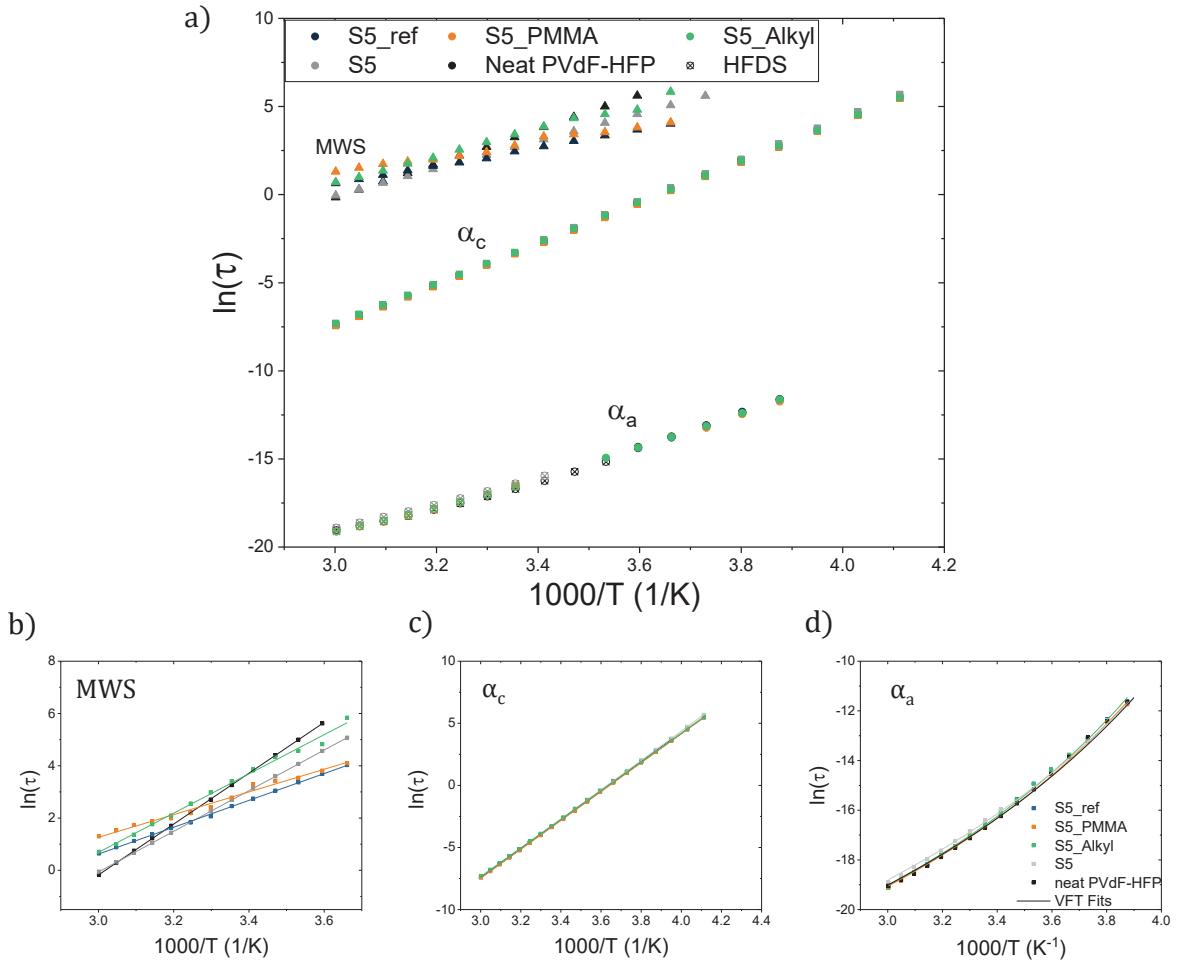

Figure 5.13: a) Global relaxation maps of the PVdF-HFP:$BaTiO_3$ nanocomposites S5_ref, S5_PMMA, S5_Alkyl, compared to their reference S5 and neat PVdF-HFP for the b) MWS, c) α_c and d)α_a relaxation processes.

The fit analysis of the dielectric spectra also provides the magnitude of the α_c and MWS relaxations. As described chapter 4, these values are normalized by those of the neat PVdF-HFP and plotted in Figure 5.14 a) and b) as a function of temperature for the α_c and MWS relaxations, respectively. The permittivity enhancement ratio R_ε is then calculated as the average value of $\Delta\varepsilon^{\alpha_c}_{normalized}(T)$ between 273 K and 323 K as described in section 4.3.2. The R_ε values are reported in Table 5.5 and compared to neat PVdF-HFP and S5. Since the $\Delta\varepsilon^{MWS}_{normalized}$ values of the nanocomposites S5_ref, S5_PMMA and S5_Alkyl exhibit very different trends with temperature as compared to that of neat PVdF-HFP and S5, R_{MWS} is not calculated.

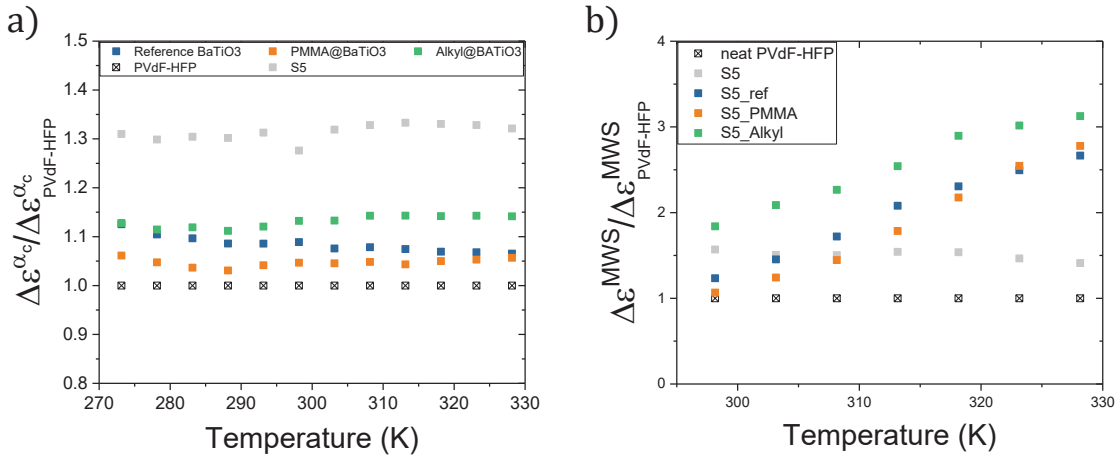

Figure 5.14: Evolution of the magnitude of the a) α_c and b) MWS relaxation normalized in both cases by neat PVdF-HFP as a function of Temperature for the nanocomposite samples filled with the two modified $BaTiO_3$ NPs and their reference and for neat PVdF-HFP and S5 as reference.

Table 5.5: Mean values of R_ε for the nanocomposite samples filled with 5 vol% of the two modified $BaTiO_3$ NPs and their reference and compared to neat PVdF-HFP and the sample S5 filled with 5 vol% of as received $BaTiO_3$ NPs.

Sample	$BaTiO_3$ NP content (vol%)	R_ε
PVdF-HFP	0	1
S5 (from section 4)	5	1.31 ± 0.1
S5_ref	5	1.09 ± 0.1
S5_PMMA	5	1.05 ± 0.1
S5_Alkyl	5	1.13 ± 0.1

Concerning the α_c relaxation, it can be observed in Figure 5.14 a) that $\Delta\varepsilon^{\alpha_c}_{normalized}(T)$ does not significantly depend on temperature for all nanocomposites, as previously observed. Then, the nanocomposites S5_ref, S5_PMMA and S5_Alkyl exhibit relatively similar values of R_ε which are all between those of neat PVdF-HFP and the sample S5. This confirms the observations previously done on the dielectric spectra at 298 K (see Figure 5.12):

- R_ε exhibits different levels in the nanocomposites S5_ref and S5. The only difference between the two samples is that the $BaTiO_3$ NPs of S5_ref have followed the functionalization process without modifier, as a reference. Several hypotheses may be formulated: The first one is that there could be a difference in the dispersion state between the nanocomposites S5_ref, S5_PMMA and S5_Alkyl and the nanocomposite S5 fabricated in section 4 in spite of the very similar size distributions obtained by image analysis. A second hypothesis is that the

difference in the drying step would have changed the morphology of the crystallites, which may affect the magnitude of the α_c relaxation that presumably comes from chain loop motion at the crystal-amorphous interphase and polymer chain twisting inside the crystals[150]. A third hypothesis would be that the functionalization process may have introduced low permittivity impurities into the NPs batches, even though the FTIR analyses do not indicate the presence of impurities.

- Then, the R_ε values of the nanocomposites S5_ref, S5_PMMA and S5_Alkyl are almost all within the standard deviation (10%) associated with the dielectric spectroscopy accuracy. Thus, the observed differences in R_ε are not significant. It can be concluded that the Alkyl and PMMA chains grafted on the $BaTiO_3$ NP surface do not affect the permittivity enhancement of the matrix by the high-ε NPs. This result also confirms that some step of the process may be responsible for much lower R_ε in the case of the S5_ref, S5_PMMA and S5_Alkyl (dispersion state, drying process, impurities…)

Concerning the MWS polarization, Figure 5.14 b) shows that $\Delta\varepsilon^{MWS}_{normalized}(T)$ increases with temperature with the same slope in the case of the nanocomposites S5_ref, S5_PMMA and S5_Alkyl. Conversely, $\Delta\varepsilon^{MWS}_{normalized}(T)$ does not depend on temperature for the sample S5. This suggests that the conduction mechanisms at the origin of these MWS interfacial polarizations are very different in the nanocomposites S5_ref, S5_PMMA and S5_Alkyl as compared to sample S5 and neat PVdF-HFP.

As a consequence, the dielectric properties of S5_ref, S5_PMMA and S5_Alkyl exhibit significant differences with neat PVdF-HFP and sample S5, especially on $\Delta\varepsilon^{MWS}_{normalized}$. It suggests that one or several steps of the fabrication process used in this section impacts the dielectric properties of the nanocomposites. These steps are likely to be part of the surface functionalization process which is the main difference between the samples S5_ref, S5_PMMA and S5_Alky and the sample S5. Indeed, the introduction or the modification of electrical charge carriers could explain the differences of dielectric properties observed between these samples. However, the difference in crystalline morphology suggested by DSC thermograms in Figure 5.10 may also affect the interfacial polarization of the PVdF-HFP matrix.

5.5 Conclusion

In this chapter, a methodology to study the relationship between the interfacial features and the dielectric properties in high permittivity polymer-based nanocomposites was proposed. Two modifications of the $BaTiO_3$ NP surface were

performed: (1) PMMA was grafted using PMMA-co-MAA in order to improve the affinity between the NPs and the PVdF-HFP matrix and (2) Alkyl chains were grafted using stearic acid in order to create an electrically passive layer with high band gap and low conductivity. Both functionalizations were performed using the same process and a batch of $BaTiO_3$ NPs has also followed this process without modifier to serve as a reference.

First, the surface modifications have shown to drastically change the affinity between the $BaTiO_3$ NPs and some solvents. These effects are consistent with the Hansen theory and with the predicted effects of surface modification on the Hansen Dispersibility Parameters (HDPs) of the NPs. It was demonstrated that the surface modification can be used as a tool to develop and improve a solvent casting process in terms of NP dispersion.

Secondly, PVdF-HFP-based nanocomposites were fabricated with the modified $BaTiO_3$ NPs and their reference. The structural and morphological characterizations did not reveal significant impact of the surface modification on the dispersion state, the crystalline fraction and the crystalline structure. However, the drying step, which was effectively realized 10 °C higher than in chapter 4 is found to modify the secondary melting temperature. This corresponds to some change in the morphology of the matrix at the scale of the crystalline lamellae. The dielectric characterizations showed that the surface modification has no impact on the dynamics of the polarization mechanisms (α_a and α_c) intrinsic to the PVdF-HFP. A lower permittivity enhancement factor was found after surface modification as compared to the equivalent nanocomposites S5 filled with as-received $BaTiO_3$ NPs described in chapter 4. The modification of the crystalline morphology has been proposed to explain this observation, since no significant differences were observed between the three nanocomposites S5_ref, S5_PMMA and S5_Alkyl. Concerning the local conduction mechanism revealed by the MWS polarization, the quite different behaviour exhibited by these nanocomposites as compared to neat PVdF-HFP and S5 tends to suggest that the modification process has more impact on the MWS polarization than the type of surface modification. It was hypothesised that the functionalization process could have brought impurities leading to the presence of different charge carriers and thus to different MWS types polarization behaviour.

Conclusion and perspectives

Conclusion

The methodology proposed in this work has consisted in controlling the dispersion state of $BaTiO_3$ Nanoparticles (NPs) in PVdF-HFP matrix in order to separately study the effect of NP dispersion state, of interfacial features and of electronic structure on the dielectric properties in nanocomposites.

Among the variety of systems defined at first in this approach, only PVdF-HFP:$BaTiO_3$ nanocomposites have allowed controlling the NP dispersion state and thus have enabled a detailed experimental study. The examples of Ag and WO_3 NPs show that a successful dis-agglomeration of the NPs at first is crucial in designing NP dispersion state in nanocomposites. The Hansen interaction parameters between PVdF-HFP, $BaTiO_3$ NPs and various solvents were experimentally determined. As a result, two possible ways to produce stable NP suspensions upon the selection of a solvent with specific Hansen interaction parameters have been identified. The first one is based on the strong affinity between the solvent and the NP surface, which produces stable suspensions with or without the polymer. The second one is based on the selection of a solvent whose Hansen Solubility Parameter (HSP) values promote the adsorption of the polymer onto the NP surface, thus stabilizing the NP suspension. Both methods allow fabricating nanocomposite films with good NP dispersion state by solvent casting.

However, the second method, based on the adsorption of PVdF-HFP onto $BaTiO_3$ NPs, requires redistributing the NPs, which agglomerate and sediment before the addition of the polymer. As a consequence, the size of the agglomerates can be controlled by the shear stress applied to the suspension. This technique was used to fabricate two series of PVdF-HFP:$BaTiO_3$ NPs exhibiting 0 to 10 vol% of $BaTiO_3$ NPs with distinct dispersion states.

The effect of the dispersion state on dielectric properties in nanocomposites was studied in these two series of nanocomposites. After having checked that both the presence of NPs and their dispersion state has no significant effect on the structure and the molecular dynamics of PVdF-HFP (amorphous and crystalline phases), the dielectric properties of the samples were characterized by dielectric spectroscopy. As expected, the high permittivity $BaTiO_3$ NPs lead to increase the effective permittivity of the nanocomposites as the content in NPs increases. However, this effect was found more pronounced in nanocomposite with agglomerated NPs as compare to well dispersed NPs and two different effects were discriminated:

1- At frequency between 10^2 and 10^5 Hz, the complex effective permittivity of nanocomposites is simply the enhancement of the matrix one by a factor, called

R_ε which depends neither on temperature nor on frequency in the considered frequency range. R_ε is higher in nanocomposites with agglomerated NPs as compared to well dispersed NPs. The presence of occluded polymer inside the agglomerates that leads to increase the effective content of NP has been proposed to explain such effect of the dispersion state (see Figure 4.19).

2- At frequency between 10^{-2} and 10^{2} Hz, an additional Maxwell-Wagner-Sillars polarization related to water-assisted charge carrier conduction at the surface of the NPs was found to have larger magnitude in nanocomposites with agglomerated NPs as compared to well dispersed NPs. The local percolation of the interphases within the agglomerates was proposed to explain this result. Depending on the respective conductivities of the nanocomposite components, controlling the NP dispersion state allows tuning both ε' and ε" in nanocomposites.

Finally, the properties at the interfaces in PVdF-HFP:$BaTiO_3$ nanocomposites were designed by performing two distinct surface modifications of the NPs by grafting chemical moieties by esterification. The NP surface was then separately modified with 1.9 mg/m^2 of PMMA chains (PMMA@$BaTiO_3$ NPs) in order to improve the affinity between PVdF-HFP and $BaTiO_3$ NPs and with 1.1 mg/m^2 of alkyl chains (Alkyl@$BaTiO_3$ NPs) in order to create an insulating layer at the interfaces. One reference sample, denoted $BaTiO3^{ref}$, followed the whole functionalization process without addition of any modifier to assess the influence of the process conditions.

The stability of $BaTiO_3$ NPs was modified by the surface modification, from very stable to unstable and reversely in some solvents. These results are consistent with the Hansen theory and the expected HDPs evolutions towards the positions of the modifiers. This confirms the possibility of tuning the interactions between NPs and solvent by performing surface modification and thus designing a nanocomposite fabrication process by solvent casting.

Three PVdF-HFP nanocomposites with almost identical dispersion states were then fabricated with PMMA@$BaTiO_3$, Alkyl@$BaTiO_3$ and $BaTiO_3^{ref}$ NPs. No significant effect of the surface modification was found on the structure and the molecular dynamics of the PVdF-HFP. Nevertheless, dielectric spectroscopy revealed significant differences between the nanocomposites filled with $BaTiO_3^{ref}$ NPs and those filled with as received NPs and that were studied in chapter 4. This result suggests that the surface modification process has a strong impact on the dielectric properties of the fabricated nanocomposites. Moreover, the difference in dielectric properties between the three nanocomposites fabricated with PMMA@$BaTiO_3$, Alkyl@$BaTiO_3$ and $BaTiO_3^{ref}$ NPs is very low. This suggests that the effect of NP surface modification onto the complex

permittivity of nanocomposites, at equivalent dispersion state, is lower than that of the process conditions used during the NP surface modification.

Perspectives

This work offers several perspectives. The first concerns the Hansen interaction parameters which were only studied on one polymer:NPs system. Indeed, it would be interesting to extend this approach to other polymers and other NPs to validate the method proposed to fabricate nanocomposites with controlled dispersion state. In addition, a complete characterization of the $BaTiO_3$ HDPs after surface modification by performing sedimentation tests in the whole set of solvents would allow a more quantitative analysis of the surface modification by PMMA and alkyl chains.

Concerning the effect of the NP dispersion state on dielectric properties, a better characterization of the agglomerate structure would allow a deeper insight in the identified mechanism. The volume fraction of occluded polymer within agglomerates may be evaluated in order to bring an experimental evidence of its effect on permittivity enhancement. Similarly, the structure of the agglomerates could be coupled with modelling to estimate the surface conductivity of the NPs. This could then enable the indirect study of the interfacial conductivity through the Maxwell-Wagner-Sillars (MWS) polarization in agglomerates.

Moreover, the fabrication and the dielectric characterization of nanocomposites with intermediate dispersion states could provide further information about the relationship between dispersion state and dielectric properties in nanocomposites. Similarly, repeating this study with a low loss matrix would enable a precise quantification of the MWS polarization mechanism and thus a more precise study of these relationships.

The preliminary work on NP surface modification may constitute a starting point for future work. The identification of the impurities and their origin would enable repeating the NP surface modification experiments and studying the corresponding nanocomposites. Moreover, the nanocomposites must be fabricated at 10 vol% in NPs in order to amplify the differences in dielectric behaviour that seem to be tiny between two different kinds of surface modified NPs. As mentioned before, the study of nanocomposites with various surface modified NPs and various dispersion states could provide information about the relationship between the nature and the conductivity of the interfaces through the MWS polarization in agglomerates.

In all this study, the characterizations of the nanocomposites dielectric properties were performed in the linear regime at low electric fields. Their characterization at high

electric fields is very important to draw the global relationships between dispersion state, interfacial properties or electronic structure and the dielectric properties in nanocomposites. Notably, it would allow studying the compromise between permittivity, dielectric losses, and electrical strength. Also, the impact of NP surface modification is mostly expected at high fields where the interfaces and their electronic structures are thought to drive the electrical insulating properties of nanocomposites.

Appendix A

The initial approach was based on the state of the art about polymer-based nanocomposites for dielectric uses. It included two polymer matrices (PVdF-HPF and Polycarbonate), three kinds of NPs (Ag, WO_3, and $BaTiO_3$) and three approaches of NP surface modification (affinity improvement, passivation and activation of the interface).

The whole approach has depended on our ability to fabricate the nanocomposite materials with controlled NP dispersion state and controlled interfacial properties. Thus, the first step of this work was to elaborate a process in order to meet these requirements. Both melt mixing and solvent casting were considered.

Melt mixing

A twin-screw micro compounder was used. After introducing both the polymer and NPs in the barrel, large shear stresses must be applied to efficiently dis-agglomerate the NPs. With this lab tool, the NP dis-agglomeration can be improved by increasing the rotation speed of the screws, the mixing time, the viscosity of the matrix or the NP content.

The first trials of NP dis-agglomeration by melt mixing have shown rather promising results for $BaTiO_3$ NPs. Indeed, a homogeneous distribution of small agglomerates has been obtained in both PVdF-HFP and PC as shown in Figure A.1 a) and b). However, for Ag NPs, melt mixing has led to the formation of large, nearly macroscopic platelets (100µm to 1mm) in both matrices, as shown in Figure A.1 c) and d). This phenomenon is assigned to the low melting temperature of metallic NPs which promotes their sintering during melt mixing. In the case of WO_3 NPs, safety issues prevented their use in melt mixing. After obtaining such results, we did not investigate the melt mixing process further, even though improvements could still be expected on the dispersion state of $BaTiO_3$ NPs in both matrices.

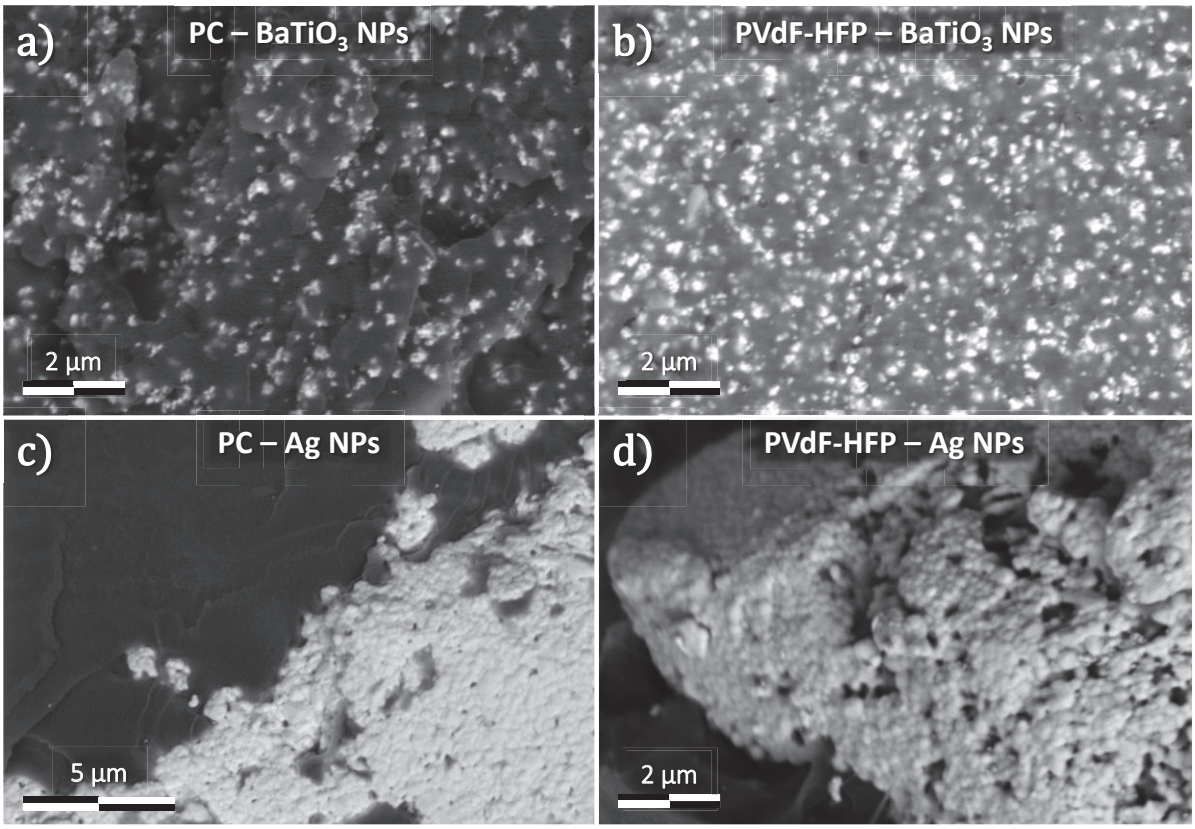

Figure A.1: Scanning Electron Microscopy (SEM) pictures of nanocomposites fabricated by melt mixing with a) PC:$BaTiO_3$ NPs 10 vol%, b) PVdF-HFP:$BaTiO_3$ NPs, c) PC:Ag NPs, and d) PVdF-HFP:Ag NPs. Observation in the cross section obtained by cryofracture. On the SEM pictures, polymers are dark and the NPs are in bright.

Solvent Casting

In the solvent casting process, the NPs are first dis-agglomerated by high power sonication before adding the polymer to the suspension. The solution is then casted on glass substrates and the solvent is removed to produce free-standing films (see chapter 2).

Both the quality of the obtained polymer film and the dispersion state of the NPs have to be considered in developing the solvent casting process. This development was performed by studying the interaction between polymer, NPs and solvent through the Hansen theory. The Hansen Solubility Parameters (HSP) and the Hansen Dispersibility Parameters (HDP) have been determined by solubility and sedimentation tests for polymers and NPs, respectively. These experiments are presented in chapter 3. The results, illustrated in Figure A.2 and reported in Table A.1, enabled the identification of potential solvents/dispersants suitable for the process development.

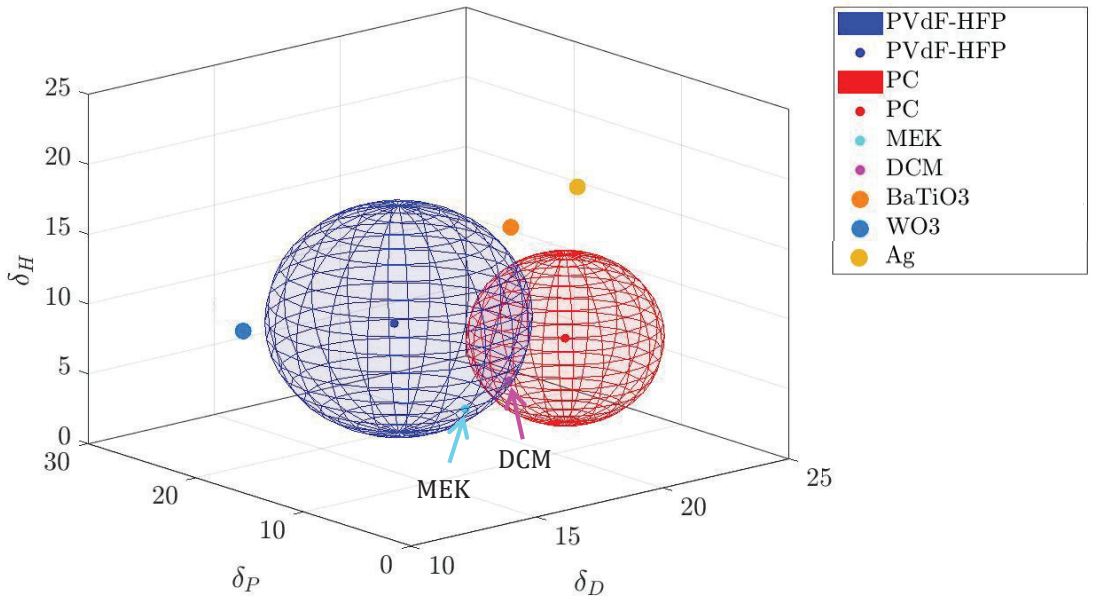

Figure A.2: Hansen representative positions of Ag, WO_3 and $BaTiO_3$ NPs and of both PVdF-HFP and Polycarbonate (PC). The position of dichloromethane (DCM) and Methyl Ethyl Ketone (MEK) are also represented.

Table A.1: Hansen Dispersibility Parameters and Hansen Solubility Parameters experimentally determined for both NPs and polymer matrices considered in the initial methodology

Polymer/NPs	δD	δP	δH
$BaTiO_3$ NPs Grade 1	20	13.7	15.5
$BaTiO_3$ NPs Grade 2	20	13.9	15.3
WO_3 NPs	12.1	20.5	9.5
Ag	16.6	0.1	22.9
PVdF-HFP	14.6	11.9	11.4
PC	19.7	8.5	8.7

The dis-agglomeration of NPs were performed with high power sonication. For $BaTiO_3$ NPs, the sonication was sufficient to break the large agglomerates of the as-received powders, as determined from sedimentation tests and Dynamic Light Scattering (DLS) analysis. Nevertheless, WO_3 and Ag NPs suspensions still exhibited large agglomerates (probably strongly bounded aggregates) that sediment immediately after hours of sonication. Thus, the fabrication of nanocomposites with well dispersed Ag and WO_3 NPs was not possible in this way.

For PC, several good solvents were identified. However, in most cases the formation of a glassy crust during solvent evaporation prevented the fabrication of transparent

homogeneous films[165]. Dichloromethane (DCM) was the only solvent from which nice thin films were fabricated with maximum thicknesses of 30 µm. Indeed, above this thickness, a honeycomb-like structure appears in the thickness of the film which is no longer homogeneous. Nevertheless, DCM was not a good dispersant for the selected NPs. For $BaTiO_3$, in addition to the fast re-agglomeration (see Figure A.3 c) of the NPs, a honeycomb-like heterogeneous distribution of $BaTiO_3$ NPs was observed at macroscopic scale as shown in Figure A.3 a) and b). A phase separation was thought to induce these honeycomb-like structures.

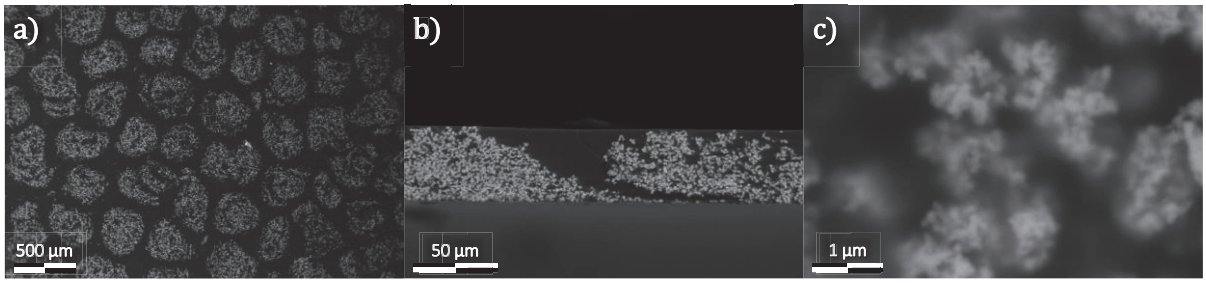

Figure A.3: SEM images of a PC:$BaTiO_3$ nanocomposite fabricated by solvent casting in DCM. Observation on a) the surface of the nanocomposite film at magnification x34 and in the cross section prepared by cryofracture at magnifications of b) x500 and c) x20k.

Concerning PVdF-HFP, nice transparent and flat polymer films could be obtained with several solvents. Its low glass transition temperature facilitates the diffusion of solvent in the thickness of the polymer film, which prevents the formation of a glassy crust. Among these solvents, DMF and MEK have allowed fabricating nanocomposite films with well dispersed $BaTiO_3$ NPs, as shown in Figure A.4 a). The mechanisms of stabilization of the suspensions are presented in chapter 3.

As expected from sedimentation tests and DLS analysis, nanocomposites films prepared with WO_3 and Ag NPs in MEK do not exhibit good dispersion states. As shown in Figure A.4 b), the dis-agglomeration of WO_3 NPS was not fully achieved during sonication. Indeed, several large aggregates with a round shape are present in the nanocomposite films. However, a fraction of the NPs is rather well dispersed in PVdF-HFP matrix. This could be due to the adsorption of PVdF-HFP onto WO_3 NPs, which is predicted by the Hansen theory (χ_s~2, more details about the adsorption parameter χ_s are given in chapter 2). Figure A.4 c) shows the dispersion state of Ag NPs in PVdF-HFP matrix. Again, dis-agglomeration of Ag NPS has not been fully achieved during sonication.

The HDPs values of Ag NPs are associated with a high uncertainty due to the low number and the off-centre HSPs (high δ_H) of good dispersants experimentally found. Indeed, the sphere of the sphere is not accurate at all. This might be expected from the

very high surface energy of metallic particles. Other stabilization mechanisms, such as ionic stabilization, may be involved in this case.

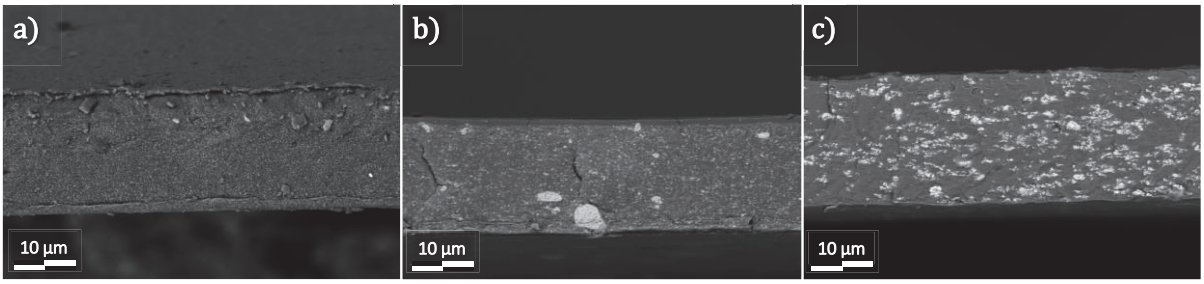

Figure A.4: SEM images of a PVdF-HFP based composites filled with 10 vol% of a) $BaTiO_3$, b) WO_3 and c) Ag NPs and fabricated by solvent casting in MEK. Observation at magnification x2k in film cross section prepared by cryofracture

Concerning the surface modification of the NP surface, three approaches were identified on the basis of the literature:

1- The improvement of the affinity between the matrix and the NPs is relatively simple to design. It consists in grafting a chemical species that has strong affinity with the polymer matrix on the NP surface. In some cases, polymer chains identical or similar to the matrix are used.
2- The creation of an electrically passive layer consists in grafting a chemical species that has high LUMO (or high ionization energy, IE) and low HOMO (or high electron affinity, AE). Without knowing the exact electronic structure of the nanocomposite components, the selection of a modifier with a high band gap allows creating an electrically passive layer either for electrons, for holes or for both of them.
3- The creation of an electrically active layer is much more complex. It requires knowing the electronic structure of the nanocomposite components (i.e. at least two parameters among EA, IE and band gap) to design specific localized states whose spatial density and distribution must be controlled as well to avoid the formation of conduction paths in the interphase.

As a result, the study was focused on PVdF-HFP:$BaTiO_3$ nanocomposites processed by solvent casting. $BaTiO_3$ NPs were functionalized following the first two approaches, which do not require electronic structure characterization. They aim at improving the affinity between matrix and NPs and at creating an electrically passive layer at the interfaces.

Bibliography

(1) Teyssedre, G.; Laurent, C. Advances in High-Field Insulating Polymeric Materials over the Past 50 Years. *IEEE Electr. Insul. Mag.* **2013**, *29* (5), 26–36. https://doi.org/10.1109/MEI.2013.6585854.

(2) *Dielectric Polymer Nanocomposites*; Nelson, J. K., Ed.; Springer US: Boston, MA, 2010. https://doi.org/10.1007/978-1-4419-1591-7.

(3) Streibl, M.; Karmazin, R.; Moos, R. Materials and Applications of Polymer Films for Power Capacitors with Special Respect to Nanocomposites. *IEEE Trans. Dielectr. Electr. Insul.* **2018**, *25* (6), 2429–2442. https://doi.org/10.1109/TDEI.2018.007392.

(4) Pleşa, I.; Noţingher, P.; Schlögl, S.; Sumereder, C.; Muhr, M.; Pleşa, I.; Noţingher, P. V.; Schlögl, S.; Sumereder, C.; Muhr, M. Properties of Polymer Composites Used in High-Voltage Applications. *Polymers* **2016**, *8* (5), 173. https://doi.org/10.3390/polym8050173.

(5) Sun, W.; Mao, J.; Wang, S.; Zhang, L.; Cheng, Y. Review of Recent Advances of Polymer Based Dielectrics for High-Energy Storage in Electronic Power Devices from the Perspective of Target Applications. *Front. Chem. Sci. Eng.* **2021**, *15* (1), 18–34. https://doi.org/10.1007/s11705-020-1939-4.

(6) Zha, J.-W.; Zheng, M.-S.; Fan, B.-H.; Dang, Z.-M. Polymer-Based Dielectrics with High Permittivity for Electric Energy Storage: A Review. *Nano Energy* **2021**, *89*, 106438. https://doi.org/10.1016/j.nanoen.2021.106438.

(7) Lewis, T. J. Interfaces: Nanometric Dielectrics. *J. Phys. Appl. Phys.* **2005**, *38* (2), 202–212. https://doi.org/10.1088/0022-3727/38/2/004.

(8) Zhang, H.; Marwat, M. A.; Xie, B.; Ashtar, M.; Liu, K.; Zhu, Y.; Zhang, L.; Fan, P.; Samart, C.; Ye, Z. Polymer Matrix Nanocomposites with 1D Ceramic Nanofillers for Energy Storage Capacitor Applications. *ACS Appl. Mater. Interfaces* **2020**, *12* (1), 1–37. https://doi.org/10.1021/acsami.9b15005.

(9) Wang, Y.; Yao, M.; Ma, R.; Yuan, Q.; Yang, D.; Cui, B.; Ma, C.; Liu, M.; Hu, D. Design Strategy of Barium Titanate/Polyvinylidene Fluoride-Based Nanocomposite Films for High Energy Storage. *J. Mater. Chem. A* **2020**, *8* (3), 884–917. https://doi.org/10.1039/C9TA11527G.

(10) Luo, H.; Zhou, X.; Ellingford, C.; Zhang, Y.; Chen, S.; Zhou, K.; Zhang, D.; Bowen, C. R.; Wan, C. Interface Design for High Energy Density Polymer Nanocomposites. *Chem. Soc. Rev.* **2019**, *48* (16), 4424–4465. https://doi.org/10.1039/C9CS00043G.

(11) Laurent, C.; Teyssedre, G. Energetics of Charge Transport in Insulating Polymers. In *2017 International Symposium on Electrical Insulating Materials (ISEIM)*; IEEE: Toyohashi, 2017; pp 3–9. https://doi.org/10.23919/ISEIM.2017.8088679.

(12) Chen, L.; Batra, R.; Ranganathan, R.; Sotzing, G.; Cao, Y.; Ramprasad, R. Electronic Structure of Polymer Dielectrics: The Role of Chemical and Morphological Complexity. *Chem. Mater.* **2018**, *30* (21), 7699–7706. https://doi.org/10.1021/acs.chemmater.8b02997.

(13) Wu, K.; Bell, M.; Oakes, A.; Ratcliff, T.; Lanzillo, N. A.; Breneman, C.; Benicewicz, B. C.; Schadler, L. S. The Effects of Nanoparticles and Organic Additives with Controlled Dispersion on Dielectric Properties of Polymers: Charge Trapping and Impact Excitation. *J. Appl. Phys.* **2016**, *120* (5), 055102. https://doi.org/10.1063/1.4959771.

(14) Lewis, T. J. Charge Transport in Polyethylene Nano Dielectrics. *IEEE Trans. Dielectr. Electr. Insul.* **2014**, *21* (2), 497–502. https://doi.org/10.1109/TDEI.2013.004173.

(15) *Broadband Dielectric Spectroscopy*; Kremer, F., Schönhals, A., Eds.; Springer Berlin Heidelberg: Berlin, Heidelberg, 2003. https://doi.org/10.1007/978-3-642-56120-7.

(16) Gallot-Lavallee, O.; Gonon, P. Caractérisation des polymères par spectroscopie diélectrique. *Techniques de l'Ingénieur* **2016**, 26.

(17) Li, B.; Chen, H.; Zhou, J. Electromechanical Stability of Dielectric Elastomer Composites with Enhanced Permittivity. *Compos. Part Appl. Sci. Manuf.* **2013**, *52*, 55–61. https://doi.org/10.1016/j.compositesa.2012.11.013.

(18) Ravichandran, R.; Wang, A. X.; Wager, J. F. Solid State Dielectric Screening versus Band Gap Trends and Implications. *Opt. Mater.* **2016**, *60*, 181–187. https://doi.org/10.1016/j.optmat.2016.07.027.

(19) Lee, M.; Youn, Y.; Yim, K.; Han, S. High-Throughput Ab Initio Calculations on Dielectric Constant and Band Gap of Non-Oxide Dielectrics. *Sci. Rep.* **2018**, *8* (1), 14794. https://doi.org/10.1038/s41598-018-33095-6.
(20) Mannodi-Kanakkithodi, A.; Pilania, G.; Huan, T. D.; Lookman, T.; Ramprasad, R. Machine Learning Strategy for Accelerated Design of Polymer Dielectrics. *Sci. Rep.* **2016**, *6* (1), 20952. https://doi.org/10.1038/srep20952.
(21) Baer, E.; Zhu, L. 50th Anniversary Perspective: Dielectric Phenomena in Polymers and Multilayered Dielectric Films. *Macromolecules* **2017**, *50* (6), 2239–2256. https://doi.org/10.1021/acs.macromol.6b02669.
(22) Laurati, M.; Sotta, P.; Long, D. R.; Fillot, L.-A.; Arbe, A.; Alegrìa, A.; Embs, J. P.; Unruh, T.; Schneider, G. J.; Colmenero, J. Dynamics of Water Absorbed in Polyamides. *Macromolecules* **2012**, *45* (3), 1676–1687. https://doi.org/10.1021/ma202368x.
(23) Wypych, G. *Handbook of Polymers*, 2nd edition.; CP, ChemTec Publishing: Toronto, 2016.
(24) Barber, P.; Balasubramanian, S.; Anguchamy, Y.; Gong, S.; Wibowo, A.; Gao, H.; Ploehn, H.; Zur Loye, H.-C.; Barber, P.; Balasubramanian, S.; Anguchamy, Y.; Gong, S.; Wibowo, A.; Gao, H.; Ploehn, H. J.; Zur Loye, H.-C. Polymer Composite and Nanocomposite Dielectric Materials for Pulse Power Energy Storage. *Materials* **2009**, *2* (4), 1697–1733. https://doi.org/10.3390/ma2041697.
(25) Philippot, G.; Elissalde, C.; Maglione, M.; Aymonier, C. Supercritical Fluid Technology: A Reliable Process for High Quality BaTiO3 Based Nanomaterials. *Adv. Powder Technol.* **2014**, *25* (5), 1415–1429. https://doi.org/10.1016/j.apt.2014.02.016.
(26) Kao, K. C. *Dielectric Phenomena in Solids: With Emphasis on Physical Concepts of Electronic Processes*; Elsevier Academic Press: Amsterdam, 2004.
(27) Raju, G. G. *Dielectrics in Electric Fields: Tables, Atoms, and Molecules*, 2nd edition.; CRC Press: Boca Raton, 2016.
(28) Laurent, C. Diélectriques solides et charge d'espace. *Techniques de l'Ingénieur* **1999**, 18.
(29) Chen, L.; Huan, T. D.; Ramprasad, R. Electronic Structure of Polyethylene: Role of Chemical, Morphological and Interfacial Complexity. *Sci. Rep.* **2017**, *7* (1). https://doi.org/10.1038/s41598-017-06357-y.
(30) Landau, L. D.; Lifshitz, E. M.; Pitaevskii, L. P. *Electrodynamics of Continuous Media: Volume 8*; Elsevier Science, 1995.
(31) Dissado, L. A.; Fothergill, J. C. *Electrical Degradation and Breakdown in Polymers*; 2008.
(32) Themlin, J.-M. Propriétés électroniques des surfaces solides - Introduction, généralités, concepts. **2011**, 23.
(33) Taleb, M.; Teyssedre, G.; Le Roy, S.; Laurent, C. Modeling of Charge Injection and Extraction in a Metal/Polymer Interface through an Exponential Distribution of Surface States. *IEEE Trans. Dielectr. Electr. Insul.* **2013**, *20* (1), 311–320. https://doi.org/10.1109/TDEI.2013.6451372.
(34) Chiu, F.-C. A Review on Conduction Mechanisms in Dielectric Films. *Adv. Mater. Sci. Eng.* **2014**, *2014*, 1–18. https://doi.org/10.1155/2014/578168.
(35) Bourgeois, O.; Guillou, H. Conduction électrique dans les solides - Transport et propriétés physiques des électrons de conduction. *Techniques de l'Ingénieur* **2011**, 25.
(36) Hill, R. M. Poole-Frenkel Conduction in Amorphous Solids. *Philos. Mag. J. Theor. Exp. Appl. Phys.* **1971**, *23* (181), 59–86. https://doi.org/10.1080/14786437108216365.
(37) Segui, Y. Diélectriques - Courants de conduction. *Techniques de l'Ingénieur* **2000**, 16.
(38) Le Roy, S.; Teyssedre, G.; Laurent, C. Charge Transport and Dissipative Processes in Insulating Polymers: Experiments and Model. *IEEE Trans. Dielectr. Electr. Insul.* **2005**, *12* (4), 644–654. https://doi.org/10.1109/TDEI.2005.1511090.
(39) Nasyrov, K. A.; Gritsenko, V. A. Transport Mechanisms of Electrons and Holes in Dielectric Films. **2013**, 14.
(40) Fernandez, J. Damage Mechanisms in High-Voltage Insulating Polymer Materials, 2021.
(41) Karkkainen, K. K.; Sihvola, A. H.; Nikoskinen, K. I. Effective Permittivity of Mixtures: Numerical Validation by the FDTD Method. *IEEE Trans. Geosci. Remote Sens.* **2000**, *38* (3), 1303–1308. https://doi.org/10.1109/36.843023.
(42) Zhang, L.; Bass, P.; Cheng, Z.-Y. Physical Aspects of 0-3 Dielectric Composites. *J. Adv. Dielectr.* **2015**, *05* (02), 1550012. https://doi.org/10.1142/S2010135X15500125.

(43) Roscow, J. I.; Bowen, C. R.; Almond, D. P. Breakdown in the Case for Materials with Giant Permittivity? *ACS Energy Lett.* **2017**, *2* (10), 2264–2269. https://doi.org/10.1021/acsenergylett.7b00798.

(44) Garnett, J. C. M.; Larmor, J. XII. Colours in Metal Glasses and in Metallic Films. *Philos. Trans. R. Soc. Lond. Ser. Contain. Pap. Math. Phys. Character* **1904**, *203* (359–371), 385–420. https://doi.org/10.1098/rsta.1904.0024.

(45) Markel, V. A. Introduction to the Maxwell Garnett Approximation: Tutorial. *JOSA A* **2016**, *33* (7), 1244–1256. https://doi.org/10.1364/JOSAA.33.001244.

(46) Bouharras, F. E.; Raihane, M.; Ameduri, B. Recent Progress on Core-Shell Structured BaTiO3@polymer/Fluorinated Polymers Nanocomposites for High Energy Storage: Synthesis, Dielectric Properties and Applications. *Prog. Mater. Sci.* **2020**, *113*, 100670. https://doi.org/10.1016/j.pmatsci.2020.100670.

(47) Tuncer, E.; Serdyuk, Y. V.; Gubanski, S. M. Dielectric Mixtures -- Electrical Properties and Modeling. *IEEE Trans. Dielectr. Electr. Insul.* **2002**, *9* (5), 809–828. https://doi.org/10.1109/TDEI.2002.1038664.

(48) Zhang, D.; Zhou, X.; Roscow, J.; Zhou, K.; Wang, L.; Luo, H.; Bowen, C. R. Significantly Enhanced Energy Storage Density by Modulating the Aspect Ratio of BaTiO3 Nanofibers. *Sci. Rep.* **2017**, *7* (1). https://doi.org/10.1038/srep45179.

(49) Wang, Z.; Keith Nelson, J.; Hillborg, H.; Zhao, S.; Schadler, L. S. Dielectric Constant and Breakdown Strength of Polymer Composites with High Aspect Ratio Fillers Studied by Finite Element Models. *Compos. Sci. Technol.* **2013**, *76*, 29–36. https://doi.org/10.1016/j.compscitech.2012.12.014.

(50) Tang, H.; Zhou, Z.; Sodano, H. A. Relationship between $BaTiO_3$ Nanowire Aspect Ratio and the Dielectric Permittivity of Nanocomposites. *ACS Appl. Mater. Interfaces* **2014**, *6* (8), 5450–5455. https://doi.org/10.1021/am405038r.

(51) Hu, X.; Yi, K.; Liu, J.; Chu, B. High Energy Density Dielectrics Based on PVDF-Based Polymers. *Energy Technol.* **2018**, *6* (5), 849–864. https://doi.org/10.1002/ente.201700901.

(52) Zhong, S.-L.; Dang, Z.-M. High Energy Storage Dielectric Polymer Materials With Hierarchical Microstructures. In *Dielectric Polymer Materials for High-Density Energy Storage*; Elsevier, 2018; pp 165–197. https://doi.org/10.1016/B978-0-12-813215-9.00005-1.

(53) Huang, X.; Sun, B.; Zhu, Y.; Li, S.; Jiang, P. High-k Polymer Nanocomposites with 1D Filler for Dielectric and Energy Storage Applications. *Prog. Mater. Sci.* **2019**, *100*, 187–225. https://doi.org/10.1016/j.pmatsci.2018.10.003.

(54) Xie, B.; Zhang, H.; Zhang, Q.; Zang, J.; Yang, C.; Wang, Q.; Li, M.-Y.; Jiang, S. Enhanced Energy Density of Polymer Nanocomposites at a Low Electric Field through Aligned BaTiO3 Nanowires. *J. Mater. Chem. A* **2017**, *5* (13), 6070–6078. https://doi.org/10.1039/C7TA00513J.

(55) Shen, Z.-H.; Wang, J.-J.; Lin, Y.; Nan, C.-W.; Chen, L.-Q.; Shen, Y. High-Throughput Phase-Field Design of High-Energy-Density Polymer Nanocomposites. *Adv. Mater.* **2018**, *30* (2), 1704380. https://doi.org/10.1002/adma.201704380.

(56) Mackey, M.; Schuele, D. E.; Zhu, L.; Flandin, L.; Wolak, M. A.; Shirk, J. S.; Hiltner, A.; Baer, E. Reduction of Dielectric Hysteresis in Multilayered Films via Nanoconfinement. *Macromolecules* **2012**, *45* (4), 1954–1962. https://doi.org/10.1021/ma202267r.

(57) Tseng, J.-K.; Tang, S.; Zhou, Z.; Mackey, M.; Carr, J. M.; Mu, R.; Flandin, L.; Schuele, D. E.; Baer, E.; Zhu, L. Interfacial Polarization and Layer Thickness Effect on Electrical Insulation in Multilayered Polysulfone/Poly(Vinylidene Fluoride) Films. *Polymer* **2014**, *55* (1), 8–14. https://doi.org/10.1016/j.polymer.2013.11.042.

(58) Tseng, J.-K.; Yin, K.; Zhang, Z.; Mackey, M.; Baer, E.; Zhu, L. Morphological Effects on Dielectric Properties of Poly(Vinylidene Fluoride-Co-Hexafluoropropylene) Blends and Multilayer Films. *Polymer* **2019**, *172*, 221–230. https://doi.org/10.1016/j.polymer.2019.03.076.

(59) Murugaraj, P.; Mainwaring, D.; Mora-Huertas, N. Dielectric Enhancement in Polymer-Nanoparticle Composites through Interphase Polarizability. *J. Appl. Phys.* **2005**, *98* (5), 054304. https://doi.org/10.1063/1.2034654.

(60) Shan, X. HIGH DIELECTRIC CONSTANT 0-3 CERAMIC-POLYMER COMPOSITES. *Polym. Compos.* **2009**, 327.

(61) Yuan, J. Percolation of Carbon Nanomaterials for High-k Polymer Nanocomposites. *Chin. Chem. Lett.* **2017**, *28* (11), 2036–2044. https://doi.org/10.1016/j.cclet.2017.08.020.
(62) Zhao, B.; Hamidinejad, M.; Zhao, C.; Li, R.; Wang, S.; Kazemi, Y.; Park, C. B. A Versatile Foaming Platform to Fabricate Polymer/Carbon Composites with High Dielectric Permittivity and Ultra-Low Dielectric Loss. *J. Mater. Chem. A* **2019**, *7* (1), 133–140. https://doi.org/10.1039/C8TA05556D.
(63) Al-Saleh, M. H. Carbon-Based Polymer Nanocomposites as Dielectric Energy Storage Materials. *Nanotechnology* **2019**, *30* (6), 062001. https://doi.org/10.1088/1361-6528/aaf12c.
(64) Luna, A.; Yuan, J.; Néri, W.; Zakri, C.; Poulin, P.; Colin, A. Giant Permittivity Polymer Nanocomposites Obtained by Curing a Direct Emulsion. *Langmuir* **2015**, *31* (44), 12231–12239. https://doi.org/10.1021/acs.langmuir.5b02318.
(65) Luna, A.; Pruvost, M.; Yuan, J.; Zakri, C.; Neri, W.; Monteux, C.; Poulin, P.; Colin, A. Giant Electrostrictive Response and Piezoresistivity of Emulsion Templated Nanocomposites. *Langmuir* **2017**, *33* (18), 4528–4536. https://doi.org/10.1021/acs.langmuir.6b04185.
(66) Kochervinskii, V.; Malyshkina, I.; Gavrilova, N.; Sulyanov, S.; Bessonova, N. Peculiarities of Dielectric Relaxation in Poly(Vinylidene Fluoride) with Different Thermal History. *J. Non-Cryst. Solids* **2007**, *353* (47–51), 4443–4447. https://doi.org/10.1016/j.jnoncrysol.2007.03.034.
(67) Yamamura, Y.; Yoshida, K.; Kawate, K.; Osaka, N.; Saito, H. Dielectric Relaxation Study of the Crystalline Chain Motion of Poly(Vinylidene Fluoride) under Carbon Dioxide. *Polym. J.* **2010**, *42* (5), 419–422. https://doi.org/10.1038/pj.2010.19.
(68) Arous, M.; Amor, I. B.; Kallel, A.; Fakhfakh, Z.; Perrier, G. Crystallinity and Dielectric Relaxations in Semi-Crystalline Poly(Ether Ether Ketone). *J. Phys. Chem. Solids* **2007**, *68* (7), 1405–1414. https://doi.org/10.1016/j.jpcs.2007.02.046.
(69) Jin, Y.; Gerhardt, R. A. Simulation of the Effects of Nano-Filler Interactions in Polymer Matrix Dielectric Nanocomposites. **2016**, 7.
(70) Bowen, C. P.; Newnham, R. E.; Randall, C. A. Dielectric Properties of Dielectrophoretically Assembled Particulate-Polymer Composites. *J. Mater. Res.* **1998**, *13* (1), 205–210. https://doi.org/10.1557/JMR.1998.0027.
(71) Kushimoto, K.; Moriyama, M.; Shimosaka, A.; Shirakawa, Y.; Hidaka, J.; Ishihara, S.; Kano, J. Measurement Method for Dispersion States of Filler Particles in Particulate Composite Materials by Macroscopic Permittivity. *Adv. Powder Technol.* **2021**, *32* (1), 272–282. https://doi.org/10.1016/j.apt.2020.12.003.
(72) Zhang, X.; Wang, Y.; Sheng, Y.; Ye, H.; Xu, L.; Wu, H. Enhanced Energy Density in Hydroxyl-Modified Barium Titanate/Poly(Fluorovinylidene-Co-Trifluoroethylene) Nanocomposites with Improved Interfacial Polarization. *Chem. Phys. Lett.* **2019**, *723*, 89–95. https://doi.org/10.1016/j.cplett.2019.03.027.
(73) Zhang, L.; Wang, Y.; Xu, M.; Wei, W.; Deng, Y. Multiple Interfacial Modifications in Poly(Vinylidene Fluoride)/Barium Titanate Nanocomposites via Double-Shell Architecture for Significantly Enhanced Energy Storage Density. *ACS Appl. Energy Mater.* **2019**, *2* (8), 5945–5953. https://doi.org/10.1021/acsaem.9b01052.
(74) Wu, L.; Wu, K.; Lei, C.; Liu, D.; Du, R.; Chen, F.; Fu, Q. Surface Modifications of Boron Nitride Nanosheets for Poly(Vinylidene Fluoride) Based Film Capacitors: Advantages of Edge-Hydroxylation. *J. Mater. Chem. A* **2019**, *7* (13), 7664–7674. https://doi.org/10.1039/C9TA00616H.
(75) Xu, W.; Yang, G.; Jin, L.; Liu, J.; Zhang, Y.; Zhang, Z.; Jiang, Z. High- k Polymer Nanocomposites Filled with Hyperbranched Phthalocyanine-Coated BaTiO3 for High-Temperature and Elevated Field Applications. *ACS Appl. Mater. Interfaces* **2018**, *10* (13), 11233–11241. https://doi.org/10.1021/acsami.8b01129.
(76) Wang, J.; Xie, Y.; Liu, J.; Zhang, Z.; Zhuang, Q.; Kong, J. Improved Energy Storage Performance of Linear Dielectric Polymer Nanodielectrics with Polydopamine Coated BN Nanosheets. *Polymers* **2018**, *10* (12), 1349. https://doi.org/10.3390/polym10121349.
(77) Hu, P.; Gao, S.; Zhang, Y.; Zhang, L.; Wang, C. Surface Modified BaTiO3 Nanoparticles by Titanate Coupling Agent Induce Significantly Enhanced Breakdown Strength and Larger

Energy Density in PVDF Nanocomposite. *Compos. Sci. Technol.* **2018**, *156*, 109–116. https://doi.org/10.1016/j.compscitech.2017.12.025.

(78) Liu, S.; Zhai, J. Improving the Dielectric Constant and Energy Density of Poly(Vinylidene Fluoride) Composites Induced by Surface-Modified SrTiO3 Nanofibers by Polyvinylpyrrolidone. *J. Mater. Chem. A* **2014**, *3* (4), 1511–1517. https://doi.org/10.1039/C4TA04455J.

(79) Zhou, T.; Zha, J.-W.; Cui, R.-Y.; Fan, B.-H.; Yuan, J.-K.; Dang, Z.-M. Improving Dielectric Properties of BaTiO3/Ferroelectric Polymer Composites by Employing Surface Hydroxylated BaTiO3 Nanoparticles. *ACS Appl. Mater. Interfaces* **2011**, *3* (7), 2184–2188. https://doi.org/10.1021/am200492q.

(80) Yu, K.; Niu, Y.; Zhou, Y.; Bai, Y.; Wang, H. Nanocomposites of Surface-Modified $BaTiO_3$ Nanoparticles Filled Ferroelectric Polymer with Enhanced Energy Density. *J. Am. Ceram. Soc.* **2013**, *96* (8), 2519–2524. https://doi.org/10.1111/jace.12338.

(81) Zhang, X.; Zhao, S.; Wang, F.; Ma, Y.; Wang, L.; Chen, D.; Zhao, C.; Yang, W. Improving Dielectric Properties of BaTiO3/Poly(Vinylidene Fluoride) Composites by Employing Core-Shell Structured BaTiO3@Poly(Methylmethacrylate) and BaTiO3@Poly(Trifluoroethyl Methacrylate) Nanoparticles. *Appl. Surf. Sci.* **2017**, *403*, 71–79. https://doi.org/10.1016/j.apsusc.2017.01.121.

(82) Luo, H.; Zhou, X.; Ellingford, C.; Zhang, Y.; Chen, S.; Zhou, K.; Zhang, D.; Bowen, C. R.; Wan, C. Interface Design for High Energy Density Polymer Nanocomposites. *Chem. Soc. Rev.* **2019**, *48* (16), 4424–4465. https://doi.org/10.1039/C9CS00043G.

(83) Kim, P.; Jones, S. C.; Hotchkiss, P. J.; Haddock, J. N.; Kippelen, B.; Marder, S. R.; Perry, J. W. Phosphonic Acid-Modified Barium Titanate Polymer Nanocomposites with High Permittivity and Dielectric Strength. *Adv. Mater.* **2007**, *19* (7), 1001–1005. https://doi.org/10.1002/adma.200602422.

(84) Chen, S.; Lv, X.; Han, X.; Luo, H.; Bowen, C. R.; Zhang, D. Significantly Improved Energy Density of $BaTiO_3$ Nanocomposites by Accurate Interfacial Tailoring Using a Novel Rigid-Fluoro-Polymer. *Polym. Chem.* **2018**, *9* (5), 548–557. https://doi.org/10.1039/C7PY01914A.

(85) Huzayyin, A.; Boggs, S.; Ramprasad, R. An Overview of Impurity States and the Basis for Hole Mobility in Polyethylene. *IEEE Electr. Insul. Mag.* **2012**, *28* (6), 23–29. https://doi.org/10.1109/MEI.2012.6340521.

(86) Tanaka, T.; Kozako, M.; Fuse, N.; Ohki, Y. Proposal of a Multi-Core Model for Polymer Nanocomposite Dielectrics. *IEEE Trans. Dielectr. Electr. Insul.* **2005**, *12* (4), 669–681. https://doi.org/10.1109/TDEI.2005.1511092.

(87) Gao, H.; Yue, Z.; Liu, Y.; Hu, J.; Li, X. A First-Principles Study on the Multiferroic Property of Two-Dimensional BaTiO3 (001) Ultrathin Film with Surface Ba Vacancy. *Nanomaterials* **2019**, *9* (2). https://doi.org/10.3390/nano9020269.

(88) Shandilya, A.; Schadler, L. S.; Sundararaman, R. First-Principles Identification of Localized Trap States in Polymer Nanocomposite Interfaces. *J. Mater. Res.* **undefined/ed**, 1–9. https://doi.org/10.1557/jmr.2020.18.

(89) Luo, B.; Wang, X.; Tian, E.; Yao, Y.; Cai, Z.; Xi, K.; Song, H.; Song, H.; Li, B.; Li, L. Interfacial Electronic Properties of Ferroelectric Nanocomposites for Energy Storage Application. *Mater. Today Energy* **2019**, *12*, 136–145. https://doi.org/10.1016/j.mtener.2018.12.010.

(90) Ghosh, K.; Guo, J.; Lopez-Pamies, O. Homogenization of Time-Dependent Dielectric Composites Containing Space Charges, with Applications to Polymer Nanoparticulate Composites. *Int. J. Non-Linear Mech.* **2019**, *116*, 155–166. https://doi.org/10.1016/j.ijnonlinmec.2019.06.007.

(91) Kubyshkina, E. Ab Initio Modelling of Interfaces in Nanocomposites for High Voltage Insulation, KTH Royal Institute of Technology, 2018.

(92) Roy, M.; Nelson, J. K.; MacCrone, R. K.; Schadler, L. S. Candidate Mechanisms Controlling the Electrical Characteristics of Silica/XLPE Nanodielectrics. *J. Mater. Sci.* **2007**, *42* (11), 3789–3799. https://doi.org/10.1007/s10853-006-0413-0.

(93) Zhang, H.; Shang, Y.; Wang, X.; Zhao, H.; Han, B.; Li, Z. Mechanisms on Electrical Breakdown Strength Increment of Polyethylene by Aromatic Carbonyl Compounds Addition: A

Theoretical Study. *J. Mol. Model.* **2013**, *19* (12), 5429–5438. https://doi.org/10.1007/s00894-013-2028-0.

(94) Li, S.; Min, D.; Wang, W.; Chen, G. Linking Traps to Dielectric Breakdown through Charge Dynamics for Polymer Nanocomposites. *IEEE Trans. Dielectr. Electr. Insul.* **2016**, *23* (5), 2777–2785. https://doi.org/10.1109/TDEI.2016.7736837.

(95) Siddabattuni, S.; Schuman, T. P.; Dogan, F. Dielectric Properties of Polymer-Particle Nanocomposites Influenced by Electronic Nature of Filler Surfaces. *ACS Appl. Mater. Interfaces* **2013**, *5* (6), 1917–1927. https://doi.org/10.1021/am3030239.

(96) Wang, W.; Li, S. Improvement of Dielectric Breakdown Performance by Surface Modification in Polyethylene/TiO2 Nanocomposites. *Materials* **2019**, *12* (20), 3346. https://doi.org/10.3390/ma12203346.

(97) Kubyshkina, E.; Unge, M. Impact of Interfacial Structure on the Charge Dynamics in Nanocomposite Dielectrics. *J. Appl. Phys.* **2019**, *125* (4), 045109. https://doi.org/10.1063/1.5078800.

(98) Dou, X.; Liu, X.; Zhang, Y.; Feng, H.; Chen, J.-F.; Du, S. Improved Dielectric Strength of Barium Titanate-Polyvinylidene Fluoride Nanocomposite. *Appl. Phys. Lett.* **2009**, *95* (13), 132904. https://doi.org/10.1063/1.3242004.

(99) Alhabill, F. N.; Ayoob, R.; Andritsch, T.; Vaughan, A. S. Introducing Particle Interphase Model for Describing the Electrical Behaviour of Nanodielectrics. *Mater. Des.* **2018**, *158*, 62–73. https://doi.org/10.1016/j.matdes.2018.08.018.

(100) Praeger, M.; Hosier, I. L.; Vaughan, A. S.; Swingler, S. G. The Effects of Surface Hydroxyl Groups in Polyethylene-Silica Nanocomposites. In *2015 IEEE Electrical Insulation Conference (EIC)*; 2015; pp 201–204. https://doi.org/10.1109/ICACACT.2014.7223514.

(101) Niu, Y.; Bai, Y.; Yu, K.; Wang, Y.; Xiang, F.; Wang, H. Effect of the Modifier Structure on the Performance of Barium Titanate/Poly(Vinylidene Fluoride) Nanocomposites for Energy Storage Applications. *ACS Appl. Mater. Interfaces* **2015**, *7* (43), 24168–24176. https://doi.org/10.1021/acsami.5b07486.

(102) Kim, P.; Doss, N. M.; Tillotson, J. P.; Hotchkiss, P. J.; Pan, M.-J.; Marder, S. R.; Li, J.; Calame, J. P.; Perry, J. W. High Energy Density Nanocomposites Based on Surface-Modified $BaTiO_3$ and a Ferroelectric Polymer. *ACS Nano* **2009**, *3* (9), 2581–2592. https://doi.org/10.1021/nn9006412.

(103) Zhang, G.; Brannum, D.; Dong, D.; Tang, L.; Allahyarov, E.; Tang, S.; Kodweis, K.; Lee, J.-K.; Zhu, L. Interfacial Polarization-Induced Loss Mechanisms in Polypropylene/BaTiO3 Nanocomposite Dielectrics. *Chem. Mater.* **2016**, *28* (13), 4646–4660. https://doi.org/10.1021/acs.chemmater.6b01383.

(104) Yang, L.; Li, X.; Allahyarov, E.; Taylor, P. L.; Zhang, Q. M.; Zhu, L. Novel Polymer Ferroelectric Behavior via Crystal Isomorphism and the Nanoconfinement Effect. *Polymer* **2013**, *54* (7), 1709–1728. https://doi.org/10.1016/j.polymer.2013.01.035.

(105) Hu, X.; Yi, K.; Liu, J.; Chu, B. High Energy Density Dielectrics Based on PVDF-Based Polymers. *Energy Technol.* **2018**, *6* (5), 849–864. https://doi.org/10.1002/ente.201700901.

(106) Zhou, X.; Zhao, X.; Suo, Z.; Zou, C.; Runt, J.; Liu, S.; Zhang, S.; Zhang, Q. M. Electrical Breakdown and Ultrahigh Electrical Energy Density in Poly(Vinylidene Fluoride-Hexafluoropropylene) Copolymer. *Appl. Phys. Lett.* **2009**, *94* (16), 5–7. https://doi.org/10.1063/1.3123001.

(107) Zhu, L.; Wang, Q. Novel Ferroelectric Polymers for High Energy Density and Low Loss Dielectrics. *Macromolecules* **2012**, *45* (7), 2937–2954. https://doi.org/10.1021/ma2024057.

(108) Brunauer, S.; Emmett, P. H.; Teller, E. Adsorption of Gases in Multimolecular Layers. *J. Am. Chem. Soc.* **1938**, *60* (2), 309–319. https://doi.org/10.1021/ja01269a023.

(109) Li, C.-C.; Chang, S.-J.; Lee, J.-T.; Liao, W.-S. Efficient Hydroxylation of BaTiO3 Nanoparticles by Using Hydrogen Peroxide. *Colloids Surf. Physicochem. Eng. Asp.* **2010**, *361* (1–3), 143–149. https://doi.org/10.1016/j.colsurfa.2010.03.027.

(110) Parks, G. A. The Isoelectric Points of Solid Oxides, Solid Hydroxides, and Aqueous Hydroxo Complex Systems. *Chem. Rev.* **1965**, *65* (2), 177–198. https://doi.org/10.1021/cr60234a002.

(111) Hansen, C. M. *Hansen Solubility Parameters: A User's Handbook, Second Edition*; CRC Press, 2007.

(112) Barton, A. F. M. *CRC Handbook of Solubility Parameters and Other Cohesion Parameters: Second Edition*, 2nd ed.; Routledge, 2017. https://doi.org/10.1201/9781315140575.
(113) Pétrier, C.; Gondrexon, N.; Boldo, P. Ultrasons et sonochimie. **2008**, 18.
(114) Pedroli, F. Dielectric Strength and Leakage Current : From Synthesis to Processing Optimization. These de doctorat, Lyon, 2020.
(115) Socrates, G. *Infrared and Raman Characteristic Group Frequencies: Tables and Charts*, 3. ed.; Wiley: Chichester, 2001.
(116) Tamura, H.; Mita, K.; Tanaka, A.; Ito, M. Mechanism of Hydroxylation of Metal Oxide Surfaces. *J. Colloid Interface Sci.* **2001**, *243* (1), 202–207. https://doi.org/10.1006/jcis.2001.7864.
(117) Clabel H, J. L.; Awan, I. T.; Pinto, A. H.; Nogueira, I. C.; Bezzon, V. D. N.; Leite, E. R.; Balogh, D. T.; Mastelaro, V. R.; Ferreira, S. O.; Marega, E. Insights on the Mechanism of Solid State Reaction between TiO2 and BaCO3 to Produce BaTiO3 Powders: The Role of Calcination, Milling, and Mixing Solvent. *Ceram. Int.* **2020**, *46* (3), 2987–3001. https://doi.org/10.1016/j.ceramint.2019.09.296.
(118) León, A.; Reuquen, P.; Garín, C.; Segura, R.; Vargas, P.; Zapata, P.; Orihuela, P. FTIR and Raman Characterization of TiO2 Nanoparticles Coated with Polyethylene Glycol as Carrier for 2-Methoxyestradiol. *Appl. Sci.* **2017**, *7* (1), 49. https://doi.org/10.3390/app7010049.
(119) Rosenberg, Y.; Siegmann, A.; Narkis, M.; Shkolnik, S. The Sol/Gel Contribution to the Behavior of γ-Irradiated Poly(Vinylidene Fluoride). *J. Appl. Polym. Sci.* **1991**, *43* (3), 535–541. https://doi.org/10.1002/app.1991.070430314.
(120) Strobl, G. R. *The Physics of Polymers: Concepts for Understanding Their Structures and Behavior*; Springer Science & Business Media, 2007.
(121) Neidhöfer, M.; Beaume, F.; Ibos, L.; Bernès, A.; Lacabanne, C. Structural Evolution of PVDF during Storage or Annealing. *Polymer* **2004**, *45* (5), 1679–1688. https://doi.org/10.1016/j.polymer.2003.12.066.
(122) Marand, H.; Alizadeh, A.; Farmer, R.; Desai, R.; Velikov, V. Influence of Structural and Topological Constraints on the Crystallization and Melting Behavior of Polymers. 2. Poly(Arylene Ether Ether Ketone). *Macromolecules* **2000**, *33* (9), 3392–3403. https://doi.org/10.1021/ma9913562.
(123) ZETASIZER NANO Series. Malvern.
(124) Flory, P. J. Thermodynamics of High Polymer Solutions. *J. Chem. Phys.* **1942**, *10* (1), 51–61. https://doi.org/10.1063/1.1723621.
(125) DeBoyace, K.; Wildfong, P. L. D. The Application of Modeling and Prediction to the Formation and Stability of Amorphous Solid Dispersions. *J. Pharm. Sci.* **2018**, *107* (1), 57–74. https://doi.org/10.1016/j.xphs.2017.03.029.
(126) Hildebrand, J. H.; Scott, R. L. *The Solubility of Nonelectrolytes,*; Reinhold Pub. Corp.: New York, 1950.
(127) Hildebrand, J. H.; Scott, R. L. *Regular Solutions*; Prentice-Hall: Englewood Cliffs, N.J., 1962.
(128) Israelachvili, J. N. *Intermolecular and Surface Forces*; Elsevier, 2011.
(129) AID, S.; EDDHAHAK, A.; Khelladi, S.; ORTEGA, Z.; CHAABANI, S.; Tcharkhtchi, A. On the Miscibility of PVDF/PMMA Polymer Blends: Thermodynamics, Experimental and Numerical Investigations. *Polym. Test.* **2019**, *73*, 222–231. https://doi.org/10.1016/j.polymertesting.2018.11.036.
(130) Gennes, P.-G. *Scaling Concepts in Polymer Physics*; Cornell University Press: Ithaca, N.Y, 1979.
(131) Lindvig, T.; Michelsen, M. L.; Kontogeorgis, G. M. A Flory–Huggins Model Based on the Hansen Solubility Parameters. *Fluid Phase Equilibria* **2002**, *203* (1), 247–260. https://doi.org/10.1016/S0378-3812(02)00184-X.
(132) Mansoori, G. A. A Perturbation Theory Modification of the Flory-Huggins Polymer Solution Theory. *Condens. Matter Phys.* **2005**, *8* (2), 389. https://doi.org/10.5488/CMP.8.2.389.
(133) Tang, S.; Zhang, R.; Liu, F.; Liu, X. Hansen Solubility Parameters of Polyglycolic Acid and Interaction Parameters between Polyglycolic Acid and Solvents. *Eur. Polym. J.* **2015**, *72*, 83–88. https://doi.org/10.1016/j.eurpolymj.2015.09.009.
(134) Anderson, B. D. Predicting Solubility/Miscibility in Amorphous Dispersions: It Is Time to Move Beyond Regular Solution Theories. *J. Pharm. Sci.* **2018**, *107* (1), 24–33. https://doi.org/10.1016/j.xphs.2017.09.030.

(135) Hansen, C. Solubility Parameters. *Paint Coat. Test. Man. 15th Ed. Gardner-Sward Handb.* **2012**. https://doi.org/10.1520/MNL12218M.
(136) *Hansen Solubility Parameters: A User's Handbook*, 2. ed.; Hansen, C. M., Ed.; CRC Press: Boca Raton, 2007.
(137) Laurens, J. Compréhension des interactions silice-polymère et du rôle de l'interface grâce à l'utilisation de solvants, 2020. Science des matériaux [cond-mat.mtrl-sci]. Université de Lyon, 2020. Français. ffNNT : 2020LYSE1139ff. fftel-03346667f
(138) Abbott, S.; Hansen, C. M. Hansen Solubility Parameters in Practice. 269.
(139) Bottino, A.; Capannelli, G.; Munari, S.; Turturro, A. Solubility Parameters of Poly(Vinylidene Fluoride). *J. Polym. Sci. Part B Polym. Phys.* **1988**, *26* (4), 785–794. https://doi.org/10.1002/polb.1988.090260405.
(140) Akkoyun, M.; Carrot, C.; Blottière, B. Ternary Diagrams of Poly(Vinylidene Fluoride) and Poly[(Vinylidene Fluoride)-Co-Hexafluoropropene] in Propylene Carbonate and Dimethyl Sulfoxide. *Macromol. Chem. Phys.* **2012**, *213* (5), 587–593. https://doi.org/10.1002/macp.201100595.
(141) Link, J. Stabilization and structural study of new nanocomposite materials, 2019.
(142) Raghavan, S. R.; Walls, H. J.; Khan, S. A. Rheology of Silica Dispersions in Organic Liquids: New Evidence for Solvation Forces Dictated by Hydrogen Bonding. *Langmuir* **2000**, *16* (21), 7920–7930. https://doi.org/10.1021/la991548q.
(143) Howell, J. S.; Stephens, B. O.; Boucher, D. S. Convex Solubility Parameters for Polymers. *J. Polym. Sci. Part B Polym. Phys.* **2015**, *53* (16), 1089–1097. https://doi.org/10.1002/polb.23753.
(144) Silberberg, A. Adsorption of Flexible Macromolecules. IV. Effect of Solvent–Solute Interactions, Solute Concentration, and Molecular Weight. *J. Chem. Phys.* **1968**, *48* (7), 2835–2851. https://doi.org/10.1063/1.1669540.
(145) Laurens, J.; Jolly, J.; Ovarlez, G.; Fay, H.; Chaussée, T.; Sotta, P. Competitive Adsorption between a Polymer and Solvents onto Silica. *Langmuir* **2020**, *36* (26), 7669–7680. https://doi.org/10.1021/acs.langmuir.0c01312.
(146) Faasen, D. P.; Jarray, A.; Zandvliet, H. J. W.; Kooij, E. S.; Kwiecinski, W. Hansen Solubility Parameters Obtained via Molecular Dynamics Simulations as a Route to Predict Siloxane Surfactant Adsorption. *J. Colloid Interface Sci.* **2020**, *575*, 326–336. https://doi.org/10.1016/j.jcis.2020.04.070.
(147) Fleer, G. J.; Stuart, M. A. C.; Scheutjens, J. M. H. M.; Cosgrove, T.; Vincent, B. *Polymers at Interfaces*; Springer Netherlands: Dordrecht, 1998. https://doi.org/10.1007/978-94-011-2130-9.
(148) *Rheology and Processing of Polymer Nanocomposites*; Thomas, S., Muller, R., Abraham, J., Eds.; Wiley: Hoboken, New Jersey, 2016.
(149) Cai, X.; Lei, T.; Sun, D.; Lin, L. A Critical Analysis of the α, β and γ Phases in Poly(Vinylidene Fluoride) Using FTIR. *RSC Adv.* **2017**, *7* (25), 15382–15389. https://doi.org/10.1039/C7RA01267E.
(150) Mijovic, J.; Sy, J.-W.; Kwei, T. K. Reorientational Dynamics of Dipoles in Poly(Vinylidene Fluoride)/Poly(Methyl Methacrylate) (PVDF/PMMA) Blends by Dielectric Spectroscopy. *Macromolecules* **1997**, *30* (10), 3042–3050. https://doi.org/10.1021/ma961774w.
(151) Teyssedre, G.; Bernes, A.; Lacabanne, C. Influence of the Crystalline Phase on the Molecular Mobility of PVDF. *J. Polym. Sci. Part B Polym. Phys.* **1993**, *31* (13), 2027–2034. https://doi.org/10.1002/polb.1993.090311316.
(152) Miyamoto, Y.; Miyaji, H.; Asai, K. Anisotropy of Dielectric Relaxation in Crystal Form II of Poly(Vinylidene Fluoride). *J. Polym. Sci. Polym. Phys. Ed.* **1980**, *18* (3), 597–606. https://doi.org/10.1002/pol.1980.180180318.
(153) Karasawa, N.; Goddard, W. A. Dielectric Properties of Poly(Vinylidene Fluoride) from Molecular Dynamics Simulations. *Macromolecules* **1995**, *28* (20), 6765–6772. https://doi.org/10.1021/ma00124a010.
(154) Hirschinger, J.; Schaefer, D.; Spiess, H. W. Chain Dynamics in the Crystalline A-Phase of Poly(Vinylidene Fluoride) by Two-Dimensional Exchange 2H NMR. *Macromolecules* **1991**, *24* (9), 6.

(155) Rekik, H.; Ghallabi, Z.; Royaud, I.; Arous, M.; Seytre, G.; Boiteux, G.; Kallel, A. Dielectric Relaxation Behaviour in Semi-Crystalline Polyvinylidene Fluoride (PVDF)/TiO2 Nanocomposites. *Compos. Part B Eng.* **2013**, *45* (1), 1199–1206. https://doi.org/10.1016/j.compositesb.2012.08.002.

(156) Nakagawa, K.; Ishida, Y. Dielectric Relaxations and Molecular Motions in Poly(Vinylidene Fluoride) with Crystal Form II. *J. Polym. Sci. Part -2 Polym. Phys.* **1973**, *11* (8), 1503–1533. https://doi.org/10.1002/pol.1973.180110804.

(157) Chanmal, C. V.; Jog, J. P. Dielectric Relaxations in PVDF/BaTiO3 Nanocomposites. *Express Polym. Lett.* **2008**, *2* (4), 294–301. https://doi.org/10.3144/expresspolymlett.2008.35.

(158) Bikard, J. Internal Report. Solvay.

(159) Padurariu, L.; Curecheriu, L. P.; Mitoseriu, L. Nonlinear Dielectric Properties of Paraelectric-Dielectric Composites Described by a 3D Finite Element Method Based on Landau-Devonshire Theory. *Acta Mater.* **2016**, *103*, 724–734. https://doi.org/10.1016/j.actamat.2015.11.008.

(160) Stauffer, D.; Aharony, A. *Introduction To Percolation Theory: Second Edition*, 2nd ed.; Taylor & Francis: London, 2017. https://doi.org/10.1201/9781315274386.

(161) Zhang, H. Fundamental Studies of Interfacial Rheology at Multilayered Model Polymers for Coextrusion Process. These de doctorat, Lyon, INSA, 2013.

(162) Draye, M.; Estager, J.; Malacria, M.; Goddard, J.-P.; Ollivier, C. Sonochimie organique. **2009**, 17.

(163) Laurens, J.; Jolly, J.; Ovarlez, G.; Fay, H.; Chaussée, T.; Sotta, P. Competitive Adsorption between a Polymer and Solvents onto Silica. *Langmuir* **2020**, *36* (26), 7669–7680. https://doi.org/10.1021/acs.langmuir.0c01312.

(164) Muthukumar, M. Nucleation in Polymer Crystallization. In *Advances in Chemical Physics*; Rice, S. A., Ed.; John Wiley & Sons, Inc.: Hoboken, NJ, USA, 2004; pp 1–63. https://doi.org/10.1002/0471484237.ch1.

(165) de Gennes, P. G. Solvent Evaporation of Spin Cast Films: "Crust" Effects. *Eur. Phys. J. E* **2002**, *7* (1), 31–34. https://doi.org/10.1140/epje/i200101169.